

# Interfacing DNA Nanostructures with Biology



William L. Whitehouse

University College London

This dissertation is submitted for the degree of  
*Doctor of Philosophy*

Supervisor: Professor Stefan Howorka  
June 2021

## Abstract

DNA nanostructures are powerful tools for synthetic biology with great promise as drug delivery devices. Their strength lies in the unique programmability offered by Watson-Crick base pairing and the ability to site-specifically incorporate bioactive components with nanoscale resolution. For example, lipid anchor cholesterol have been used to control binding of DNA nanostructures to synthetic and biological bilayer membranes. Additionally, various bioactive components have been attached to guide nanostructure interaction with eukaryotic cells. Yet, there is a lack of fundamental understanding of how cholesterol modification affects DNA nanostructure binding by cells and their uptake. Similarly, the endosome escape of DNA nanostructures remains a challenge and has not been achieved using programmed incorporation of escape-mediating components.

This thesis explores both topics using two archetypal DNA nanostructures, a 6-duplex bundle and a rectangular DNA origami. The first is used to interrogate how individual cholesterol anchors affect membrane binding and uptake by cancer cells, using fluorescence microscopy as read-out and a nuclease digestion strategy. The second is used as a basis to explore programmed presentation of the cell-penetrating GALA peptide with known membrane destabilising properties to probe endosomal release.

The findings reveal a clear correlation between cholesterol anchor number on the 6-duplex nanobundle, membrane binding and cell uptake kinetics. Fetal bovine serum is found to inhibit uptake but not membrane binding, suggesting an interplay between serum components, DNA nanostructures and the internalisation process in HeLa cells<sup>1</sup>. By comparison, presenting GALA peptides in defined number and position on a 50 x 60 nm DNA origami rectangle enhances binding to small unilamellar vesicles with the pH selectivity expected for GALA. The peptide also enhances origami-cell uptake as indicated by live-cell microscopy, with less certain results regarding endosome destabilisation and release.

The insight on cholesterol-mediated cell uptake of DNA nanostructures as a function of protein environment will guide the design cell-specific nanostructures. Furthermore, programming endosomal release with cell-penetrating peptides on DNA nanostructures has potential implications for the development of nano therapeutic strategies.

<sup>1</sup>Cholesterol anchors enable efficient binding and intracellular up-take of DNA nanostructures (2019) W. L. Whitehouse, J. Noble, M. Ryadnov, S. Howorka, *Bioconjug Chem* 30(7): 1836-1844.

## Impact statement

Much of the data presented here in Project – I was published in the ACS Journal Bioconjugate Chemistry, as follows: Cholesterol Anchors Enable Efficient Binding and Intracellular Uptake of DNA Nanostructures, *Bioconjugate Chem.* 2019, 30, 7, 1836-1844. The article may be found at the following address:

<https://doi.org/10.1021/acs.bioconjchem.9b00036>. The article describes how cholesterol can be used to augment and potentially control DNA nanostructure uptake into cancer cells, highlighting this strategy as a useful approach for applications in synthetic biology. The scope of this work has been expanded by recent publications from the group, demonstrating potential for translation into medical technologies<sup>91</sup>.

The work presented for this thesis as Project – II was severely interrupted by the Covid pandemic but is being pursued by colleagues in the Howorka Group with the aim of publishing findings, pending on experimental results, TBD.

## **Acknowledgements**

My thanks and love go to my parents Margie and Simon Whitehouse, for their never-ending support and encouragement. The same again for Yui, and my friends who I consider as family, members of the Howorka group from 2017-2021 and colleagues at the National Physical Laboratory. Without their support, this thesis would not have been possible. Finally, my thanks go to my PhD supervisors Max Ryadnov and especially Stefan Howorka who gave me enduring support and guidance throughout my studies at UCL.

## Table of contents

Abstract.....	2
Impact statement.....	3
Acknowledgements.....	4
Table of Contents.....	5
Acronyms.....	7
<b>1 Project – I: Introduction.....</b>	<b>9</b>
1.1 DNA Nanotechnology.....	9
1.1.1 The DNA origami Method.....	11
1.1.2 Assembly of DNA origami.....	14
1.1.3 Emerging Method For Fabrication of DNA Nanostructures.....	16
1.2 Interfacing DNA Nanotechnology with Biology.....	20
1.2.1 Stability of DNA Nanostructures under Biological Conditions.....	20
1.2.2 Strategies Used to Control and Augment DNA Nanostructure Interactions with Phospholipid Membranes.....	26
1.2.3 Delivery, Cellular Uptake & Processing of DNA Nanostructures....	30
<b>2 Project – I: Aims &amp; Rationale.....</b>	<b>43</b>
2.1 Components of Study.....	43
<b>3 Project – I: Results &amp; Discussion.....</b>	<b>43</b>
3.1 Assembly & Characterisation of the 6-duplex DNA Nanobundle.....	45
3.2 6-Duplex DNA nanobundle Interaction with HeLa Cells.....	46
3.3 Membrane Binding vs. Cellular Internalization.....	49
3.3.1 Nuclease Digestion Strategy - CLSM.....	52
3.3.2 Nuclease Digestion Strategy – Flow Cytometry.....	55
3.4 Nanobundle-Cell Binding as a Function of FBS presence.....	57
3.5 Intracellular Localisation.....	61
3.6 Nanobundle Induced Reduction of Cell Viability .....	66
<b>4 Project – I: Conclusions.....</b>	<b>68</b>
<b>5 Project – II: Introduction.....</b>	<b>70</b>
5.1 Cell Penetrating Peptides (CPPs) .....	70
5.1.1 CPPs: Endosome Escape.....	71
5.1.2 CPPs: Influence of Cargo.....	73
5.1.3 CPPs: Multivalency.....	75
5.1.4 GALA: A synthetic Amphipathic Cell Penetrating Peptide.....	78
5.2 Peptide-Oligonucleotide Conjugates.....	81

5.2.1	POCs: Applications & combination with DNA Nanotechnology.....	83
<b>6</b>	<b>Project – II: Aims &amp; Rationale</b> .....	89
6.1	Design – DNA origami scaffold for display of GALA Peptide.....	90
<b>7</b>	<b>Project – II: Results &amp; Discussion</b> .....	95
7.1	Assembly & Characterisation.....	95
7.2	GALA Induced Binding to Model Membranes.....	100
7.3	GALA Induced Cell Binding & Uptake - Flow Cytometry.....	104
7.4	GALA Induced Cell Binding & Uptake - CLSM.....	107
7.5	Stability in Biological Media.....	110
<b>8</b>	<b>Project – II: Conclusions</b> .....	113
<b>9</b>	<b>Conclusion - Summary</b> .....	114
<b>10</b>	<b>Methods &amp; Materials (project – I)</b> .....	117
10.1	6-duplex DNA Nanobundle Preparation.....	117
10.2	Cell Culture.....	117
10.3	Flow Cytometry Analysis on Cell Interaction of DNA Nanobundles.....	117
10.4	Nuclease Digestion & Flow Cytometry.....	118
10.5	Fluorescence Microscopy for Nanobundle Binding.....	118
10.6	Microscopy Analysis of Enzyme-treated Cells.....	118
10.7	Fluorescence Microscopy (Nanobundle Localisation in HeLa cells)....	119
10.8	Cell Viability.....	119
<b>11</b>	<b>Methods &amp; Materials (project – 2)</b> .....	120
11.1	DNA Origami Schematics.....	120
11.2	DNA Origami Staple Sequences.....	121
11.3	DNA Conjugate Sequences.....	125
11.4	DNA Origami Purification & Preparation.....	126
11.5	Gel Electrophoresis.....	127
11.6	AFM Analysis.....	127
11.7	SUV Formation.....	128
11.8	Vesicle Binding Assays.....	128
11.9	FC Analysis on DNA Origami Interaction with HeLa cells.....	129
11.10	Microscopy Assays for Origami Binding and Uptake.....	129
11.11	Electrophoresis Analysis of GALA handle hybridisation.....	130
11.12	Biotin-Streptavidin Binding Assay.....	130
11.13	Cy3-Competition binding.....	131
<b>12</b>	<b>Supporting Information</b> .. .....	132
<b>13</b>	<b>Bibliography</b> .....	133

## Acronyms (abbreviations)

0H origami	DNA origami scaffold with zero handles
100H origami	DNA origami scaffold with one hundred handles
AF647	AlexaFlour-647
CLSM	Confocal Laser Scanning Microscopy
CPP	Cell penetrating peptide
Cy3	Cyanine 3
DMEM	Dulbecco's Modified Eagle Medium
DNS	DNA nanostructure
DX cross over	Double-crossover
FC	Flow Cytometry
NB-0C	Nanobundle with zero cholesterol anchors
NB-1C	Nanobundle with one cholesterol anchors
NB-3C	Nanobundle with three cholesterol anchors
Opti-MEM	Optimised minimal essential media
PBS	Potassium-buffered saline
PCR	Polymerase chain reaction
PEG	Polyethylene glycol
PH	Peptide-handle
POC	Peptide-oligonucleotide conjugate
PX cross over	Paranemic-crossover
ssDNA	Single stranded DNA
WBC	White blood cell

## **Declaration**

I, William L. Whitehouse confirm that the work presented in this thesis is my own. Where information has been derived from other sources, I confirm that this has been indicated in the thesis.

# 1. Introduction

## 1.1. DNA nanotechnology

DNA nanotechnology constitutes a highly versatile strategy for bottom-up design of increasingly sophisticated nanoscale structures. This is owed to the highly programmable self-assembly properties of DNA<sup>1</sup>, which has nanometre-scale sizing between its smallest individual components (nucleotides). Strict base-pairing rules between these units mean that length, positions and orientation between oligonucleotides can be controlled in a programmed manner<sup>1</sup>. These factors, along with the increasing ease of access to DNA, make DNA nanotechnology an attractive platform for biomolecular engineering<sup>2</sup> and subsequent development into an array of functional devices<sup>3</sup>.

One of the key roles of DNA in nature is to serve as a repository of genetic information for coding of proteins, which can be complex in terms of structure. By comparison, DNA is mostly limited to linear double-helix structures though deviations in biology do exist<sup>4</sup>. These observations prompted researchers to investigate whether DNA can be programmed to assemble into more complex non-canonical conformations. In the early 1980s, Ned Seeman addressed this subject by proposing the 'four-way junction' (Figure 1 – A), an alternate arrangement of DNA sequences made from alignment of four separate oligonucleotide strands<sup>5</sup>. This work paved the way for design of simple 2D and 3D DNA nanostructures, albeit with limited scope in terms of possible geometries and persistence lengths<sup>6</sup>. It would take just over ten years for the next step in structural DNA nanotechnology, whereby the double-crossover motif was designed<sup>7</sup> (Fig 1 – B). These new arrangements of DNA allowed for fabrication of increasingly sophisticated 2D structures with larger dimensions and maintained rigidity<sup>8-9</sup>.

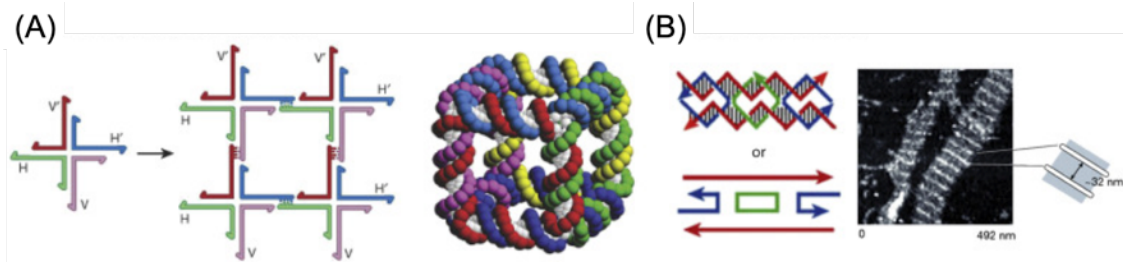


**Figure 1. DNA motifs fundamental to DNA Nanotechnology. (A)** Schematic illustration of a four-way DNA ‘Holiday’ junction and the first 3D DNA assembly. **(B)** Schematic of the most simple double-crossover motif. Self-assembly of this motif with sticky ends resulted in a striped pattern extended tile type structure, imaged with AFM. *\*Images are adapted from reference X ‘DNA in a material world’ by Nadrian C. Seeman – Reference 4.*

The next step in DNA nanotechnology was made roughly ten years after report of the double-cross over motif, by the introduction of DNA origami<sup>10-11</sup>. This new method improved ease of access to the non-expert for design of even more sophisticated structures that could be rationally engineered to adopt complex 3D shapes<sup>12</sup>. Following this, several other methods have been developed to expand the design approaches for DNA nanostructures, including DNA ‘brick-assembly’<sup>13</sup> and ‘wire frame’<sup>14</sup> strategies, which have enabled fabrication of larger structures still, and have paved the way for engineering of even more complex geometries, with sizes ranging from tens of nanometers up to the micron scale<sup>15-16</sup>. Subsequently, design of mechanized DNA nanostructures was realised, by combining advances in structural DNA nanotechnology along with development of a range of dedicated softwares to aid the design process<sup>17</sup>.

Engineering of ‘dynamic’ DNA nanostructures depends upon programmed switching of structure conformations and has allowed for development of a wide range of functional devices with applications in biosensing<sup>18-19</sup>. Such devices can exploit molecular algorithms or so-called ‘DNA computation’<sup>20-21</sup>. Furthermore, DNA nanostructures have been designed to serve as: platforms for biological assays<sup>22-23</sup>, or as cargo sorting devices<sup>24</sup>, robotic or ‘mechanical actuators’<sup>25-26</sup>, and drug delivery vectors<sup>27-28</sup>. Dynamic DNA nanotechnology is rapidly advancing in a near exponential manner, a time-line for which is depicted in figure 2.

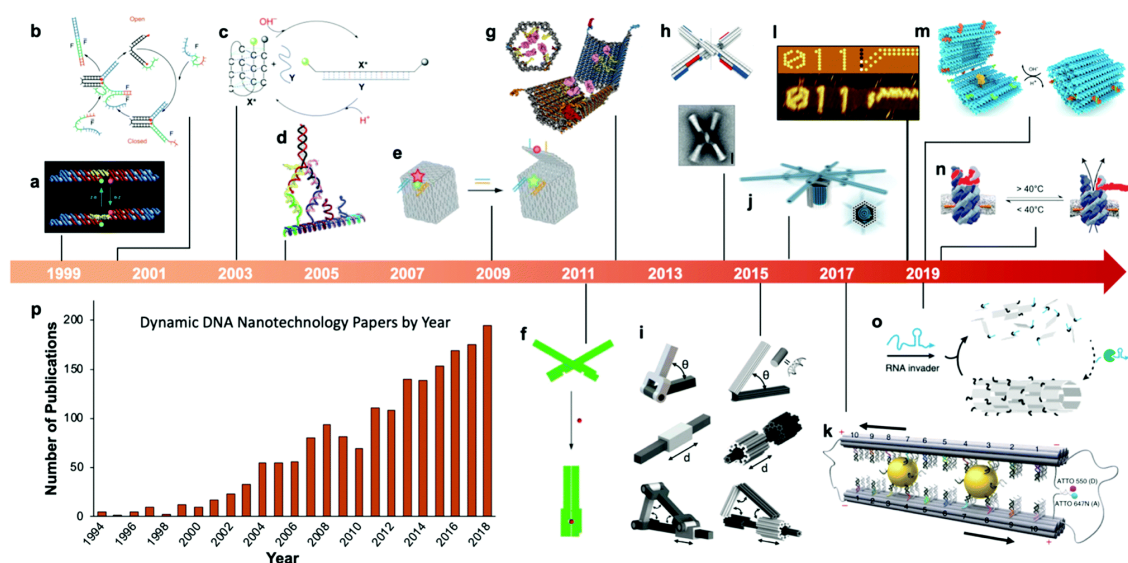


**Figure 2. Timeline infographic of dynamic DNA nanostructures.** Inspired by the pioneering work of Nadrian Seeman, advances in DNA nanotechnology have allowed for design of increasingly sophisticated dynamic DNA nanostructures. *\*Note - figure adapted from the review article ‘Dynamic DNA nanotechnology: toward functional nanoscale devices’<sup>29</sup>.*

### 1.1.1. DNA origami method

DNA origami is a powerful method for design and fabrication of DNA-based nanostructures, developed initially by Paul Rothemund and reported in their seminal article ‘Folding DNA to create nanoscale shapes and patterns’, *Nat*, 2016<sup>30\*</sup>. The method involves folding long, single-stranded DNA oligonucleotides into arbitrary 2D or 3D shapes with the help of numerous, shorter oligonucleotides referred to as ‘staples strands’. The longer ‘scaffold’ strand is mixed with staples which subsequently self-assemble in a ‘one-pot’ reaction process. The design process is aided by computer software, the most popular of which is caDNAo<sup>30</sup>, and starts with building of a geometric model, which can be done by hand. The model serves as a template, which is used to approximate the desired shape of the nanostructure (Fig 3 – A). In the figure below, featured in Rothemund’s original article, an example shows a scaffold shape filled from top to bottom by an even number of parallel duplex helices represented as cylinders.

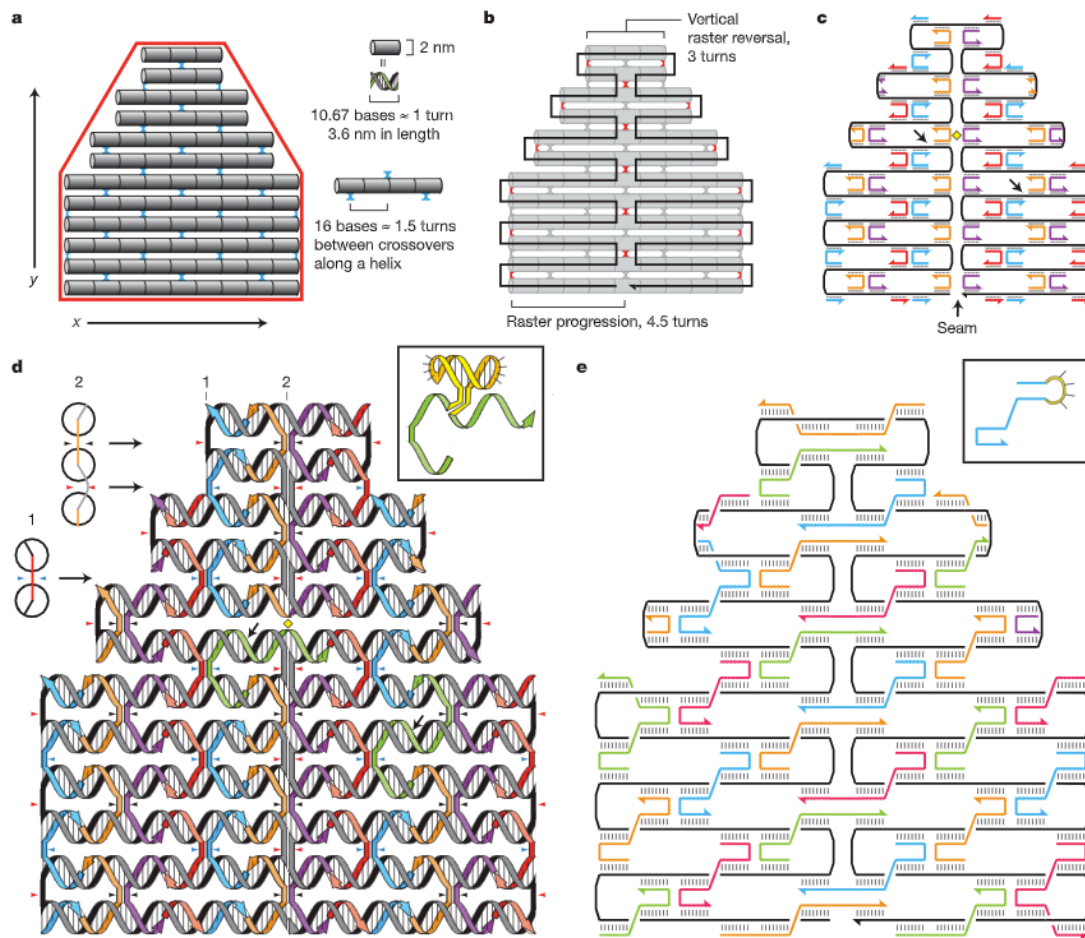


**Figure 3. DNA origami design process.** (A) A desired shape (red) is approximated by parallel alignment of double helices, bridged by periodic crossovers (blue). (B) A single scaffold strand (black) runs through each helix to form additional ‘scaffold crossovers’. (C) Computed design closely matches the ‘hand drawn’ design (a). (D) depicts an alternate representation of (C) with strands represented as helices. Crossover positions ‘1 and 2’ (from top left of the structure model) are represented with side-view cross-sections (top left), which indicate backbone positions using coloured lines, and major/minor grooves with small and large interceding angles. (E) The finished design after readjusting along the structure seams. Most staples have been computed to be 32nt long and span three helices as opposed 16mer staples initially conceived in the first design stages (C-D). \*Figure adapted from the original article ‘Folding DNA to create nanoscale shapes and patterns, by Paul Rothmund – Reference 28.

DNA helices can be adjusted in length to fit the desired shape and are constrained by integers of full-turns around the DNA helix (axis). Binding of the helices is then achieved by implementing a periodic array of staple ‘cross overs’

(see Fig 1), which determine the point at which the DNA strand from one helix bridges over to its adjacent helix, linking the two strands together. The next step, illustrated in Fig 3 – B, is achieved by folding a single ‘scaffold’ sequence along the aligned helices so that it comprises one of the two strands used in each duplexed DNA helix. The progression of this scaffold strand thus creates an additional set of ‘scaffold crossovers’ (indicated in Fig 3-b by small red crosses). Importantly, the scaffold is restrained to fold only over positions where helices align according to the DNA twist. I.e., for the scaffold strand to run between adjacent helices, it must be an odd number of half turns (of a full DNA alpha helix twist). Subsequently, the distance between scaffold-crossovers must fulfil an even number of half-turns to reverse its direction (vertically), so that it returns to previously aligned helices. The central seam in the structure (depicted in Fig 3) is typical of DNA origami nanostructures and is compatible with scaffold strands that close their own loop.

Following design of the structure model and folding paths, a list of DNA sequences is generated along with offset parameters defined in units of half-turns. These lists are then used in combination with the scaffold DNA sequence as an input for dedicated software, which generates a list of staple strand sequences to provide base-pairing links (which complement the scaffold sequence and create the required crossovers). The resulting staple crossovers are anti-parallel with respect to the scaffold direction and proceed in the opposite direction. This process is used to achieve a stable configuration of DNA links generally required to generate even simple DNA nanostructures<sup>7</sup>.

Global twisting of the structure must also be factored by taking into account the non-integer number of base pairs per half-turn, along with the asymmetric nature of the DNA helix originated from its minor and major grooves<sup>31</sup>. To account for this, the scaffold-crossover twist is calculated and altered to minimize global strain across the structure. Staple strand sequences are generated accordingly, to take into account the required individual base pair alterations. Fundamentally, strain is caused by representing 1.5 turns with 16 base-pairs, which is overcome by arranging period crossovers with a ‘glide

symmetry' (Fig 3 – D). This involves facing of the minor grooves in opposite directions to one another, across alternating columns of DNA helices.

Figure 3 – D also depicts the 'nicks' that occur in the DNA backbone as a result of staples meeting one another, which occur on the termini of helices, i.e., at the bottom and top of each helix face. The final step in the design process involves expanding the binding domains between staples and complementary sequences in the scaffold strand in order to promote binding specificity and increase the subsequent melting temperature of the assembly. This process involves merging pairs of adjacent staples to yield a smaller number of longer staples (Fig 3 – E). Additional breaks and or nicks may then be generated to strengthen seams (regions where the scaffold strand does not cross). This final step is important to yield staples that bridge across the seam, and can have important implications in the resultant patterning that can be exploited to load functional moieties after assembly of the structure.

### 1.1.2. Assembly of DNA origami

The integral components of a DNA origami folding reaction generally comprise of the DNA scaffold strand, DNA staple strands (usually in the range of 5-10x molar excess over the scaffold), mono and/or divalent cations provided as salts and a pH buffer component (usually Tris-acetate-EDTA) – (TAE). After the components have been mixed, the reaction is heated to ensure all DNA components are single-stranded, followed by controlled cooling to slowly anneal the strands. The cooling step is usually conducted across a 'thermal ramp', i.e., a reduction of temperature across discrete steps and cycles. The heating and cooling is conducted in a polymerase chain reaction (PCR) thermocycler to control the process and to find the optimal step parameters for efficient folding of the structure.

Divalent cations are generally required to provide electrostatic screening between the DNA strands that comprise a DNA nanostructure, and thereby enable their bridging<sup>32,255</sup>. Due to their higher coordination power over  $\text{Ca}^{2+}$

ions, divalent  $Mg^{2+}$  ions are most commonly utilised in this context and provide the most sensitive electrostatic screening capabilities for DNA compaction. Notably, multi-layered DNA origami nanostructures can fail to assemble correctly without sufficient  $Mg^{2+}$  concentration or may complex to form dimers or multimers of structures if concentrations are too high. A  $Mg^{2+}$  screening process is usually carried out to find the optimal concentration in combination with the required staple to scaffold molar ratio<sup>33</sup>.

Much work has been done since the initial conception of DNA origami, to investigate the mechanisms underlying the assembly process. To this end, folding pathways for multi-component DNA origami nanostructures have been investigated, in order to improve design of structures with complex geometry and mechanical actuating features<sup>34</sup>. A novel approach using fluorescence monitoring and cryogenic reaction quenching was utilised by Dietz and co-workers in 2012, to investigate the folding thermodynamics of DNA origami, revealing discrete transition temperatures for assembly and thus suggesting strong cooperativity as an underlying factor controlling the process<sup>35</sup>.

Later work revealed that certain DNA origami nanostructures could be efficiently folded using isothermal assembly conditions, a strategy now confirmed by numerous other groups<sup>36-37</sup>. Notably, Dietz et al recently (2019) provided a comprehensive reference dataset for the kinetics of a multi-layer DNA origami folding process<sup>38</sup>, along with novel 'folding maps' that describe the assembly process for a model 42-helix bundle structure (Fig 4, pg. 16). This was achieved by measuring the folding kinetics of every constituent staple strand along with their terminal segments during the folding process of the DNA origami nanostructure. The team used this approach to innovatively uncover the sequence of events along the folding pathway, providing molecular resolution to the overall process in terms of strand routing and kinetic parameters (Fig 4, A - C).

Advancements to the assembly process of DNA origami and the methods used to generate the required components, especially the long single-stranded scaffold DNA, are discussed in the following section.

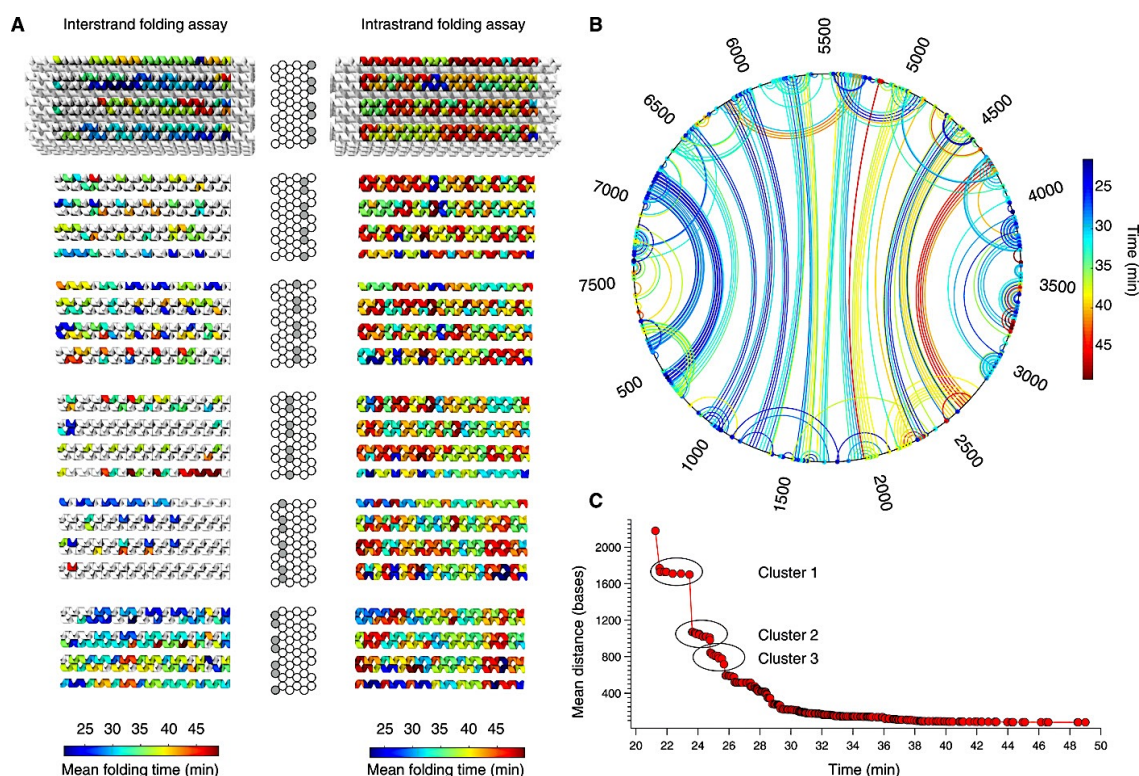


**Figure 4. Folding pathway and routing of DNA origami staple strands. (A)** 3D model of a 42-helix multi-layered DNA nanobundle. Experimentally measured mean-folding time for each staple strand is provided by colour coding. **(B)** Folding pathway map where arcs denote crossover points between staple strand segments. Discs at the map periphery denote terminal strand positions. Numbers denote scaffold strand base indices. Colour coding indicates the mean-folding time for each strand terminal segment as resolved by the interstrand assay (described on pg. 16). **(C)** Plot depicting estimation of average interbase distance across the scaffold as a function of folding time. Circles represent new ‘compaction’ events produced by binding of a new staple segment at the mean time resolved by the interstrand assay.

### 1.1.3. Emerging methods for fabrication of DNA nanostructures

Numerous applications in biosciences and especially in DNA nanotechnology require the use of single-stranded oligonucleotides. Examples include multiplexed PCR<sup>39</sup>, DNA-PAINT<sup>40</sup>, and fluorescence in situ hybridisation (FISH)<sup>41</sup>. Additionally, the most widely utilised method for DNA nanostructure engineering (the origami method) require long (>200nt) ssDNAs which are difficult and costly to produce by chemical synthesis methods<sup>42</sup>. To these ends,

polymerase chain reaction (PCR) is the most tried and tested enzymatic method for oligonucleotide amplification and is used routinely in DNA nanostructure assembly. However, when coming to large-scale synthesis of ssDNAs there are certain limitations. These include the fact that PCR is not amenable to scaling-up<sup>43</sup> and furthermore, that PCR produces double-stranded DNA (dsDNA) which must be subsequently treated via cost and time-consuming methods in order to produce the required ssDNA oligonucleotides.

Specifically, a major cost for fabrication of DNA origami nanostructures relates to the relatively long bacteriophage ssDNA used as the ‘scaffold strand’ (see section 1.1.1). In this context, scaling-up of PCR provides limitations, as the maximum amplicon lengths achievable are still smaller than the most widely used scaffold ssDNA (m13mp18 ssDNA, composed of 7249 nucleotides). Notably, strand-displacement amplification could provide an alternate enzymatic route for oligonucleotide synthesis as this method involves the direct production of ssDNAs (Fig 5), but comes with the unfortunate drawback of synthesis scales being limited to nanogram quantities<sup>44</sup>.

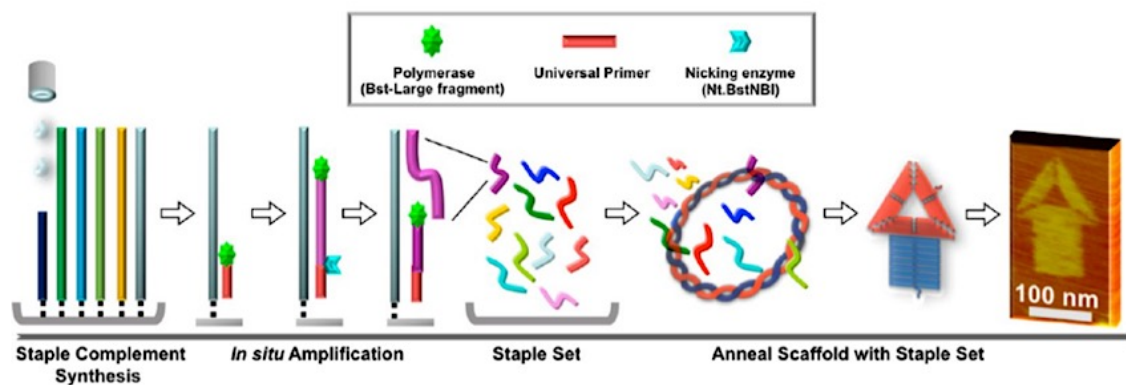


**Figure 5. Assembly of a 14kb DNA origami nanostructure achieved by strand-displacement strategy.** Re-useable surface-bound template (complement) strands are synthesised *in-situ* using a piezoelectric inkjet system, and are appended to the chip surface via a universal 25-mer linker (left). DNA polymerase (green) then extends and displaces preceding strands whilst a nicking endonuclease (blue) separates the staple from universal linker (red) to generate new 3'-ends for the next round of extensions. Amplified staple sets are taken and used for downstream fabrication of large heterodimeric origami nanostructures. \*Image reproduced from reference 5.

Alternative to the abovementioned methods, stoichiometric ssDNA (14-378nt) can be produced from clonal templates (i.e., sequence-verified pseudogenes) using *Escherichia coli* in the form of phagemid DNA. This method was reported in 2013 by Hogberg et al<sup>45</sup>, and was validated by using the produced ssDNAs to assemble DNA crystals and nanostructures. Numerous methods are advancing access to oligonucleotides, including inkjet printing methods (microarray-chip-synthesised libraries)<sup>46</sup>, light-assisted<sup>47</sup> and electrochemical synthesis<sup>48</sup>, and rolling circle amplification<sup>49-50</sup>. Prices associated with oligonucleotides produced via microarray or 'synthesis on a chip' methods are up to two-orders of magnitude lower than with traditional column-based automated synthesis but come the limitation of synthesis at attomolar ( $10^{-18}$ ) scale production per oligonucleotide<sup>51</sup>. Indeed, only nanomolar quantities are typically required for research-scale synthesis of DNA nanostructures, yet price is dictated by production efficacy, and thus remains a prohibitive cost for many researchers in comparison to larger amounts of shorter ssDNAs that can be produced at higher yields with improved efficiency.

Abovementioned methods such as the clonal-template strategy provide rigorous control over ssDNA production. However, many applications for oligonucleotides, including DNA origami, do not require fastidious stoichiometric control and can bear similar error rates of oligonucleotide sequences comparable to those produced by automated solid-phase synthesis<sup>52-53</sup>. To these ends, rolling circle amplification (RCA) is a well-studied technique that can be used to produce long (>70Kda) ssDNA<sup>54</sup>.

RCA is an isothermal, enzymatic process and can be controlled using a single DNA polymerase (typically Phi29). The technique can continuously elongate a complementary ssDNA around circular ssDNA template and has been used extensively for ultrasensitive DNA detection<sup>54</sup>. More recently, RCA has been applied to generate large-scale ssDNA templates for downstream assembly into discrete DNA nano-architectures including; Y-type assemblies for siRNA delivery (Fig 6)<sup>55</sup>, padlock-type probes for miRNA detection<sup>56</sup>, and larger DNA origami-based nano-ribbons for delivery of immunostimulatory drugs<sup>57</sup>. The strategy of RCA is outlined in Fig 6, with reference to work by Hong et al.

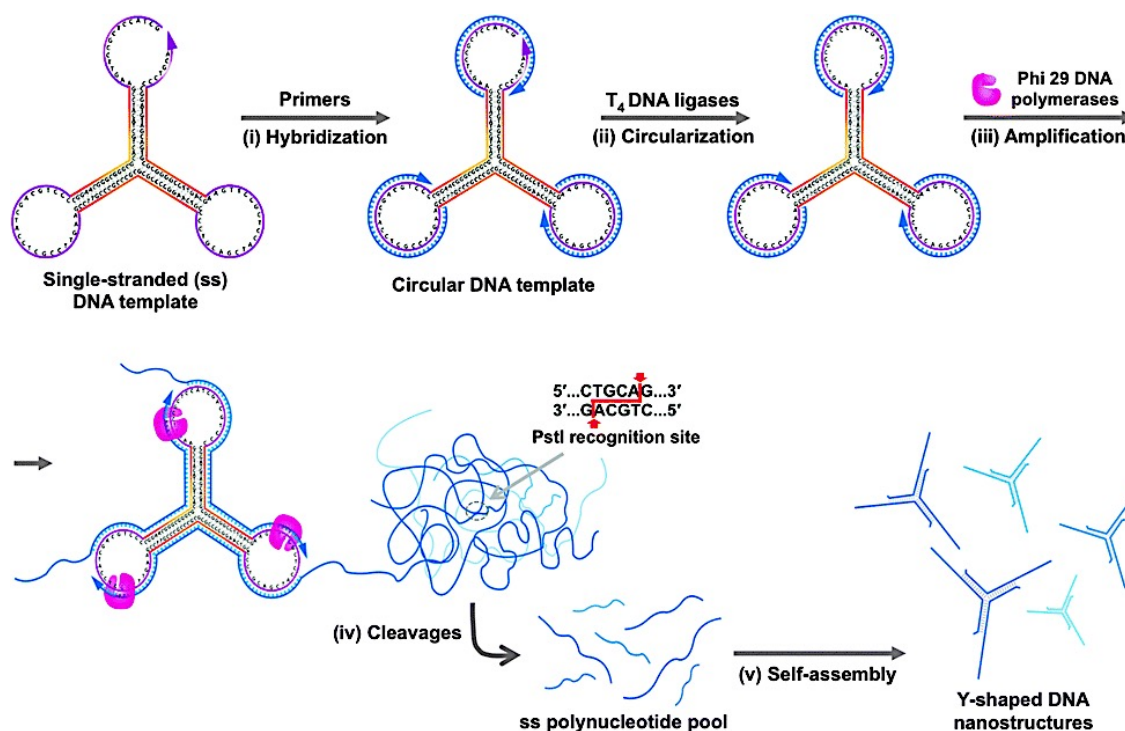


**Figure 6. Schematic illustration of stepwise approach for preparation of Y-shaped DNA nanostructures using the RCA.** Steps: (1) ssDNA (159nt) DNA templates were designed to self-assemble into Y-shaped DNA nanostructures with three-way junction at their core and three-hairpin loops at each arm. The three arms contain two closed loops and one open loop with a nick, which encodes a short (20 nt) primer recognition sequence in addition to a short (6 nt) palindromic restriction site for endonuclease PstI enzyme. (2) The 5'-phosphate group and 3'-hydroxyl group in the open loop can be closed via enzymatic ligation producing closed ssDNA circular templates as substrates for subsequent RCA. (3) In the presence of Phi29 DNA polymerases, the primer 3'-ends are continuously elongated around the circular ssDNA template at a constant temperature. (4) Elongated ssDNA is finally digested by PstI to produce a DNA polynucleotide pool, from which Y-DNA nanostructures are produced, identical in sequence to the initial Y-shaped DNA templates.

Up to now, DNA nanostructures have mostly been assembled and characterised in-vitro. This is due to the control afforded in terms of environment, which is likely necessary to carry out precise self-assembly of nucleic acids into defined structures. Nevertheless, recent research has proved that in-vivo synthesis of DNA nanostructures is indeed possible, albeit difficult to assess. Lin and colleagues recently reported the first instance of holiday junction (the four-way junction) assembly in-vivo<sup>58</sup>. This simple but fundamental

motif was used as the basis to explore the possibility that rationally designed DNA nanostructures can be assembled in a cellular environment. Indeed, recent reports indicate that paranemic cross-over nanostructures (see section 1.2.1, pg. 24) could be synthesised in-vivo, and displayed improved ratios of full-length to truncated products relative to those achieved via in-vitro experiments<sup>58-59</sup>. In-vivo replication of DNA can provide for much longer sequences (>1kb) than those made via solid-phase synthesis of oligonucleotides (150-200nt), providing the means to fabricate much larger extended, modular structures.

## 1.2. Interfacing DNA nanostructures with biology

The key challenge in the development of all drug delivery systems is to achieve targeted and specific delivery. Non-viral delivery vectors benefit from their freedom of design<sup>60</sup> and reduced propensity to elicit immune responses<sup>61</sup>. To this end, a wide range of archetypal DNA nanostructures (DNSs) have become readily available to researchers, spurring interest in their functionalization with various pharmaceuticals and biologically relevant molecules<sup>62</sup>. The ease with which DNSs can be functionalized with chemical or bioactive molecules is being made increasingly straightforward by advances in synthesis protocols for DNA bioconjugates<sup>63-64</sup>. These advances, coupled with means to engineer such structures as 'dynamic devices' constitutes a highly malleable platform for engineering of responsive and biocompatible DNSs for drug delivery<sup>62-65</sup>. However, delivery into biological environments is complicated by harsh conditions found in the physiological environment, including the presence serum nuclease enzymes<sup>66</sup>, elevated temperatures and low concentrations of divalent cations<sup>67</sup>, which may be required to ensure stability of DNSs along with their subsequent function.

This chapter focuses first on stability considerations (1.2.1) to outline key factors precluding application of DNSs in biological environments. Strategies to control and augment DNS interactions with phospholipid membranes are discussed focussing on lipid modification (1.2.2). Finally, the section concludes with a section on cellular uptake and processing of DNSs (1.2.3) to highlight key trends observed in this context including endosomal escape, a bottleneck for DNS-mediated drug delivery. Section 1.2 aims to place this thesis into context with respect to the literature and the recent work conducted in the Howorka group, that has enabled project – I.

### 1.2.1 Stability under biological conditions

Precluding their application in biological environments, DNSs must be designed with stability in mind. DNA is sensitive to temperature, ion-depletion and digestion by deoxyribonucleases<sup>65-66</sup>. These vulnerabilities are commonly overcome by chemically modifying DNA<sup>68-69</sup>, supplementing the cell culture

medium with salts<sup>70</sup> (for *in-vitro* work), or by incorporating design features that sterically block access to enzymes<sup>69</sup>. Examples of such approaches are the focus of this section. However, it is worth noting that DNA's intrinsic sensitivity can also be exploited, in order to fine-tune bioactivity of therapeutic cargo. In this context, Chan and co-workers recently demonstrated how vulnerability of DNA in the physiological environment could be exploited to reduce toxicity of inorganic nanoparticles that would otherwise have proven difficult to degrade<sup>71</sup>. The team used a colloidal superstructure DNA-based strategy to achieve this, where upon interaction with tissues and cells, the large colloid-type DNA-based assemblies were enzymatically digested into their constituent parts. Crucially, this was shown to reduce nanoparticle retention by specialised cell types whilst simultaneously enhancing their *in-vivo* efficacy towards tumours.

Fetal bovine serum (FBS) is an essential component used in cell and tissue culture medium, and contains numerous nuclease enzymes known to digest nucleic acids in a non-specific manner<sup>72</sup>. Consequently, numerous studies have sought to assess and improve stability of DNSs in FBS<sup>73-74</sup> with the caveat however that functional differences may be missed with respect to human-specific serum components. Notably however, the lower nuclease activity of human serum relative to FBS can be mimicked by heat inactivation\*. Tetrahedral DNSs, one of the most utilised architectures, have been shown to remain stable for at least 12 hours *in-vivo*<sup>73</sup> (Fig - 7), and up to 42 hours in cell media supplemented with 10% FBS. Steric accessibility of restriction sites in these structures, to nuclease enzymes, was found to be the key factor for their observed stability properties, which are provided for by rigid tri-dimensional topology. Notably, further stability was achieved against nuclease digestion by ligation of DNA nicks in the structure. As a control, the rate of digestion of a single-stranded DNA (ssDNA) was found to be three times faster than that for the fully assembled structure (Fig 7 – A). In this context, Sleiman and colleagues demonstrated that oligonucleotides could be significantly protected from nuclease digestion by folding the DNA into a triangular prism topology (Fig 7 – B). Addition of hexaethylene glycol units was shown to confer further stability, allowing the structure to retain structural integrity for up to 62h in FBS containing media (Fig 7 - B)<sup>75</sup>.

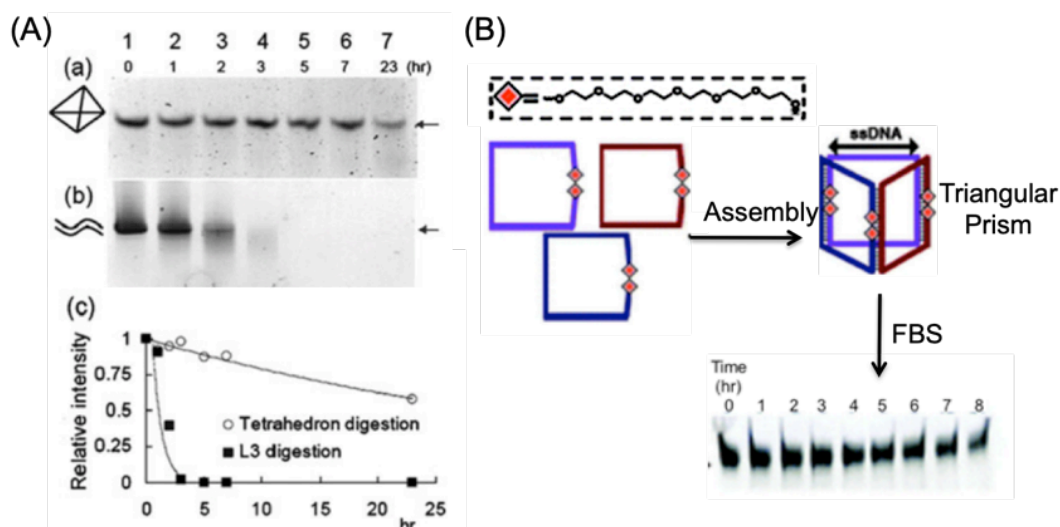


**Figure 7. Stability of DNA nanostructures towards nuclease digestion**  
**(A)** Denaturing PAGE of DNA tetrahedron digestion vs. a respective linear DNA duplex. (a) The DNA tetrahedron is significantly more stable than its (b) 'linear' counterpart. (c) Band intensities fit a first-order decay profile. Figure reproduced from *H. Bermudez and J. Keum\**. **(B)** Chemically modifying the protruding strands from a DNA nanostructure with hexaethylene glycol units can enhance stability to serum nucleases as demonstrated by PAGE analysis. Figure reproduced refs 73 and 75.

The significance of topology and nucleic acid conformation on DNS stability was further scrutinised by Graugnard and colleagues in 2015<sup>76</sup>. The team used a DNS capable of assuming three distinct topological states (Fig 8 – A). Whilst ssDNA controls were readily digested, the nanodevice retained its ability to undergo conformational operations for up to 6h in human serum. The study revealed the importance of carefully considering molecular conformation of DNA in the context of overall structure topology. Crucially, this work found that human serum produced less drastic effects on stability vs. FBS, emphasising the importance of serum components from different biological origins. It is worth noting that these findings have to some extent however been conflicted, with some studies suggesting that topological considerations were of minimal effect<sup>77\*</sup>. Perrault et al, found instead that topology of DNSs had little effect on serum stability and that rather; structure stability was due to cation depletion, which was time and design-dependant (Fig 8 - B). Either way, systematic studies focused on using human-relevant serum will be crucial in order to advance DNSs in the context of clinically relevant applications.

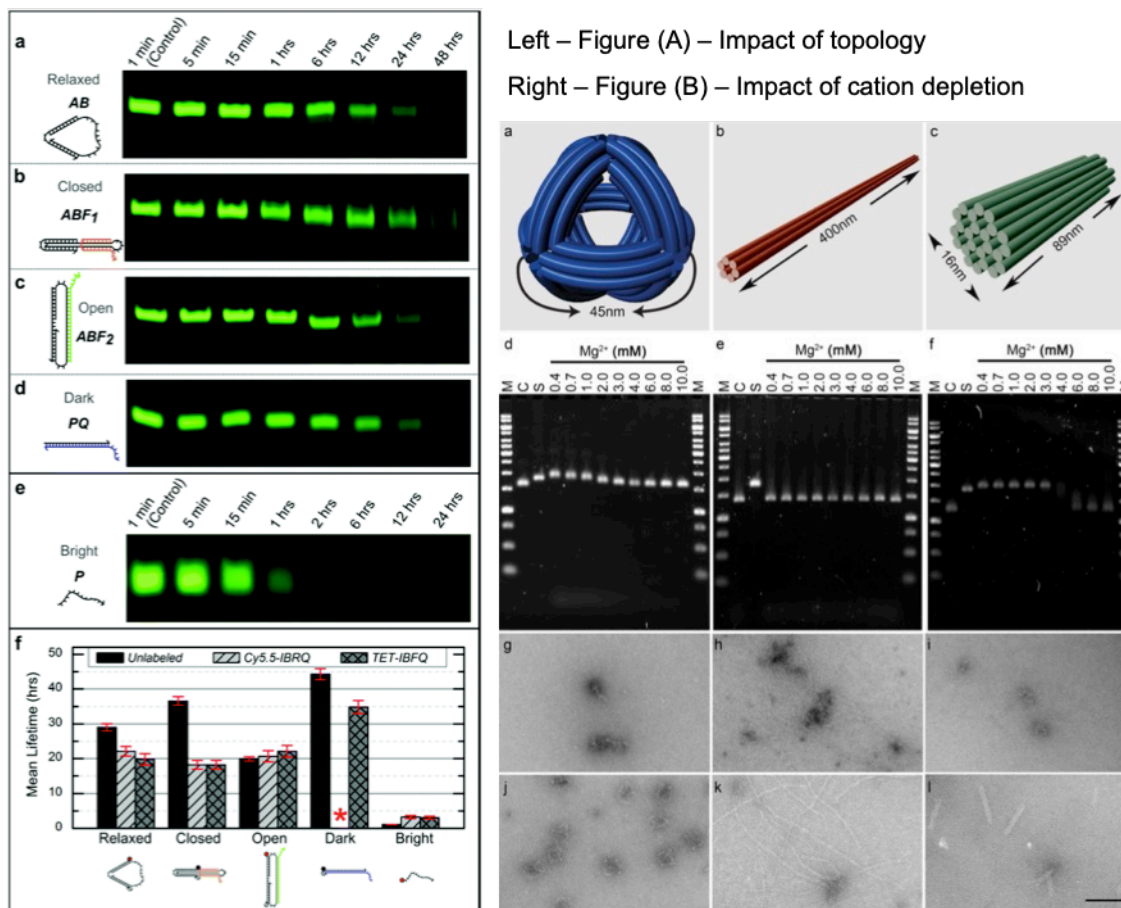


**Figure 8. Effects of topology on DNA nanodevice stability.** (A) The molecular conformation of a nanodevice has a significant effect on its stability in human serum at 37°C, as demonstrated by PAGE analysis. \*Figure reproduced from reference 75. (B) Effects of cation depletion on DNA nanostructure stability as analysed by agarose gel electrophoresis (AGE). Three test nanostructures show distinct migration patterns as a function of divalent cation depletion in culture medium, indicating varying degrees of structural stability. \*Figure reproduced reference 76, by Perrault, et al.

The fundamentals of DNA conformation and their effect on stability of higher order assemblies cannot be overstated. This is demonstrated in nature but also by significant advances made in structural DNA nanotechnology (see section 1.1.1). In the context of molecular and structural conformation of nucleic acids, Halvorsen and colleagues made important contributions by studying cross-over dependent nuclease resistance and biostability, finding that certain multi-stranded DNA motifs called ‘paranemic’ cross-overs (PX) were capable of imparting significant stability properties against nuclease digestion<sup>78</sup> (Fig 9 A-C). The pronounced difference was owed to changes in

the DNA helical-twist, as well as alterations to the nature of base-pairing density in relation to crossovers or DNA junctions. DNase I, a well-known nuclease present in most serums, has been shown to require a substrate with at least 6-8 base pairs for efficient digestion<sup>79</sup>. For PX DNA, the cross-overs occur only every half-turn, thereby producing double-helical regions between cross-overs with only 5-6 base-pairs which may inhibit access to DNase I to reduce modes of digestion. Such studies have important implications for DNA nanotechnology in the context of biostability, by expanding the repertoire of design approaches from the ‘bottom-up’.

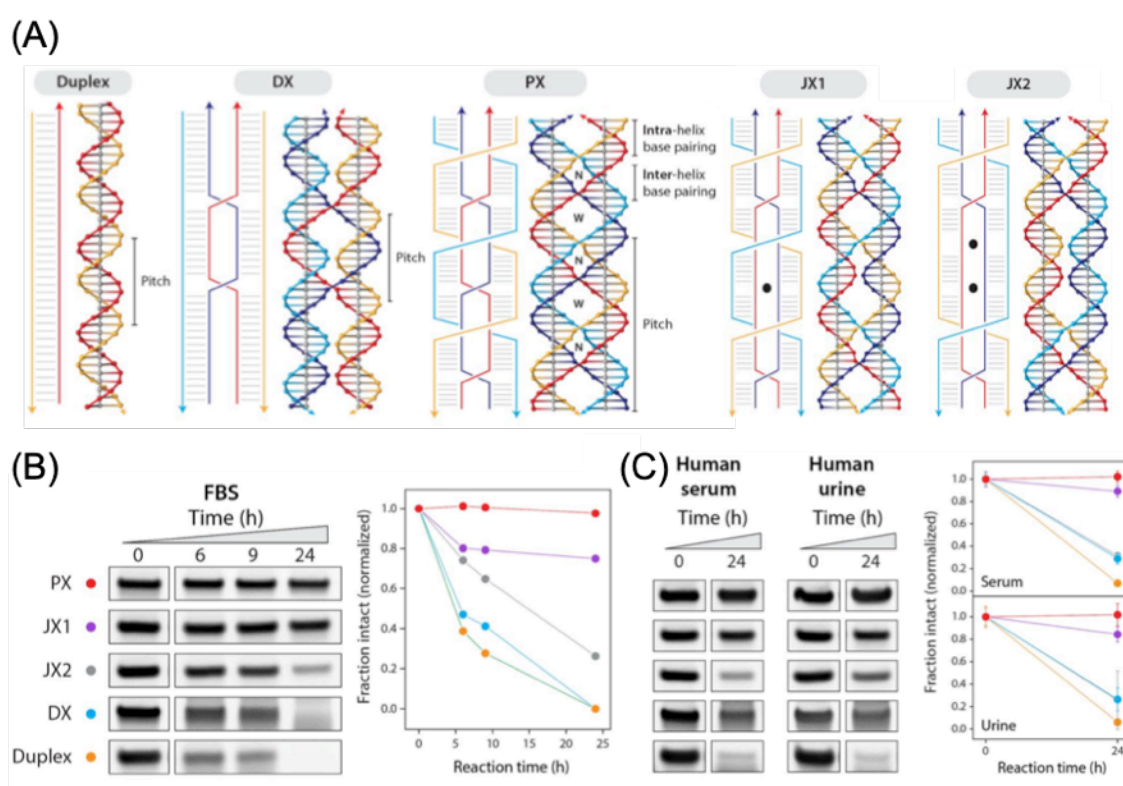


**Figure 9. Structural motifs in DNA nanotechnology and their stability to nuclease digestion. (A)** Design and structures of paranemic crossover (PX) DNA. Schematic models of; B-DNA duplex, a double crossover (DX) motif, a paranemic crossover (PX) motif, and two PX variations JX1 and JX2, which lack 1 and 2 crossovers respectively (shown as black dots). **(B)** Non-denaturing gels and degradation plots of control structures alongside PX DNA in 10% FBS. **(C)** Gel analysis and corresponding quantitative plots in 10 % human serum and human urine for 24h. *Figures adapted from reference 77, Halvorsen, et al.*

With direct relevance to the findings presented in this PhD project, Burns and Howorka recently reported on biostability of 6-duplex ‘DNA nanobundles’, by investigating their water-solubility in various buffered solutions<sup>80</sup>. Notably, results showed that aggregation of these structures was induced by their modification with hydrophobic lipid moieties, which were used to augment their interaction with phospholipid membranes (Fig 10 – A/B).

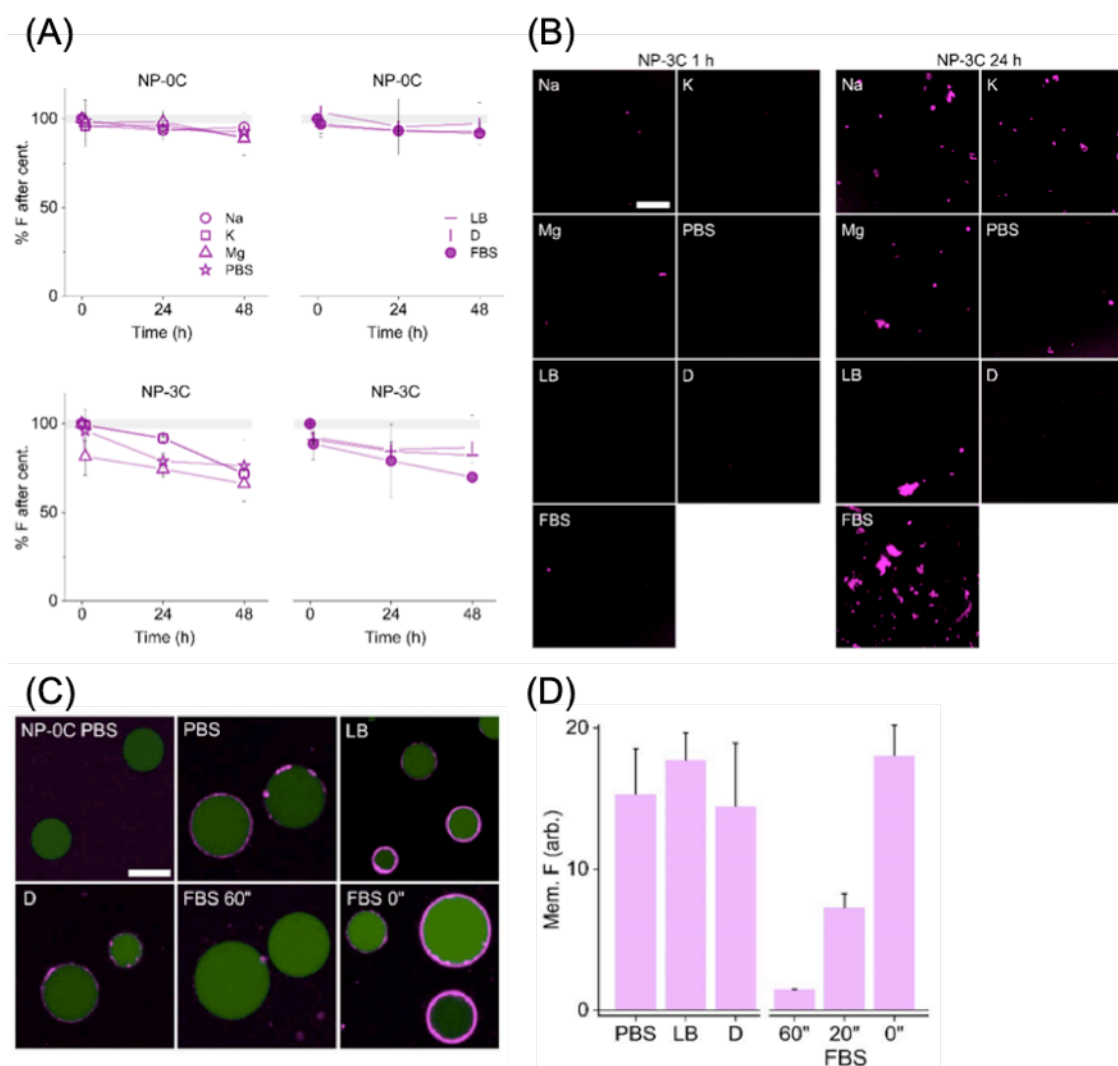


**Figure 10. Biostability of 6-Duplex DNA Nanobundles.** (A) Time-dependent aggregation of DNA nanostructures in different environments. Buffers contained either physiological levels of salts or were Lysogeny Broth (LB), Dulbecco's modified Eagle medium (D) or D+10% FBS (B) LSCM images of cy3-labelled cholesterol-modified DNA nanopores, in the stated buffers at 1 and 24 h. Scale bar 50  $\mu$ m. (C-D) Binding of DNA nanobundles to GUVs in different buffers, scale bar 10  $\mu$ m. \*Images reproduced from reference 79, by Burns and Howorka.

The study by Burns and Howorka revealed that aggregation of DNA nanobundles occurred in a time-dependent manner, but only in solutions containing FBS. In contrast, little or no aggregation was observed for structures incubated in PBS, or other buffered solutions (Fig 10 – A/B). Subsequently, aggregation as a function of protein content and time was in turn found to affect membrane-binding ability of the structures, as revealed using fluorescence microscopy and giant unilamellar vesicles (GUVs) as surrogate membranes (Fig 10 – C/D). It was noted by the authors that serum proteins likely caused aggregation due to electrostatic complexing with the negatively charged DNA. These observations agree with those presented here as a part of this thesis (project – I) and were presented following publication of this work (see - impact statement, pg. 3).

Numerous chemical and structural modifications to nucleic acids have been used to inhibit their digestion by serum nucleases<sup>68,81</sup>. These modifications enabled development of the so-called 1<sup>st</sup> to 4<sup>th</sup> generation of antisense oligonucleotides<sup>82</sup>. However, incorporation of these modified oligonucleotides into DNSs remains challenging, due to deviations in their fundamental physicochemical properties. This has driven the need for more straightforward modifications that can be incorporated through introduction of single-end modifications or click reactions<sup>83</sup>. The following sub-section focuses on lipid modifications to DNA, in the context of DNA nanostructure functionalisation for controlled interaction with phospholipid membranes.

### 1.2.2. Strategies to control and augment DNA nanostructure interaction with phospholipid membranes

Cholesterol, and other hydrophobic moieties have been used extensively to augment and control DNS interaction with phospholipid membranes<sup>84-85</sup>. Before a brief literature section on such studies, it is worth noting that hydrophobic modifications to DNA nanostructures have also been used to mimic the selective association of side chains that determine protein organization<sup>86</sup>, thereby advancing the assembly strategies that can be

exploited to direct base pairing and subsequent assembly of DNA-based nanostructures. Cholesterol especially has found widespread use within the field of DNA nanotechnology, due in part to its ease of access in terms of commercially modified oligonucleotides that are readily available and relatively inexpensive to purchase or produce relative to other hydrophobic modifications<sup>64</sup>.

Cholesterol has been used to guide controlled aggregation of DNA nanostructures<sup>87</sup>, and extensively to facilitate interaction with model and cellular lipid membranes<sup>84-86,88-89</sup>. DNA is negatively charged and as such does not readily interact with lipid membranes. In order to do so, hydrophobic modifications, such as cholesterol can be incorporated, commonly through short aliphatic linkers such as tetraethyleneglycol (TEG). A range of hydrophobic molecules have been used to this end (Fig 11), with preference depending on the chemical composition of the membrane of interest and the affinity of a particular hydrophobic moiety toward specific lipid domains<sup>90</sup>. Notably, porphyrins, a class of polycyclic biomolecules, can be used to permit insertion of DNA nanostructures into lipid membranes as demonstrated by Howorka and colleagues, who used porphyrin molecules as anchors to enable membrane insertion of a DNA nanopore<sup>91</sup>. As a benefit, hydrophobic moieties such as porphyrins, or tocopherols, come with the advantage of providing fluorescence properties, allowing for imaging and analysis without requiring addition of separate fluorophores that could impact the system of interest.

Recently, a 6-duplex DNA nanobundle was shown to interact preferentially with a 400-fold selectivity to white blood cells *via* cholesterol-membrane interactions<sup>92</sup>. This selectivity of cholesterol-modified structures for White blood cell (WBCs) over erythrocytes was owed to the increased membrane fluidity of the former membrane-type. It was shown also that DNA nanobundles could functionally modulate WBCs by suppressing immune response to pro-inflammatory endotoxins, likely caused by the masking of the cell-surface by a layer of bound structures. These discoveries underscore how hydrophobic anchors can be used to mediate DNA nanostructure-membrane binding and are supported by the findings presented in this thesis, in project - I.

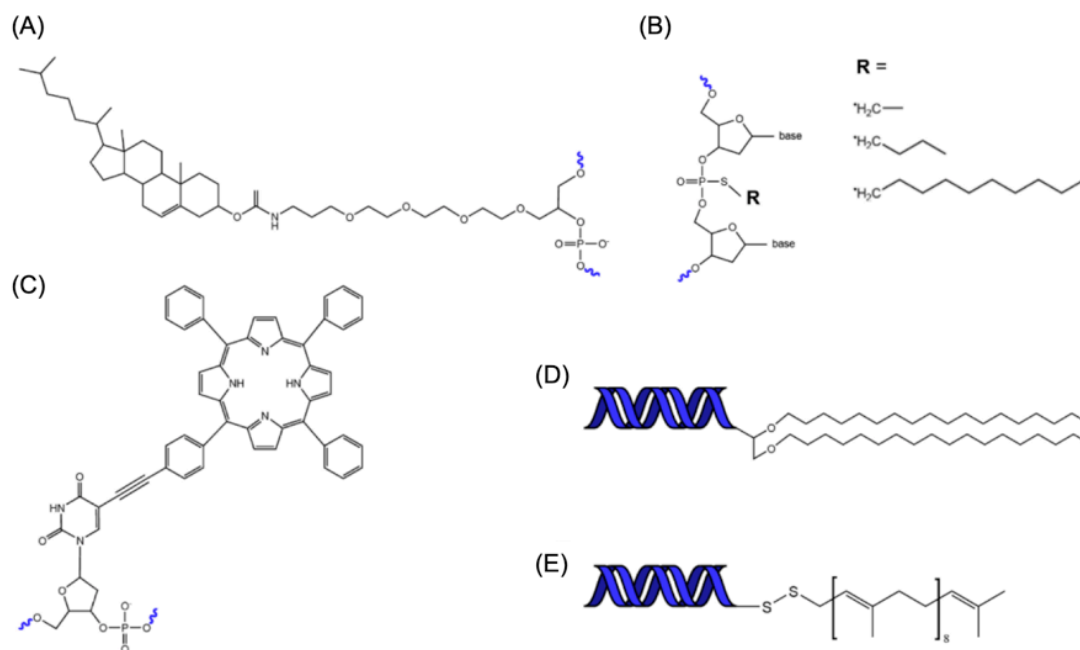


**Figure 11. Hydrophobic chemistries for functionalization of DNA. (A)** Cholesterol modified DNA via TEG linker. **(B)** Alkylated DNA. **(C)** Porphyrin modified DNA. **(D)** Diglycerol ether modified DNA. **(E)** Elanesol modified DNA. \*Figure adapted from the article ‘The Fusion of Lipid and DNA Nanotechnology’, reference 89.

The usual means of incorporating hydrophobic moieties onto DNA nanostructures involve either: folding structures with numerous modified staple strands in a single assembly process, or conversely, incorporation via ‘indirect conjugation’, after assembly of the structure. The latter approach is achieved by means of introducing modified ssDNA either to a membrane first, to recruit the DNA nanostructure with complementary ssDNA handles, or to the structure itself, which can be engineered to present those same ‘anti handles’ used for recruiting the modified strands. Otherwise, covalent strategies are available that can be used to link modified strands directly to DNA origami, or other DNA-based nanostructures<sup>93</sup>. Notably, Thiol-modified DNA staples have been used to conjugate lipid molecules such as DOPE and PE, via maleimide chemistry<sup>94,95</sup>. This strategy can be used either prior to assembly of the DNA nanostructure or after. Hydrophobic protein motifs have also been used as bioconjugates with DNA origami staple strands to serve as membrane anchors<sup>96</sup>.

The Howorka group, in which the work for this thesis was conducted, has focussed on hydrophobic cholesterol anchors as a means to realise membrane interaction of DNA nanostructures. In particular, cholesterol, alongside other hydrophobic anchors, have been exploited by the group to achieve transmembrane insertion of several DNA-based constructs to mimic natural protein-based nanopores and expand the functional repertoire synthetic nanopores<sup>97</sup> (Fig 12).

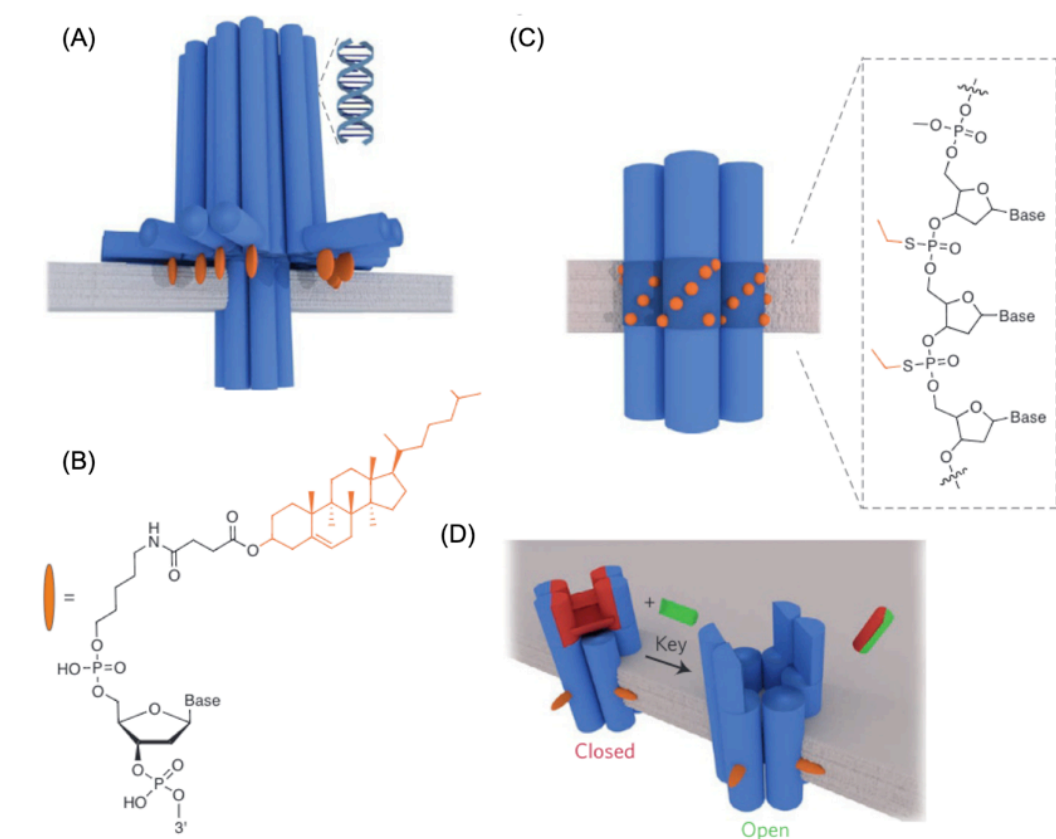


**Figure 12. Cholesterol and ethyl hydrophobic modifications for membrane insertion of DNA nanopores.** (A) Biomimetic DNA nanopore inspired by the naturally occurring  $\alpha$ -haemolysin protein pore. (B) Cholesterol modified DNA used to anchor DNA-based nanopores as shown in A and D. Cholesterol is depicted in orange and is linked to DNA via 5' TEG spacer. (C) Alkylated DNA (ethyl moieties) are enabled via phosphorothioate chemistry and are used to achieve transmembrane insertion of an archetypal 4-duplex DNA nanopore. (D) Functional ligand-triggered opening of a DNA nanopore, which is inserted into a lipid bilayer via cholesterol anchoring. \*Image adapted from the article 'Building membrane nanopores', by Stefan Howorka, reference 96.

### 1.2.3. Delivery, cellular uptake & processing of DNA nanostructures

To date, DNA nanostructure-based drug delivery has focussed on targeting cancerous cells and tissues<sup>61,64</sup>. However, before reaching cancer cells, nanoparticles must first accumulate or localize in the target organ or tissue where the target cells exist. This stage of delivery is referred to as 'primary targeting'. Once DNA nanostructures have successfully arrived at the physiological target they must then be directed in a controlled fashion to the targeted cell-type and/or sub-cellular locale, referred to as 'secondary' and 'tertiary' targeting steps<sup>98</sup>. This chapter first starts with a brief overview of primary targeting considerations, then moves on to cover underlying cell biology (with respect to secondary and tertiary targeting). The aim of this review chapter is to highlight key discoveries in the context of cellular uptake and processing of DNA nanostructures, along with the emerging chemical strategies that are being explored to control these processes.

#### ***Primary targeting.***

---

Cancers with high morbidity rates typically occur in the lung, liver, lymph, bone and brain<sup>99</sup>. In order to control delivery to these organs, nanoparticles must be carefully tailored to meet specific criteria<sup>100</sup>. Two key aspects that must be tightly controlled in this context are size and surface properties<sup>101</sup>. Most nanoparticles smaller than the globular filtration size limit (approx. 5.5nm) are prone to renal filtration, and quickly leave the body through urinary excretion<sup>102</sup>. Particles larger than this are prone to be retained by specialised liver cells, termed kupffer cells. Notably, *in-vivo* studies have shown that small DNA origami nanostructures (<50nm diameter) of rectangular, triangular and tubular shapes preferentially accumulate in the kidneys<sup>103</sup>. DNS may however be designed with near unrivalled control over topology, with sizes ranging from <10nm to Gigadalton, micrometer scales<sup>104,105</sup>. Additionally, DNA programmability allows for nanoscale control over surface modification, providing the means to meet requirements of nanomedicines and nanoscale theranostic devices (Table 1, and Fig 19, pg. 42).

Target organ	Particle Size	Surface property
Brain	5-100 nm, uptake efficiency decreases exponentially with size	Lipophilic moieties and neutral charge for uptake enhancement
Lung	>100 – 200 nm, particles are trapped in lung capillaries	Positive surface charge
Liver	<100 nm for hepatocyte targeting. Internalization by Kuppfer cells >100nm	No specificity required
Lymph Nodes	6-34 nm: intra-tracheal administration. 80 nm for subcutaneous administration.	Non-cationic, non-pegylated and sugar-based particles or surface modification.
Bone	Unknown	Numerous chemical moieties available for bone targeting.

**Table 1. General considerations for nanoparticle delivery to organs.** *Table adapted from reference 101.*

The intravenous (IV) route has numerous advantages over oral drug administration<sup>106</sup> and delivers nanoparticles or nano-sized pharmaceuticals directly into the vascular system, allowing quick access to peripheral tissues and organs. Once they have entered the vascular system, nanoparticles quickly encounter blood stream where various cells alongside regulatory and plasma proteins interact with these components according to their overall physicochemical properties<sup>107</sup>. Typically, a protein ‘corona’ is formed around the particle in seconds to minutes<sup>108</sup>, altering its original size, referred to as *in-vivo* hydrodynamic diameter (HD).

The HD of a nanoparticle is directly related to its rate of filtration by the kidneys and thus also to its blood and whole body half-life<sup>109</sup>. Protein opsonisation, also referred to as protein ‘fouling’ of the nanoparticle can significantly alter the particle’s intended function<sup>110,111</sup>. Notably, endothelial cells have been used for In-vitro studies to model vascular transport of nanoparticles, revealing a strong link between protein adsorption, opsonisation

and cellular interaction<sup>112</sup>. In this context, the work presented as part of this thesis sought to investigate how serum proteins affect cellular uptake of small DNSs, the findings of which are presented in section 2. Briefly, it was found that presence of FBS in cell-culture media accounted for significant increase in cell-binding but not uptake of cholesterol modified DNA nanostructures<sup>113</sup>.

The most challenging organ to target via IV administration is the brain, due to the blood-brain-barrier (BBB). This physiological boundary favours transport of small biomolecules and gases but may be significantly altered by pathologies such as cancer, providing opportunities to deliver larger particles such as DNA-based nanovectors or polymeric delivery vehicles that can package nucleic-acid payloads for gene-silencing<sup>114</sup>. Numerous studies have reported a size-limitation for efficient transport across the BBB of <15nm<sup>115-116</sup>. Spherical nucleic acid (SNA) type nanostructures have proven useful for transport of small organic molecules across the BBB<sup>117</sup>. DNA-coated gold nanoparticles have also been used in combination with focused ultrasound to successfully target specific locations of the brain<sup>118</sup>.

Framework nucleic acid type structures (FNAs) are another promising approach for delivery of therapeutic compounds or imaging probes into the brain. In this context, FNAs based on the tetrahedral type DNA nanostructure (Fig 13) architecture, have been used as a building blocks for presentation of bioactive peptide-based probes to target specific markers in the brain, revealing enhanced uptake properties across the BBB and establishing FNAs as a versatile theranostic tools for brain tumour mapping and study<sup>119</sup>. DNSs based on this architecture have been used to deliver antisense peptide nucleic acids<sup>120</sup>, DNAzymes<sup>121</sup> and small molecule therapeutics<sup>122</sup>. Regarding DNA-based nanomedicines, it is important to note that SNA type nanoparticles are distinct from 'DNA nanostructures' by basis of their synthesis. Unlike the latter, the former are assembled via chemical bonds are thus assembled independently of nucleic acid sequence and hybridisation interactions<sup>123</sup>.

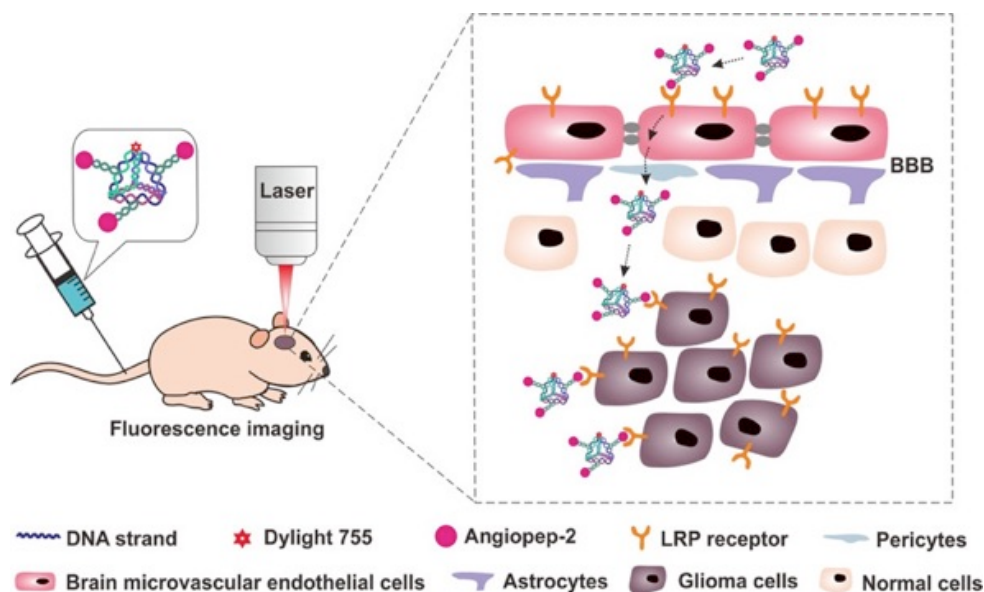


**Figure 13. Schematics for DNA-based brain-targeting imaging using tetrahedral DNA nanostructures (TDNs).** Angiopeptin-2 is introduced to mediate BBB permeability and cell uptake of TDNs. \*Figure reproduced from reference 119.

Unlike the brain, where particle functionalization with lipophilic moieties has shown great promise<sup>124</sup>, relatively little is known about targeting bones reflecting few studies to date using nanoparticles to target these organs. Bone is largely composed of calcium-containing minerals termed hydroxyapatites, which have to-date served as the primary target for small molecules and proteins such as aspartic acid and alendronate<sup>125</sup> (table 1).

Lymph nodes are another important organ responsible for cancer metastases and disease progression, and have been targeted using cell-based nanotechnologies that involve equipping nanoparticles with ligands to target leukocyte receptors<sup>126</sup>. These specialised cell types are then trafficked as part of the immune response to lymph nodes. DNSs may be promising in this context (leukocyte targeting), as negatively charged particles are preferentially internalized by this cell-type<sup>127</sup>. Notably, non-cationic particles with size ranges between 6-34 nm have been shown to accumulate with fast uptake profiles into lymphatic tissues<sup>128</sup>, further pointing at DNSs as promising vectors for these applications.

Toxicity levels associated with anionic nanoparticles are less severe than that produced by cationic nanoparticles, which are known to cause problems from both primary and latter stage targeting<sup>129</sup>. Indeed, cationic agents are known to produce better permeation abilities than neutral or negatively charged alternatives<sup>130</sup>, but lead to higher levels of toxicity<sup>131</sup>. The intrinsic net negative charge associated with DNA nanostructures may be exploited in this context to avoid non-specific internalization pathways, which are understood to cause the more significant toxicity associated with cationic nanoparticles that directly translocate across cell membranes. Disadvantages associated with negatively charged nanoparticles include their slower uptake kinetics<sup>127</sup> and their tendency to electrostatically complex and aggregate with oppositely charged serum proteins<sup>132</sup> (this topic is discussed with respect to DNA nanostructures in section 1.2 and with respect to the findings presented as part of project 1 in section 3). Besides size and charge considerations, nanoparticle shape and morphology also mediate interaction with cells, factors which must be taken into account for effective drug delivery<sup>132</sup>.

### ***Secondary & tertiary targeting.***

---

The plasma membrane, also known as the cytoplasmic membrane, provides the structural boundary of cells and thereby the basis for compartmentalisation of the numerous sub-cellular organelles that define and control cellular functions. Entry and exit to the cellular cytoplasm is tightly controlled through these natural membrane-boundaries, via selective permeation to ions and organic molecules. Nanoparticles, including DNA nanostructures<sup>133</sup>, are able to traffic across the cell membrane via numerous internalization pathways collectively referred to as endocytosis. Endocytosis is broadly divided into two sub-categories; Phagocytosis and Pinocytosis (Fig 14 - A). The latter process is highly regulated and unlike phagocytosis occurs in virtually all cell types via several distinct mechanisms. These are the so-called clathrin-mediated, caveolae-mediated and caveolae-independent endocytosis pathways<sup>134</sup>. By contrast, phagocytosis is a less selective internalization process by which larger particles (>250 nm) may be internalized into specific cell types<sup>135</sup> (Fig 14 – B). Non-phagocytotic pathways include the macropinocytosis, an endocytotic process that differs from other pinocytosis pathways by the size of engulfed

materials and the specificity with which they are internalised (FIG 14 – A/B). This pathway allows for internalization of smaller materials in comparison to phagocytosis (<250 nm)<sup>135</sup> but in a non-selective fashion.

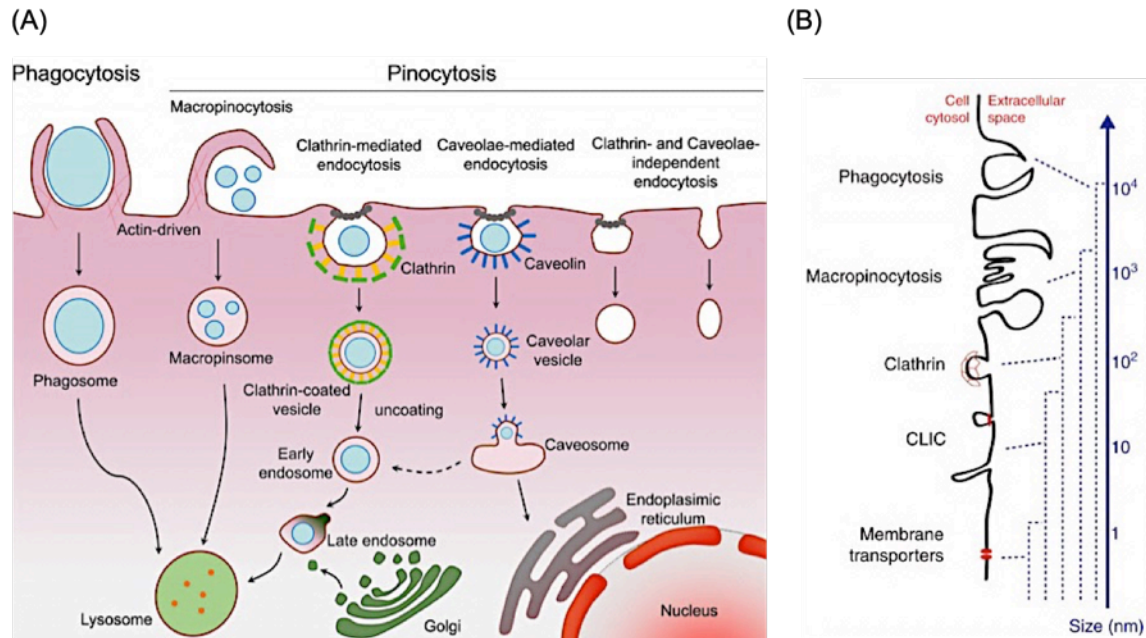


**Fig 14. Endocytosis pathways. (A)** Cellular entry pathways for nanoparticle internalization. **(B)** Mechanisms of endocytosis and their relationship with nanoparticle size. *Figures Reproduced from reference 134 & 135.*

The process of macropinocytosis is an actin-driven event that begins with invagination of the cell plasma membrane and subsequent formation of macropinosomes, which are large endocytotic vesicles, known to range in diameter from 1 to 5  $\mu\text{m}$ <sup>135-136</sup>. Macropinosomes shrink and acidify as they mature inside the cell cytoplasm and can eventually fuse with other acid containing compartments to degrade entrapped materials. Conversely, they may be recycled to the cell surface to regurgitate materials back out of the cell in a process termed exocytosis<sup>135</sup>. Macropinocytosis has been implicated in uptake of DNA nanostructures but is generally understood not to display any selectivity, likely owing to the absence of any specific membrane-receptors<sup>137</sup>. In 2013, Kim and co-workers reported that uptake of a DNA tetrahedron occurred mainly via macropinocytosis<sup>133</sup>.

Clathrin, a ubiquitous protein found in the cell cytoplasm plays a role in specific pinocytosis-internalization mechanisms termed the clathrin-dependent pathways or collectively referred to as clathrin-mediated-endocytosis (CME)<sup>138</sup>. These processes have been implicated for uptake of numerous DNA nanostructures<sup>133,139</sup> and are involved in various fundamental processes including intracellular signalling and uptake of nutrients. Numerous ‘accessory’ proteins are implicated in CME membrane deformation processes, yet their exact mechanisms remain relatively unknown<sup>140</sup>.

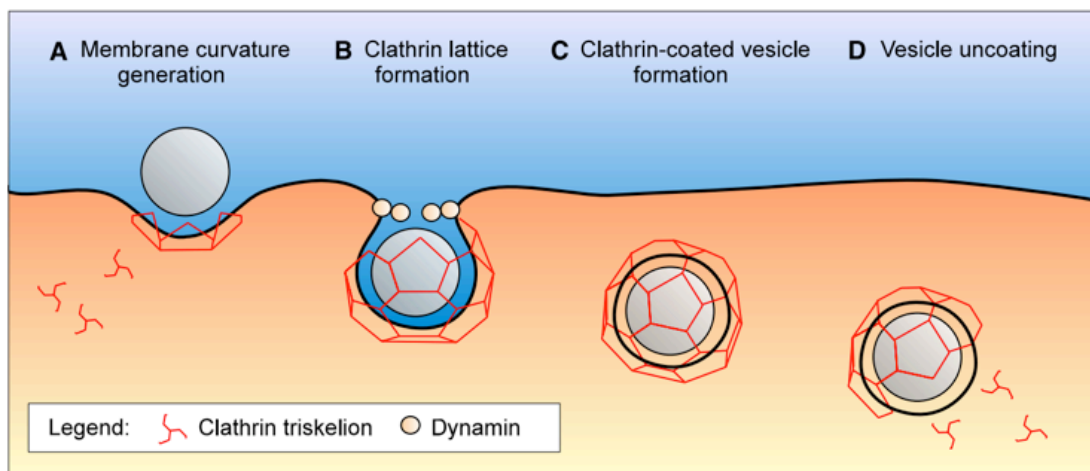


**Figure 15. Vesicle formation during the clathrin-mediated process. (A)** The 3D topology of clathrin is triskelion in nature, which allows the protein to interact with itself and form a dynamic polygonal-type lattice that coats the plasma membrane and helps to form a membranous invagination referred to as a clathrin-coated pit. **(B)** Dynamamin, a cell-membrane endogenous GTPase is then recruited at the pit apex to mediate vesicle formation by driving membrane separation, a process referred to as fission. **(c)** Following the process outline in B, complete internalization and cytosolic release of the clathrin coated-vesicle occurs, which have diameters of approximately 150nm. Subsequently, the clathrin lattice disassembles allowing recycling of the clathrin-triskelia and producing vesicles with an average size of 100 to 120 nm (Fig 14 – B). \*Figure reproduced from reference 139.

CME was thought to be exclusively mediated by receptor driven recognition and as such was originally referred to as ‘receptor mediated endocytosis’ (RME). However, CME has since been observed to also occur without the aid of receptor recognition<sup>140</sup>. Additionally, despite internalization specificity varying between these two processes (receptor-mediated vs. receptor

independent CME), the intracellular processing of materials remains the same<sup>140</sup>. Endocytosed materials through both pathways end up in the lysosome where they are ultimately degraded by numerous enzymes. In order to avoid this fate and effectively deliver drugs and other bioactive cargo to intended targets, numerous studies have sought to equip DNA nanostructures with chemical or biological moieties that can elicit 'endosome release'<sup>141</sup> (this topic is addressed in section 5.1.1). Additionally, the biodegradable nature of DNA has been exploited to engineer DNSs as drug-delivery devices, to predicate their disassembly in the lysosome and release cargo that can escape these compartments<sup>142</sup>, (example, Fig 16).

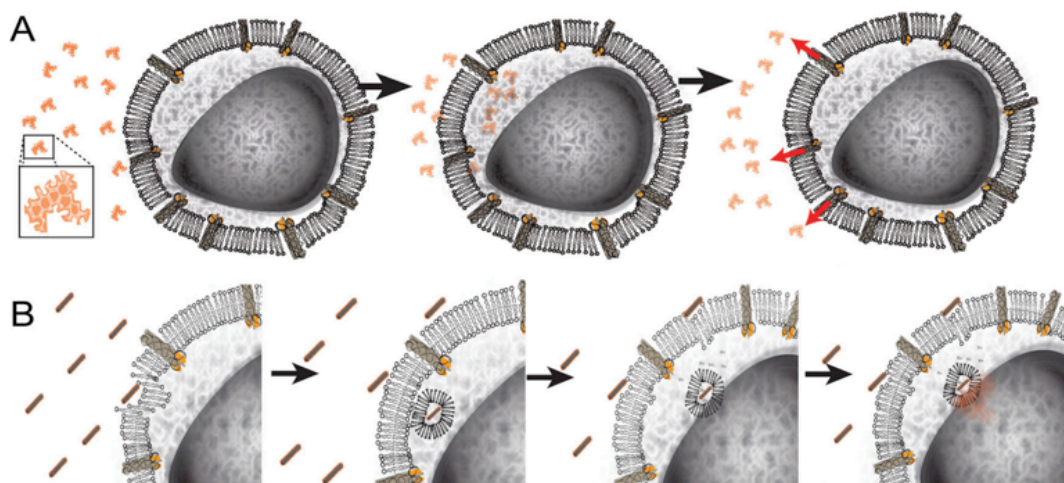


**Figure 16. Daunorubicin-loaded Horse DNA nanostructure drug delivery system.**

(a) Free drug daunorubicin (a cyclic chemotherapeutic compound that loads into the DNS by means of intercalation) – enters cells via passive diffusion but is quickly expelled via efflux pumps. (b) DNA nanostructures are used to deliver daunorubicin payloads and circumvent drug-efflux by exploiting the endolysosomal pathway. Escape of the drug from lysosomes is owed by speculation to increased acidity and reduced ion concentrations. Positively charged daunorubicin can then passively diffuse out of lysosomes and enter the cell nucleus where it interacts with and inhibits DNA replication. \* Figure reproduced from 141.

Internalization of nanostructures through receptor-independent CME is achieved via electrostatic or hydrophobic induced interactions between the nanoparticle and cell membrane<sup>139</sup>. Notably, receptor-independent CME has been shown to have slower internalisation rates compared to receptor-mediated CME<sup>139,143</sup>. Receptor-mediated entry however provides the basis for specific and selective uptake of drug delivery devices, which may be rationally designed to display ligands and incorporate pharmaceutical payloads. To this end, numerous DNA nanostructures have been designed to exploit receptor-guided uptake, making use of aptamers<sup>144</sup> and antibodies<sup>145</sup>. In order to carry out their intended function however, a key priority for any drug delivery device is that it must be able to escape the endolysosomal pathway and reach intended subcellular organelles. This final targeting stage can be termed ‘tertiary targeting’, and is important in order to increase specificity for effective drug delivery and minimise off-target effects responsible for nanotoxicity<sup>137</sup>.

In 2014, Kim and co-workers found that non-modified DNA tetrahedrons internalise into cells via CME but also via other, non-clatharin mediated pathways<sup>146</sup>. Another distinct route for receptor-mediated pinocytosis is the caveolae-mediated endocytosis pathway (CvME). Unlike CME, CvME is a highly regulated process, which can be tightly controlled by properties of the nanoparticle itself. Ligands known to control CvME include albumin, a protein commonly found in FBS, folic acid and cholesterol. Albumin<sup>147</sup>, folic acid<sup>145</sup> and now cholesterol<sup>133</sup> have all been used to enhance DNS uptake into cancer cells. Uptake enhancement into cancer cells using cholesterol modified DNA nanobundles was reported in the publication presented as part of this thesis (see impact statement, along with project – I, section 2).

### **Size dependence for cellular uptake of DNA nanostructures**

Numerous studies have sought to interrogate DNA nanostructure internalization pathways, yet much remains to be uncovered regarding how structure, topology and surface functionalisation affect cellular interaction and processing. Choi and co-workers recently used transmission electron microscope (TEM) to validate the caveolae-mediated internalization of spherical nucleic acids (SNAs) into numerous cell types, finding size to be a

key determining factor in uptake efficiency<sup>148</sup>. Likewise, Lim and colleagues made use of various chemical inhibitors to track and validate internalization of Zn/DNA clusters of varying size by macropinocytosis<sup>149</sup> (Fig 17).

Excluding phagocytosis (which occurs mainly in specialised cell-types), description of uptake pathways in relation to nanoparticle properties remains a challenge and must be studied in-vitro. Cells typically employ numerous uptake pathways simultaneously, a process indeed observed with uptake of DNSs<sup>65</sup>. Furthermore, different cell lines utilise the same pathways to varying degrees with results being implicated regarding intracellular localization. To these ends, Medintz and co-workers recently collated a table to order possible cellular localisation of DNSs by size and cell type, providing a useful starting point for researchers to help guide rational design considerations and choice of cell-types for experiments (table 2, pg. 40). This table however comes with the caveat that transformed cell lines are not wholly representative of their natural counterparts and may provide for erroneous conclusions regarding biophysical interactions, which may occur due to differences in morphology. These limitations have however to some extent been addressed by using more advanced model systems including 3D cell cultures<sup>150</sup> and extending studies to organoids to better mimic interactions with real in-vivo organs.

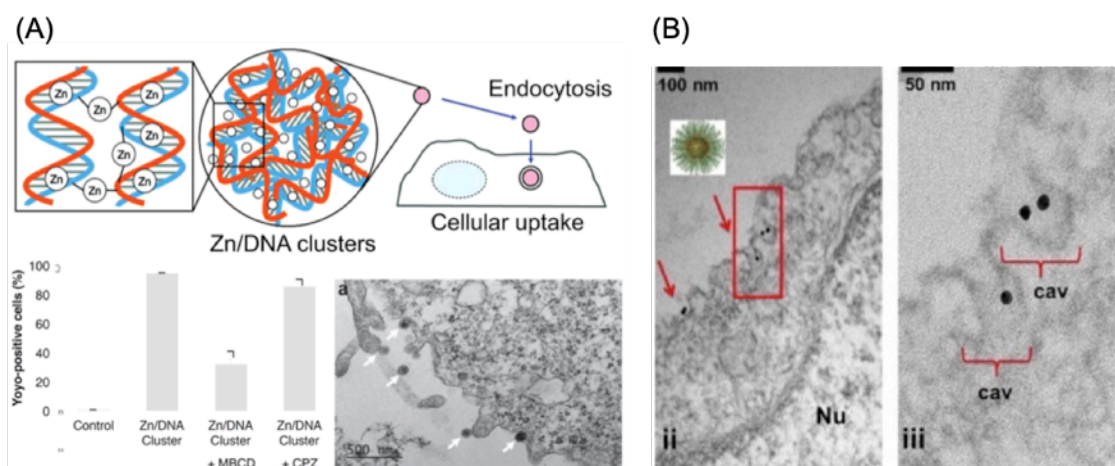


**Figure 17.** (A) Internalization of Zn/DNA clusters. Chemical inhibitors; MβCD and CPZ were used to block endocytosis and validate internalization via flow cytometry in combination with TEM analysis. (B) TEM images of cells incubated with SNAs, validating Caveolae mediated endocytosis. Abbreviations; caveolae – cav; Nucleus – Nu. \*Image adapted from reference 149.

Shape	Synthesis type	Size/nm	Cell type	Incubation period/h	Uptake mechanism	Localization
SNA	SNA	~20	RAW264.7	4	U	En
	SNA	~20	RAW264.7	4	U	En
	SNA	~20	C66	4	Ca	Late En, Cy
	ProSNA	~17	HaCaT, C166, SKOV3	12	Ca	Cy
	Au-DNA 3D superstructure	1000	U87	2	U	Cy
Nanotube	Origami	80	HEK293	4	U	Nuclei
	—	10 000–40 000	KB	1	U	Cy
	—	800	HeLa	6	U	Cy
	Origami	138	MCF7, MDA-MB-231, MDA-MB-468	2	E	En
	—	14	Pulmonary arterial smooth muscle cells	12	E	En
	—	41	RAW 264.7	3	E	En
	Origami	80	Splenocytes	4	E	Ly
	Origami	300	MCF7	6	E	Ly
	Origami	380	MCF7	12	E	Ly
	Origami	92.5	HL-60/ADR	9	E	Ly
Tetrahedron	—	7	HEK293	24	E	Cy, Ly
	—	7	HeLa	4	U	Cy
	—	7	HeLa	5	U	Cy
	—	14	DLD-1, SW480	2	E	Cy
	—	7	HeLa	3	Ca	Ly
	—	6	RAW264.7	2	U	Ly
	—	7	RAW264.7, bone marrow derived dendritic cells	2	U	Ly
	—	7	HeLa, NIH3T3	5	E	Ly
Other geometries	DNA prism	8	HeLa	24	U	Cy
	DNA microsponge	223	SKOV3	3	E	Cy
	DNA nanocube	7	LNCaP, HeLa and primary B-lymphocytes	6	E	Cy
	Aptamer-tethered DNA nanotrain (aptNTrs)	100	CEM, Ramos	2	E	En
	DNA nanoclew	150	MCF7	0.5	E	En
	DNA nanoclew	56	U2OS,EGFP	2	Ma	En
	Polypod-like DNA nanostructure	10	RAW264.7	8	E	En

**Table 2. Table of uptake mechanisms and localization of some DNA nanostructures.** Abbreviations: Caveolae – Ca; clatharin – Cl; cystol – Cy; endocytosis – E; endosome – EN; lysosome – Ly; macropinocytosis – Ma; unknown – U. *Table adapted from reference 133.*

As mentioned above, uptake pathways can be highly dependent on particle size. The idea that shape and size of nanoparticles, especially pathogens, can determine to some extent their entry into target cells has prompted studies using bio-inspired nanoparticles, including DNA nanostructures<sup>151</sup>. Notably, DNSs may be uniquely positioned in this context, as they may be designed with near unrivalled control over nanoscale topology and size (Fig 19). Studies have demonstrated that DNS size and density affect uptake pathways and kinetics<sup>152</sup>. Protein opsonisation of nanoparticles is known to be highly dependent on these factors (size, shape, topology and charge), which, as mentioned previously, furthermore work to mediate or inhibit specific entry pathways.

In an effort to better understand how size, topology and density affect cell uptake of DNSs, William Shih and co-workers examined the cell-uptake of a panel of 11 distinct DNA-origami nanostructures with varying topologies across three separate cell-lines<sup>153</sup> (Fig 18). The size of structures ranged from 50-400 nm. Findings showed that larger particles with greater compactness were preferentially internalized compared to higher aspect-ratio structures, with uptake kinetics proving to be more cell-type dependent than shape-dependent. Such rigorously designed studies are expected to provide useful information on the importance of nanoparticle size in relation to uptake specifics.

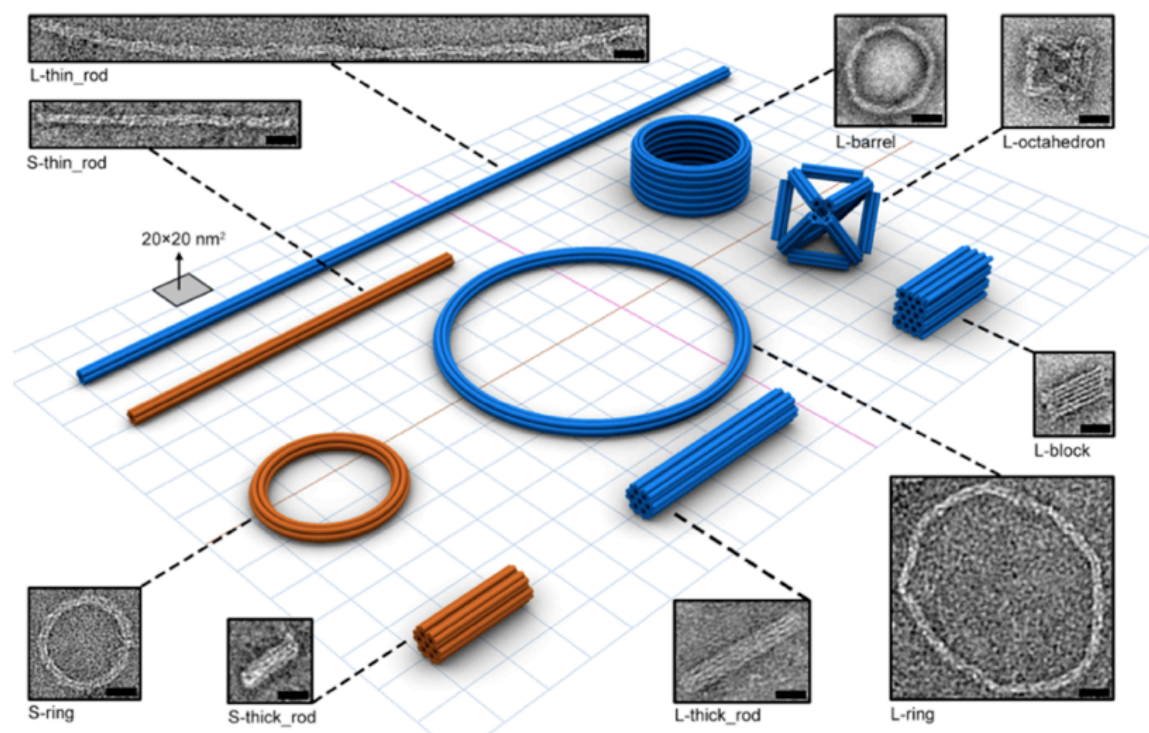


**Figure 18.** Computer models and TEM images of DNA origami nanoparticles used to interrogate relationships between DNA nanostructure size, shape and internalization pathways and kinetics. \*Figure reproduced from reference 152.

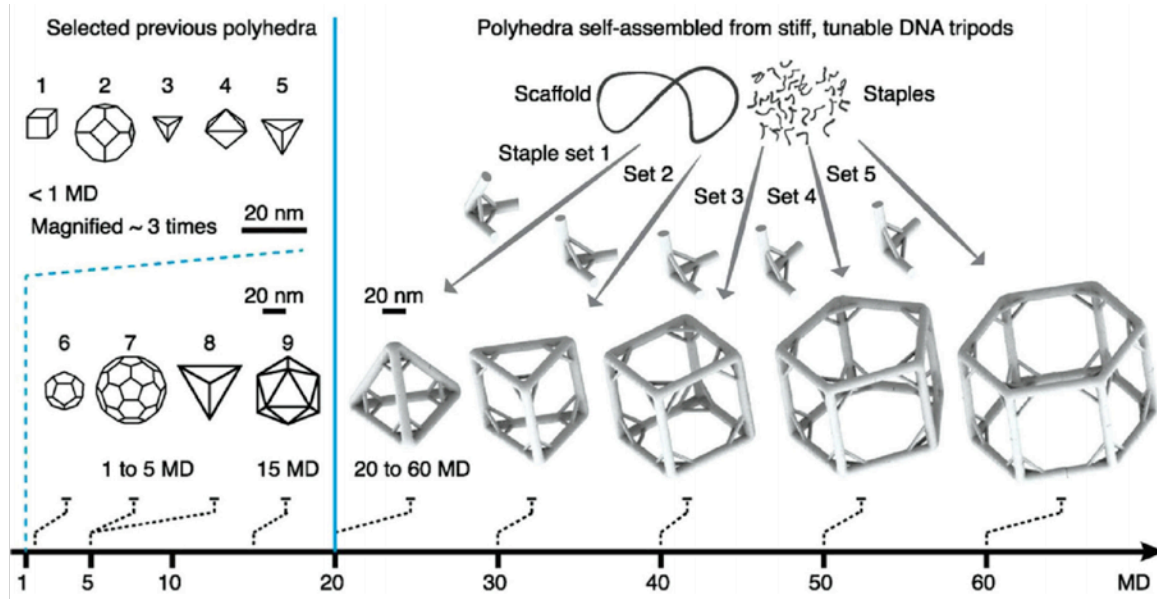


**Figure 19.** Size and topology control of DNA Nanostructures with relevance for delivery to specific organs, tissues and carrying drug payloads. *Figure reproduced from reference 62.*

## 2. Project I - aims

DNA nanotechnology offers nanoscale control over topology, size, and mechanical movement of user-defined nanostructures<sup>26,64,152</sup>. As mentioned previously, bottom-up design, coupled with the ability to site-specifically hydrophobic moieties, make DNA nanostructures (DNSs) a unique and advancing tool-set for research across cell and synthetic biology, to investigate for example cell-surface interactions with extracellular components. Cholesterol modifications to DNSs have been used extensively to control and augment anchoring of various structures to synthetic lipid-membranes<sup>85,87,89,91,52,155,156-157</sup>. Additionally, lipid moieties such as cholesterol have been used to augment delivery and uptake of therapeutic oligonucleotides<sup>156,157</sup>. However, lipid functionalisation to DNSs has not been explored as a means to augment cell uptake. To probe fundamental questions in this context, this project thus aimed to investigate how cholesterol-anchors affect DNS interaction with cells, using a modular structure described below (Fig 20).

### 2.1. Components of study

The DNS used for this project was designed by Burns and Howorka<sup>158</sup>, and was conceived as a hollow-barrel type nanopore to puncture lipid membranes. The 'barrel' is composed of six hexagonally arranged, interconnected DNA duplexes that enclose a 2-nm-wide opening which forms a channel through the structure, having the overall dimensions of approximately 9 x 5 x 5 nm\* (Fig 20 – A, pg. 44).

The structure architecture is composed of 6 concatenated DNA strands, where each strand connects two neighbouring duplexes at their respective termini via single-stranded loops (Fig 20 - B). Up to three cholesterol moieties are incorporated onto the bundle exterior to enable its interaction with bilayer lipid-membranes (Fig 20 - C). To measure nanobundle-cell interactions, fluorescent reporters (either Alexaflour-647, or 6FAM) were incorporated onto the nanobundle exterior via the 5' terminus of a non-cholesterol modified DNA strand (Fig 20 - A), as described in reference<sup>159</sup>.

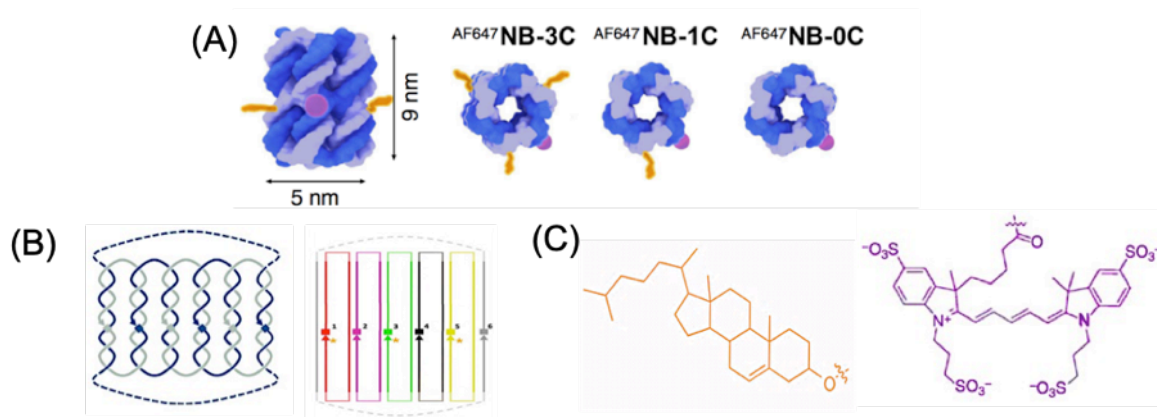


**Figure 20. 6-Helical DNA nanobundle, design features and schematics. (A)** Structural model of the 6 Helical DNA nanobundle including cholesterol anchors (orange) and fluorophore Alexa Flour 647 (purple). **(B)** Two-dimensional map illustrating the connectivity of the DNA strands in the structure (left) and 2D schematic map of the 6-helical DNA nanobundle, where orange asterisks denote terminal positions used for 3' cholesterol modification (right). **(C)** Chemical structure of and cholesterol and Alexa Flour 647, which are attached to 3' end of component oligonucleotides. *Images adapted from the article 'Multi-functional DNA nanostructures that puncture and remodel lipid membranes into hybrid materials, Nat Commun, (2018), reference 158.*

Designing DNSs using the traditional DNA origami approach involves utilising numerous 'staple strands' to crossover and link together a larger 'scaffold' strand (section 1.1.1). By comparison, the connectivity in the 6-Helix DNA bundle was purposefully simplified by making use of connections at the duplex ends (Fig 20 - B), thereby avoiding internal cross-overs known to produce structural deviations from parallel aligned duplexes<sup>160</sup>. As a result, only 6 oligonucleotide strands are required for complete assembly of the structure, via linking of the 6 resulting DNA duplexes (Fig 20 - B). The oligonucleotide sequences used to fabricate the structure are featured in table 3 (pg. 45).

Strand #	Sequence 5' ---> 3'
1	AGCGAACGTGGATTTTGTCCGACATCGGCAAGCTCCCTTTTTTCGACTATT
2	CCGATGTCGGACTTTTACACGATCTTCGCCTGCTGGGTTTTGGGAGCTTG
3	CGAAGATCGTGTTTTTCCACAGTTGATTGCCCTTCACTTTTCCCAGCAGG
4	AATCAACTGTGGTTTTTCTCACTGGTGATTAGAATGCTTTTGTGAAGGGC
5	TCACCAGTGAGATTTTTGTTCGTACCAGGTGCATGGATTTTTGCATTCTAA
6	CCTGGTACGACATTTTTCCACGTTTCGCTAATAGTCGATTTTATCCATGCA

**Table 3.** Oligonucleotide sequences used for DNA nanobundle assembly. Sequences are labelled as 1-6 and are listed 5' to 3'. Cholesterol anchors, when used, were attached to the 3' end of oligonucleotide sequences 1,3 and 5 via a tetraethylene glycol spacer. Fluorophore tags 6FAM or AlexaFlour647 were introduced to the 3' end of sequence 2.

### 3.0 Results & discussion

#### 3.1. Assembly & characterisation of the 6-duplex DNA nanobundle

Nanobundle assembly was characterised by gel electrophoresis (Fig 21). Migration of bands for each nanobundle variant (nanobundles with zero, one or three cholesterol anchors) agreed with observations in previously published works<sup>157-158</sup>, and has been described in published work since<sup>161</sup>. Gel analysis further confirmed that nanobundle assembly proceeds to completion in phosphate buffered saline (PBS) 1x, which was selected as folding buffer to avoid offsetting the osmotic balance of cell culture media upon addition of nanobundle samples.

Visual inspection of the gel electrophoresis reveals a high folding efficiency. Polyacrylamide gel electrophoresis (PAGE) provides enhanced separation and analysis of smaller DNA nanostructures in comparison to AGE and shows that only small fractions of one or more of the six component-oligonucleotides typically remained unused for nanobundle assembly (Fig 21). Low Mw bands relative to the fully assembled structure are sometimes observed (Fig 21), and are consistent in migration distance to either single or duplexed oligonucleotides observed in step-wise assembly of the 6-duplex DNA bundle<sup>157</sup>. I.e., all six oligonucleotides must be equimolar for a theoretical folding efficiency of 100%, and it is likely that one or more of these oligonucleotides will always be in slight excess over its counterparts.

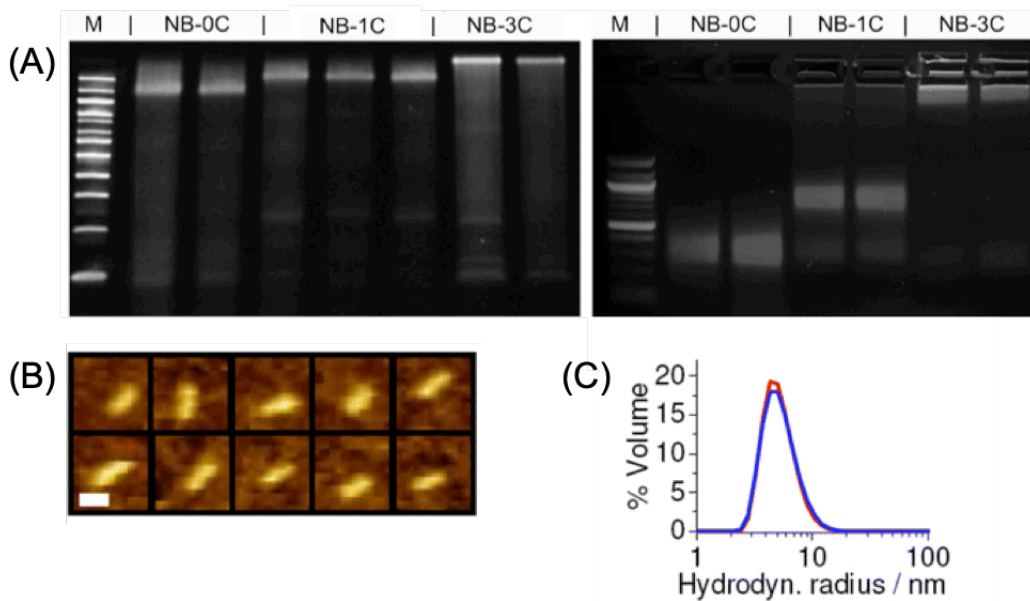


**Figure 21. DNA nanobundle assembly and characterization. (A – Left): Analysis of nanobundle assembly with SDS-PAGE.** Lane 1, 100bp marker. Nanobundles with zero, one or three cholesterol anchors (termed NB-0C, NB-1C and NB-3C) migrate at different rates due to cholesterol anchor interactions with the PAGE matrix. Sample duplicates or triplicates are included representing separate nanobundle assemblies. **(A – Right): Agarose gel analysis.** 3% AGE provides for enhanced separation of nanobundles according to cholesterol anchor number. **(B)** Atomic force microscopy (AFM) images of individual nanobundles. **(C)** Monomeric nature and dimensions of the 6-helix bundle DNA nanobundle confirmed by dynamic light scattering. *\*Note – images shown in B & C are adapted from work published by other members of the Howorka group<sup>162</sup>, Christopher Ingold building, UCL.*

Incorporating cholesterol onto the DNA bundle is shown to decrease electrophoretic migration, consistent with published observations<sup>157</sup>. The reasons for this are that cholesterol likely interacts with the gel matrix, slowing the structure's electrophoretic passage. Cholesterol is a hydrophobic moiety and could thus be expected to cause aggregation of structures via the hydrophobic effect, which was tested for by conducting SDS-PAGE (Fig 21-A). Notably, observation of cholesterol number-dependent gel shifts for nanobundles in both gel systems rules this possibility out. However, aggregation has been observed to occur only at higher folding concentrations ( $>1\mu\text{M}$ ) – (data not shown, unpublished work) or, where assembly conditions contain concentrations of divalent ions exceeding those typically suitable for assembly and stability of DNSs ( $>20\text{mM}$ ).

### 3.2. 6-Duplex DNA nanobundle interaction with HeLa Cells

To investigate the effect of lipid anchor number on cellular interaction, nanobundles with zero, one or three cholesterol anchors were incubated with HeLa cells in two separate conditions; 10% FBS supplemented media, or FBS-free nutrient optimized cell media (optiMEM 'reduced serum media'), I.e., Opti-MEM with 0% FBS addition. FBS-free cell- media was used to avoid protein fouling of the DNA nanostructures and thereby to give a picture of how cellular interaction proceeds without significantly changing their physicochemical properties.

Using AF647-tagged nanobundles, with concentrations ranging from 0.1 to 100nM, flow cytometry revealed that cellular interaction was concentration dependent, and that cholesterol anchors produced a significant increase in cell binding activity (Fig 22 - A). Incubated in FBS-free conditions, the strongest increase in cellular interaction was observed where nanobundles were equipped with three cholesterol anchors. In FBS-free conditions, addition of just one cholesterol anchor enhanced cellular association by approximately 4-fold compared to the nanobundle without cholesterol modification (NB-0C). At the highest concentration tested (100nM), addition of three cholesterol anchors enhanced association by 6-10 fold, after 3 to 4h respectively (Fig 22 – A, Fig 23).

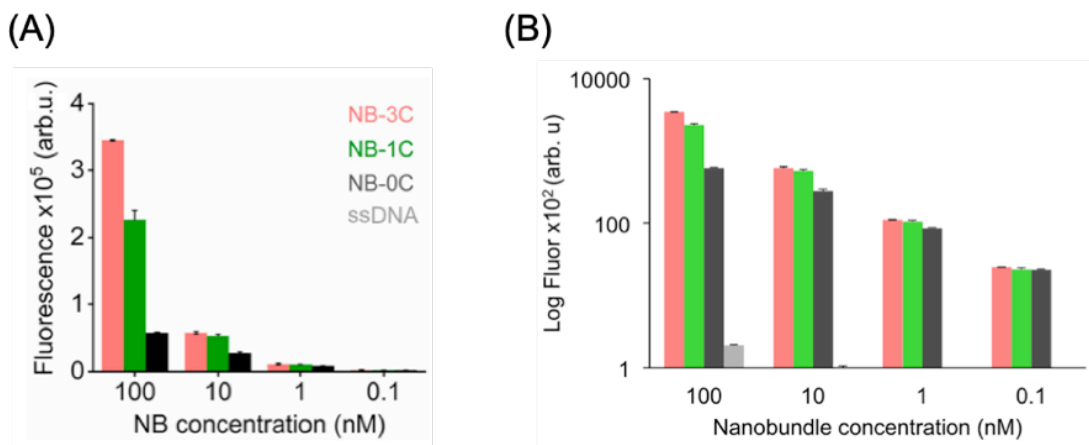


**Figure 22. Concentration and lipid anchor effect on cellular interaction, measured by flow cytometry.** (A) Nanobundles variants NB-0C, NB-1C and NB-3C, carrying an Alexa Flour (AF) 647 tag were incubated in FBS-free conditions with HeLa cells for 3 h. *\*Note, error bars are + standard deviation from triplicate repeated measurements, where each sample pool consisted >3000 singlet cell events.* (B) Log plot of data represented in Fig-A. AF647-tagged ssDNA was used as a negative control and is visible in the Log plot.

These observations made by flow cytometry analysis, and later supported by experiments using confocal laser scanning microscopy (CLSM) – (see section Figs 25-27, 29 & 31-32), suggest that cholesterol anchors likely play a role in mitigating the otherwise unfavorable interactions between net-negatively charged DNA and similarly charged cancer cell membrane surfaces<sup>163</sup>. Notably, non-modified nanobundles showed nearly a 300-fold increase in cellular association compared to a 50nt ssDNA that was likewise not modified with cholesterol (Fig 23 - B). This observation reveals that the size and compact nature of the DNA nanobundle plays a role in augmenting cellular interaction vs. a flexible control DNA strand. At concentrations of 100nM, binding was stronger by comparison to flexible ssDNA by over 1000-fold for NB-1C and nearly 2000-fold for NB-3C. Notably, when FBS-free medium was replaced by Dulbecco's Modified Eagle Medium (DMEM) supplemented with 10% FBS, nanobundles showed approximately 100- to 200-fold higher increase in cell binding relative to NB-0C when modified with one or three cholesterol anchors respectively (Fig 23 - B). This is an enhancement of around 10-20 when compared to FBS-free conditions (Fig 22).

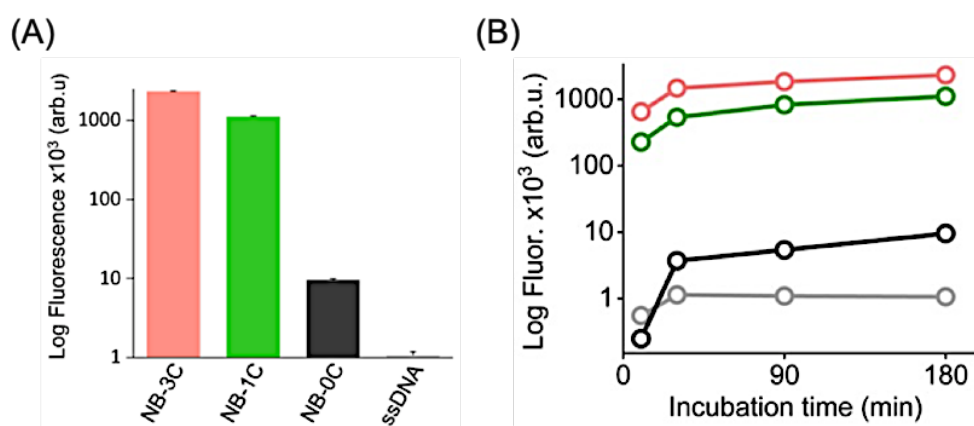


**Figure 23. Relative interaction of nanobundle variants to HeLa Cells. (A)** Nanobundles were incubated with HeLa cells at 100nM for 3h in DMEM + 10% FBS. A 50nt ssDNA component strand of the DNA nanobundle (without cholesterol modification) was used as a negative control. Error bars are standard deviation from triplicate readings. All nanobundles were tagged with AF647. **Binding kinetics of cholesterol-modified nanobundles to HeLa Cells, analyzed by flow cytometry (B).** Line-plots are shown comparing cell association for AlexaFluor-647 labeled nanobundle variants (NB-0C, NB-1C and NB-3C), incubated with cells at a final concentration of 100nM for the indicated time points. Nanobundles were incubated in DMEM + 10% FBS. Each time point was measured in triplicate for each nanobundle variant where each replicate included >3000 cell singlet event readings.

It is worth noting that lipid membrane binding activity of cholesterol-modified nanobundles was later found to be largely unaffected by presence of FBS until incubation approached time durations of 1h or more<sup>79</sup>. Indeed, kinetics measurements of cell-binding using flow cytometry (Fig 23, Fig 30 – B, pg. 55) show that nanobundle interaction with cells is rapid, hence avoiding inhibition of binding that may be caused by aggregates that are observed to form with longer incubation periods in FBS containing solutions (discussed in section 3.4, pgs. 57-61). Kinetics were obtained by flow cytometry analysis for 10, 30, 90 and 180 minute incubations, revealing fast nanobundle-cell interaction within the first 30 minutes followed by a slower phase of increase for all each variant, including nanobundles without cholesterol modification.

### 3.3. Membrane binding vs. cellular internalization

Fluorescence microscopy was used firstly to validate membrane binding of cholesterol-modified nanobundles (Fig 24), and confirmed the rapid binding kinetics observed by flow cytometry analysis.

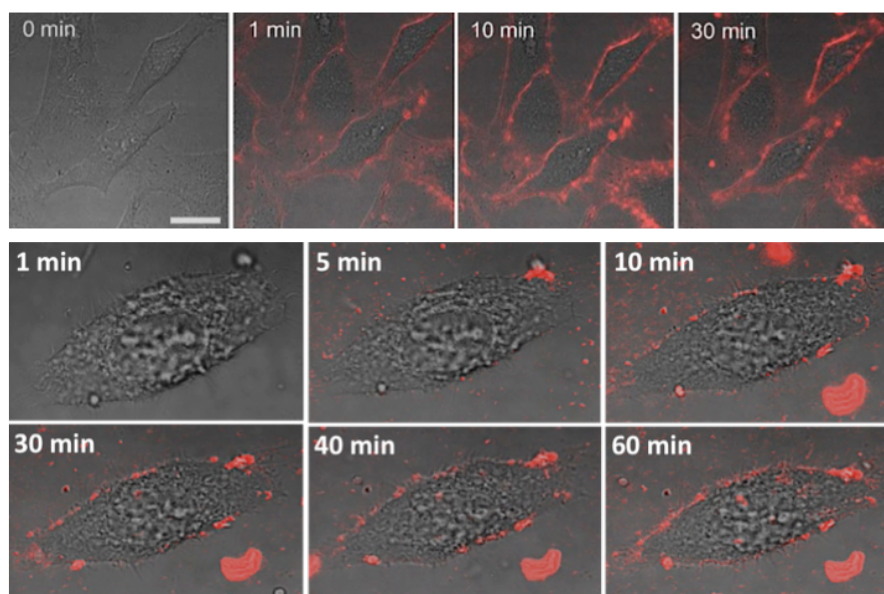


**Figure 24. Fluorescence microscopy images show that cholesterol-modified nanobundles bind to the surface of HeLa cells within 30 minutes.** NB3C was tagged with AF647 and incubated with HeLa cells at a final concentration of 100nM in FBS-free opti-MEM (**top row**), scale bar 10 $\mu$ M. Incubation in FBS containing cell media induces nanobundle aggregation, indicated by micron-scale particles (**single cell images**).

To investigate the effect of cholesterol anchors on internalization kinetics, NB-1C and NB-3C were equipped with separate fluorophores and incubated simultaneously with HeLa cells. Cross-sectional analysis of single-cells revealed enhanced intracellular signal associated with NB-3C (Fig 25, A – B), whilst signal associated with both variants (NB-1C and NB-3C) was observed to co-localize at the cell membrane. Alexaflour-647 (AF647) and 6FAM were selected as fluorescent reporters owing to their unique spectral properties. Appropriate band-pass filters were used in combination with sequential image acquisition to rule out cross-talk between the reporter fluorophores and ensure that there was no risk of obtaining false-positive signal in either channel. Comparing signal intensity between 6FAM and AF dyes in this way may however constitute a methodological limitation owing to the chemical behavior of 6FAM, which unlike AF647, is known to be quenched in acidic environments such as the endolysosomal organelles involved in cellular uptake and processing of DNSs<sup>139</sup>.

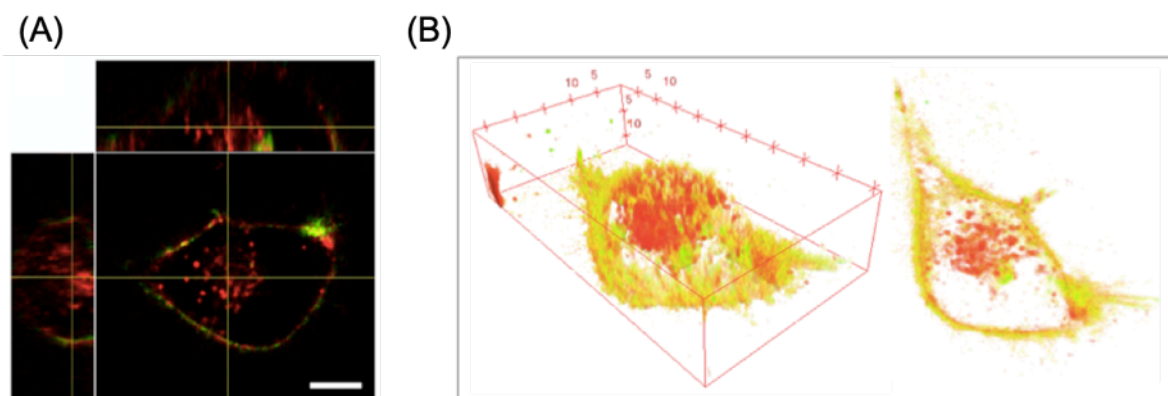


**Figure 25. Nanobundle interaction with single-cells, visualized by confocal microscopy. (A) Orthogonal XY/ZY cross-section of a single HeLa cell. NB3C (AF647/red) colocalises with NB-1C (6FAM/green) at the cell membrane but shows enhanced uptake. Scale bar 10µM. (B) Z-stack 3D reconstruction. Enhanced uptake is observed for NB3C relative to NB1C. Co-localization of signal associated with NB-1C and NB-3C is observed at the cell membrane (yellow), whilst intracellular signal is associated predominantly with NB-3C. HeLa cells were incubated with nanobundles at a final concentration of 100nM for 3h in FBS-free opti-MEM cell media.**

Nanobundle internalization into cells was observed to produce a ‘punctate’ signal consistent with reports for numerous other DNSs<sup>139</sup>. Signal produced by AF647-tagged NB3C was clearly observed to be punctate, whilst signal associated with 6FAM-tagged NB1C does not appear to be punctate to the same degree of intensity (Figs 26 - 27). This observation was found for true experimental replicates, whereby nanobundle samples were independently prepared (Figs 26, 27 & 29). Punctate signal distribution is indicative of endosomal uptake and lysosomal trafficking, confirmed here and discussed in section 3.5.

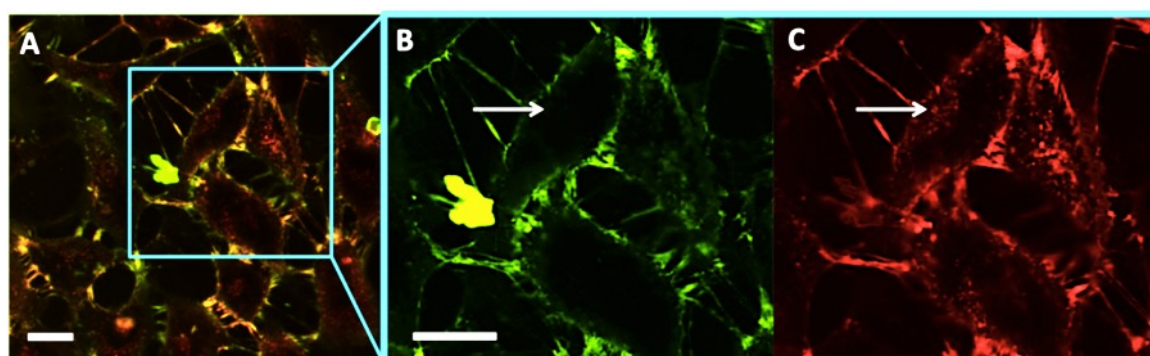


**Figure 26. Uptake comparison visualized with fluorescence microscopy.** NB-3C was tagged with AF647 (red channel) and co-incubated with 6-FAM tagged NB-1C (green channel), at a final concentration of 50nM for 2h in FBS-free opti-MEM. (A) Merged channels used for 6FAM (B) and AF647 (C). White arrows indicate enhanced uptake of NB-3C over NB-1C. Scale bar 20 $\mu$ M.

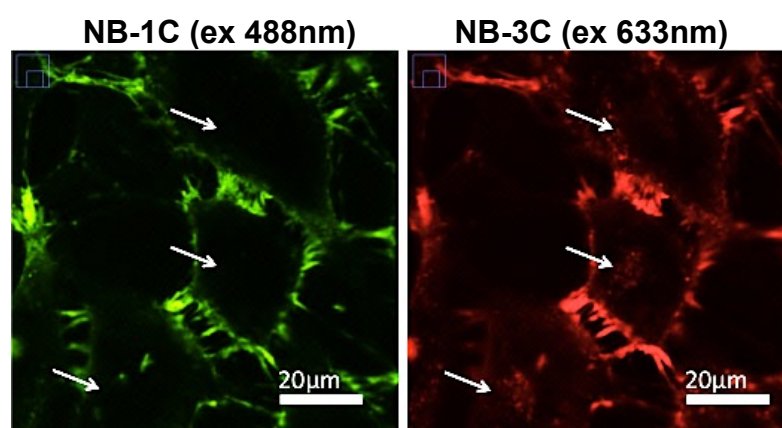


**Figure 27. Uptake kinetics comparison visualized with fluorescence microscopy – II.** Repeat of experiment showed in Fig 26. Intracellular signal associated with NB-3C (red) is observed, whereas NB1C signal (green) is primarily associated to cell membranes.

As mentioned, this observation could be explained by the known pH-dependent quenching associated with fluorescein-based dyes. I.e., signal intensity associated with 6FAM labeled nanobundles (NB-1C) might thus be expected to give a false impression, or underestimation, of uptake relative to Alexaflour-labeled NB-3C. To overcome these uncertainties, a quantitative flow cytometry assay was designed to exploit nuclease digestion of surface-accessible nanobundles, whereby each nanobundle variant was tagged with the same pH-insensitive fluorophore, AF-647. The assay is described in the following section and was used to discriminate between membrane-associated and internalized nanobundle fractions as a function of cholesterol anchor number.

### 3.3.1. Nuclease digestion assay – LSCM

To distinguish between cell-surface associated and internalized nanobundles, a nuclease digestion strategy was used and validated first using fluorescence microscopy (Fig 28). In the assay, DNase(I) is added at high concentrations to digest cell-surface associated nanobundles while leaving internalized DNA nanostructures unaffected. DNase(I) is an endonuclease that non-specifically digests single and dsDNA by hydrolyzing internucleotide phosphodiester bonds to produce mono- and oligodeoxynucleotides<sup>164</sup>. Controls without DNase incubation showed no observable signal loss, confirming that signal loss was indeed due to endonuclease digestion and not photo-bleaching (Fig 28).

The abovementioned observations are backed-up by previous studies in the Howorka group, where exponential decay profiles were obtained for Cy3-tagged nanobundles incubated with 5u/mL, BAL-31 endonuclease<sup>165</sup>. It is speculated that reduction of fluorescence signal is owed to quenching interactions that arise when the fluorophores are conformationally freed from the nanostructure, and thus able to interact with nearby nucleobases or with one-another to self-quench by photo-dimerisation<sup>162</sup>.

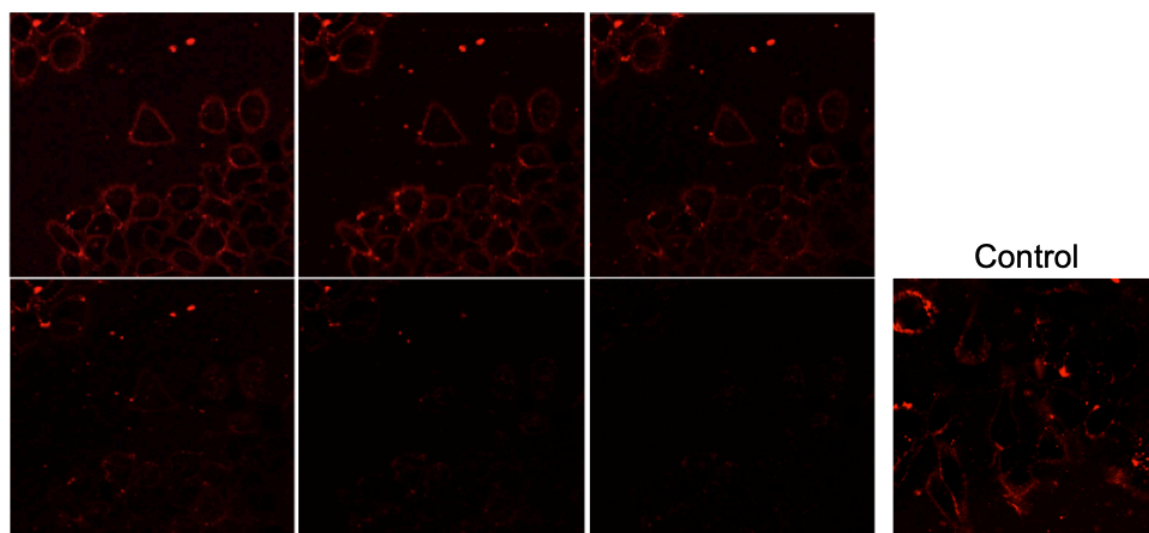


**Figure 28. DNase(I) digestion of surface-associated nanobundles analysed by fluorescence microscopy.** NB1C was tagged with AF647 (red) and incubated with HeLa cells for 1h followed by incubation with DNase(I) at 5U/mL. Each image from top left to bottom right represents 2.5 minutes of incubation with DNase(I). Signal associated with nanobundles is near completely eliminated after 15 minutes incubation. A control sample shows HeLa cells after 20 minutes of incubation with NB1C but without enzyme digestion. The control sample was imaged at the same respective time intervals to rule out photo bleaching by laser irradiation.

Nuclease digestion confirmed observations supported by later flow cytometry analysis (section 3.3.2), whereby larger fractions of NB-3C appeared to be internalized into cells vs. nanobundles equipped with only one cholesterol anchor (Fig 29). Efficient digestion was observed for both variants that localized at the cell membrane (Fig 29). Withstanding the aforementioned limitations associated with cross-comparing fluorescein and AlexaFlour dyes, NB-3C consistently appeared brighter inside cells which could be explained by the fact that NB-3C but not NB-1C can insert into lipid-bilayers<sup>162</sup>.

Additional cholesterol anchors may facilitate oligomerisation of nanobundles in or on the cell membrane as has been reported in other publications from the Howorka group<sup>159, 162</sup>, and may explain the apparent increased nanobundle internalization kinetics observed here, across experiments.

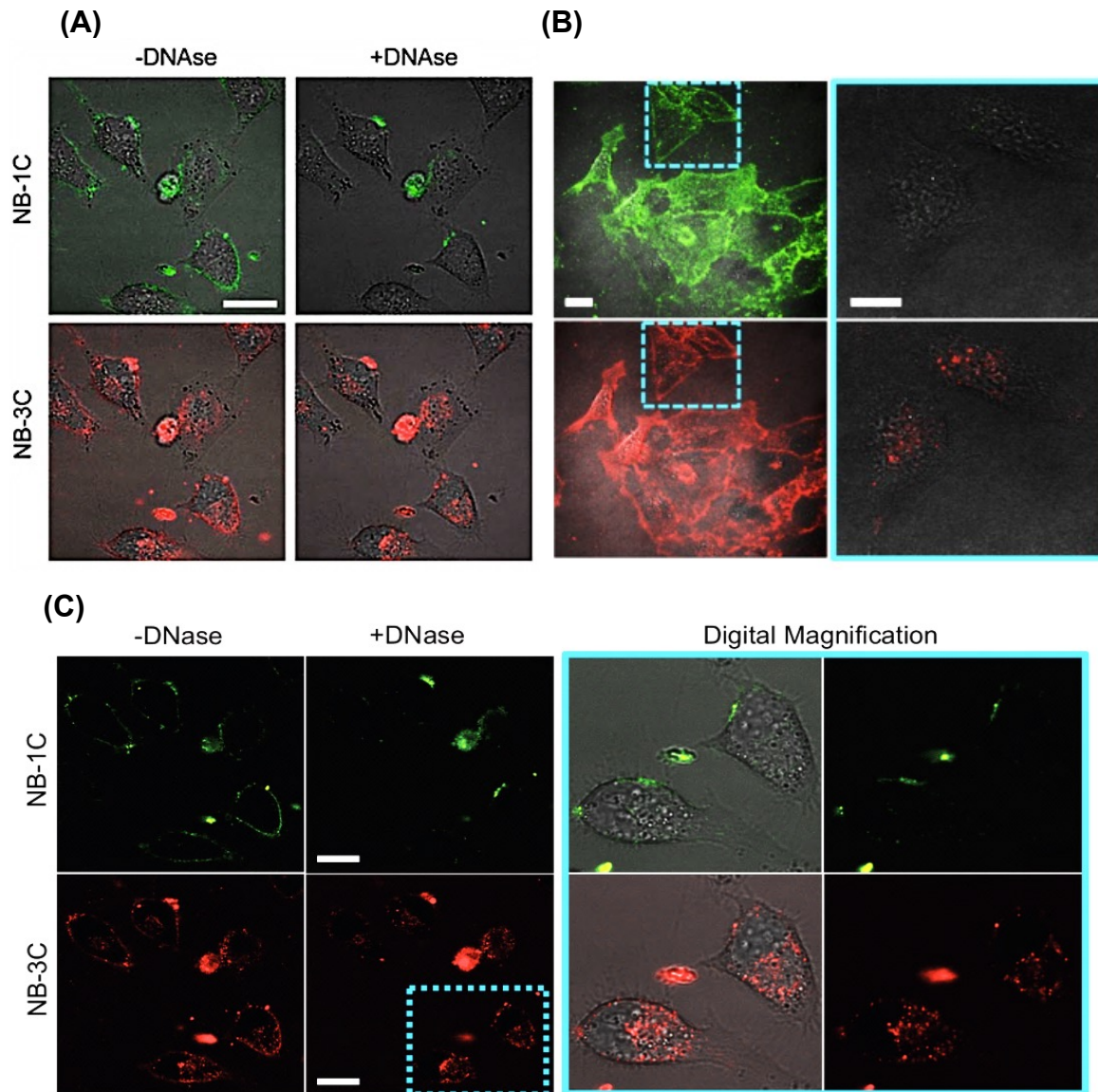


**Figure 29. Confocal fluorescence images showing cellular binding and uptake of nanobundles assessed by nuclease digestion.** DNase(I) is used to digest surface-accessible DNA nanobundles, leaving internalized structures intact. Cells were co-cubated with NB-1C and NB-3C at 100nM for 2 hours in opti-MEM without FBS supplementation. NB-3C was tagged with AlexaFlour-647 (red channel) and NB-1C with 6FAM (green channel). Images in **A** are images shown in **C** without transmitted-light overlay, then plus transmitted light as a digital zoom-in. Images in **B** are from an experimental repeat. Scale bar A, 20μM. B, 10μM.

### 3.3.2 Nuclease digestion assay – Flow Cytometry (FC)

Quantitative information regarding nanobundle membrane binding vs. uptake kinetics was obtained by FC analysis. Cells were incubated with all three nanobundle variants (nanobundles with zero, one or three cholesterol anchors) for 4 hours, followed by nuclease digestion. Importantly, and unlike the method used for microscopy analysis, all nanobundle variants were labeled with the same pH-insensitive fluorophore (AlexaFlour-647). When incubated in FBS free conditions, FC data revealed that the fraction of internalized NB-3C and NB-1C amounted to approximately 66 and 62% of total nanobundles respectively (Fig 30 - A). By comparison, when cell culture media was supplemented with FBS, the fraction of internalized nanobundles was much smaller at <10% (Fig 30 - B).

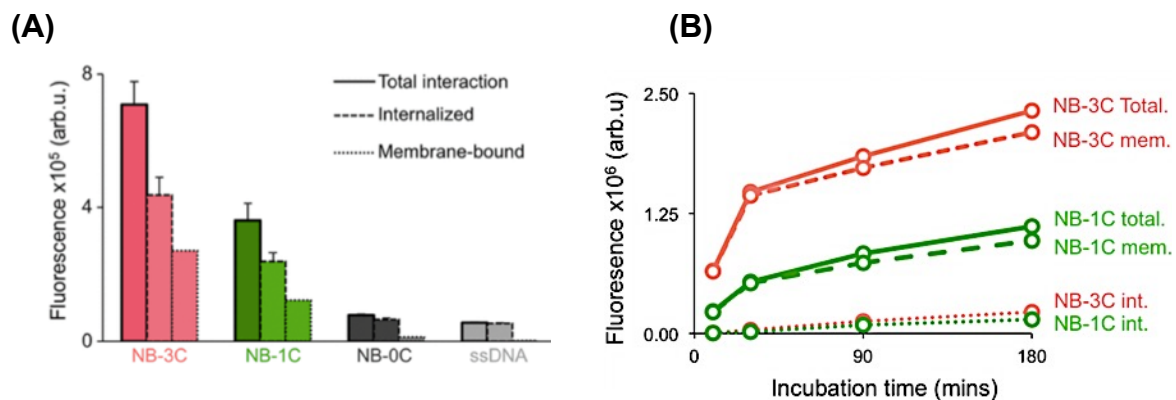


**Figure 30. (A) Ratios of cell membrane-bound vs. internalized nanobundles.** Cells were incubated with nanobundles at a final concentration of 100nM in FBS-free opti-MEM. After 3 hours incubation, cells were washed thrice with PBS 1x then subjected to nuclease digestion with DNase(I) at 10U/mL final concentration and analyzed by flow cytometry. Total nanobundle-cell interaction was obtained from a non-enzyme treated sample group. Membrane-associated fractions were obtained by subtracting the enzyme-treated (internalized) from non-treated (total) values. Standard errors are only available for total and internalized samples (conducted with experimental triplicates). **(B) Relative membrane binding and uptake kinetics of NB-3C vs. NB-1C, in the presence of FBS.** Nanobundles were incubated with HeLa cells at 100nM for 10, 30, 90 and 120 minutes in DMEM + FBS, 10%. After replacing buffer, cells were subjected to DNase(I) digestion to remove membrane-associated nanobundles. Median fluorescence per cell is plotted against incubation time to yield a kinetics profile of cells with internalized nanobundles (enzyme-treated) vs. membrane-associated bundles (non-enzyme treated minus enzyme-treated values).

In comparison to FBS-free conditions a fraction of >90% membrane-associated nanobundles is high and suggests that serum proteins increase cell membrane binding without corresponding increases in uptake (Fig 30 A - B). FBS contains more than 20 proteins including albumin, which can vary in concentration between batches but on average reach levels of up to 300ug/mL<sup>166</sup>. Similarly sized but oppositely charged IgG antibodies are another major component of FBS and can be expected to complex with DNA nanobundles via electrostatic interactions. These complexes may be expected to increase binding to cells via cellular recognition events. Additionally, offsetting DNA charge in this way may be expected to reduce repulsive interactions between net-negatively charged DNA and similarly charged cancer cell membranes, leading to increased binding. Decreased uptake however may be attributed to increased particles size as is consistent with studied effects of protein opsonization for numerous organic and inorganic nanoparticles (as is discussed in section 1).

Flow cytometry analysis also revealed that binding occurred faster than uptake kinetics (Fig 30 - B), as might be expected for the two sequential process. Notably, the nuclease digestion assay measured by flow cytometry, confirmed the observed positive correlation between nanobundle cholesterol number, membrane binding and uptake (Fig 30). Cholesterol-anchor number however did not proportionally augment uptake kinetics when cell media was supplemented with FBS (Fig 30 - B). When incubated in FBS free conditions, three cholesterol anchors provided for an approximate 8- and 4-fold increase in cellular association over NB-0C and NB-1C respectively. No significant interaction was observed where nanobundles lacked cholesterol tags, further confirming the importance of hydrophobic anchors for active uptake of DNA nanostructures. Indeed, recent studies report that similar sized DNA nanostructures are scarcely internalized without the aid of transfection reagents<sup>167</sup>.

Membrane-immobilized structures could be internalized by mediating membrane distortion events, e.g., transmembrane flip-flop<sup>168</sup> and membrane deformation<sup>169</sup>. Recent studies report that NB-3C, and not NB-1C is capable of deforming lipid bilayer membranes<sup>163</sup>, where the hypothesis is such that three cholesterol anchors are required to mediate nanobundle insertion into lipid bilayers to cause a

disruption in membrane curvature. These studies employed biomimetic vesicles as membrane surrogates, to reveal that a single cholesterol anchor can only mediate membrane tethering, as opposed to insertion, thereby reducing the likelihood of membrane distortion events. As numerous endocytosis pathways begin with membrane deformation events, it is not unreasonable to assert that the positive correlation seen here, between cholesterol-anchor number and uptake, can be explained by increased propensity for membrane insertion, which may be linked, to deformation and subsequent induced uptake.

Notably, endocytosis has been reported as the primary uptake pathway for cholesterol-DNA probes, where a reverse correlation was found between uptake kinetics and hydrophobicity of the DNA probe<sup>170</sup> (i.e., reduced internalization kinetics with increased probe hydrophobicity). However, these DNA-based probes were found to freely diffuse back into cell incubating solution, where outflow rate was reduced with increased probe-hydrophobicity. The opposite trend was observed here for small, cholesterol-modified DNA nanostructures but only in the absence of FBS. These observations may be explained by (i) the compact nature of DNA nanostructures vs. flexible ssDNA-based probes and (ii) the interplay between hydrophobicity, aggregation, insertion and cellular internalization. Specifically, a greater hydrophobic surface area may be required to offset the larger energetic penalty associated with membrane insertion of a DNA nanostructure vs. a flexible, single-stranded DNA-based probe.

### 3.4 Nanobundle-cell binding as a function of FBS presence in cell media.

CLSM revealed significant aggregation when diluting cholesterol-modified nanobundles directly into FBS containing cell media (Fig 31 - A). Aggregation and association to cells appeared to be significantly reduced where nanobundles had no cholesterol anchors (Fig 31-32, pgs. 58-59). Z-stack XY/ZY projections suggest that micron-scale aggregates appear at the cell-membrane interface and possibly traverse regions of cellular membranes (Fig 25 - B). The reduced fluorescence signal associated with NB-0C is likely due to its limited binding to cellular membranes. I.e., freely diffusing NB-0C may be difficult to 'see' compared to relatively immobilized NB-3C, which is closely associated to the cell membrane.

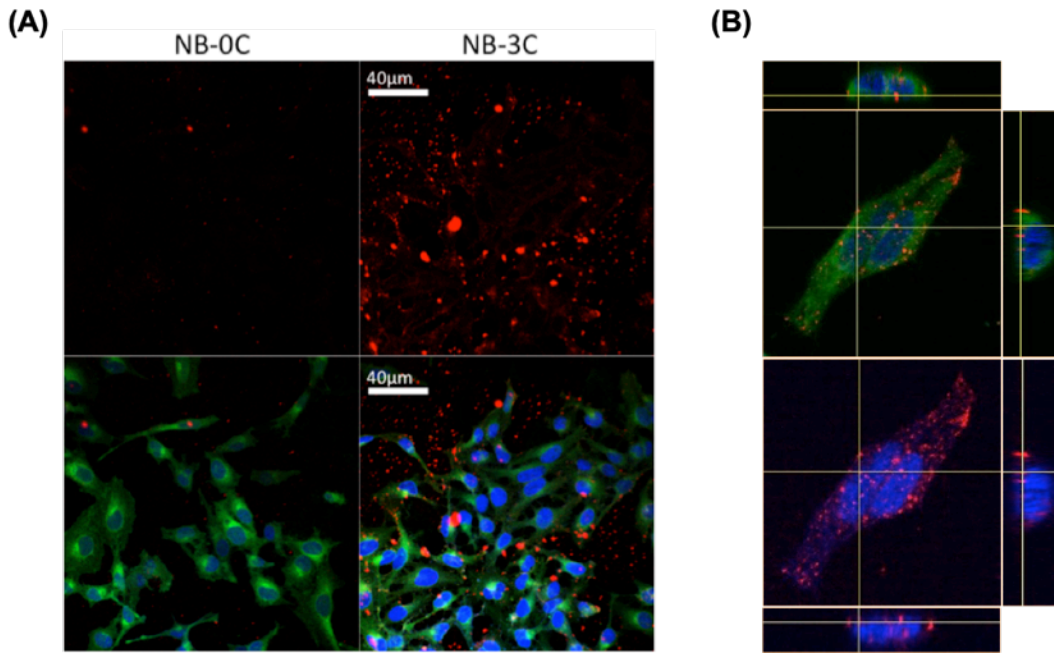


**Figure 31. (A) CLSM analysis of nanobundle aggregation and interaction with HeLa cells.** Nanobundles with zero or three cholesterol anchors (red, ex/em 633/690nm) were incubated with HeLa cells for 3 hours by diluting into DMEM + FBS 10% to a final concentration of 50ug/mL. Cells were washed thrice with PBS, 1x and stained with cell-mask green (green, ex 522/535nm). DAPI was used to stain nuclei and excited using a 405nm laser line. An objective 40x lens was used for image collection. **(B) Z-stack XY/YZ projection of NB-3C interacting with single HeLa cells.** Images are composites of channels used to visualize cell-mask green for membrane staining (green), DAPI for nuclei staining (blue) and nanobundles tagged with AlexaFluor-647 (red). An objective 60x lens was used for image acquisition.

To further investigate FBS-dependent binding and uptake of nanobundles, a 60x objective lens with a reduced numerical aperture (1.4um) and pinhole diameter (135um) was used to achieve enhanced resolution for Z-stack analysis and 3D image reconstructions (Fig 33, pg. 60). It is worth noting that optical section thickness achieved with these settings is on the order of  $0.4\mu\text{m}^{171}$ . This means that aggregates (of DNA nanostructures) smaller than this optical-section size limit cannot be truly resolved. However, structures with dimensions exceeding this limit should be readily resolved, meaning that comparisons can be drawn from the gathered data, albeit in a qualitative fashion.

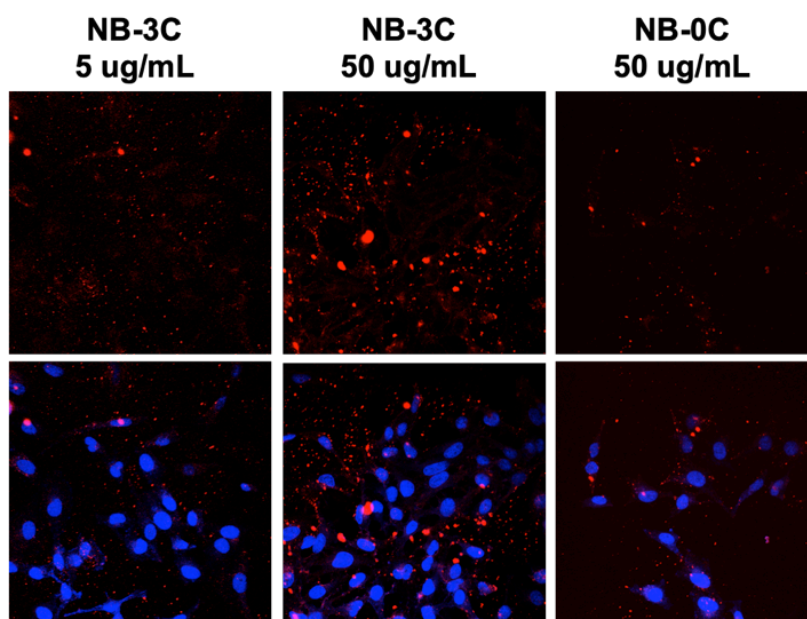


**Figure 32. Effect of FBS and cholesterol modification on DNA nanobundle aggregation and cell interaction.** Nanobundles lacking cholesterol anchors (NB-0C) or with three cholesterol anchors (NB-3C) were incubated with HeLa cells at the designated final concentrations. DMEM was used as an incubating medium which was supplemented with FBS to a final concentration of 10% W/V (after addition of nanobundles).

3D-rendered Z-stack reconstructions further revealed FBS-dependent nanobundle aggregation and micron-scale aggregates appearing at the cell-surface (Fig 33). Notably, micron-scale aggregates were observed where nanobundles were incubated in DMEM+FBS but only in FBS-free conditions. Additionally, perinuclear localization is observed in FBS-free conditions that might be otherwise masked by the increased membrane binding observed in FBS+ conditions. Recent in-vitro studies assessing the stability of DNA nanobundles in biological media suggest that FBS prevents significant membrane binding but only after a significant time-window<sup>80</sup>. In this light, Burns et al showed that chol-modified nanobundles were able to bind to GUVs in the presence of FBS for up to 20-30 minutes but that binding was significantly inhibited after longer time durations (Fig 10, pg. 26). Taken together, these observations agree with the rapid binding kinetics observed here by FC analysis and suggest that serum proteins are the primary culprits causing nanobundle aggregation (as opposed to the differences in small-molecule composition between opti-MEM and DMEM). However, the effect of differences in nutrient compositions cannot be ruled-out here, prompting the need for expanded assays to take these factors into account and provide a deeper understanding.

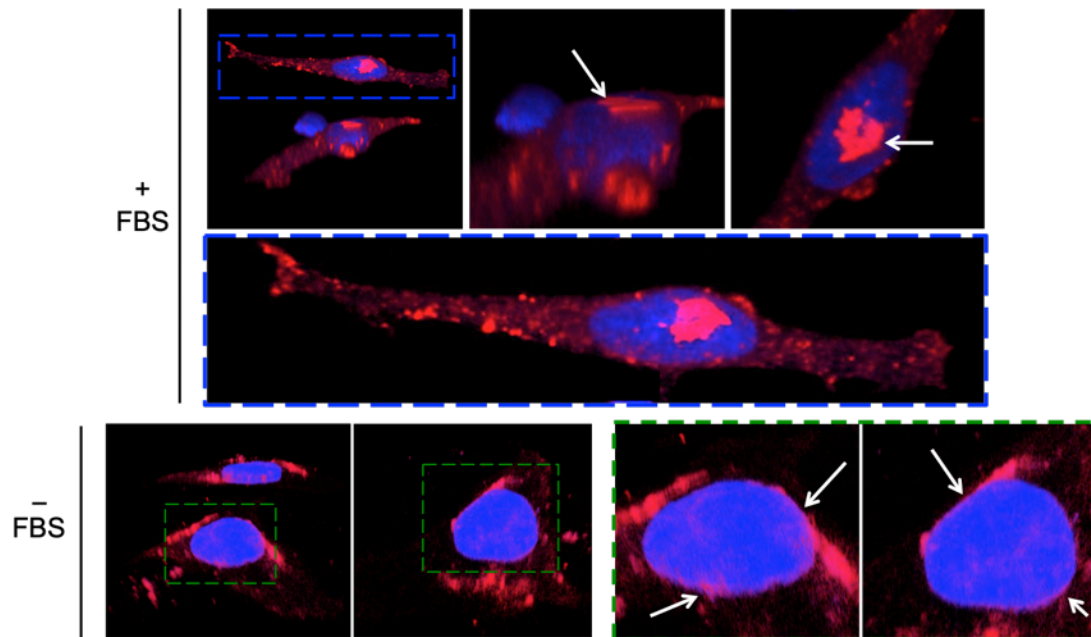


**Figure 33. Effect of FBS on nanobundle-cell interactions visualized by 3D Z-stack reconstruction.** Nanobundles with three cholesterol anchors were diluted into DMEM + 10% FBS or FBS-free DMEM, then immediately incubated with cells for 3 hours and imaged using Laser-Scanning Confocal Microscopy. Micron-scale aggregates are observed at the plasma membrane surface under FBS+ conditions, indicated by white arrows (top image block). By contrast, larger aggregates were not observed in FBS-free conditions (bottom image row). Perinuclear localization of nanobundles can be seen in FBS-free conditions, indicated by white arrows in the magnified image pane (blue box).

A significant concentration of DNase(I) was required to completely digest membrane associated nanobundles after 15 minutes, according to the fluorescence-based nuclease digestion results. Furthermore, binding kinetics of cholesterol-modified nanobundles was also observed to proceed rapidly (section 3.3.2). Together, these observations suggest that micron-scale aggregates are likely the result of complexes forming between nanobundles and serum proteins, which occur outside of the immediate time-window across which nanobundles are observed to interact and with and internalize into cells. As mentioned previously with reference to work published by Howorka & Howorka & Burns<sup>79</sup>, the time-window for cholesterol mediated binding of nanobundles to cells appears to be in the order of one hour after dilution into FBS-containing media. Once complexes have formed, membrane binding is reduced, yet the exact nature of this process remains unclear.

Notably, aggregation of cholesterol modified nanobundles was observed to be significantly greater than that observed for nanobundles lacking cholesterol anchors when incubated with cells in the presence of FBS. These observations suggest that DNA nanobundles may interact with serum proteins via both electrostatic and hydrophobic interactions, the latter of which may dominate to cause aggregation. The data presented in this chapter further supports more recent observations in this context<sup>80</sup> and highlights the need for more detailed examination to better understand interplay between lipid modified DNA nanostructures, similarly sized proteins and interaction with membranes.

### 3.5 Intracellular localization of DNA nanobundles

Confocal microscopy was used to investigate the intracellular localization of DNA nanobundles. As discussed in section 1.2.3., the localization of nanoparticles, including DNSs, can depend on uptake pathway<sup>138,152</sup>. Here, LysoTracker was used to probe the suspected endolysosomal trafficking of DNA nanobundles. LysoTracker Red DND-99 is a red-fluorescent dye for labeling and tracking acidic organelles, and consists of a fluorophore linked to a weak base, which is only partially protonated at neutral pH<sup>172,173</sup>. This features allows LysoTracker probes to permeate cellular membranes for live or fixed-cell imaging.

Time-course imaging of HeLa cells revealed that nanobundles first localized with cell membranes (Figs 34 - 35), followed by co-localization with LysoTracker after 2 hours. Signal co-localization with LysoTracker suggests endolysosomal trafficking of nanobundles, consistent with reports for numerous other DNSs, as mentioned previously<sup>138, 151</sup>. Additionally, imaging after 24-hours revealed perinuclear localization of nanobundles (Figs 34-36), a fate observed for numerous types of nanoparticles that are unable to escape endolysosomal trafficking. These observations however come with the caveat that internalized structures may not be structurally intact, as has been reported in one recent study<sup>259</sup>. Nevertheless, numerous studies have reported maintained intracellular stability for similarly sized DNA nanostructures<sup>233</sup>.

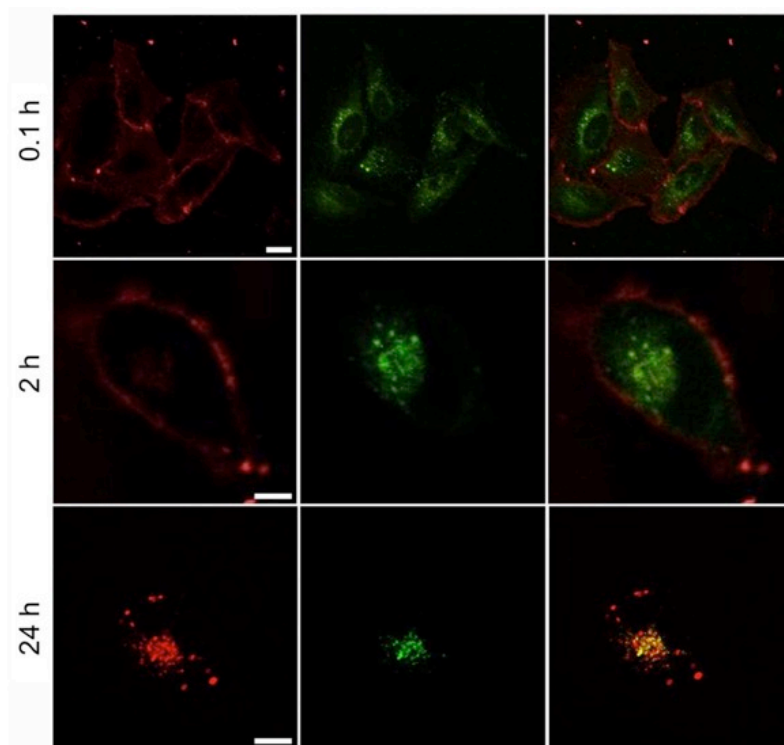


**Figure 34. Cellular uptake of DNA nanobundles.** Nanobundles with three cholesterol anchors (NB-3C) were labeled with AF-647 (red) and incubated with HeLa cells for 2 h at a final concentration of 100nM. Samples were then aspirated and cells were washed thrice with PBS 1x, followed by incubation with LysoTracker (green) in DMEM+FBS for 1 hour at a final concentration of 100nM. Co-localization between NB-3C and endolysosomal compartments was observed after 3 hours incubation. Co-localization persisted 24 hours after incubation with signals localizing at perinuclear regions. Images from each laser line were acquired sequentially to prevent cross talk between AF-647 and LysoTracker fluorophores.

Inability to escape from endosomes constitutes a major hurdle for nanoparticle-mediated drug delivery<sup>174</sup> and drug delivery in general<sup>175</sup>. The inability to escape from endosomes has been found for other tube-like DNSs<sup>133,139</sup>, with the exception of some larger structures that may bypass endosomal uptake due to their size<sup>139</sup> (see table 2, pg. 40). DNA nanostructures have however been successfully routed to other cellular organelles by covalently attaching ‘nuclear localization signal’ (NLS) peptides<sup>176</sup>. In 2014, Liang et al. observed microtubule-dependent shuttling of their NLS-tagged tetrahedral DNA nanostructure<sup>177</sup>. Chan & Lo., also observed microtubule controlled trafficking of their DNA nanocage induced by functionalization with subcellular localizing peptides (SLPs), and were able to

target specific organelles by selecting different SLPs<sup>178</sup>. This was however only achieved by using nanoneedle technology to physically inject their structures into cell cytoplasm, allowing the researchers to avoid the issue of endosomal uptake and entrapment altogether while preserving the structural integrity of their DNA nanocages. By comparison, the study here sought to probe interplay with serum-proteins and thereby provides some insight into these interactions with DNA nanostructures and the subsequent effects for cell binding and uptake.

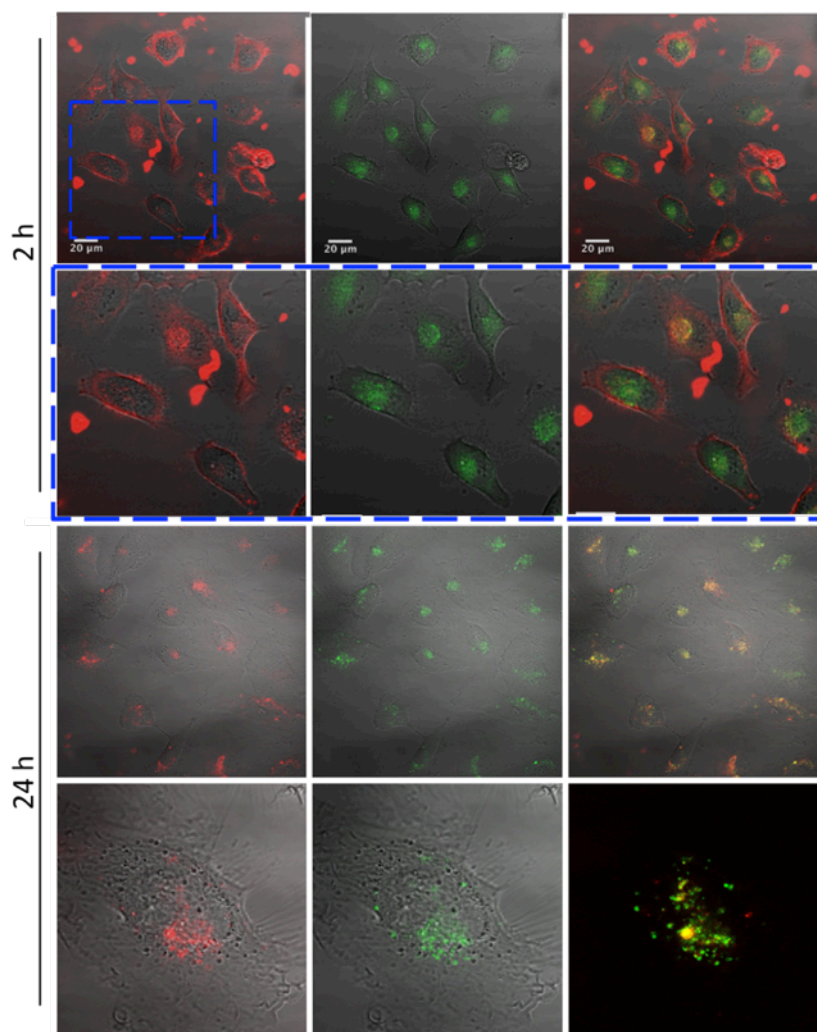


**Figure 35. Cellular uptake of DNA nanobundles – II.** Cholesterol-modified nanobundle localization imaged by LSCM at 2 and 24-hour post incubation. Nanobundles (red) are partly internalized 2-hours post incubation and co-localise with lysotracker (green). Nanobundles have internalized into cells completely after 24 hours and are shuttled toward perinuclear regions. The bottom right 24-hour image without bright-field overlay is a corresponding maximum intensity projection from z-stack analysis. All images collected with a 40x objective, 2h images are digitally magnified.

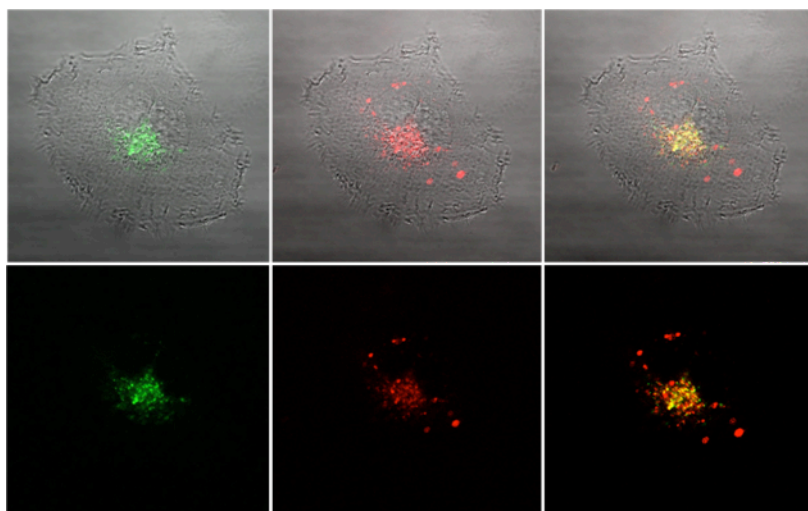


**Figure 36. Nanobundles localize at perinuclear positions.** Image analysis of single HeLa cells reveals perinuclear localization of nanobundles 24-hours after incubation. Transmitted light overlay (top row) reveals a representative cell undergoing mitosis, where nanobundles (red) co-localize with LysoTracker (green) around the two dividing nuclei.

Endosomal uptake and trafficking of cholesterol-modified nanobundles is consistent with the uptake of 5'-cholesterol-modified oligonucleotides, which have been shown to internalize via receptor-specific endocytosis pathways<sup>179</sup>. You et al., recently showed that cholesterol-DNA as well as other lipid-modified DNA conjugates internalize preferentially through clathrin- or caveolae-mediated endocytotic pathways, with the majority of their DNA-based probes being located either inside late endosomes or lysosomes where they are degraded or rejected out of cells<sup>170</sup>.

Perhaps of particular relevance, the abovementioned work by You et al revealed enhanced membrane binding and insertion kinetics for their DNA-based probes when in monomeric vs. aggregated forms, and also that cholesterol-DNA exhibited the highest insertion efficiency vs. various other lipid-DNA conjugates, with endocytosis kinetics for such probes increasing inversely with lipid hydrophobicity. Furthermore, less-hydrophobic lipid-DNA based probes were found to form more compact aggregates and internalize but also detach from cell membranes more rapidly. This study and others<sup>180</sup>, have revealed complex interplay between hydrophobicity of lipid-modified DNA, critical aggregation concentration (CAC), membrane binding persistence and uptake. Likewise, the project presented in this chapter suggests interplay between aggregation of lipid-modified DNA

nanostuctures and their uptake efficiency using HeLa cells as a model cell line. DNA nanobundle aggregation, digestion and/or subsequent loss of structural integrity could all interplay to mediate cell-membrane binding and uptake.

Leading on to the final and brief sub-section of this chapter, the work presented thus far highlights a need for more robust assays aimed at screening serum and cell media components against observed changes in nanostructure-cell interactions. Deeper insights into these interactions will pave the way for more informed design considerations of DNA nanostructures so that their interaction with biological systems can be controlled with greater precision. Next, a brief section reports a tentative investigation into the how hollow-barrel type DNA nanostructures might be used to control membrane poration in living cells. This topic was not the focus of the chapter but has been included to expand the scope of future work and broaden discourse around the potential applications of such devices.

---

### 3.6 Nanobundle-induced reduction of cell viability

Numerous protein or peptide based toxins can kill eukaryotic cells by self-assembling to form nanopores capable of porating lipid bilayer membranes<sup>181-182</sup>. As such, design of artificial DNA based pores for the same purpose may provide a novel route for targeted cell killing<sup>93</sup>. The DNA nanostructure used for this project was designed as a synthetic nanopore and has been used to control molecular flux across artificial lipid bilayers<sup>91,157-158</sup>. To date, only one example can be found for DNA-based cytotoxic nanopores<sup>183</sup>, which however could not directly attribute cell killing to membrane poration. This is likely due to the difficulty in assessing membrane puncturing in living cells and as such, most studies to date have focused on biomimetic vesicles to model cellular membranes.

To tentatively probe if the structure used for this project could porate living cells, an assay making use of the metabolic activity reagent AlamarBlue was conducted. The rationale underlying this experiment is that cellular regulation of in- and out-bound ions as well as small molecules is essential for cell viability<sup>184,185</sup>. Cell viability would presumably be altered if the 6-duplex nanobundle was able to puncture or significantly destabilize cellular membranes, which can be measured for using metabolic activity reagents such as AlamarBlue<sup>186</sup>.

Cell viability was reduced by over 20% at the maximum nanobundle concentration tested (500nM) but returned after 24-hours (Fig 37 – pg. 67). FBS was completely excluded from the incubation media in order to avoid nanobundle fouling or aggregation induced by interaction with serum proteins. To this end, Opti-MEM was used as an incubation medium to offset for loss of cell viability, which, according to the manufacturer, can be achieved via reduction of serum supplementing by a factor of 50%. The absence of FBS itself could have caused a reduction in cell viability, which was not tested for as a control factor. Indeed, without such a control it is difficult to attribute reduction in cell-viability to pore-forming or membrane-destabilizing activity of the nanobundles. However, dose-dependent effect was observed, suggesting that reduction of cell viability could at least be partially attributed to action of the DNA nanostructures.

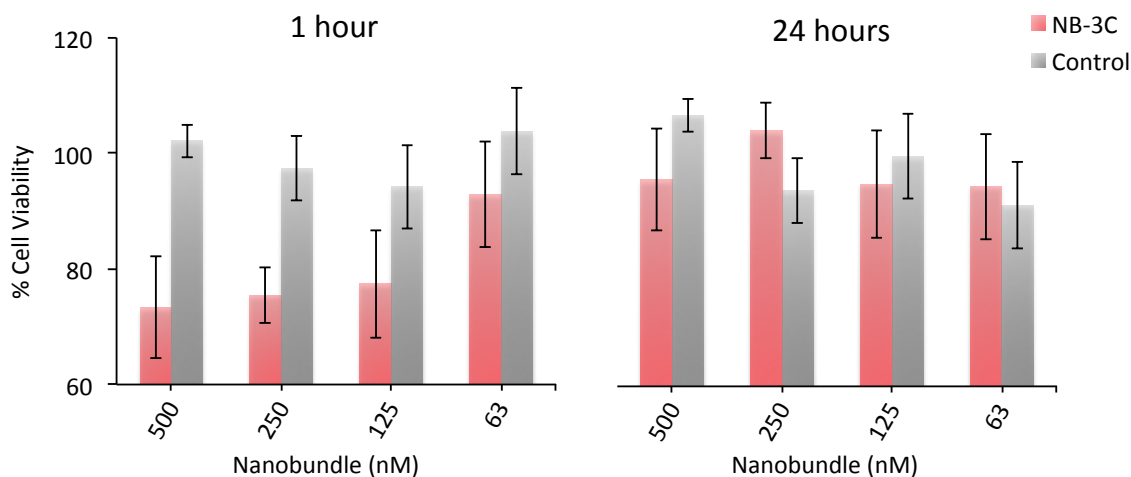


**Figure 37. Cell viability assay of NB3C with HeLa cells.** HeLa cells were brought to confluence, seeded into a 96-well plate and left to grow for 24-hours prior to incubation with nanobundles (see experimental section 10.8). After aspiration of 10% FBS containing media (DMEM), and washing of cells (PBS 1X), nanobundles were incubated with HeLa cells from approximately 60 to 500nM for 3 hours in FBS-free cell media (opti-MEM). Nanobundles lacking cholesterol anchors (NB-0C) were used as a structural control. The metabolic activity reagent AlamarBlue was used to measure cell viability by fluorescence absorption. Analysis was conducted using a calibration plot of seeded cells vs. fluorescence emission maxima from triplicate readings, where R-values for each plot were  $\geq 0.99$ . The cell number calibration range was from 20,000 to 625 cells.

Notably, control DNA nanobundles lacking cholesterol moieties did not cause a reduction in cell viability. These observations are supported by earlier studies that revealed cell-cytotoxic activity associated only where 6-duplex DNA nanobundles were functionalized with ethyl-phosphorothioate moieties to create a hydrophobic 'belt' around the structure exterior<sup>180</sup>. It was hypothesized that this hydrophobic character was required to offset energetic mismatch between the net-negatively charged DNA and the cell-membrane surface, thereby providing a means to potentially insert the structure into cell membrane, yet the exact mechanism underlying observed reduction in cell viability was not elucidated. The results presented here are likewise tentative and do not prove whether or not DNA nanopores can puncture living cells. For instance, as opposed to membrane puncturing, cholesterol-modified nanobundles could simply be masking the cell surface to abrogate in and out-bound flux of metabolic compounds that control cellular viability.

#### 4. Conclusions & future work – Project I

The work presented in this chapter explored how simple chemical functionalization with cholesterol anchors can augment DNA nanostructure-cell interactions. The structure used for this study was designed as a synthetic DNA-based nanopore, but was used here instead as a model system, to probe the effect of individual cholesterol anchors on both (i): cell-membrane binding and (ii): cellular uptake.

The findings presented in this chapter show that a single hydrophobic cholesterol anchor significantly increases binding of a 9x5x5nm DNA nanostructure to HeLa cell membranes. Three cholesterol anchors were shown to significantly enhance nanobundle-cell association. Additionally, the presence of serum proteins was found to significantly affect DNA nanostructure interaction with cells. A positive correlation between cellular uptake and cholesterol anchor number was observed only in the absence of FBS, via a nuclease digestion method, which was used to discriminate between cell surface-associated and internalized nanobundle fractions. Increased internalization of DNA nanobundles equipped with three cholesterol anchors (over their one-cholesterol modified analogues) can be attributed to the added hydrophobic surface area provided for by each additional cholesterol anchor. Each anchor is expected to help offset the electrostatic repulsion between DNA structure-exterior anionic phosphate groups and the negatively charged membrane-surface of HeLa cells. Indeed, studies using biomimetic lipid membranes suggest that >1 cholesterol anchors are required for membrane insertion of the 6-duplex DNA nanobundle<sup>162</sup>, which may explain the observations made here, in terms of positive correlation between cholesterol anchor number and cellular uptake.

Notably, cholesterol has been used in combination with DNA nanostructures to mediate membrane deformation<sup>187</sup>, bend individual DNA nanostructures<sup>94</sup>, induce controlled aggregation<sup>87</sup> and ‘programmed’ assembly of sub-units<sup>88</sup>. Aggregation of the 6-duplex DNA nanobundle has indeed been shown to be dependent on cholesterol anchor number<sup>79</sup>, which may also provide an explanation for increased uptake in FBS-free conditions. Larger nanobundle aggregates may be excluded from certain internalization pathways according to size, limiting their uptake.

Aggregation of DNA nanobundles is likely mediated by the presence of ions in the incubating solution used for cell-uptake experiments, as well as residual serum proteins that may remain after washing steps in serum-free conditions. Crucially, divalent ions are known to induce DNA binding to neutral and negatively charged membranes<sup>185, 255</sup>, which was avoided here by preparing DNA nanostructures in Magnesium-free PBS.

In order to advance DNA nanostructures as therapeutic devices or more broadly as biotechnology tools, we must better understand their interplay with other similarly sized particles in the physiological environment. Nanoparticle ‘fouling’, a process also known as protein-opsonization, is a growing area of interest in pharmacology and nanomedicine<sup>107-108, 110</sup>, and has already advanced to provide for some specific design criteria depending on the particle material and physiochemistry, route of (nanoparticle) administration and intended physiological target<sup>101-102, 106</sup>. Crucially, hydrophobic molecules used to augment uptake, such as cholesterol, can interact preferentially with specific serum proteins<sup>188</sup> and could thereby be exploited as a generic design strategy for DNA nanostructure-cell type targeting, by not only addressing membrane binding preference but also protein-membrane induced interactions<sup>189</sup>, DNA nanostructure stability<sup>190</sup> and bioavailability<sup>187</sup>.

In the context of developing DNA nanostructures as membrane-porating agents, further assays that make use of live-dead staining methods alongside more appropriate experimental techniques, such as EM, will be useful. EM could be used to prove whether lipid-modified nanobundles are capable of membrane insertion and could be used alongside metabolic activity assays to better understand observed effects. Indeed without such robust approaches here, alongside additional controls, only limited conclusions can be drawn from the cell-cytotoxicity data presented here, presented in sub-chapter 3.6.

To date, the work presented in this chapter has been cited 10 times, with reference to cholesterol as a useful chemistry to both control DNA nanostructure-membrane interactions, and augment delivery of DNA nanostructures and other DNA-based therapeutics into various cell-types.

## 5. Project – II: Introduction

### 5.1 Cell penetrating peptides

Cell penetrating peptides (CPPs) are typically short peptides (<30 residues), capable of penetrating biological membranes to facilitate internalization and intracellular distribution of bioactive cargo<sup>191</sup>. Early research into CPPs focused on mutagenesis studies of various proteins with well-known cell transduction properties, giving rise to the former term ‘protein transduction domains’ (PTDs). The first and perhaps most significant example of CPPs are from over 20 years ago and were focussed on the HIV-transactivating protein domain (TAT)<sup>192-193</sup>. Around this time, Derossi et al., discovered a short peptide sequence: RQIKIYFQNRRMKWKK, termed penetratin, derived from the fruit fly *Drosophila Antennapedia*<sup>194</sup>. Design of CPPs was subsequently inspired by these positively charged species but has since expanded to probe different combinations of charge, structure and polarity following discovery of numerous other naturally occurring CPPs with varying physicochemical properties<sup>189,195</sup>. Indeed, positively and negatively charged CPPs with amphiphatic and non-amphiphatic features are used widely today, for in-vitro and in-vivo studies across bioscience fields.

As of 2021, the online repository termed ‘CPP version 2.0’ catalogues some 1855 entries for unique CPPs<sup>196</sup>. Notably, of the 1855 CPPs listed in this database, approximately 95% are linear (Fig 38 - A). The statistical breakdown provided for on this web-based repository show that the majority of CPPs have been used to deliver fluorescent cargo (58.4%) – (fig 38 - C). Therapeutically relevant cargo delivery is found to be mostly nucleic acids (16.2%), followed by nanoparticles (7.83%), proteins (9.80%), peptides (4.74%) then small molecules (1.9%) and peptide-nucleic acids (1.29%) – (Fig 38 - C). Interestingly, research into CPPs has shifted from being mostly focused on protein derived peptides to a near equal match with synthetic sequences (54.8 to 41.7% respectively) – (Fig 38 - B).

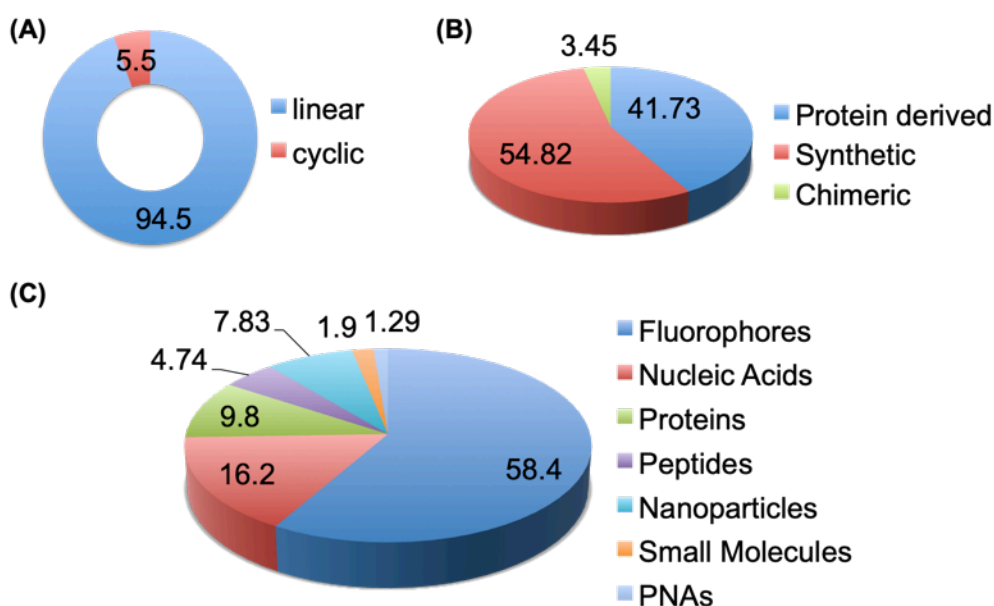


**Figure 38. Statistical breakdown of cell-penetrating peptides (CPPs) reported in literature as of June 2021.** CPPs distribution on the basis of (A) origin of peptide, (B) types of structure and (C) types of cargo delivered. Note – statistics taken from the CPP 2.0 database, from reference 194.

Based on their physicochemical features, CPPs can be broadly grouped into three categories: Cationic CPPs, hydrophobic CPPs, and amphipathic CPPs. Cationic CPPs show the greatest affinity to cell membranes by virtue of electrostatic interactions, but come with the drawback of higher cytotoxicity<sup>189-193</sup>. Negatively charged cell membrane glycoproteins attract cationic CPPs, thereby facilitating cell binding and uptake independently from receptor-mediated recognition<sup>197</sup>. More than 40% of CPPs are amphipathic, containing polar and non-polar motifs and are derived from numerous natural sources<sup>194</sup>. By comparison, hydrophobic CPPs are relatively rare and consist mainly of a large number of non-polar residues; typically with no more than 20% of their overall sequence containing charged amino acids<sup>194</sup>.

### 5.1.1 CPPs: Endosome escape

CPPs mainly internalize into cells via endocytosis pathways<sup>189,193</sup>. Briefly, the endocytosis process consists of uptake (of extracellular material) via encapsulation into vesicular compartments, 'endosomes', that bud inwards from

the cell plasma membrane. Crucially, material (bioactive cargo, drugs and nanoparticles etc.) internalized via endocytosis must be released from endosomes to reach its intended intracellular target<sup>122</sup>. This process is referred to as ‘endosome escape’ and constitutes the major rate-limiting step for efficient delivery of drugs and their delivery vehicles<sup>122,172</sup>. \*Note - Endocytosis is covered in some detail in section 1.2.3 (pgs. 34-40) in the context of uptake of DNA nanostructures.

In nature, viruses ubiquitously employ hydrophobic amino acid containing motifs to achieve membrane destabilization<sup>198</sup>. Inspired by this, Dowdy et al., have developed panels of so-called ‘endosome escape domains’ (EEDs) to enhance intracellular delivery of various covalently linked macromolecular therapeutics (Fig 39)<sup>199</sup>. These domains and similar motifs occur in numerous virus types, and have been attributed to the ability of membrane lytic proteins used ubiquitously by viruses. Likewise, the N-terminal domain of the Adenovirus protein VI was recently found to induce membrane destabilization<sup>200</sup>. As with the EEDs studied by Dowdy et al., the sequence is rich in hydrophobic residues and was found to control the adeno virus protein VI membrane lytic activity completely, suggesting that pH-dependent conformation change in the protein was responsible to expose the amphipathic motif (sequence: AFNWGGIWSGIKNFGSNVKNW).

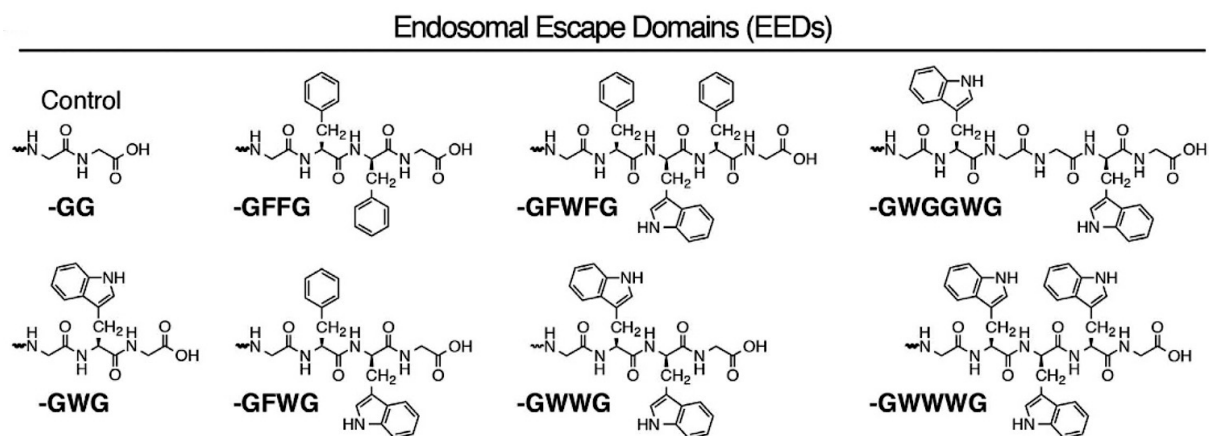


**Figure 39. Peptide sequences used to optimize endosome escape domains (EEDs).** Dowdy et al., combined different combinations of tryptophan, phenylalanine and glycine finding that EEDs showed significantly enhanced cytoplasmic delivery when containing two aromatic indole rings or one indole ring and two aromatic phenyl groups, at a fixed distance of six PEG units from the their macromolecule cargo. \*Image adapted from reference 197.

Notably, CPPs have been designed to exhibit pH-sensitive activity in order to avoid undesired interaction with non-target membranes and thereby abrogate chances for off-target effects<sup>201</sup>. In this context, CPPs can alter their conformation to become membrane destabilizing upon a reduction of pH as happens endosomes<sup>202</sup>. One such example is the new pH-activatable CPP, sequence: LHHLLHHLHLLHH-NH<sub>2</sub>(LH) devised by Jingman Ni et al., which can activate and penetrate into cells at pH 6.0 but not at pH 7.2<sup>203</sup>. Another example is the GALA peptide<sup>204</sup>, sequence: WEAALAEALAEALAEHLAEALAEALEALAA, which has an overall net-negative charge at neutral pH conditions such as those found in extracellular regions. Upon reduction of pH, the GALA peptide is induced to switch conformation from random-coil to alpha helix. Once it has done so, the peptide can then bind to- and lyse endosome membranes, and has been used to deliver various cargos including nanoparticles<sup>205</sup>. (This peptide was selected to work with for project II – and is discussed in detail, in section 5.1.4, pg. 78).

### 5.1.2. CPPs: Influence of cargo

CPPs are able to enhance the intracellular delivery of therapeutically relevant molecules and bioactive cargo in-vitro and in-vivo<sup>189, 199, 203-204</sup>. Recently, the number of CPP-based clinical trials has greatly increased<sup>206</sup>, yet the majority of studies remain focused on pre-clinical research in an effort to better understand the underlying factors that control CPP activity, and thereby to better direct their rational design. Indeed, as of 2021, no CPPs have yet found their way into clinical use or have been approved by the US Food and drug administration<sup>207</sup>. Cargo can be joined to CPPs via covalent modifications or via non-covalent means by exploiting weak interactions such ionic bonds (Fig 40)<sup>208</sup>. CPPs have been covalently conjugated to proteins, peptide based drugs, small molecule chemotherapeutics and nucleic acids<sup>209, 210</sup> (Fig 41), yet the majority of examples with respect to oligonucleotide delivery have been to-date dependent on the electrostatic formation of complexes between positively charged species (of peptide) with negatively charged nucleic acids<sup>211</sup>. Indeed, the non-covalent strategy has proven to be highly efficient for delivery of nanoparticles and siRNA<sup>212-213</sup>.

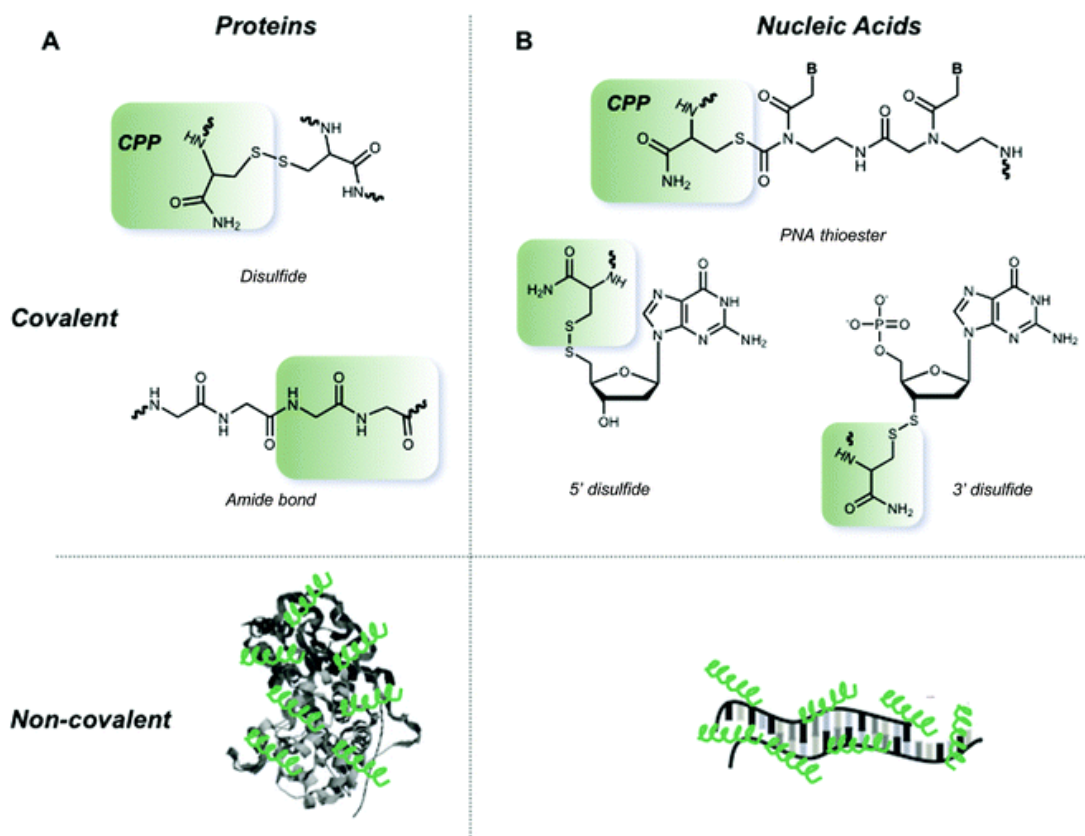


**Figure 40. Linkages of CPPs to nucleic acid and protein cargos.** Covalent and non-covalent links can be utilized to join CPPs with bioactive cargo, including proteins and nucleic acids. CPPs are depicted in green. Proteins/nucleic acids are depicted in black/grey. Note – this image was reproduced from the review ‘cell-penetrating peptides as delivery vehicles for biology and medicine by Shana Kelley et al<sup>214</sup>.

CPP mediated internalization of cargo can proceed through numerous pathways, which can occur simultaneously and depend upon the size of the complex or conjugate<sup>204</sup>. Arginine-rich CPPs, along with the previously mentioned HIV-TAT peptide, are capable of cell entry via both endocytosis and direct translocation across the cell plasma membrane, induced via electrostatics<sup>195</sup>. The latter has been shown to internalize into cells via macropinocytosis, lipid-raft dependent endocytosis and/or caveolae-mediated endocytosis when conjugated to macromolecules and nanoparticles<sup>215</sup>. Notably, Futaki et al., investigated the properties of polyarginine CPPs, finding that hydrophobic-induced peptide-peptide and peptide-nucleobase interactions in DNA/CPP complexes can reduce the overall particle size, with the effect of increasing delivery efficiency for nucleic acid therapeutics both in-vitro and in-vivo<sup>216-215</sup>.

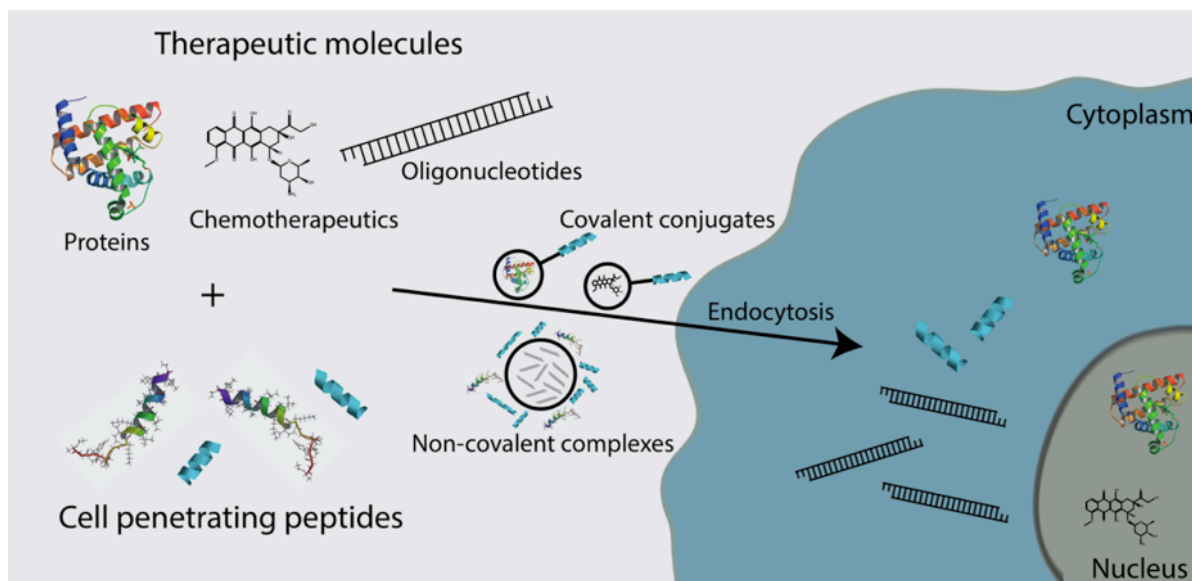


**Figure 41. Intracellular delivery of CPP – cargo units.** CPPs can be used to augment intracellular delivery of numerous therapeutics and bioactive cargos including proteins, chemotherapeutic small molecules and nucleic acids, either by covalent conjugation or electrostatic complexes. *Note – image adapted from the review article ‘Cell-Penetrating Peptides: Design, Synthesis and Applications’<sup>217</sup>.*

Of particular importance to this research project, Biao and colleagues recently reported that the CPP ‘GALA’ could retain its functionality in terms of pH-driven helix-coil transition when immobilized onto gold-nanoparticles<sup>218</sup>. The team first confirmed that addition of a cysteine to the peptide C-terminus does not interfere with the pH-driven switching between conformation states in bulk D<sub>2</sub>O, then proceeded to show that this covalent conjugation strategy could be used to generate a self-assembled monolayer (SAM) of GALA, and that this process did not impede functionality of the peptide (an observation of importance for project – II presented here as part of this thesis).

### 5.1.3. CPPs: Multivalency

An emerging parameter of key significance for CPP activity is their *multivalency*, which can be defined as “a key principle in nature to establish strong, but also reversible chemical interactions between two or more units”<sup>219</sup>. Multivalent interactions are crucial for numerous biological interactions<sup>220-221</sup>. The impact of

multivalency has been explored for nucleic acid based dendrimers<sup>222</sup> and CPP-functionalized nanoparticles<sup>223</sup>, where CPPs can be controlled in terms of density arranged in 3D space. As mentioned previously, DNA nanostructures may be uniquely positioned in this respect, by providing unrivalled nanoscale control for loading of functional moieties (examples are given later).

As much work has focused on positively charged and mostly arginine based CPPs, it was discovered early on that a minimum of 6 residues of this type are required for efficient CPP membrane translocation<sup>224</sup>. Lowik et al., recently advanced extended peptides based on oligoarginines, and showed that small inactivated fragments (R4) could be activated via C-terminal cysteines with R<sub>4</sub> or R<sub>5</sub> sequences<sup>225</sup>. This work was based on the knowledge that at least 6 arginine residues are required for efficient translocation of such positively charged CPPs and revealed that uptake into HeLa cells was similar to that of control R<sub>8</sub> and R<sub>9</sub> peptides. Crucially, overall oligoarginine length, concentration and structural arrangement of the residues were shown to be important parameters regarding membrane translocation activity.

Saludes et al, recently showed that dimeric branched peptides based on oligoarginine have enhanced membrane penetrating activity compared to linear counterparts. Based on the HIV-TAT peptide, Saludes et al., developed a dimeric-branching sequence capable of controlled dimerization via bis-Fmoc protected lysine near the peptide C-terminus and showed that enhanced uptake was produced vs. controls<sup>226</sup>. Importantly, non-linear uptake dependence on concentration was achieved at sub-micromolar concentrations. Additionally, the dimers were non-toxic to HeLa cells with the study overall revealing that membrane-translocating activity was tightly controlled as a consequence of enhanced local concentration or density of the peptides. Ohtsuki et al., also used TAT in combination with another peptide derived from the apoptosis 'Bim' protein and showed that dimeric presentation of the cell-penetrating component (TAT) significantly enhanced the activity of Bim peptide compared to its monomeric counterpart<sup>227</sup> (Fig 42). Such studies highlight how multivalency can be exploited to enhance the activity of CPPs, and guide rational design principles.

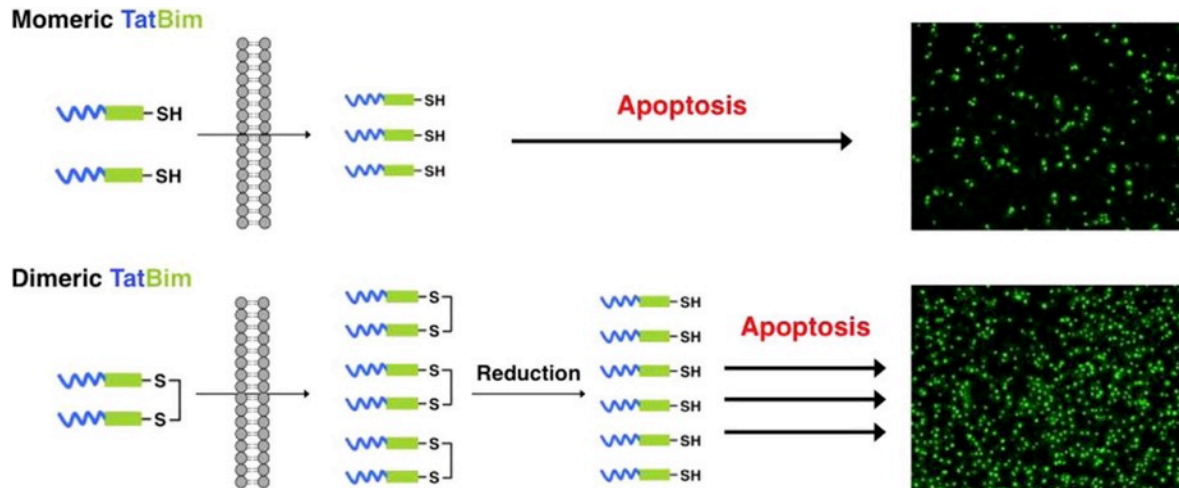


**Figure 42. Multivalent presentation of the TAT CPP enhances internalization and activity of the apoptosis inducing Bim peptide.** Ohtsuki et al., used bioreducible linkages to join TAT-Bim units finding that internalization was twice as high for dimeric vs. monomeric conjugates. *Note – Image reproduced from the research article ‘Enhanced intracellular peptide delivery by multivalent cell-penetrating peptide with bioreducible linkage’ - reference 225.*

Along another route, the relationship between CPP multivalency and activity has been explored using linear scaffolds to more faithfully mimic the arrangement of peptides at the membrane interface, at a high local density. Using oligoarginine based CPPs, Chakrabarti et al., recently showed that nona-arginine (R9) sequences significantly enhanced cell-binding and uptake induced by multivalency, where R9 coupled to a linear dextran scaffold was shown to produce direct cytoplasmic uptake similar to free R9 at concentrations exceeding  $10\mu\text{M}^{228*}$ . The team showed that multivalent presentation of R9 CPPs induces strong membrane binding and cell-aggregation in RBCs, but interestingly that severe toxicity was only observed in cells showing uptake. Overall, this work revealed that multivalent presentation increased arginine-based CPP capacity for cell plasma membrane association but at the cost of potentially undesirable cytotoxicity induced by membrane perturbation.

It is important to note that toxicity associated with positively charged CPPs can however be avoided with amphipathic and net-negatively charged sequences, that display pH-responsive characteristics<sup>200-202</sup>. Such peptides are designed to

preferentially interact with intracellular (typically endosomal) membranes, to abrogate undesired interaction and damage to cell plasma membranes. An important model CPP in this regard, the GALA peptide, is discussed next, and was selected, as mentioned previously, to work with for project – II.

#### 5.1.4. GALA: A synthetic amphipathic cell penetrating peptide

Water-soluble synthetic polyanions are employed in numerous industrial and biomedical applications<sup>229</sup>. Such biopolymers have increasingly been the focus for drug-delivery research and can be used to deliver biologics either as complexes or covalent conjugates<sup>125</sup>. Recently, the especially well-studied synthetic CPP termed GALA (sequence: WEAALAEALAEALAEHLAEALAEALEALAA) has been used to augment uptake of lipid nanoparticles for targeted delivery of plasmid DNA to the lungs<sup>230</sup>, and has been shown to increase permeation of non-charged lipid membranes when presented in a clustered vs. uniform valence on nanoparticles<sup>231</sup>. These observations make GALA and other amphipathic CPPs increasingly promising candidates for drug delivery, and highlight the need to better understand how peptide multivalence affects activity for cell binding and membrane destabilization in the context of endosome release.

As mentioned, GALA is a well-studied synthetic, pH-responsive and amphipathic CPP with applications in drug and gene delivery. GALA is a 30 amino-acid sequence composed of repeating glutamic acid-alanine-leucine-alanine units (EALA), and was designed to investigate how viral fusion proteins interact with lipid membranes<sup>228-232</sup>. The sequence was designed to feature sufficient alpha-helical length to span typical cell-membrane lipid bilayers (Fig 43). The peptide glutamic acid residues have been shown to provide a pH-dependent negatively charged side-chain, with the EALA repeat component providing a hydrophobic (opposing) face to enable membrane interaction (Fig 43). As with various other amphipathic CPPs, GALA converts from random coil to coiled  $\alpha$ -helix when the pH is reduced from neutral to acidic conditions.

GALA has been used to augment uptake of nanoparticles via copper-free click chemistry to deliver antigen-encoding mRNA<sup>233</sup>. Covalent conjugation to GALA has also been used for delivery of nucleic acids, but has potential drawbacks in terms of reduced pH-sensitivity and endosomolytic activity when conjugating to the peptide C-terminus<sup>234</sup>. Early studies with GALA suggested that the peptide N-terminal tryptophan residue might serve to facilitate oblique trans-membrane insertion<sup>235</sup>. This has however been contested by more recent studies which suggest that GALA's membrane binding and destabilizing properties are maintained irrespective of which terminus is selected for conjugation to DNA and other bioactive cargo<sup>233</sup>. The contradictions between these studies suggest that GALA's desirable properties may not exclusively depend on which terminus is used for bioconjugation, but also the chemistry or biophysical properties of the cargo itself. Indeed, this phenomenon has been reported for numerous other 'cargo-vector' systems as is discussed briefly in section 5.1.2.

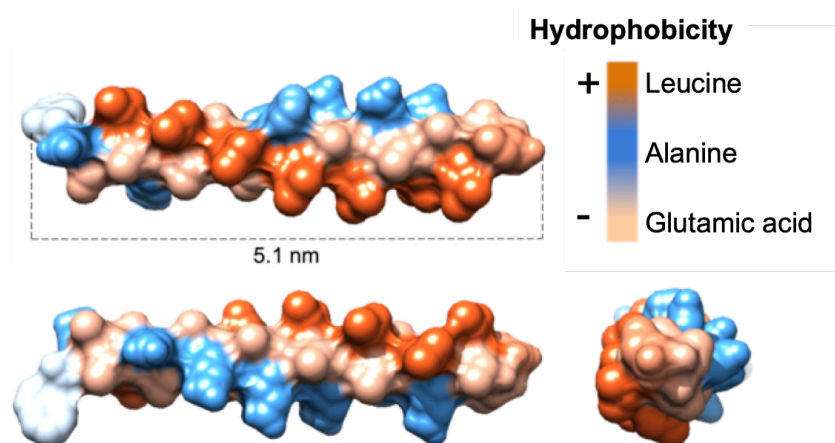


**Figure 43. 3D Hydrophobic surface area representation of the pH-responsive Cell Penetrating Peptide (GALA).** GALA is depicted in alpha-helical conformation where amino-acid residues are shown in dark orange (leucine), light orange (glutamic acid), blue (Alanine) and white (tryptophan). Glu residues are protonated at low pH to reduce the peptide charge and induce subsequent  $\alpha$ -helix conformation by aligning oppositely to the hydrophobic leucine face. Together with glutamic acid, Leucine repeats provide amphipathic membrane-binding properties to the peptide. His residues additionally provide for pH responsiveness, via their imidazole moieties. 3D Models were generated for this project using the molecular modeling software UCSF Chimera<sup>254</sup>. The extended  $\alpha$ -helical length of GALA was measured between atoms in the outermost tryptophan and histidine terminal residues.

Notably, membrane insertion of self-assembled GALA units has been shown to significantly accelerate transmembrane ‘flip-flop’, which has been used to explain the reported membrane destabilising properties of this peptide. Early studies revealed that GALA can induce fusion of small-unilamellar vesicles (SUVs) composed of unsaturated phospholipids<sup>236</sup>, and can self-assemble to form transmembrane pores<sup>237</sup>. Dye-release experiments have been used extensively to show that GALA-membrane insertion and orientation depends upon lipid bilayer composition<sup>238</sup>. Cholesterol is an endogenous component of certain cellular membranes and has been shown to inhibit GALA-mediated membrane destabilization<sup>239</sup>. This sits well with the fact that cholesterol is increasingly depleted from endosomal membranes as they mature and fuse with larger, more acidic lysosomal organelles. These features, taken together with the observation that multivalence can be used to enhance CPP activity (section 5.1.3) are the basis for project – II, the aims and rationale for which are outlined in section 6.

Next, a final introduction section seeks to present the chemical strategies used to combine peptides with DNA. This final introduction section is intended to provide a last piece of context for project – II, and covers peptide-oligonucleotide chemistry, followed by applications of peptide-oligonucleotide conjugates (POCs) and some recent advances made in this field of research.

## 5.2 Peptide-oligonucleotide conjugates

Peptide-oligonucleotides conjugates (Fig 44) provide both the programmable self-assembly properties of nucleic acids, along with the chemical diversity and bioactivity of polypeptides<sup>240, 241</sup>. Numerous examples of supramolecular association between nucleic acids and polypeptides exist in biological systems (e.g., in the ribosome, chromatin and transcription factors). Natural covalent links between oligonucleotides and nucleic acids are however restricted to biological systems that are challenging to adapt synthetically<sup>242</sup>. As such, POC research has until only recently been the remit of synthetic organic chemists, who have developed useful strategies to synthesize these bioconjugate molecules. Indeed, nucleic acids and polypeptides can now be synthesized by both chemical and in-vitro biosynthesis methods, and are subsequently becoming more readily available

for research in biosciences. Figure 44 - A shows a schematic of a 20-nucleotide ssDNA oligonucleotide conjugated to peptides of varying length, in order to demonstrate the relative size of each component alongside a typical 12-carbon long linker. Figure 44 - B shows the chemical structures of DNA and peptides.

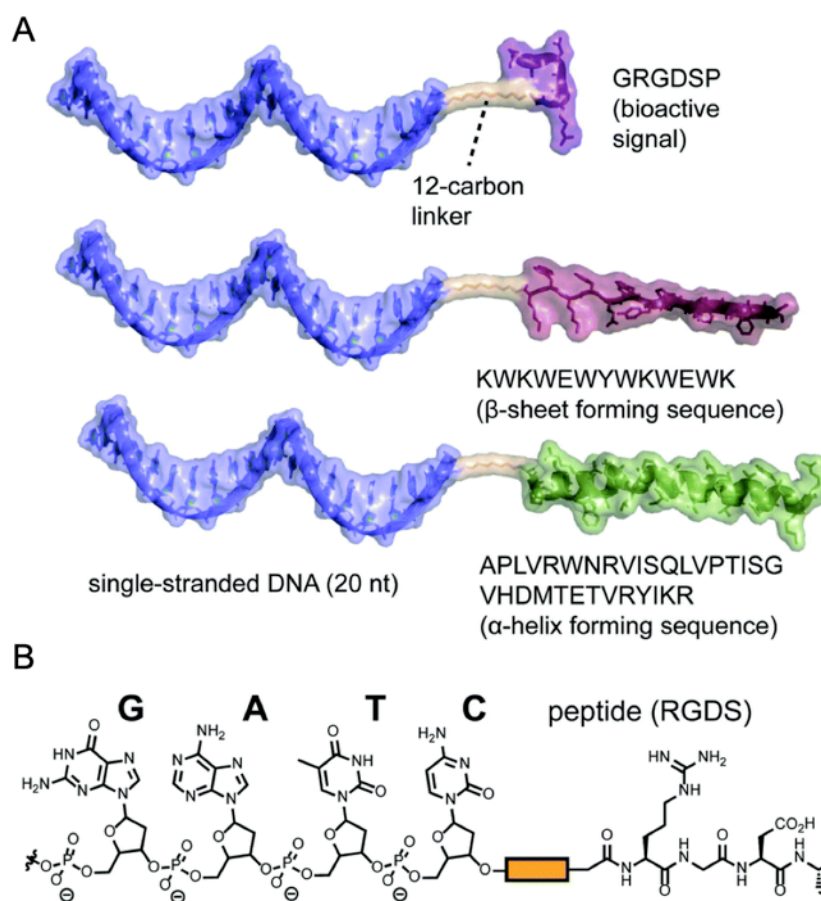


**Figure 44. The structure of peptide-oligonucleotide conjugates.** (a) Accurately scaled molecular representations of ssDNA linked to peptide sequences of varying residue composition and length. (b) The chemical structure of DNA bases linked to a short peptide, to demonstrate the relative size of each molecule. *Note - Image reproduced from reference 238.*

The incentive for research into POCs is to merge the exclusive properties of each component into an individual system, e.g., the sequence specific base-pairing properties of nucleic acids with the membrane-interacting properties of cell penetrating peptides. Recently, POCs have found widespread use, with research focused on their application as: functional biomaterials for manipulation of cell biology, agents for delivery of therapeutic cargo, components of hybrid self-

assembling systems, conjugates for coupling into macromolecular species and fabrication of functional nanostructures, and also as a means to interrogate peptide function on oligonucleotide-based scaffolds. The purpose of this introduction section is not to cover each of these areas in extensive detail as this has been done elsewhere<sup>238</sup>. Instead, this section seeks to briefly introduce the concept of POCs and present some recent advances made in the context of their application and combination with DNA nanotechnology.

### 5.2.1 POCs: Applications & combination with DNA nanotechnology

POCs have found growing use over the last half-decade to impart bioactivity onto DNA-based materials and structures including; nanofibers, hydrogels and surfaces which can be carefully engineered to interact with target analytes or cells. Peptides have been used to generate numerous bioactive materials by functionalization of scaffolds in addition to providing a means for self-assembly of scaffolds themselves<sup>243-244</sup>. Despite this, only a few examples can be found regarding POC integration with DNA nanostructures, due mostly to the prohibitive costs associated with DNA synthesis, potential limitations regarding immunogenicity and difficulty in conjugating oligonucleotides to peptides. Nevertheless, oligonucleotides can be exploited to provide unique programmable properties that are challenging to achieve with other materials, including controlled nanoscale spacing and presentation of ligands<sup>245</sup>, or multiplexed signal generation, as is used for emerging technologies such as DNA PAINT<sup>39</sup>.

Recently, Stephanopoulos and co-workers combined DNA nanotubes with the integrin-binding (cell-adhesion) RDGS peptide<sup>246</sup>. Component DNA strands (of the nanotube structure) were used to tether the RGDS peptide via copper-free click chemistry, resulting in a multivalent presentation of the peptide moiety across the structure surface. The group was able to show that alteration of the DNA base pairing (used to engineer the structure) could be exploited to probe independently the effect of nanotube architecture on peptide bioactivity for stem cell differentiation. Two years later, the Stupp group used DNA as a functional linker to attach peptides onto a surface coated with alginate, a non-bioactive polymer (Fig 45)<sup>247</sup>. The crucial advantage of DNA in this context was to provide for

dynamic elimination of the peptide from an immobilized surface, via toehold mediated strand displacement (Fig 45 - C). The team used the approach to direct cell adhesion onto the alginate surface and reversible growth of those cells over multiple cycles (Fig 45 – C), demonstrating elegantly that DNA can also serve as a molecular ruler to control distance-dependent synergy between two peptides. Finally, the team showed that orthogonally placed DNA handles were able to dynamically regulate two distinct bioactive (peptide) signals in an extracellular matrix (Fig 45 - D).

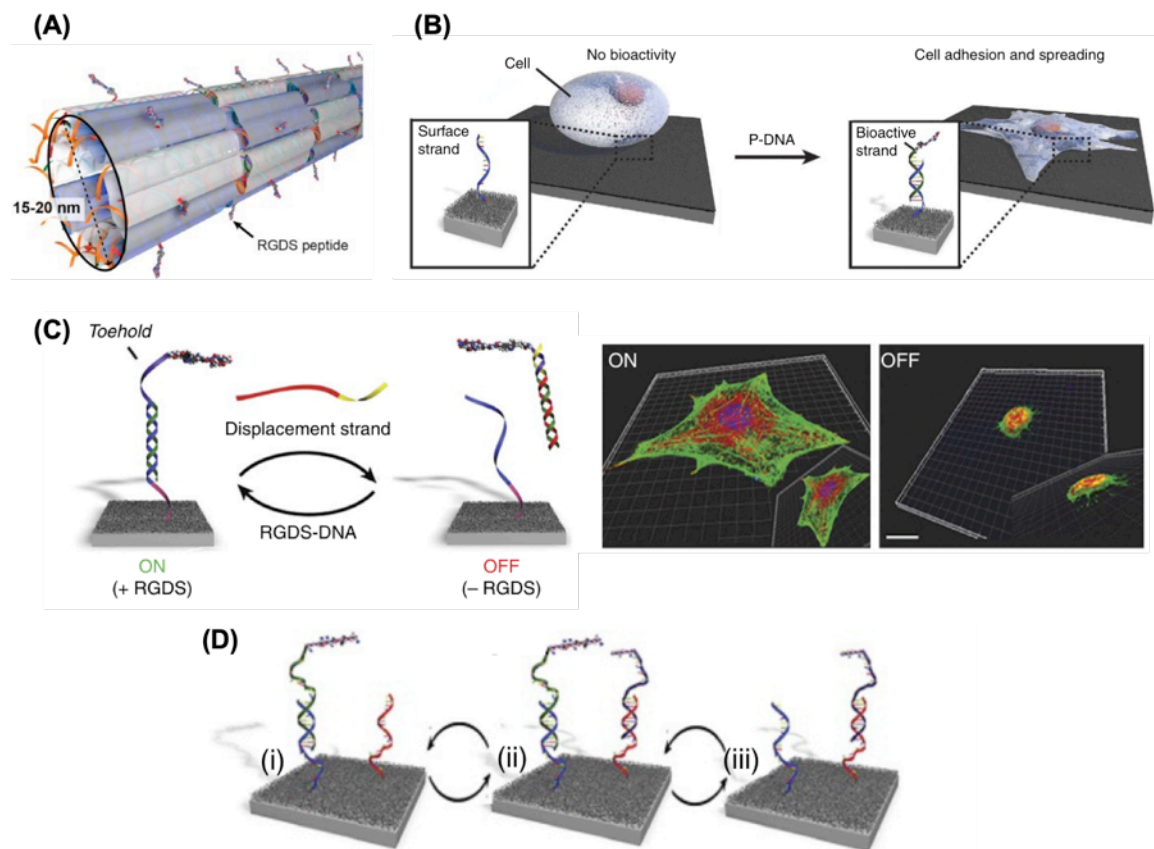


**Figure 45. DNA-based peptide presentation via peptide-oligonucleotide chemistry.** (A) Illustration schematic of a DNA nanotube with multivalent display of cell adhesion (integrin binding) peptide. (B) Bioactive POC presentation from a solid surface, controlled via functional DNA linkages. (C) Reversible loading and presentation of POCs via toehold-mediated strand displacement is used to attach and controllably grow mammalian cells on a solid surface. (D) Separate peptide signals can be independently controlled via orthogonal strand-displacement DNA handles. *Note – images adapted from reference 245.*

Nanoscale assemblage and coordination of biological signals is a fundamental property in living systems, e.g., in cells, which achieve highly controlled signal coordination mostly through protein-based self-assembly. Much research has focused on recreating these process using de-novo designed proteins, which whilst promising, provides certain limitations with respect to ease of access to the non-expert. Such methods require intimate understanding of the physical principles that underlie protein folding, which are arguably more complex than DNA-based self-assembly. A rapidly emerging alternative is to instead use DNA to fabricate scaffolds that can programmably display peptides or proteins to interrogate their functions, interdependence and activity as a function of their spatial presentation and proximity<sup>245-248</sup>. Crucially, this approach allows for separating of the scaffold design from the biological signal, and can be achieved with the help of dedicated design tools, and access to a range of pre-designed structures of various geometries and sizes (see section 1).

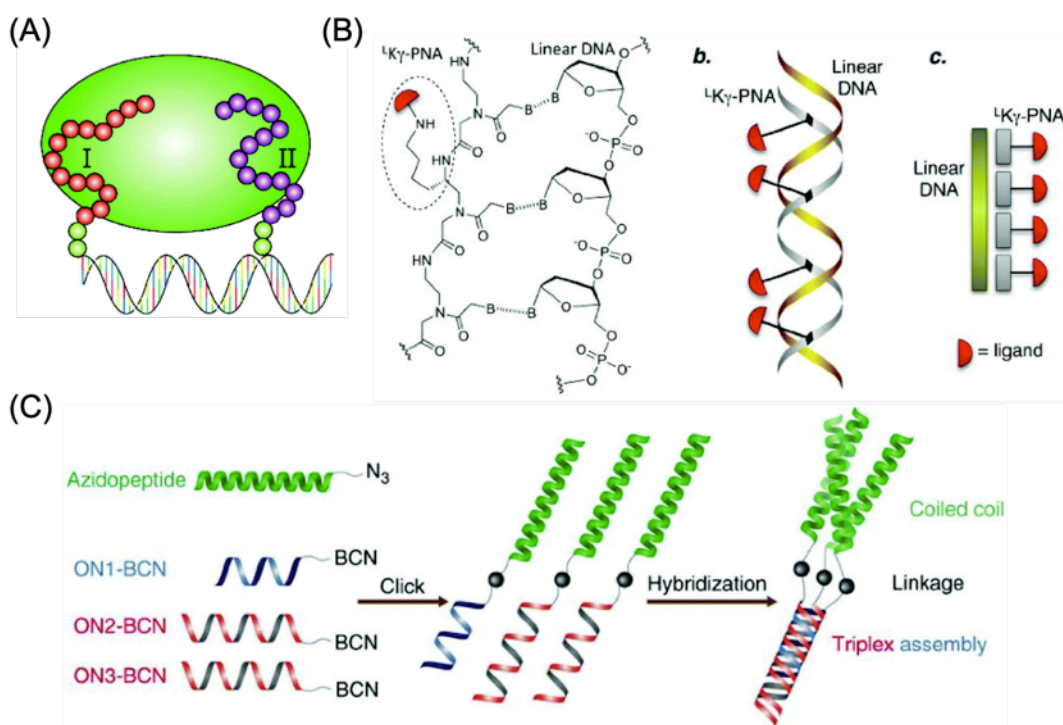


**Figure 46. DNA-based scaffolds for peptide display.** (A) Duplexed-DNA as a tunable template for peptide immobilization and can be used to interrogate binding affinity to a target, as a function of their spacing. (B) DNA as a repeating scaffold for multivalent presentation of peptides-nucleic acid conjugates. (C) DNA-triplex structure for enhanced stability and controlled presentation of peptides as a homotrimeric coiled-coil assembly.

*\*Note – images adapted from references 248, 247 and 243.*

DNA-based scaffolds can be fabricated with increasing ease, thanks to the research conducted in DNA nanotechnology and development of software dedicated to these ends. As a result, DNA-based scaffolds of varying size and topologies can be readily produced, which can be decorated with peptide (or POCs) via duplex hybridization to ssDNA handles featured from the structure surface or via other conjugation chemistries<sup>249</sup>.

The simplest scaffold for presentation of POCs is in fact a DNA duplex. In 2009, Chaput and Johnston used a DNA-duplex to recruit two different POCs to create an artificial antibody, or 'synbody'<sup>250</sup> (Fig 46 – A). The peptides of interests were synthesized as POCs and combined with the DNA-duplex 'scaffold' to produce heterobivalent arrays that could be screened to investigate which combinations produced the greatest binding enhancement to target receptors. The key advantage of using DNA as a functional scaffold in this context was to allow for spatial tuning between the peptides of interest, by carefully alternating distance and angle via changes made to the number of intervening base-pairs. As a result, the team was able to discover a synbody for the protein Gal80, with a 1000-fold increase binding affinity compared to the individual peptides alone. Subsequently, numerous other groups have used this approach to answer fundamental biological questions<sup>251</sup>, and have developed DNA-based scaffolds as molecular rulers to also present analytes in order to probe enhanced binding to their target proteins or protein-motifs in a bivalent fashion<sup>251-252</sup>.

Beyond duplex and triplex-DNA based scaffolds, DNA can be used to engineer extended 2D and 3D templates via programmed assembly of multiple components strands<sup>253</sup>. POCs can be introduced to such structures either through co-assembly using un-modified strands or via binding to ssDNA handles that load peptides via duplex hybridization. In 2007, 2D nano-display of peptides was reported by the Chaput group working in collaboration with Yan et al., whereby four separate double-crossover DNA-based 'tiles' were used to fabricate an extended scaffold<sup>254</sup> (Fig 48 – A, pg. 87). Co-assembly of the tiles was used to present ssDNA handles with highly controlled nanometer spacing. Subsequently, the team showed that proteins could be recruited by the immobilized peptides with the same precision, demonstrating the approach as a highly sensitive bio-sensing

platform for protein detection with single-molecule scale resolution, using AFM as a readout. In 2020, De-Greef and colleagues reported use of a rectangular DNA nanostructure as a “programmable molecular platform for the systematic analysis of signaling proteins”<sup>245</sup>. The team engineered a synthetic DNA origami-based version of the apoptosome, a multi protein complex that regulates apoptosis by colocalizing multiple caspase-9 monomers. The DNA origami platform was used to tether wild-type and inactive caspase-9 variants in order to investigate enzymatic activity as a function of proximity-driven dimerization with ‘half-of-sites reactivity’ (Fig 47). Additionally, the platform was used to reveal multivalent activity enhancement in oligomers of three and four enzymes, offering fundamental insights into caspase-9 enzyme activity and demonstrating elegantly the power of DNA-origami based protein assembly platforms to infer function of other multi-enzyme complexes involved in various biological processes.

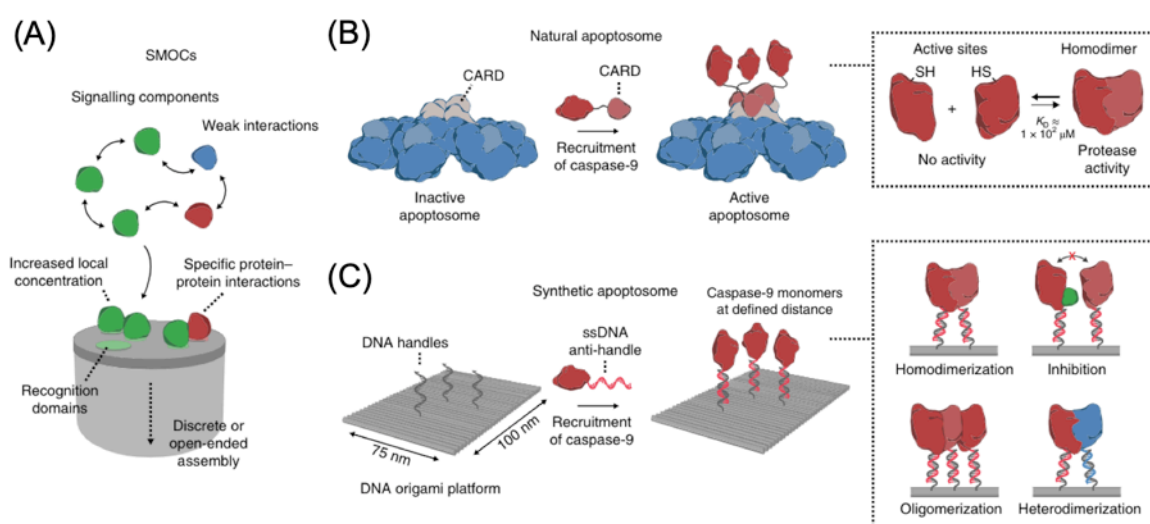


**Figure 47. Concept & design elements for the construction of a DNA-based synthetic apoptosome. (A)** Schematic concept of supramolecular organizing centers (SMOCs). **(B)** Schematic illustration of the natural apoptosome that functions via assemblage of inactive caspase-9 monomers through caspase-recruiting domains (CARDs). Proteolytic cleavage of caspases and induced apoptosis is controlled by enhancing caspase-9 local concentration and dimerization. **(C)** Schematic illustration of the DNA-origami based synthetic apoptosome. ssDNA handles presented on the origami surface recruit caspase-9 monomers with precise control over position, number and spatial organization, allowing for characterisation of protein-protein interactions including; dimerization, oligo- and heterodimerisation and inhibition of activity. \*Image reproduced from reference 245.

POC display has also found use for design of DNA nanostructures as drug delivery vehicles, demonstrated by numerous groups in the last few years. Sun et al., used a DNA-based tetrahedral nanostructure to present tumor-targeting CPPs for delivery of doxorubicin, an intercalating chemotherapeutic drug (Fig 48 – B). Notably, incorporation of the CPP was achieved after assembly of the DNA nanostructure via copper click chemistry. A similar approach was used by Anderson and co-workers, who likewise combined CPPs with a DNA tetrahedron but to deliver siRNAs<sup>255</sup> (Fig 48 – C). The team used their DNA nanostructure to systematically probe the relationship between drug-delivery efficiency and spatial arrangement of the conjugated CPPs (Fig 48 - C). Decoupling assembly of the structure from ligand functionalization allowed for rapid screening of multiple CPPs, achieved by pre-conjugating the CPPs to handle-DNA sequences that could be readily hybridized into the structure.

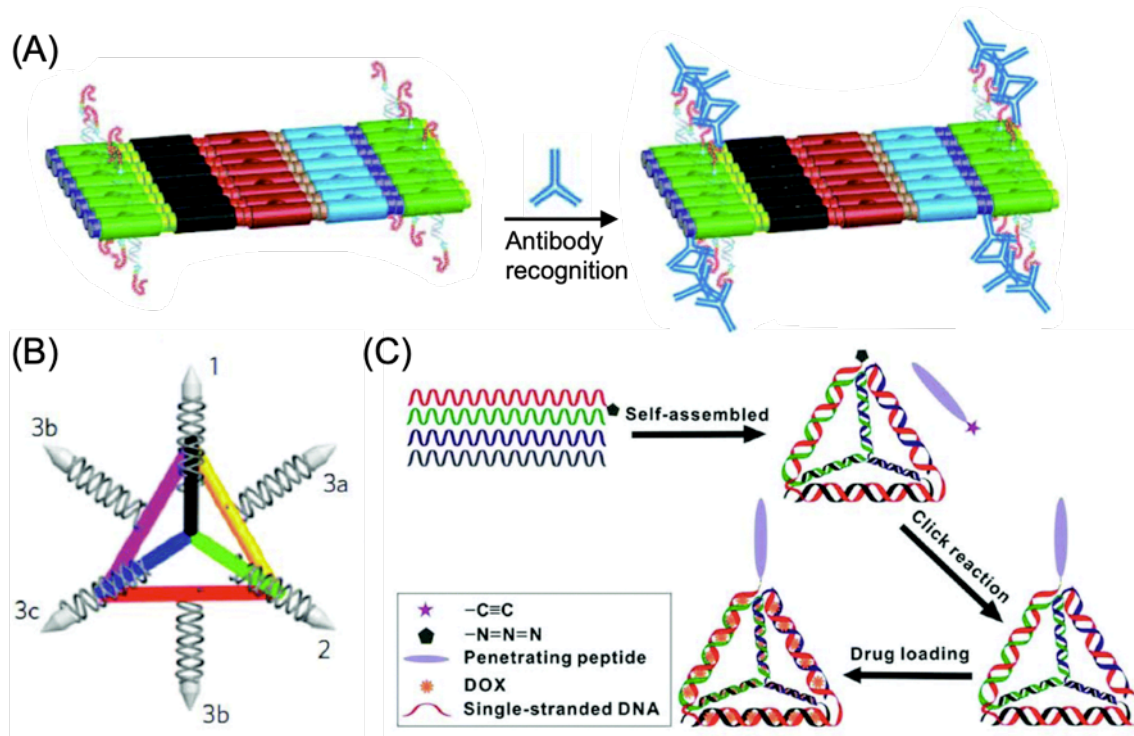


**Figure 48. Nano-presentation of CPPs using DNA nanostructures. (A)** 2D peptide arrays assembled on DNA-tile based templates. **(B)** DNA-tetrahedron for controlled display of CPPs. **(C)** DNA-tetrahedron featuring tumor-targeting CPPs for doxorubicin delivery. \*Note – images adapted from references 247, 251, and 252.

## 6. **Project II** – aims & rationale

Project 1 used a small, modular DNA nanostructure to investigate how individual cholesterol anchors affect DNA nanostructure–cell binding and uptake. Intracellular trafficking of the nanostructure was investigated using CLSM, suggesting a lysosomal fate. As mentioned throughout previous sections, the inability to escape this cell-processing destiny is a well-known bottleneck for nanoparticle-mediated drug delivery. Inspired by these findings, a secondary project was conceived to probe the possibility of incorporating cell-penetrating peptides (CPPs) with DNA nanostructures.

The project aims were to investigate if anionic CPPs could (i) be controllably combined with DNA origami via duplex hybridisation, and (ii) be used to augment delivery and/or endosome release of DNA origami. Depending on the success of these steps, a final aim (iii) was to investigate if DNA origami could be used to probe the membrane binding and/or destabilizing activity of CPPs, by controlling their multivalent presentation and nanoscale density at the interface with phospholipid membranes. First however, the project focus was to investigate the broader possibility of ‘programmed’ peptide incorporation onto a DNA nanostructure and to achieve aims (i) and (ii).

Cell-penetrating peptides are of current interest as delivery agents for nucleic acids, but are typically cationic and depend upon on non-specific interaction with DNA, or RNA. Again, as mentioned previously, positively charged CPPs can form complexes with DNA via electrostatics interactions, offsetting the net-negative charge associated with the nucleic acid and thereby promoting interaction with neutral or negatively charged cell membrane surfaces. Here, the net-anionic and pH-responsive cell-penetrating peptide GALA was selected to avoid these non-specific interactions with DNA, and thereby provide the basis for site-selective incorporation onto a DNA nanoparticle.

## 6.1. Design – DNA origami scaffold for presentation of GALA peptide

The DNA origami method was used to design a 50x60nm rectangular ‘scaffold’, capable of presenting up to one hundred ssDNA extensions from the structure surface (Fig 50 - 51). To enable incorporation onto the origami surface, GALA peptide was end modified with cysteine and conjugated to a short 15-mer oligonucleotide via a succinimodyl 4-(N-maleimidomethyl)cyclohexane linker (SMMC) to produce a peptide-oligonucleotide conjugate (POC). The DNA origami ssDNA ‘handle’ sequence was selected to complement the POC sequence, and thereby enable loading of GALA via ‘indirect’ conjugation (Fig 50, Pg. 90). I.e., by base pairing between the two oligonucleotides, one from the origami surface and the other attached to the cell-penetrating peptide sequence ‘GALA’.

Viral phage m13mp18 ssDNA was selected as the DNA origami scaffold strand following early designs of rectangular DNA nanostructures by William Shih, et al<sup>256</sup>. The DNA origami structure was designed here to consume approximately 97% of the m13 scaffold, as leaving large unincorporated segments of scaffold-ssDNA (used to generate DNA origami) can cause structure dimerization and instability, as well as non-specific adsorption of molecules of interest. To impart rigidity, the structure was designed to feature a DNA duplex double-layer (Fig 49) thereby increasing the likelihood for cell uptake as has been demonstrated for more compact and structurally inflexible DNA nanostructures (see section 1.2).

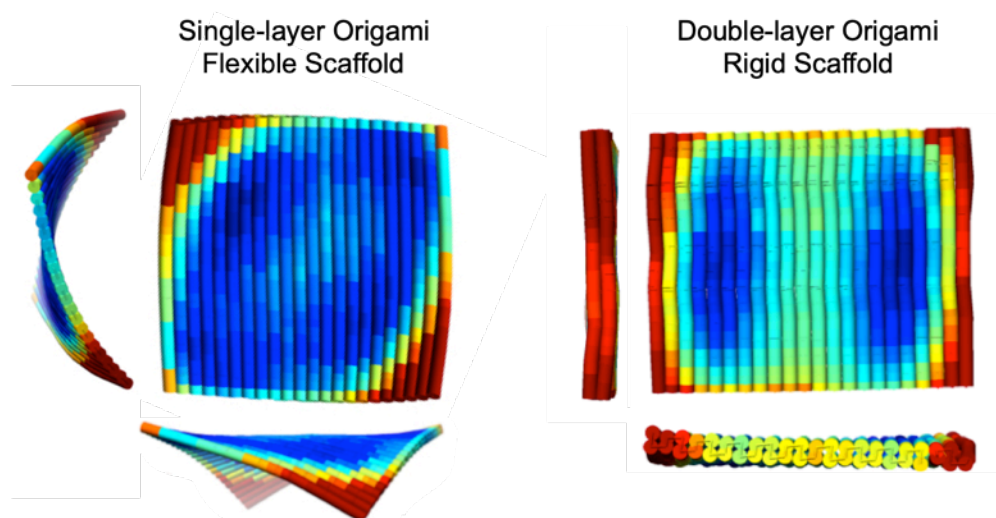


**Figure 49. RMSF models of DNA origami.** Single-layered approach yields a flexible DNA origami, whereas the double-layer design yields a rigid structurally inflexible scaffold.

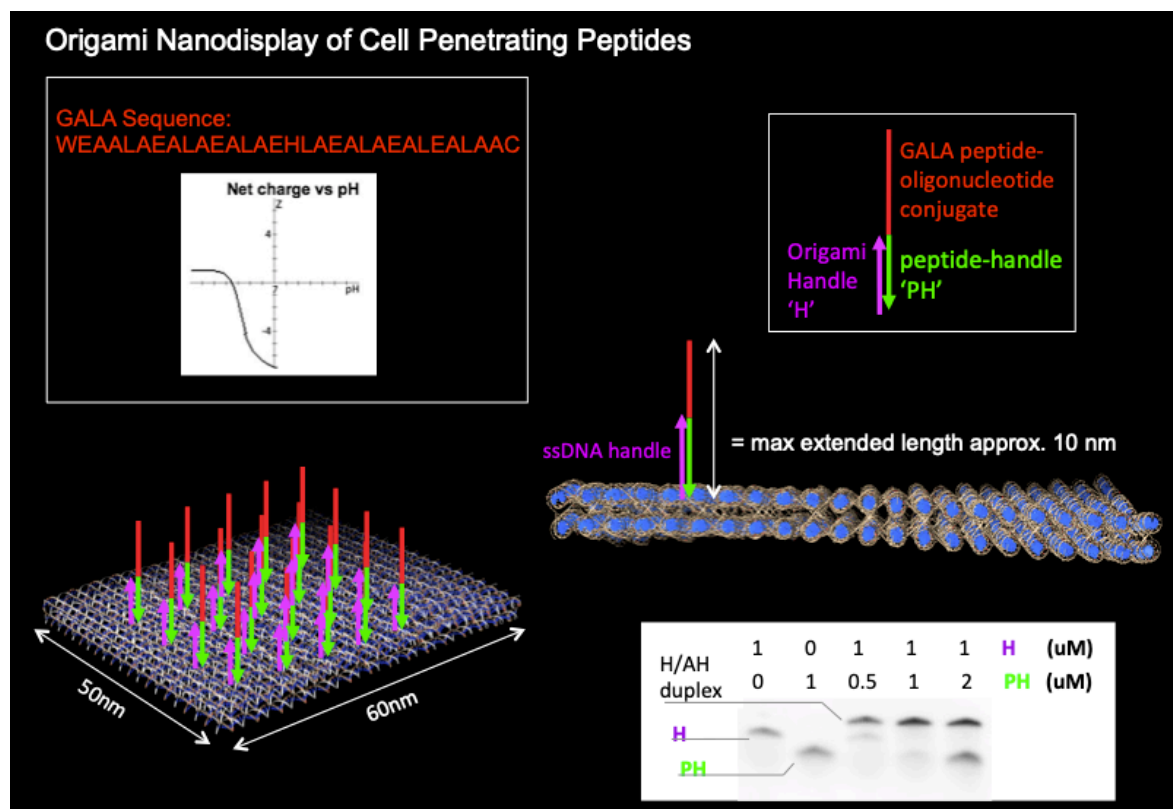


**Figure 50. DNA origami scaffold and peptide incorporation strategy.** The DNA nanostructure designed for this project was conceived as a rigid, rectangular scaffold composed of two layers of aligned DNA duplexes. ssDNA ‘handles’ are extended from staple sequences and are used to recruit GALA-DNA via duplex hybridization. The peptide of interest (GALA) was provided as a peptide-oligonucleotide conjugate (POC), which can hybridize to the ssDNA handles as is shown by the PAGE analysis (bottom right). **Handle hybridization.** Native PAGE was used to confirm origami handle ‘H’ hybridization to the peptide-handle sequence ‘PH’. 3D-models of the DNA origami scaffold were generated using the molecular modeling software *Chimera*<sup>257</sup>, and were sourced from Root-Mean-Squared-Fluctuation (RMSF) simulations generated with the *CaDNAno* package *Cando*<sup>30</sup>.

In order to allow investigation of the relationship between peptide density and activity, the DNA scaffold was designed to feature periodically positioned ssDNA extension sites (Fig 51). The extension positions for these sites were carefully selected to ensure that each position faced outward from the origami surface. Spacing between the extension sites was designed to exceed no more than 6.5nm as was determined using the *Cadnano* design schematic (appendix – 10.1), average inter-nucleotide spacing and simple trigonometry (Fig 51). This spacing distance was chosen to permit peptide-peptide interactions between adjacent units

taking into account the POC length where the GALA component would be shortened by switching to  $\alpha$ -helix confirmation, at reduced pH (approximations pg. 93).

A color-coding system was implemented to allow facile modulation of origami staple-sets, selected for as peptide-recruiting ssDNA handles. Instead of designing *denovo* oligonucleotide sequences for the origami handle (H), and peptide handle (PH), sequences from literature were selected, owing to their thorough testing for similar applications (using DNA origami to recruit and control dimerization of proteins). As is common, a polythymine region was included between the extension site terminus and ssDNA handle sequence, to maximize accessibility of the oligonucleotide sequence used for hybridization to the GALA POC.

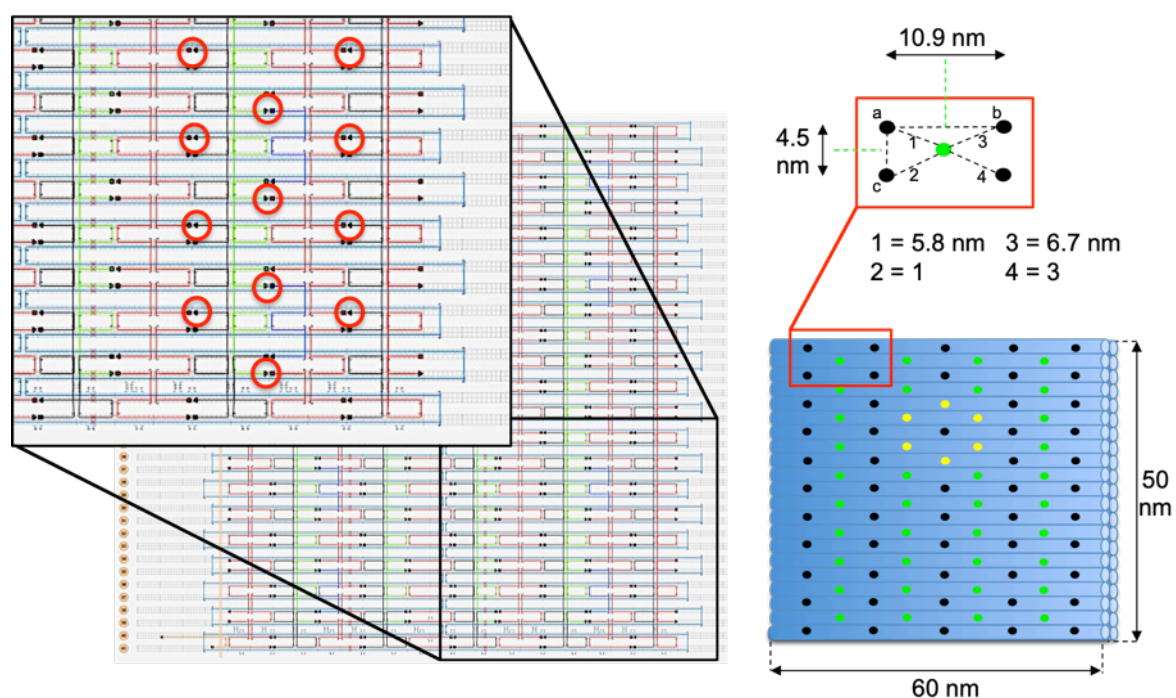


**Figure 51. DNA origami scaffold Cadnano schematic and ssDNA extension-site illustration.** Repeating extension-site positions are highlighted on the Cadnano design schematic with red circles. Staples used for ssDNA extension are color-coded in black or green, and are spaced no more than 6.5 nm from one another. The opposing face of the DNA origami nanostructure was used for fluorophore incorporation from ‘blue strands’. A ‘ring’ of extension-sites is colored yellow to demonstrate the prospect for featuring of specific handle patterns. Note\* - the complete design schematic, and sequences used for this structure are featured in the experimental sections 10.1 – 10.2.

Before assembling the structure, 3D-rendered models were generated using all-atom exported co-ordinates from Root-Mean-Squared-Fluctuation simulations, carried out using the Cadnano simulation package *Cadnano*. RMSF simulations provides for the lowest free-energy thermodynamic state of the DNA nanostructure. 3D modeling was used to confirm the spacing between ssDNA extension-site positions, as designed for using Cadnano and predicted using the average inter-nucleotide distance of 0.34nm. Atom-to-atom distances between extension-sites were measured using the molecular visualization software Chimera (Fig 52) and were found to be in good agreement to the predicted spacing of 11 and 4.5nm for black-to-black sites in the Y and X-axis respectively, and 5.8 - 6.7 nm for black-to-green site spacing (Fig 51).

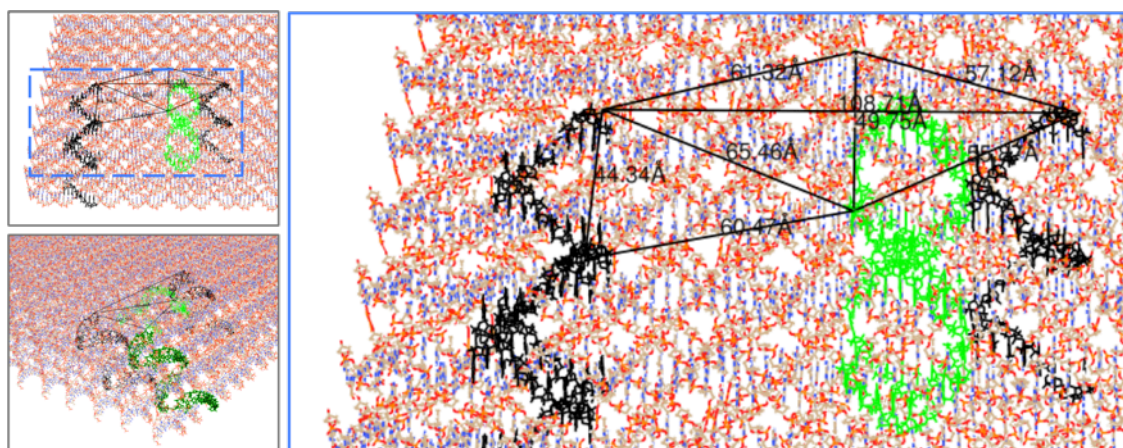


**Figure 52. Extension-site point-to-point measurements.** RMSF simulations were used to generate ‘all-atom’ co-ordinates for 3D modeling of the DNA origami structure, which was to select individual staple strands for measurements between sequence termini used as extension-sites for peptide recruiting ssDNA handles. Good agreement with predicted spacing was observed (predicted spacing is featured in figure 51). Maximum spacing distance between extension sites, as measured from 3D RMSF models, was 6.47nm.

Measurements from RMSF models were made to qualitatively confirm the desired spacing between extension-sites, according to the lowest energy state for the DNA nanostructure as predicted for using Cadnano. ssDNA handles were 20nt long including a 5nt-long polyT repeat region, giving an approximate length of 6.6nm when duplexed with the corresponding complementary oligonucleotide. This length is slightly larger than the maximum distance measured for between extension sites (Fig 52).

Using averaged amino-acid spacing of 0.35nm, the GALA peptide has a predicted length of - approx. 10.5nm in its extended random-coil conformation (Fig 43 – featured again below), which is roughly halved upon switching to  $\alpha$ -helical confirmation. Thus, the entire POC length will range from approx. 12 to 17nm providing ample freedom for the GALA peptide to interact with neighboring peptides across the DNA origami. As mentioned previously, the ability of GALA to destabilize lipid bilayer membranes has been closely attributed to its multivalent presentation on nanoparticles. Here, DNA origami was designed as a basis to potentially explore this relationship, by serving as a programmable scaffold capable of controlling peptide nanoscale density, via loading of the GALA POC through duplex hybridization. First however, the aim was to investigate the broader possibility of combining GALA with DNA origami in a programmed fashion, via duplex hybridisation (section 7.1, pg. 95).

## 7. Results & discussion

### 7.1. Assembly and characterization

Agarose gel electrophoresis and atomic force microscopy (AFM) were used to validate assembly of DNA nanostructure (Fig 53). AFM (Fig 53 - C) and TEM (SI) indicated close agreement to the predicted structure topology and dimensions of 4x 50x 60nm. Agarose gel analysis revealed a positive correlation between electrophoretic mobility shift and extension handle number, caused likely by the increased structure size and/or weight provided by successful incorporation of extended staples strands (larger structures have a reduced migration rate through gel matrices).

A serial dilution of the POC incubated against the structure did not produce any mobility shift (data not shown). The reasons for this are unknown but may be due to stripping of the duplexed POC away from the origami, under raised temperature induced by running of the electrophoresis gel at 2% weight by volume. As demonstrated in project – I, hydrophobic cholesterol moieties can reduce DNA nanostructure migration during gel electrophoresis. Here, highly hydrophobic GALA might be expected to do the same when conjugated onto the DNA origami structure. However, in project – I, the DNA nanostructure was modified with cholesterol via a covalent linker. By comparison, in project – II, DNA duplex hybridization provides the means for loading of GALA onto the DNA origami. As GALA has significant hydrophobic properties, it could be reasoned that hydrophobic induced interaction with the gel matrix may cause stripping of the GALA POC away from the DNA origami.

To confirm accessibility of the origami extension handles, a biotin-streptavidin binding assay was carried out and visualized using a AGE (Fig 53 – B). Briefly, a 5'biotin-tagged 15-mer (with the same sequence used for the GALA POC) was incubated with the origami, followed by incubation of streptavidin (experimental 10.12). Streptavidin has >15x the Mw of GALA and was thus expected to significantly reduce the origami electrophoretic migration through the agarose gel where 5'biotin-tagged ssDNA was able to hybridize to the origami ssDNA

extension handles and thereby recruit streptavidin monomers. Origami featuring 50 or 100 handles induced significant mobility shift, whilst the control origami without recruiting handle sequence did not, thereby confirming accessibility of the ssDNA handles to inbound complementary oligonucleotides tagged with functional moieties.

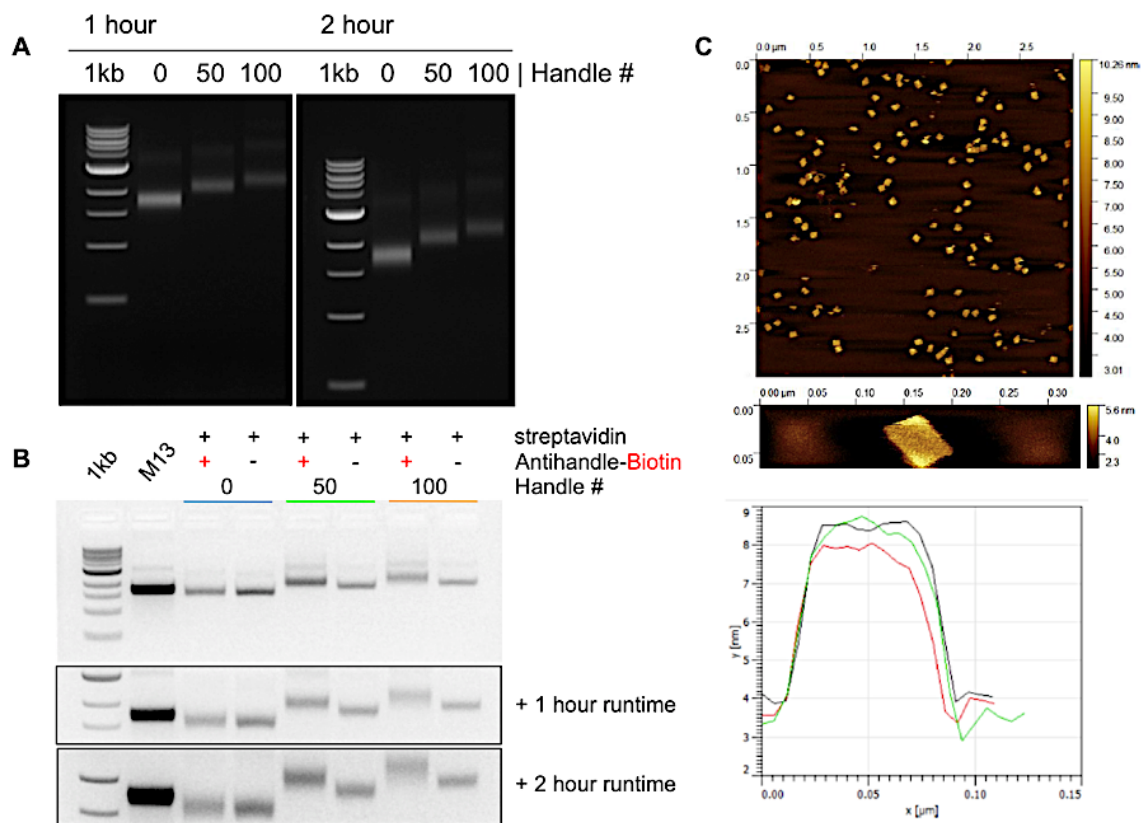


**Figure 53. DNA 'scaffold' assembly and characterization.** DNA origami with zero, fifty or one-hundred ssDNA handles was assembled and analyzed by gel electrophoresis. **(A)** Incorporation of handles is confirmed by induced mobility shift. **(B)** 5' Biotin-tagged oligonucleotides were incubated with origami to confirm handle accessibility via biotin-streptavidin induced mobility shift. **(C)** AFM analysis of DNA scaffold with 100 handles confirms successful assembly and close agreement to the predicted structure dimensions of approx. 4 x 50 nm.

Gel electrophoresis with fluorescence scanning was used to analyze fluorophore labeling of DNA origami, finding that AlexaFluor-647 tagged oligonucleotides were best incorporated at higher  $Mg^{2+}$  concentrations (Fig 54). Larger more complex DNA origami nanostructures typically require  $Mg^{2+}$  at a concentration of around 12-14 mM to assemble properly, with higher concentrations producing electrostatic

induced dimer- or multimerization<sup>258</sup>. Dimerization of the origami nanostructure was not observed by screening magnesium concentration from 8–20mM but was conversely noticeable when initially characterizing the structure assembly (indicated by one additional larger molecular band in the gel electrophoresis analysis). Furthermore, the origami appeared to assemble efficiently at the lowest  $Mg^{2+}$  concentration tested (8mM). The absence of origami dimers or multimers at higher magnesium concentrations could be explained by the efficient usage of M13mp18 ssDNA scaffold to avoid ‘loose ends’ as mentioned previously. However, incorporation of Alexaflour-tagged antihandle oligonucleotides appeared to be increasingly efficient at higher magnesium concentrations used for folding (Fig 55 – A, pg. 99). Subsequently, all further origami was prepared at  $Mg^{2+}$  concentration of 16mM to ensure efficient loading of fluorophore-labelled strands.

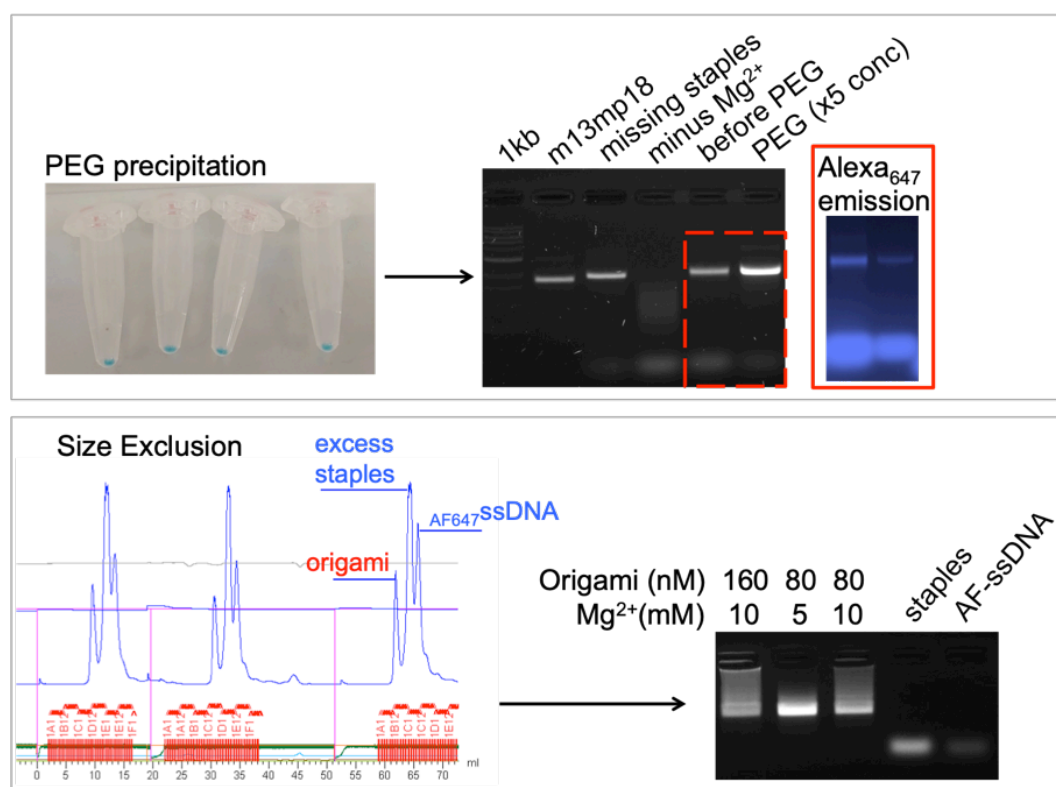


**Figure 54. Agarose gel electrophoresis analysis of origami purification by PEG precipitation and SEC.** EtBr and fluorescence (633 nm) overlay reveal insufficient removal of AF647-ssDNA from DNA origami. By comparison, Size Exclusion chromatography was found to leave no observable ssDNA band and was used thereafter to produce pure DNA origami for experiments. PEG precipitation was used after SEC to concentrate DNA origami. Aggregation of DNA origami was observed at high concentrations (>40nM) but was found to be reversible by reducing  $Mg^{2+}$  concentration.

Folding DNA origami nanostructures requires incubating a molar excess of 'staple' strands over the 'scaffold' ssDNA. Here, extended origami 'staples' serve as the peptide-recruiting ssDNA-handles, the excess for which after folding must be removed prior to peptide loading. Failing to remove this excess would result in a pool of handle sequences remaining available for duplex hybridization to the peptide-oligonucleotide conjugate, thereby potentially abrogating efficient peptide loading onto the DNA origami. Ethidium bromide staining of agarose gels suggested that excess staples and fluorophore probe strands were removed efficiently by PEG precipitation (Fig 54). This finding was however contradicted by gel visualization with fluorescence scanning, which revealed significant amounts of residual AF-ssDNA left over after multiple PEG precipitation cycles (Fig 54). These observations conflict with reports in literature, that provide only limited analysis of the PEG precipitation method as an efficient means for removal of dye-tagged strands from assembled DNA nanostructures<sup>259</sup>. Subsequently, size-exclusion chromatography (SEC) was used to produce pure DNA origami (Fig 54).

By comparison to PEG precipitation, SEC was observed to completely remove bands associated with excess staple ssDNA (Fig 54). As origami is not typically prepared at concentrations exceeded 10-20nM, PEG precipitation was used to concentrate samples after SEC purification. (Concentrating of origami was desired for downstream experiments, to avoid for example, over diluting cell-media upon addition of the origami-containing solution).

As a means to probe GALA POC loading onto the DNA origami, a binding competition assay was devised (Fig 55 - B). The assay used a 3'Cy3-tagged sequence identical to the GALA conjugate 'peptide-handle' DNA sequence (see appendix, 10.3). GALA POC was incubated with origami either before or after addition of the Cy3' competition strand, which was fixed at a constant concentration. Both GALA POC and Cy3 competition strand were incubated with origami for the same time duration. Notably, increasing the GALA POC concentration did not prevent binding of the Cy3-competition strand onto the DNA origami. In contrast, incubation of GALA POC for 1 hour prior to mixing with the competitor did prevent POC loading, inferred by the diminished band intensity

visualized with fluorescence scanning. This suggests that GALA loading onto the DNA origami is stable for at least up to 1 hour, even in the presence of excess competition strands.

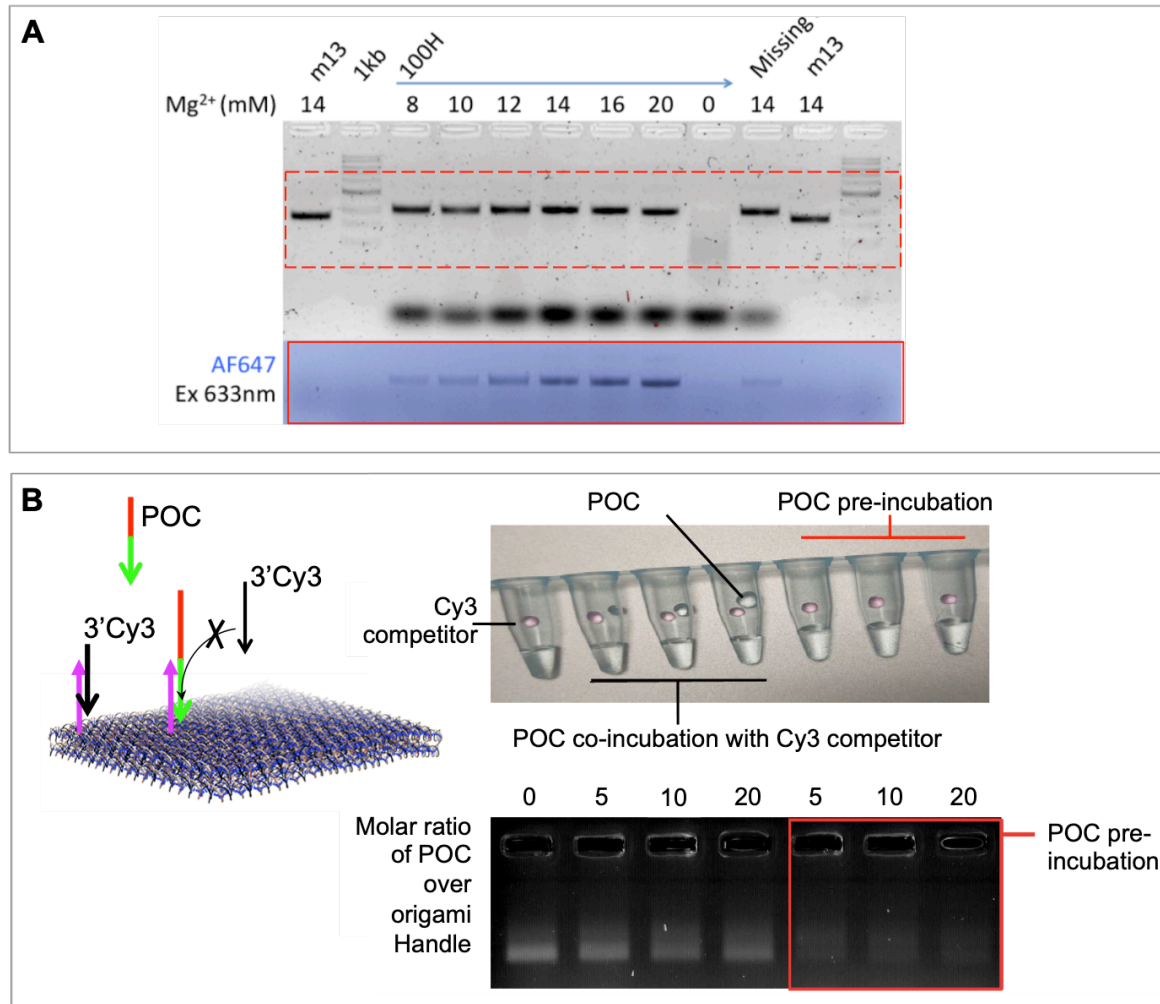


**Figure 55. Equipping DNA origami scaffold with fluorophores and GALA. (A) Mg<sup>2+</sup> screening for DNA origami assembly and AF647-ssDNA incorporation.** Ethidium Bromide staining of a 2% agarose gel shows origami assembly as a discrete monomeric species across magnesium concentration range of 8-20mM. 'Missing' denotes the origami structure assembled without fluorophore-recruiting ssDNA-handles, which is ineffective at recruiting 5'AF-647ssDNA as judged by the diminished band intensity at comparative Mg<sup>2+</sup> concentration of 14mM. **(B) Binding competition assay to probe POC-loading onto the DNA origami scaffold.** POC was titrated against origami either before or after incubation of a fixed ratio of 3'Cy3-ssDNA competitor (equimolar to origami ssDNA-handles).

## 7.2. GALA induced binding to model lipid membranes

The ability of the GALA peptide to bind to and destabilize lipid membranes has been studied thoroughly using synthetic lipid vesicles (section 5.1.4). Lipid vesicles can be used as biomimetic surrogates to model more complex biological phospholipid membranes, and have been used for vesicle-dye release experiments to investigate GALA's pH-selective activity. With relevance to this project, GALA induced membrane destabilization has been linked to multivalent presentation of individual GALA units, which serves to enhance local concentration at the lipid membrane interface. Here, DNA origami was designed as a scaffold to investigate the possibility of programmed GALA recruitment and control over nanoscale presentation.

To investigate loading of GALA POC onto the DNA origami, an electrophoretic mobility-shift binding assay was devised, using small-unilamellar vesicles (SUVs). A gel mobility-shift for the DNA origami band can be used to infer GALA mediated binding of the origami onto SUVs, which are unable to migrate into the gel matrix due to their large size. GALA mediated binding of DNA origami to SUVs was thus conceived as a means to probe the prerequisite step to membrane destabilization, which would be tested for later by live-cell microscopy.

POPC (1-palmitoyl-2-oleoyl-sn-glycero-3-phosphocholine) was selected as a model membrane phospholipid owing to its natural abundance in eukaryotic cell membranes including those of endosomal compartments<sup>260</sup>. Gel electrophoresis was used to visualize binding of the origami to POPC vesicles, assessed by mobility shift of the origami band (Fig 56 - A). To probe the pH-selective binding feature of GALA, SUVs were formed in buffered solutions at neutral (pH 7.2) or reduced pH (pH 5.0). Vesicles extrusion through a 200nm filter was used to ensure consistent sizing between the formed SUV samples at both pH values (Fig 56 - B). Notably, origami binding to vesicles was significantly enhanced at reduced pH but only when featuring peptide-recruiting ssDNA handles (Fig 56 - A). Furthermore, a positive correlation between lipid concentration and % bound

origami was observed for all samples including controls, but was enhanced by peptide-recruiting handles by approximately 2-fold (Fig 56 - C).

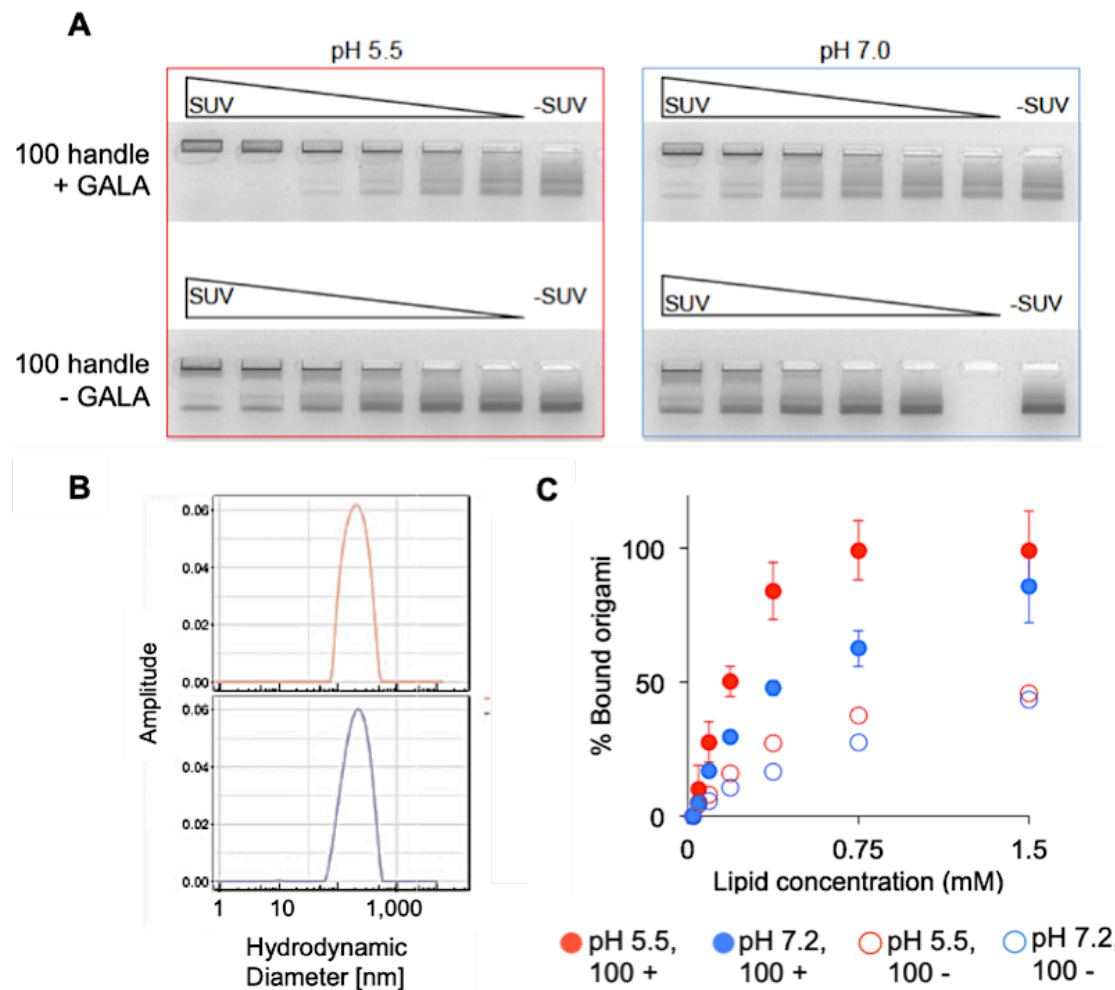


**Figure 56. pH sensitive peptide-mediated binding of DNA origami to POPC vesicles.** DNA origami is capable of recruiting the GALA-DNA conjugate to induce pH selective binding to SUVs. Origami with 100 handles = ‘100H’, origami without handles = ‘0H’. **(A)**: DNA origami binding to vesicles prevents migration into the gel matrix, is increased at reduced pH and occurs only when peptide-recruiting ssDNA handles are featured. **(B)**: DLS revealed consistent vesicle size-distributions with approximate mean vesicle diameters of 200 nm. Red/Blue color-coding indicates the experimental conditions at pH 5 and 7 respectively. **(C)**: Binding plot of the gel assay was generated by band intensity analysis, using the minus-suv control to normalize % bound origami. The number of SUVs in solution is defined by ‘lipid concentration’, which was varied across a serial titration by a factor of 50% at each step from the maximum starting value of 1.5mM POPC.

Despite reports that DNA origami can remain stable in low magnesium conditions for short periods of time, a relatively high magnesium concentration is still required to stabilize DNA origami during gel electrophoresis\*. However, electrostatic binding of DNA nanostructures to POPC bilayer membranes can be induced by divalent cations, which may explain the observed non-specific binding here (Fig 56 – A/C). Indeed, control origami scaffolds without peptide-recruiting handles, or without addition of the POC were observed to bind to POPC SUVs. Following the initial assay, non-specific binding was eliminated by reducing the gel and running buffer magnesium concentration (Fig 57), but at the cost of possible origami structural stability loss, inferred from broadening of the origami DNA bands.

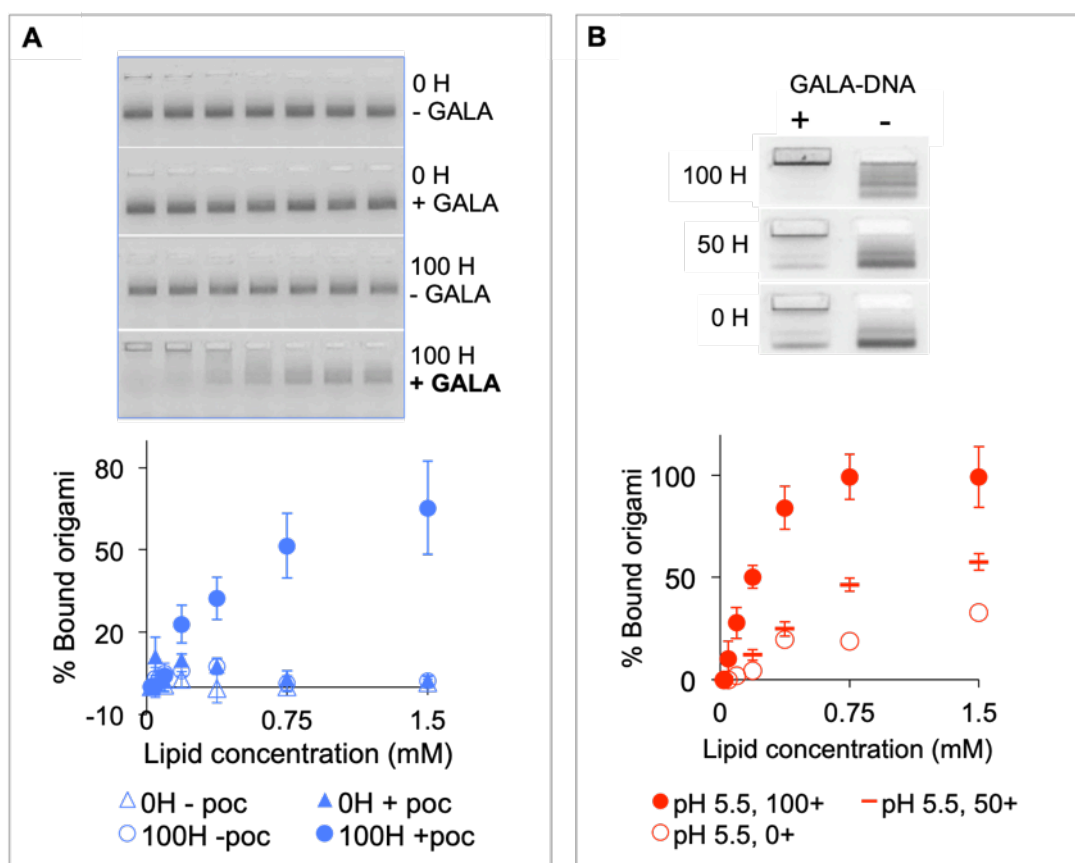


**Figure 57. (A) Reduced non-specific binding of DNA origami to POPC SUVs.** GALA recruiting ssDNA handles are required for peptide-mediated binding of DNA origami to vesicle membranes. SUV concentration is high to low from left to right. **(B): Handle number dependence for peptide-mediated origami binding to lipid membranes.** A positive correlation between handle number and origami-vesicle binding is observed. \*Figure Legends: Blue = neutral pH, Red = reduced pH. \*Salt conditions: Assay A: NaCl, 5mM. Assay B: Magnesium, 10mM. \*Origami concentrations were normalized after purification using UV-VIS absorption at 260nm. See section 10.8 for full methodology.

In magnesium-free conditions, the POC enhanced origami-SUV binding by approximately 7-fold (Fig 57 – binding plot). Good agreement was observed between the assays despite the difference in magnesium concentration, with approx. 75% of 100-handle origami being bound at the highest lipid SUV content in magnesium-free conditions (Figs 56 – 57, binding plots). Binding was increased to 100% at the respective lipid concentration in magnesium+ conditions (fig 56). Furthermore, a positive correlation was observed between peptide recruiting-handle number and binding efficiency (Fig 57 – B). The complete elimination of non-specific binding in magnesium-free gel running conditions indicates that  $Mg^{2+}$  ions in the gel matrix and/or running buffer are able to interact with gel-loaded samples through solvent exchange. More importantly, origami without POC-recruiting handles, or with handles but without POC addition, did not produce binding in magnesium-free conditions, suggesting that the DNA origami was able to ‘programmably’ recruit GALA to induce binding to POPC membranes.

Reducing non-specific binding to vesicles allowed for a more accurate analysis, of the extent to which the POC could mediate origami-membrane binding. Whilst magnesium ions facilitated non-specific binding of the origami scaffold to SUVs (i.e., binding not induced by ‘specific’ loading of the POC), the majority of GALA’s membrane binding properties appeared to be produced in accordance to pH shift from 7.2 to 5.5. This can be inferred from the efficient binding of origami to SUVs in magnesium-free conditions but with the caveat that band broadening indicates that structural integrity of the origami scaffold may have been significantly perturbed. Additionally, the magnesium-free gel assay was supplemented with NaCl, 5mM, to support origami stability by electrostatic screening. This variation in salt composition across assays introduces some uncertainty, regarding the absolute effect to which pH alone can be inferred to contribute toward GALA-induced membrane binding for the DNA nanostructure. Nevertheless, monovalent ions have been observed to produce little effect on conformation switching of GALA in comparison to divalent cations such as magnesium<sup>235</sup>.

### 7.3. GALA induced cell binding & uptake of DNA origami

To test the ability of GALA POC to induce DNA origami binding to cell membranes, origami scaffold was functionalized with either Cy3 or Alexaflour-647 fluorophores and incubated with GALA POC or GALA peptide as a control, prior incubation with HeLa cells and analysis with CLSM and Flow cytometry. Cy3 and AF647 are bright, long-lived fluorophores and are both insensitive to changes in pH that may be found for origami as it is trafficked through the endolysosomal pathway in cells. Preparation of the DNA origami, incorporation of ssDNA-AF647, and removal of unincorporated AF647 is detailed in section 7.1.

First, a dose-response assay was conducted in FBS-free cell media and analyzed by flow cytometry (Fig 58). DNA origami requires high concentrations of divalent magnesium ions to assemble, which as mentioned can induce non-specific (electrostatic) binding to neutral and negatively charged phospholipid membranes. To avoid this, magnesium concentration was reduced by approx. 85% by resuspending origami in a 2mM MgCl solution after purification by size exclusion. Origami was pre-incubated with GALA-DNA conjugate or GALA at a final concentration of 8uM for 1 hour prior to dilution into cell media and incubation with cells for 4 hours, from 50 to 5ug final origami concentration per well. Magnesium, 2mM was deemed sufficient for GALA loading onto the DNA origami (via duplex hybridization) and is at the upper threshold for physiologically relevant concentrations of this salt. Duplex hybridization of the oligonucleotide pair was tested in these conditions and confirmed by native PAGE analysis (Fig 50, pg. 90).

Flow cytometry analysis revealed a dose-dependent association of origami to HeLa Cells (Fig 58). Noticeably, the GALA peptide control (without the DNA binding handle) appeared to reduce origami-cell association by a factor of approx. 2-fold, whilst the GALA-DNA conjugate did not appear to significantly enhance origami-cell association. This observation can be explained by GALA's pH-dependent membrane binding and destabilizing properties, as is discussed in section 5.1.4. The reduction of origami association to cells in the presence of GALA peptide alone (without the DNA handle component) is more difficult to

explain, but may attributed to masking or deformation of the cell plasma membrane by bound GALA peptide. To address this observation, an additional flow cytometry assay was carried out using triplicate experimental repeats, along with analysis of singlet-cell counts for each sample variant (Fig 59, Pg. 105).

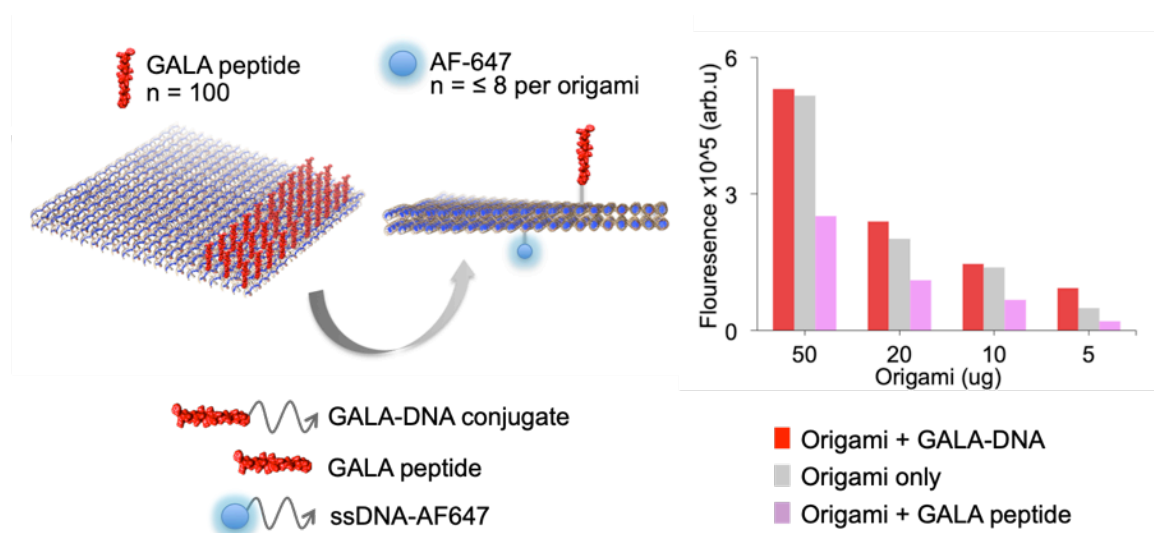


**Figure 58. Flow cytometric analysis of GALA effect on DNA origami interaction with HeLa cells.** Origami featuring the maximum number of peptide-recruiting handles (100 handles) was functionalized with AF647 reporter and incubated with GALA-DNA or GALA peptide, then incubated with HeLa cells. Cellular interaction was measured as median fluorescence per cell. No obvious enhancement for origami association to cells was found in the presence of GALA POC. By comparison, GALA peptide appeared to significantly reduce cellular association of origami. *\*Note – 50ug origami corresponds to approximately 70nM. Error analysis was not possible, due to the relatively large amount of DNA origami required for the assay. However, >8500 singlet-cell events were read for each sample. \*See section 10.9 for methodology.*

The follow-up assay (Fig 59) included added controls using the same peptide:DNA ratio (see methodology, section 10.9 - 10.10). Analysis of the single-cell count was carried out to investigate what affect, if any, the GALA peptide or origami +GALA POC had on cells, in terms of the number of single cells remaining after treatment. Either way, the number of available cells for analysis should not have affected the primary readings used to infer cellular uptake, reported for as median fluorescence intensity per cell. Origami without peptide-recruiting handles was used as an additional control to probe specific POC-induced cell-association.

GALA peptide (without the DNA handle) was again used as a control to rule out non-specific association. Finally, the positively charged HIV-TAT cell penetrating-peptide was included. HIV-TAT peptide has well known cell-transduction and membrane binding properties for DNA delivery and has been combined with DNA nanostructures to augment their cellular internalization<sup>261</sup>.

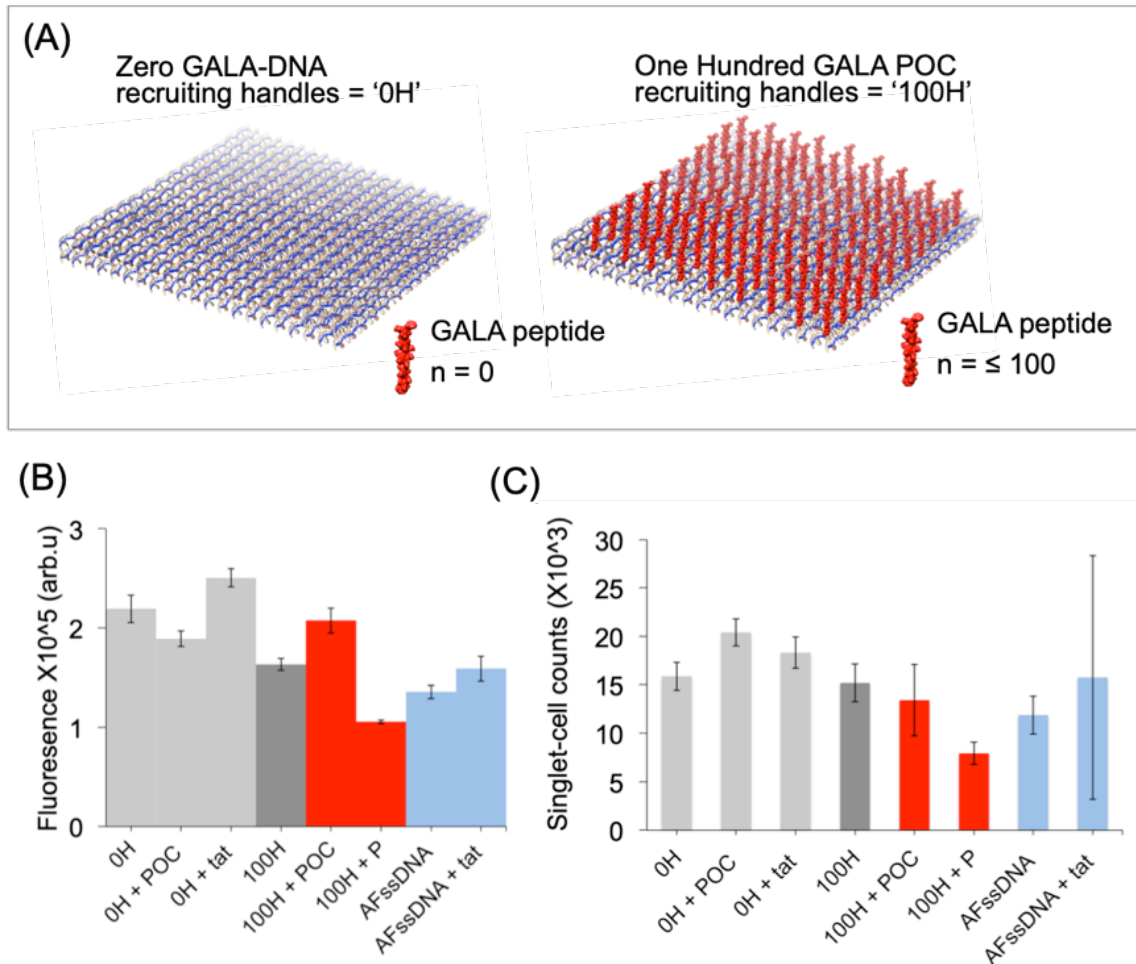


**Figure 59. Additional flow cytometry analysis of GALA effect on DNA origami interaction with HeLa cells.** (A) Flow cytometry was used to assess the ability of **GALA-DNA to mediate association of DNA origami to HeLa cells**. Positively charged Hiv-TAT peptide was included to compare against negatively charged GALA-DNA POC. Additionally, Alexa-fluor tagged ssDNA was used as a control to probe binding of origami (final concentration 40nM) relative to flexible, unmodified DNA (final concentration 300nM). (B) **Singlet-cell counts analysis of flow cytometry assay**. Singlet-event cell count is compared for the flow cytometry assay samples, indicating that GALA peptide appears to reduce the singlet cell event population. \*Sample descriptors: 'P' = GALA peptide (i.e., unconjugated GALA, without DNA handle). 'POC' = peptide oligonucleotide conjugate. 'tat' = HIV-trans-activating peptide.

As with the first flow cytometry assay, GALA peptide appeared to significantly reduce origami-cell association. The GALA POC appeared to augment origami association to cells under these conditions but minimally. Interestingly, the same approximate increase in origami-cell association was produced by the HIV-tat peptide, which is expected to non-specifically interact with DNA origami via electrostatic interaction. Origami with or without ssDNA handles appeared to interact with cells to the same order of magnitude, where a slight difference in interaction can be accounted for by inaccuracy associated with sample concentration approximation using UV-VIS absorption.

Analysis of the singlet-cell count for the flow cytometry assay reveals that GALA peptide alone appeared to significantly reduce the population of single cells available for analysis, which could be explained by the membrane-fusing properties of GALA. Numerous viridae use 'fusion domains' with similar properties to GALA, in order to enter cells or escape from endosomal compartments<sup>262</sup>. GALA was designed to study such fusion events and has known membrane fusing properties, which may have caused a reduction in the single-cell population as revealed here by flow cytometry analysis. Noticably, the HeLa cell singlet population was not affected by GALA POC, suggesting that GALA's ability to fuse membranes may have been inhibited by conjugation to a DNA oligonucleotide, or by loading onto the DNA origami.

---

#### 7.4. GALA induced cell binding & uptake of DNA origami – CLSM

Confocal laser scanning microscopy (CLSM) was used to investigate the findings presented by flow cytometry analysis, and to probe interaction of the origami with cells by providing a visual readout. Surprisingly, in contrast to the flow cytometry analysis, microscopy revealed significant enhancement of origami uptake in the presence of GALA-DNA conjugate. Substantially greater fluorescence signal was observed inside of cells where the GALA POC was incubated alongside origami featuring peptide-recruiting handles. Origami controls 0H+POC and 100H+P (terminology provided in Fig 59) showed relatively little signal (Fig 60). These

observations suggest that GALA POC was able to mediate origami binding to cell membranes to enhance intracellular uptake, the mechanism for which could be explained by loading of GALA onto the origami. Alternatively, excess GALA POC in solution could presumably bind to cell membranes to enhance association of origami in a synergistic fashion. I.e., via peptide-peptide interaction between origami-loaded and membrane-bound GALA POC. The mechanism underlying apparent enhancement of DNA origami internalization into HeLa cells remains unknown. One hypothesis is that free, excess GALA POC in cell incubating solution could bind to cells membranes as well as to the DNA origami. In this fashion, membrane anchored GALA POC could help to mediate recruitment of DNA origami to the cell plasma membrane resulting in increased cellular uptake. This process has been observed for DNA-based probes using various anchoring chemistries<sup>138,167</sup>.

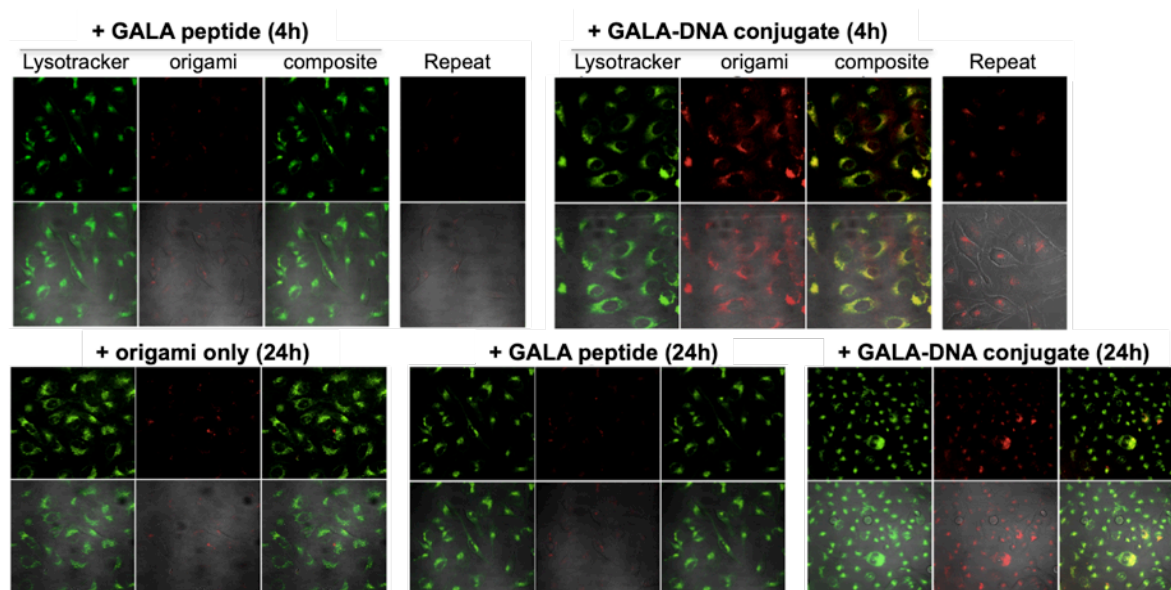


**Figure 60. Cellular Internalization of DNA origami in the presence of GALA POC.** Live-cell imaging with CLSM reveals that GALA POC is capable of enhancing DNA origami uptake into HeLa cells. Origami alone or without GALA-recruiting DNA handles, have limited uptake into HeLa cells. Signal associated with internalized DNA origami persists 24-hours after incubation whilst uptake for controls remains low. 8uM final concentration GALA or GALA-DNA were pre-incubated with DNA origami 80nM, for 1h at RT, prior to dilution of samples into cell media for 4h in FBS-free cell media. *\*(i) GALA-DNA conjugate image at 4h post incubation is shown at 2x digital magnification. \*An alternate (enlarged) presentation of this data is shown page 109 (Fig 61).*

The most obvious explanation for discrepancy between flow cytometry and CLSM observations was the final concentration of GALA-DNA used for the microscopy assay (8uM) vs. flow cytometry (2uM). Both assays involved pre-incubating GALA-DNA with origami prior to dilution into cell media and incubation with cells. However, samples were supplemented with additional GALA-DNA for microscopy experiments after dilution into cell media, bringing the final concentration to approximately half of the upper limit (16uM) beyond which GALA has been reported to aggregate in solution<sup>237</sup>. Without more rigorous assays it is indeed difficult to explain the observed discrepancy between results presented by the two sets of experiments (flow cytometry vs. CLSM), yet the most obvious answer sits with the variation in final concentration of GALA-DNA applied to cells, in the presence of the DNA origami.

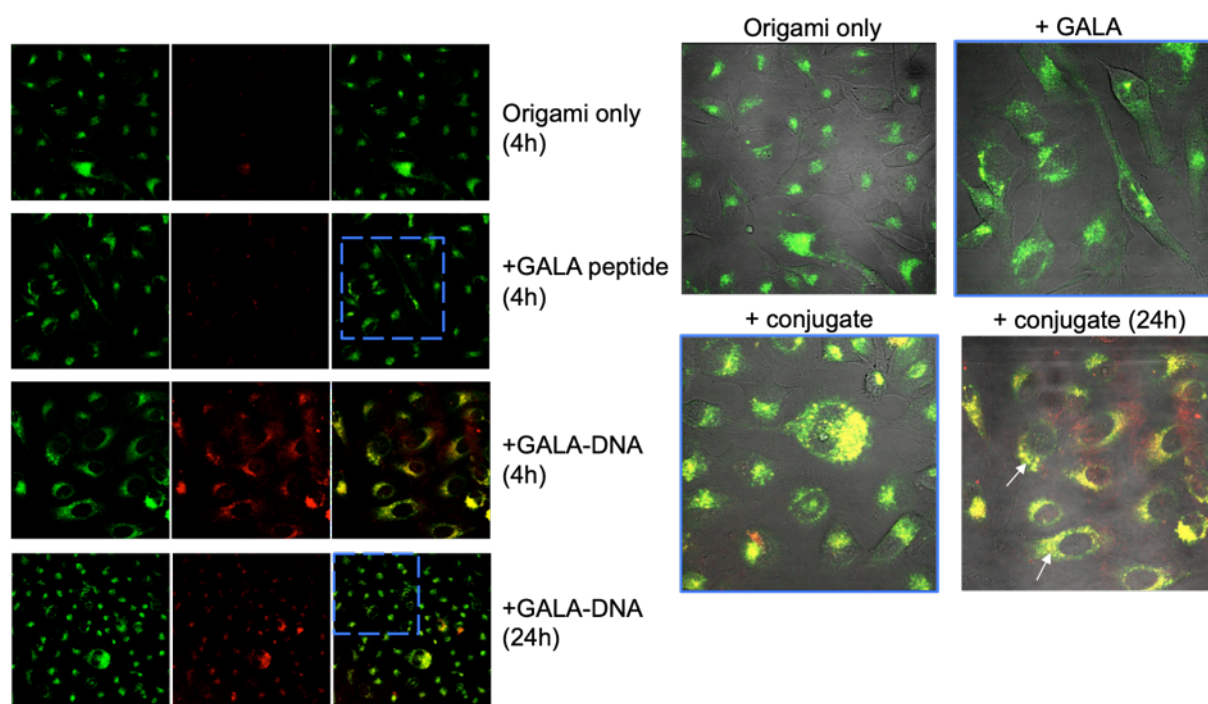


**Figure 61. GALA-DNA conjugate can augment DNA origami cell uptake – II.** Data from Figure 60 is represented again with separate transmitted-light overlays. Enhanced co-localization of Alexaflour-647 labeled DNA origami (red) with Lysotracker probe (green) indicates increased uptake mediated by GALA-DNA conjugate.

As mentioned previously, divalent ions as well as pH are known to induce conformation switching of GALA from random to coiled-coil<sup>235</sup>. The flow cytometry

assays used a magnesium concentration of 2mM for peptide incubation with origami prior to diluting into cell media. By comparison, microscopy assays used a slightly higher concentration of 5mM magnesium to match a balance between origami stability and aggregation (Fig 54 – size exclusion gel analysis). The enhanced uptake of origami in the presence of GALA could thus be explained in part by the higher concentration of  $Mg^{2+}$  ions used for the assay. As mentioned previously, divalent magnesium ions are known to mediate electrostatic binding of DNA nanostructures to neutral and negatively charged phospholipid membranes, which could further explain the observed increase uptake of DNA origami as assessed by CLSM. In both sets of experiments (flow cytometry & CLSM), origami samples were diluted by addition to cell media whilst keeping magnesium concentration constant. The final concentration of magnesium in live-cell microscopy assays was however higher (1.5mM), relative to a 0.5mM for flow cytometry assays.

As a final point, it is worth mention that the flow cytometry assays require a trypsinisation step to free adherent cells for analysis. Due to the proteolytic activity of trypsin however, cell surface proteins can be cleaved which leads to dysregulation of cell functions<sup>263</sup>. In this light, future experiments would benefit from using suspended as opposed to adherent cell cultures in order to avoid this additional factor that may obfuscate findings.

## 7.5. DNA origami stability in cell media

Recently, Sleimen and colleagues assessed the reliability of fluorophore tags to report the intracellular localization and uptake of intact DNA nanostructures<sup>264</sup>. Notably, intracellular signals associated with fluorophore-tagged DNA nanostructures were found to be misleading due to digestion of DNA nanostructures by extracellular nucleases. Degraded products were observed to internalize into cells giving a false impression of uptake (of intact DNA nanostructures). However, the structures tested for have typically been wire-frame type assemblies as opposed to more compact DNA nanostructures such as that used in this project. Here, DNA origami was incubated with cells in the absence of

FBS to avoid extracellular digestion and thereby abrogate chances for misleading intracellular signals.

Samples from CLSM experiments were recovered so that DNA origami stability could be tested at the maximum time-duration used for imaging, both in the absence and presence of FBS (Fig 62). In contrast to the report mentioned above, DNA nanostructures incubated in the presence of FBS did not produce significant intracellular signal, indicating that uptake was either limited by aggregation or digestion of the intact structure. Indeed, CLSM revealed that DNA origami incubated with HeLa cells in FBS containing cell media produced large micron scale aggregates (data not shown). To test the stability of DNA origami, samples were recovered after incubation with cells both in the presence and absence of FBS, and were visualized using agarose gel electrophoresis. Noticeably, bands corresponding to intact DNA origami were observed for samples incubated with cells in the absence of FBS. By contrast, origami was fully degraded after 24-hours of incubation in the presence of FBS. These findings are consistent with reports that indicate limited stability for unmodified DNA nanostructures in the presence of serum endonucleases<sup>74</sup>.

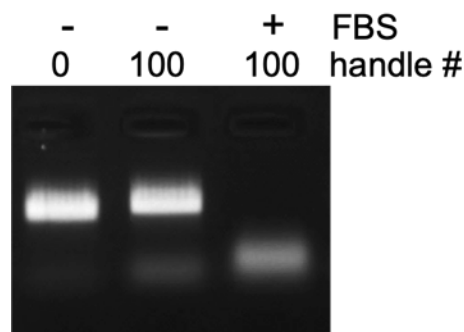


**Figure 62. DNA origami is completely degraded in the presence of FBS.** Agarose gel electrophoresis reveals complete digestion of DNA origami in FBS supplemented cell media. Origami incubated in the absence of FBS retains its handle-number dependent gel-shift (see Fig 53).

Notably, the gel analysis of recovered DNA origami reveals discrete bands (Fig 62) suggesting that DNA origami remains monomeric after incubation in FBS-free cell media, and furthermore that a significant fraction remains non-internalized after 4 hours of incubation with HeLa cells. Additionally, a migration shift is seen

between '0H' and '100H' origami, indicating that GALA recruiting ssDNA handles remain intact. This migration shift observed for origami with handles, vs. origami without handles was observed consistently when characterizing the assembly of DNA origami (Fig 53).

Stability of DNA origami and DNA-based nanostructures is important for functional activity<sup>73</sup>. The observations presented here could suggest that functional stability of a rigid DNA origami rectangle can be preserved in FBS-free conditions with implications that peptide or ligand recruiting ssDNA handles can be used in combination with DNA nanostructures for prolonged periods. The intracellular stability of DNA origami used here however cannot be deduced without more advanced analysis methods, such as FRET-based assays that have been used to assess intracellular DNA nanostructure stability<sup>254</sup>.

## 8. Conclusions – Project II

As is the case for most inorganic nanoparticles, DNA nanostructures, and nucleic acids more broadly, are not readily permeable to cell membranes. CPPs have been used to successfully augment delivery nucleic acids nanoparticles, mostly by providing for charge-neutralization of the nucleic acid and using the positively charged and amphipathic properties of CPPs to induce electrostatic and/or hydrophobic interaction cell membrane. However, positively charged particles often produce undesired cytotoxicity, which may not be a problem for certain applications but poses crucial limitations in the context of medicine, where cell-killing may not be desired. Indeed, toxicity and specificity must be tightly controlled in order to design highly efficacious drugs and nanoparticle-mediated delivery vectors. In this context, anionic CPPs maybe uniquely positioned to overcome the above-mentioned hurdles, and may furthermore be incorporated with DNA nanostructures, or nucleic acids more broadly in a programmable fashion by avoiding electrostatic and non-specific interactions. Such approaches could allow for more carefully tailored design strategies that exploit the unique molecular programmability provided for by DNA nanotechnology.

Here, the anionic CPP GALA was used as a POC, to investigate the possibility of programmed peptide incorporation onto a DNA nanostructure, and to probe the ability of CPPs to elicit endosome release of DNA origami via duplex hybridization. Binding assays using synthetic lipid vesicles, alongside live-cell imaging, suggest that CPPs can indeed be combined with DNA nanostructures, inferred from selective binding of origami to vesicles and enhanced cellular uptake of origami in the presence of the GALA POC. However, flow cytometry analysis revealed potentially conflicting observations regarding cell-uptake, making concrete conclusions difficult.

Robust assays using CLSM were planned to examine the pH-dependent properties of the GALA-peptide and their ability to mediate endosome release of DNA origami and/or co-incubated cargo. More specifically, it was envisioned that DNA origami could be used to enhance the membrane lytic activity of GALA by increasing its local density at the interface with endosome phospholipid

membranes. These assays were however not possible due to repeated loss of access to facilities. Live-cell CLSM assays were planned to exploit fluorescent membrane impermeable dyes to assess whether the origami-peptide system could elicit endosome rupturing and release. These assays were pivotal to investigate the hypotheses at the heart of project II, which have thus to some extent remained unresolved (please see covid impact statement). Nevertheless, the results presented suggest that GALA peptide can be used to control membrane binding of DNA origami via POC chemistry and duplex hybridization, and provide incentive for further research in this area. Further experiments have been planned to pursue this work and will be conducted by other members of the Howorka group.

## **9. Conclusions – Summary**

In summary, the work presented for thesis attempted to probe interplay between DNA nanostructures, functional moieties and biological systems. DNA nanostructures provide for discrete control over presentation of functional ligands that can be used to govern interaction with biological systems. Here, hydrophobic cholesterol anchors were found to significantly affect DNA nanobundle interaction with HeLa cells. The data presented in ‘project II’ suggests that hydrophobic GALA peptide can likewise augment interaction of a much larger DNA nanostructure to HeLa cells in a programmable fashion, though these findings were less conclusive due to some conflicting data.

The results of project I suggest interplay between DNA nanobundles, their lipid anchors and the environment used to test their in-vitro interaction with cells. However, the physicochemical nature of these interactions remains unknown. Future work would benefit from purposefully designed assays aimed to investigate which exact components of FBS, or other serum sources interact with DNA nanobundles and how, as certain serum components may interact preferentially with the structure DNA - or conversely with the structure’s lipid cholesterol anchors. Furthermore, number or density, as well as steric positioning of hydrophobic anchors (on DNA nanostructures) may additionally control such interactions with serum components to complicate the overall picture. Understanding these interactions will be important in order to improve rationale

design of DNA nanostructures as biomedical tools or therapeutic agents, and could be approached for example, by conducting in-vitro biological assays, where the levels serum proteins in the incubating media are controlled. E.g., by removal or spiking of specific proteins such as IgG antibodies. In this way, it might be possible to reveal how serum components interact with DNA nanostructures, by means of observing altered interactions with biological systems, such as cells or tissues. To this end, AFM or advanced imaging methods such as single-particle tracking, super-resolution microscopy or EM, could be used to reveal such interactions and thereby provide a better picture of how cholesterol anchors or indeed other hydrophobic moieties can be used in combination with DNA nanostructures, to control interactions with cancer cells, or cellular organelles and systems more broadly.

Assays aimed at probing endosome escape and/or rupture, or damage, are required to confirm the hypothesis at the heart of project II, which posed as a question here can be defined by asking: can a rigid DNA origami-scaffold mediate, or enhance the membrane destabilizing properties of cell penetrating peptides? The idea for this project builds on the rationale underlying project I, in that hydrophobic moieties can be combined with DNA nanostructures to augment interaction with cell membranes, and likewise sought to explore these interactions using cancer cells as model system but instead using a pH-responsive peptide termed GALA. Fluorescence microscopy in particular could be used to carry out semi-quantitative 'escape assays' by exploiting fluorescent dyes that produce enhanced or significant signal upon endolysosomal localisation. LysoTracker probes would be a suitable choice for these assays, which could be combined with protein markers for co-labeling of endosomes along their specific maturation stages in order to provide more detailed information regarding the nature of any observed membrane damage and escape of the entrapped fluorescent cargo.

In the context of nanoparticle interactions with cells, programmed 'loading' of peptides onto DNA origami, via POC chemistry, may provide a useful route for investigating the relationship between peptide multivalence, and activity, but may be complicated by the requirement that such peptides must be similarly charged to DNA in order to abrogate non-specific interaction with the scaffold via

electrostatics and thereby allow for disentangling of any observed change in activity from interaction with the scaffold itself. Optimistically, DNA nanostructures may provide a novel means to enhance the activity of anionic CPPs and thereby avoid the toxicity associated with their traditional and oppositely charged counterparts. Importantly, other membrane lytic peptides could be easily combined with the DNA origami designed for project II in order to probe more broadly whether or not such DNA nanostructures can be used to augment peptide activity via duplex-hybridization and POC chemistry. More broadly, controlled endosome escape of DNA nanostructures constitutes a major challenge and is largely an un-met goal, but could pave the way for significant advances for DNA nanostructures as intracellular probes, drug delivery devices or other tools to probe or manipulate biology.

## 10. Methods & Materials

Project - I

---

### 10.1. DNA Nanobundle Preparation

The six-duplex nanobundles were prepared following established protocols\* and were used within a few hours from folding. Agarose and SDS-PAGE were used to validate nanobundle folding. Sequences of component DNA strands along with 2D schematic maps of the 6-duplex DNA nanobundles have been published and are featured in section 2.1 (Fig 20, Ref 158).

### 10.2. Cell Culture

HeLa cells were grown in DMEM (Invitrogen) supplemented with 10% heat-inactivated FBS (Gibco), 10 µg/mL gentamicin, and 0.25 µg/mL amphotericin B (Invitrogen) at 37 °C in humidified air containing 5% CO<sub>2</sub>.

### 10.3. Flow cytometry Analysis on Cell Interaction of DNA Nanobundles

HeLa cells were precultured and used within 24 h after seeding onto 48-well plates at a density of 25 000 cells per well. Nanobundle stock solutions with a final concentration of 0.1, 1, 10, and 100 nM were prepared with Gibco opti-MEM. Prior to sample loading, the cell growth medium (DMEM, 10% FBS) was aspirated from each well followed by washing three times with prewarmed PBS buffer. All samples were prewarmed to 37 °C prior to incubation with cells. Samples were then pipetted into wells in triplicate. After 3 h incubation with nanobundles, samples were aspirated followed by washing twice with PBS. Cells were then trypsinized with TrypLE (Gibco), followed by trypsin inactivation and resuspension with DMEM and transferal to a 96-well plate. At least 3000 cells were analyzed for each sample using a Flex-S flow cytometer. Consistent gating based on cell size and granularity (forward and side scatter) was used to select viable single cells for analysis. Median fluorescence intensity was calculated for each sample by averaging after background subtraction.

#### **10.4. Nuclease Digestion and Flow Cytometry Analysis**

Cells were prepared in the same manner as for the concentration assay with the exception that DMEM with 10% FBS was used as incubating medium. Cells were incubated with nanobundles at 100 nM concentration for the desired time duration, followed by washing three times with prewarmed PBS and then exposure to DNase(I) at a final concentration of 10 U/mL for 1 h. In parallel, control nonenzyme-treated cells were incubated with DMEM. Enzyme-treated and nontreated groups were aspirated and washed three times with 1× PBS, followed by trypsinization and preparation for flow cytometry analysis following the same procedure as used in the concentration assay

#### **10.5. Fluorescence Microscopy for Nanobundle Binding**

HeLa cells were used 24 h after seeding into 8-well Ibidi glass chambers at a density of 25 000 cells per well. Nanobundle solutions were prepared in the same manner as for flow cytometry experiments and used at a final concentration of 100 nM in opti-MEM reduced serum medium (without FBS supplementation). NB-3C was tagged with AlexaFluor-647 via incorporation of a modified component strand with the fluorophore placed at the 5' end of one oligonucleotide as described.<sup>(93)</sup> HeLa cells were washed three times with prewarmed 1× PBS, followed by incubation with nanobundles and imaged after the described durations. Images were collected using an Olympus inverted confocal microscope using a 60× oil immersion objective lens. Laser line 633 was used for AlexaFluor-647 excitation, with appropriate band-pass filters.

#### **10.6. Microscopy Analysis of Enzyme-Treated Cells**

Nanobundles were incubated with HeLa cells following the same method as used for the localization experiments, with the exception that NB-1C was tagged with 6FAM and coincubated alongside NB-3C at final concentrations of 100 nM. For enzymatic digestion of membrane surface-associated nanobundles, DNase(I) enzyme was prepared in the same method as with flow cytometry experiments and incubated with cells after washing twice with 1× PBS. Laser lines 633 and 488 were used for AlexaFluor-647 and 6FAM excitation, respectively.

### **10.7. Fluorescence Microscopy for Nanobundle Localization**

Nanobundle preparation and incubation were carried out with the same method as with previous microscopy experiments. For endosomal staining, nanobundle (NB-3C) samples were aspirated off after the desired incubation duration, washed twice with 1× PBS, and incubated for 1 h with LysoTracker Red DND-99 (Thermo Fisher). LysoTracker was prepared to a final concentration of 100 nM in phenol containing DMEM. LysoTracker containing solution was aspirated off prior to imaging, followed by washing three times with 1× PBS and reincubation in opti-MEM for imaging. Images were collected using an Olympus inverted confocal microscope using a 60x oil immersion objective lens. 633nm and 559nm laser lines were used for AlexaFluor-647 and LysoTracker excitation, respectively, using appropriate band-pass filters. Data was collected using sequential image acquisition method.

### **10.8. Cell Viability Assay**

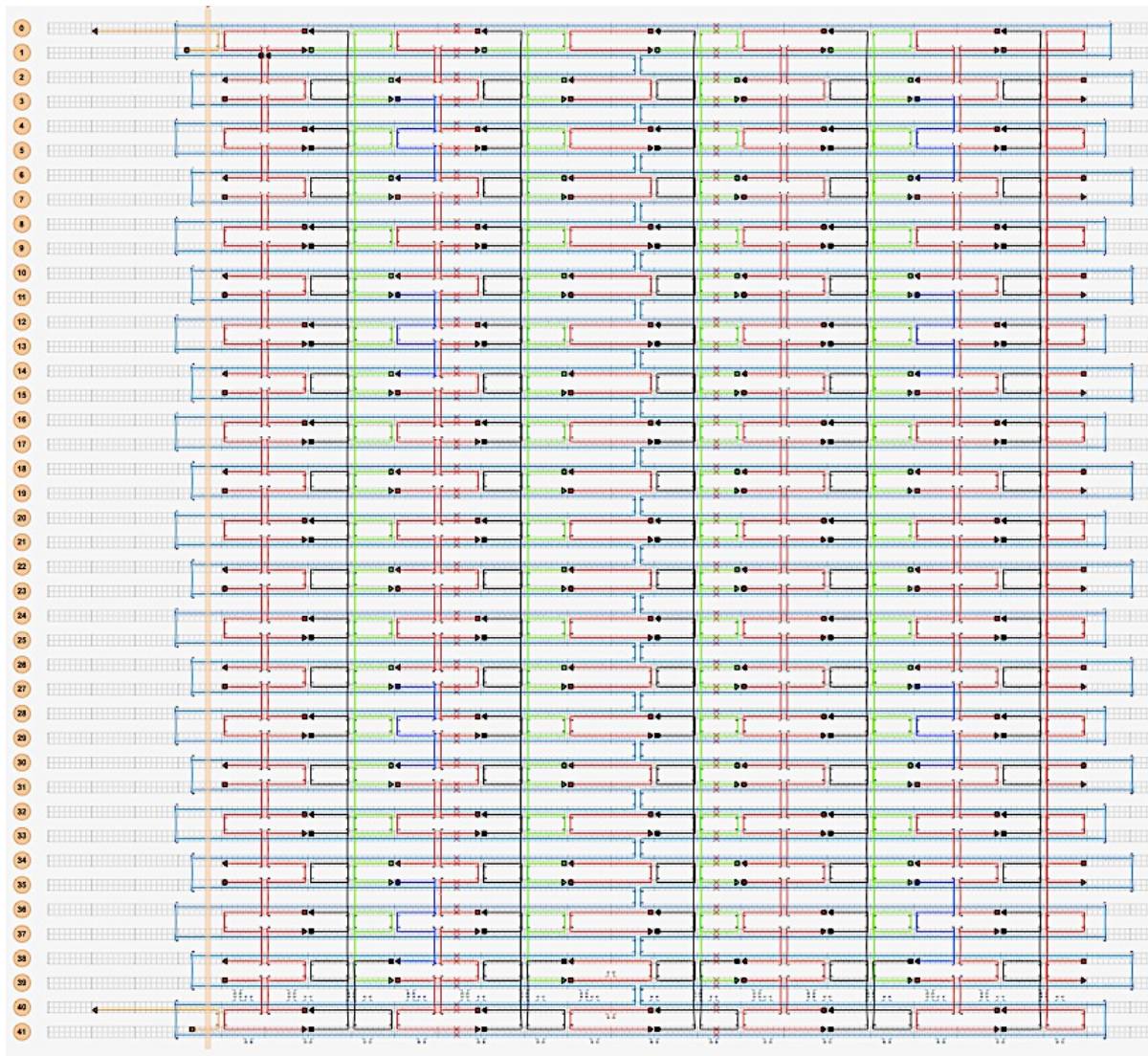
NB-3C nanobundle samples were prepared at a final concentration of 500, 250, 125, and 60 nM by diluting in DMEM + 10% FBS. Required volumes of PBS were added to each DMEM nanobundle sample to ensure consistent PBS concentration across the assay. As nanobundles were assembled in PBS, the same buffer was selected for use as a negative control. Cells were grown to confluence and then seeded into a 96-well plate at a density of 10 000 cells per well. NB-3C samples were incubated with cells for 3 h, followed by washing three times with PBS and re-incubation with DMEM + 10% FBS. Fluorescence was measured after 3 and 24 hours using Alamar Blue metabolic activity assay following the manufacturer's protocol. Data was collected using a Fluorostar Omega plate reader (BMG Labtech).

## 11. Methods & Materials

### Project – II

---

#### 11.1. DNA Origami Design Schematic



Colour code:

Black = extension set 1

Green = extension set 2

Blue = fluorophore extension set

Light blue = scaffold m13mp18 ssDNA

Red = non-modification staples (not used for ssDNA handles)

## 11.2. DNA Origami Staple Sequences

Start (bp #)	End (bp #)	Sequence 5' > 3'
37[48]	32[48]	CGACAGAACATATGGTGAGGGAAGCGAGGAAA
17[48]	12[48]	TGTGAGTGGAATATACCTGATTGCAATTATCA
21[48]	16[48]	GAATCATAAATTTATCGTTGGGTTATTTAACA
9[48]	4[48]	GCTGAACCCCTTCTGAGCTATTAGGCTGGTAA
13[48]	8[48]	GTTTGGATTAGATTAGTTTACAAACCTGCAAC
29[48]	24[48]	AAGAAACGCAAATCAGGCCAACCTAGAAAAAT
5[48]	0[48]	GAAATACCTTAGACAGGGCCACCGCGCTAGGG
33[48]	28[48]	TTACGCAGAAAGTCAGGAGTTAAGCAGAGCCT
38[63]	40[48]	TCACCGGACATACATGTTTACAAACAAATAAA
25[48]	20[48]	GTCTTTCCCAACGCCAATATAAAGTAATGGTT
41[48]	36[48]	GTAAGCGTACCAGAGCCCACCCTCTTAGCAAG
38[95]	40[80]	ATTAGCGTCTGGTAATGTTGAGGCAGGTCAGA
17[80]	12[80]	TCGCTATTATTGCGTAGCGCAGAGTGCGGAAC
29[80]	24[80]	GAAAATAGCGTAGGAAGCCTTAAACTGTTTAT
21[80]	16[80]	TATCATATTAGATTAATGCAAATCAAACAAAC
25[80]	20[80]	AAACCAAGGTAGGGCTCTGTCCAGTTTTAGTT
5[80]	0[80]	GAAATGGAGGAGCTAACAAATTAAGAAAGGAA
33[80]	28[80]	CATACATATAGACGGGATGAAATATGAATCTT
41[80]	36[80]	GGAGTGTATTGCCATCCACCAGAAGCCAGCAA
37[80]	32[80]	CTGTAGCGAAGTTTTATATTAAGGAGATAGCC
13[80]	8[80]	TTAGAACCCTAAAATACCTTTGCCAACAGAGG
9[80]	4[80]	TATCTGGTAAAGGGACCCTAAAACCCTGAGTA
17[112]	12[112]	TACAGGCACAAGAGAAAGTAATGTTAACCAAT
5[112]	0[112]	AACATACGAGCCCGAGAGGGTGGTAGCTTGAC
37[112]	32[112]	TGTAGCATTGTCAGGGTTCACGTTAAACGAAA
13[112]	8[112]	AACGGTAAGTTTGAGGGCCATCAAGGGGGATG
25[112]	20[112]	ACTAATGCATCGCGTTCTGCGGAATAAAGTAC
21[112]	16[112]	CGAGCTTCCATCCAATTGGAAGTTAAATGCAA
9[112]	4[112]	CGACAGTATCACAATTAAGGCGATGCGTATTG
33[112]	28[112]	AGGCCGCTAACTGACCAAGAATAGAGTAGTA
38[127]	40[112]	CACCAGTAGAGTAACAAGTGCCGTCGAGAGGG
29[112]	24[112]	GAAAGAGGGAATACCAGCTTGAGAGATAGCGT
41[112]	36[112]	AGTGCCTTCAAATACTAAGTATACGAATAAT
37[144]	32[144]	GCGTAACGACGCATAACAAAAGGATACGTAAT
21[144]	16[144]	ACTCCAACGCATCAATCCAATTCTGATAAAAA
5[144]	0[144]	CCTGGGGTATCGGCAAGCAACAGCATCGGAAC
17[144]	12[144]	GCAATAAAATCAGGTCAGAAAGGCCATTAAT
25[144]	20[144]	TACGAGGCAGATTAAGCCCCTCAAGCTGTAGC
9[144]	4[144]	CAGCCAGCTAGCTGTTTCCCAGTCGAATCGGC
41[144]	36[144]	GTTAATGCTGTACCGTACTCAGGATGAGAATA
13[144]	8[144]	TATGTACCAGATGGGCTGTAGCCAGGCCTCTT

33[144]	28[144]	AGCGAAAGGAGGCGCACCCAGCGATAAGGCTT
29[144]	24[144]	GGCGCATACAGGTAGATTGTGAATCAGAGGGG
38[159]	40[144]	GGAACCCACCCCTGCCTAGCGGGGTTTTGCTC
41[176]	36[176]	ATTCTGAATTTTCAGGCCGCCACCTTGCTAAA
29[176]	24[176]	AATCTTGATAATAAAAGCTCATTAATAGCGAG
25[176]	20[176]	CCCTCGTTTATAGTCAAGAATGACGGATGGCT
21[176]	16[176]	AATTGCTCTATTTTCACATTAGATTTTTGCGG
33[176]	28[176]	CGGCTACACCGCGACCCAACGGAGAATCAACG
37[176]	32[176]	GACGTTAGAGTTGCGCGCTTGCTTTTCATGAG
9[176]	4[176]	GAAACCAGGGGTACCGTGCCAAGCGTCCGGAA
5[176]	0[176]	TTAATTGCAGGCGAAATGAGAGAGTTTTTTGG
13[176]	8[176]	AAAAACAGATTGACCGCGAGTAACCTGCGCAA
17[176]	12[176]	GTTGTACCGGGTAGCTTATGATATAATTGTAA
27[64]	30[64]	GCGGGAGGCTAACGAGTTAACGTACTGAACA
35[64]	38[64]	TGACGGAAAGTAGCACGCCTTTAGAATCAAAA
3[64]	6[64]	AGTCTGTCTCAAACCTAGACGCTCACCAACAGA
11[64]	14[64]	CAACTCGTCCACCAGATGAATAATAGGTTTAA
35[160]	38[160]	TTGTATCGAACAGTTTTTTTTGTCGGCCAATA
27[160]	30[160]	GCGATTTTCTGCTCATGACCTTCAGTTACTTA
3[160]	6[160]	CTTACCGTGCCAGCTAGTGAGCTTTCGTAAT
11[160]	14[160]	CAACATTAATTTTGTTTAATCAGAGAGATCTA
22[63]	27[63]	ATATTTAATTATCATTCTGAACACCCGACTT
1[48]	3[63]	CTTAATGCGCCGCTACGGAGCGGGAGTAAAAG
6[63]	11[63]	GATAGAACTCAAATATTAACACCGCAATTTCGA
18[63]	23[63]	CAATAGTGATTACTAGCCTAAATTTACCGACA
14[63]	19[63]	CGTCAGATAATAACCTTTAATTACATATAACT
30[63]	35[63]	CCCTGAACTATGTTAGAAGGAAACGTAAATAT
34[63]	39[63]	AGAAAATTTCAAGTTTCATTACCAAGAGCCAC
10[63]	15[63]	ACAACATAATACTTCAGGAGCGGTTTGAATA
26[63]	31[63]	ATAGCAAGATTTTTTTCGCTTTTCCCAATAA
2[63]	7[63]	AAGGGATTTACATTTTTTCGGCCTTTCTTTAAT
10[95]	15[95]	AAGGTTATTACCATATTATCATTTGCGAATTA
14[95]	19[95]	ATAAAGAAAATTAATTAGATGATGCAATCGCA
34[95]	39[95]	CACGGAATCGTTTTTCAGAATTAGACCACCACC
1[80]	3[95]	GTTGCTTTGACGAGCACGTGGCGACCGTTGTA
30[95]	35[95]	AAGCGCATAAGGTGGCAAGTAAGCTGAATTAT
18[95]	23[95]	CGATAGCTGCGTTATACAAATATAACGACGAC
22[95]	27[95]	GCTCAACATACCGCACGAACGCGCTCAAGATT
6[95]	11[95]	CAGTAATACAGTTGGCGAAGATAACGAACGTT
26[95]	31[95]	ATTTTCATCAGCCTTTTTTATCCGCAATAGC
2[95]	7[95]	TCAGAGCGTTATTTACATCACTTGATCGCCAT
10[127]	15[127]	ATCTGCCATCGTAAATCATTTTTGTAGGTAA
1[112]	3[127]	TTGAGTGTTGTTCCAGCGATTTAGTTTTCTTT
22[127]	27[127]	CTTCAAATAGATACATTTAGACTGTGGTTTTAA
18[127]	23[127]	AGCATTAAAAGCGAATATGCAACTCGTCATA

6[127]	11[127]	TTATCCGCTCGGCCTCTGGCGAAAAAATAATT
14[127]	19[127]	GGAGCAAAGGCAAAGTATATTTTTTCATTCCA
30[127]	35[127]	GGGAACCGTTTGCGGGCCAACCTAGAAAATCT
2[127]	7[127]	AAAAGAATAGCCGGAAGGCGGTTTTAAGTTGG
26[127]	31[127]	AGATTTAGACAGATGAACCAGAACCACTAAAA
34[127]	39[127]	GCTGAGGCTCCACAGAAGGAATTGGCCCGGAA
14[159]	19[159]	CAAAGGCTGCCTCAGAAACGCAAGGCGAACGA
18[159]	23[159]	AAAAGGTGAGGTCAGGAATATAATATGCTTTA
30[159]	35[159]	GCCGGAACACAGCATCGGGTAAAAGCCTTTAA
1[144]	3[159]	CACTATTAAGAACGTAGCACTAATGATTGCC
2[159]	7[159]	GTTCCGAAGCCTAATGGCATTAAACGACGTT
6[159]	11[159]	CATGGTCATTTCCGGCTCGGTGCGGCTTTCAT
26[159]	31[159]	CATTATTAGGCTGGCTTCAGTGAATTATACCA
22[159]	27[159]	CATCAAAAATAGTAAGAGTTTTGCTACCTTAT
10[159]	15[159]	GTTGGTGTCCGGTTGAAAAATTCGCGGAGACA
34[159]	39[159]	CATCGCCATCTAAAGCAGCGGAGGGTTTAGT
7[160]	10[160]	GTAAAACGAAGGGCGAACCGCTTCTAGGTCAC
0[47]	2[32]	CGCTGGCAAGTGTAGCCACCACCCGCCAGAA
11[32]	14[32]	TTAGAAGCTGATTATCAATATAATACCTTTT
7[32]	10[32]	ACAATATTGCTGAGAGTCTAAAGCATAGATAA
35[32]	38[32]	ATCAACCCGTCACCAGCACCGTAGAACCGCC
19[32]	22[32]	TTAACCTCCGACCGTGATAAGAATTTTAGGCA
27[32]	30[32]	AACGCGAGAGTTACAATTATCCCATGAGCGCT
15[32]	18[32]	ACAATAACTGAATTACTACATAAAAGGTCTGA
3[32]	6[32]	TTTTTATAACAATATTAGGAAAAACGTAAGAA
31[32]	34[32]	ATAACCATAACGGAATGATTAAGGCCAAAGA
23[32]	26[32]	AGCCAGTAATCCTAATCAATCAATGGCTTATC
12[47]	9[47]	TCATATTCTATTAGACAGCCGTCAATCACCTT
24[47]	21[47]	AATATCCATAAGAGAACATGTAAAAACACCG
28[47]	25[47]	AATTTGCCGCGTTTTAATATAGAAAATCGGCT
4[47]	1[47]	TATCCAGAATCAGTGAGAACGGTACCGCCGCG
16[47]	13[47]	ATTTCAATTGGATTTCGAGTAACAGTCCTGATT
32[47]	29[47]	CGCAATAACAAGAATTAGGGTAATATCCAAAT
20[47]	17[47]	TGAAATACCGGCTTAGAAAATCATTCAATATA
39[32]	41[47]	GCCACCCTAAAGCCAGTGAATTTACCGTTCCA
8[47]	5[47]	AGTGCCACTTTGAATGCCTGAAAGCGCTCATG
36[47]	33[47]	GCCGAAAGATTGAGGTTACCAGCACTCCTTA
40[47]	37[47]	TCCTCATTGAGAACCGCACCCGATCAGTAG
23[64]	26[64]	AAAGGTAAAGATAAGTCCAAGAACCGCGCCCA
7[64]	10[64]	GCGCGAACGTGAGTATCAAACCCTGAGCACTA
15[64]	18[64]	CCAAGTTAAAACAAAATGCTTCTGAGAAGAGT
31[64]	34[64]	TAAGAGCAGTTACCAGCAAACGTACAATCAAT
0[79]	2[64]	GGGAAGAAAGCGAAAAGGGCGCGGCCGATTA
19[64]	22[64]	ATATGTAATCTTCTGAAAAAGCCGAATCGCC
20[79]	17[79]	AATTTCAATGCTGAGACGCTGTAATCG

4[79]	1[79]	GAAGAACCATCACGACAGGAGTACTATG
16[79]	13[79]	ATCAAGACAAAATCGATTTTCGGAAGGG
24[79]	21[79]	CAACAATAGTAATTTAATTGATGTTTAG
36[79]	33[79]	AATCACCATTATTCTTTGTCAGAAAATA
40[79]	37[79]	CGATTGGGAGCCGCTTTTCATCGTCAGA
28[79]	25[79]	ACCAACGTTTTGAATCATTACGGGTATT
39[64]	41[79]	CACCCTCACCTTGATAGCTTTTGATGATACA
32[79]	29[79]	GAACAAAAGAAACAAGAATTACAAAAT
12[79]	9[79]	AAAGAAAATTAAATTCTTTAGCAATCAA
8[79]	5[79]	TGAGGCGTGATAGCATTCTGGATCGTCT
39[96]	38[96]	AGAGCCGCCCAATAAACTCATAGCCCCCTT
31[96]	30[96]	TATCTTACCGAAGGCAAACCATAAAAACAGGG
7[96]	6[96]	TAAAAATACCGAATGCCACCAGTCACACGAC
3[96]	2[96]	GCAATACTTCTTTGCCATATTCCTCGTTAGAA
11[96]	10[96]	ATTAATTTTAAAAACGGAAAAGGAATTGAGG
19[96]	18[96]	AGACAAAGAACGCGTCAAACCTTGAAAACATAG
35[96]	34[96]	CACCGTCACCGACTTTAGTAACGCAAAGACAC
15[96]	14[96]	TTCATTTCAATTACTGTGACGTA AACAGAA
23[96]	22[96]	AATAACAACATGATATTAGTATAAAGCCAAC
27[96]	26[96]	AGTTGCTATTTTGTGGCATGCAAGCCGTTTTT
40[111]	41[111]	TTGGCATTGACAGGAGAAGTTTTAACGGGGTC
28[111]	29[111]	AATCACCAGCTACAAACAGAGAGAATAATTT
8[111]	9[111]	TGCCGAACCACCAGCAAATCAACAGTTGCGA
0[111]	1[111]	GGGGAAGCCGGCGAACGTATAACGTGCTGGG
20[111]	21[111]	GGTGAGAAAACCTTTTTCAAATTCTTACCAATT
32[111]	33[111]	GAGCCCTTTTTAAGAAAACATATAAAAGATAA
24[111]	25[111]	CCATTCAGCTAATGCATCATCGAGAACAATCA
16[111]	17[111]	TGCCCTGAGCAAAAGATTCCCTTAGAATCTCA
36[111]	37[111]	AATTTGAGCCATTTGGTCGGCATTTCGGGCC
12[111]	13[111]	AGGGTTTGAGTAACATCAAATTTATTTGCATG
4[111]	5[111]	GGCGATTAGTAATAACATTGGCAGATTCACAC
19[128]	22[128]	TATAACAGGTTTTAAACCAGACCGCCGAAAGA
3[128]	6[128]	TCACCAGTCGGGGAGAGCATAAAGTGAAATTG
35[128]	38[128]	CCAAAAAACAACCTAACAGCCCTCAGTTTCGT
23[128]	26[128]	AATATTCATAAAATGTAACGCCAAATCAGTTG
15[128]	18[128]	AGATTCAAACCCCTCAAATTAGCAATAGTAGT
7[128]	10[128]	GTAACGCCACGCCAGCAGGAAGATAACCGTGC
11[128]	14[128]	CGCGTCTGAAATCAGCCTAGCATGGAGAGTCT
0[143]	2[128]	CCTAAAGGGAGCCCTTTGGAACATAAATC
27[128]	30[128]	TTTCAACTCGAGAAACACGGTGTAATCATAA
31[128]	34[128]	CACTCATCCGAAGGCAATCGTCACATTCGGTC
32[143]	29[143]	GCCACTATTTGACCGACGGTCCAGACCA
16[143]	13[143]	TTTTTAGAAGGGTGATTGCCTTCAATCA
40[143]	37[143]	AGTACCATCACCGTAACACTGATAGTTA
8[143]	5[143]	CGCTATTAGGGTTTTCTGTGTGTAAG

24[143]	21[143]	GTAATAGTTGAATCAGGAAGCGAAGCAA
20[143]	17[143]	TCAACATTTGATTCTCTACTAAAATTAA
12[143]	9[143]	TTTTGTTGCCTTCCGCATCGTCGCACTC
28[143]	25[143]	GCCCTGATTAATCAAAGATTCAAGGAAT
36[143]	33[143]	GAAAGGAAAGGCTCCCGATATCCTCAGC
39[128]	41[143]	TAGGTGTAGGCGGATAGTGCCCGTATAAACA
4[143]	1[143]	CAACGCGGAGACGGAATCCCTAAGAGTC
19[160]	22[160]	GTAGATTTAATTGCTGATTAGAGAGCGGATTG
31[160]	34[160]	AGCGCGAACATTAAACGGAACGAGACAACAAC
0[175]	2[160]	GGTCGAGGTGCCGTAAGGACTCCATGATGGTG
15[160]	18[160]	GTCAAATCTTTATTTTCGCATAAAGGCGAGCTG
23[160]	26[160]	AACAGTTCGCAAAAAGAAGCAACACCGGAACAA
40[175]	37[175]	AGAGAAGGCCTCAGAAGATAGCAATCTTTCCA
4[175]	1[175]	ACCTGTCGCCTGGCCATCCTGTTACGTCAA
28[175]	25[175]	TAACAAAGAAGAAGTGCGAATAATATCATAA
32[175]	29[175]	GAAGTTTCACAAAGTATGCTCCATTCAAGAGT
8[175]	5[175]	CTGTTGGGACGGCCAGAGCTCGAAAACCTACA
24[175]	21[175]	AGGCTTTTAGAAAACGGAAGCAAAGTACCTTT
16[175]	13[175]	GAGAAGCCACCATCAAATTTTTGAAAAGCCCC
39[160]	41[175]	ACCGCCACATTAGGATTATTTCCGGAACCTATT
20[175]	17[175]	TAGAGCTTAGTTTGACTTTGGGGCCTAAATCG
12[175]	9[175]	ACGTTAATAATGTGAGTAATGGGATGGTGCCG
36[175]	33[175]	CAACTTCGTTTATCACGACAATGGGTAGCAA
38[191]	40[176]	CACCCTCAACATGAAAAGGCTGAGACTCCTCA
18[191]	23[191]	TTTAGCTACTTTTGATATTTTTGCCATAAATC
34[191]	39[191]	ATACCGATTAAATGAAATGGGATTCTCAGAAC
30[191]	35[191]	GTCGAAATGAGGCTTTAAGACTTTTCGAGGTG
26[191]	31[191]	ATCTACGTCAAGAACCATTACCCAATTTGTAT
22[191]	27[191]	CTGACTATTACCAGACAAACCAAATACCAGTC
1[176]	3[191]	GGGCGAAAAACCGTCTAAATCAAGTTGCAGCA
10[191]	15[191]	AACGGCGGGAAGATTGAATATTTATCAACCGT
14[191]	19[191]	GCCGGAGAAAAACATTGTAATACACATTTTCG
6[191]	11[191]	GGATCCCCGCAAAGCGCATTACAGGAACCCGTC
2[191]	7[191]	GCCCCAGCGTTGCGCTGCTTCCATTGCATGC

### 11.3. Sequences Used For Conjugates

Handle	Sequence 5' > 3'	Modification
Origami handle extension	TTTTTTCATACGACTCACTC	None
GALA anti-handle strand	GAGTGAGTCGTATGA	5' Peptide via SMCC linker
Origami fluorophore handle	TTTATCAGAGATCAGCATAACA	None
ssDNA fluorophore anti-handle	TGTATGCTGATCTCTGAT	5' Cy3 or AF647
Peptide competitor	GAGTGAGTCGTATGA	3' Cy3
Biotin anti-handle strand	GAGTGAGTCGTATGA	5' Biotin

## 11.4. DNA Origami Preparation

### ***DNA origami Folding***

The DNA origami structure was assembled using 7224 of the available 7249nt in the m13mp18 ssDNA scaffold, provided by Tilibit Nanosystems. Structure design was carried out using CaDNAo V2.0. DNA staple oligonucleotides (Appendix section 11.2) were prepared by solid phase synthesis by Integrated DNA Technologies, Leuven, Belgium) with desalting purification, 100uM. DNA origami was annealed in a one-pot reaction process containing 20nM final concentration scaffold m13mp18 ssDNA and 200uM staples (10x molar excess over scaffold), along with 12-16mM MgCl<sub>2</sub>, and 0.5x final concentration TAE buffer, in deionized water. 1-2mM Cy3 or AlexaFlour-647 5' tagged oligonucleotides were added to the reaction, final volume 100uL, for labeling of the structure (see section 11.3 for sequences). Solutions were heated to 90°C followed by cooling to 4°C over 40 hours using a BIO-RAD T100 Thermal Cycler (PCR). The cooling ramp used was from 60-25°C at 1h/C, and 25-10°C at 15 min/C.

### ***Purification by Polyethyleneglycol (PEG) pelleting***

PEG purification by spinning was carried out by adding a 2:1 volume of 15% (W/V) PEG (Mw 8000) solution containing 5mM Tris, 1mM EDTA and 505 mM NaCl - to folded DNA origami solutions. The solutions were briefly mixed by tube inversion followed by centrifugation at 16,000 g, at room temperature for 25 minutes (Eppendorf 5420, Hamburg, Germany). The supernatant was removed by gentle aspiration using p100 and p10 pipettes followed by gentle washing in DI H<sub>2</sub>O. Pellets were dissolved in the buffer of choice for individual experiments, TAE 0.5x with 0-14mM MgCl<sub>2</sub> or TAE 0.5x with 10mM NaCl, for 1-3 hours at RT or 30°C.

### ***Purification by Size Exclusion Chromatography (SEC)***

Purification of DNA origami by SEC was achieved using an AKTA purifier 10/100 fitted with a superdex 200 10/300 GL column (GE Healthcare), using a flowrate of 0.5-0.8 mL per minute at RT. Samples were brought to 30°C for several minutes prior to injection, to prevent aggregation of the DNA origami. Elution was

monitored using UV-vis absorption at 260 and 280nm using 14mM MgCl with 0.5x TAE buffer. Buffer solutions were degassed and filtered through 0.2 um cellulose membrane prior to SEC. Samples were subsequently concentrated by PEG pelleting as was required for downstream experiments, allowing for adjustment of buffer components.

### **11.5. Gel Electrophoresis Analysis**

Analysis of DNA origami assembly was carried out using 1-2% agarose gel electrophoresis in standard 1x TAE buffer, MgCl<sub>2</sub>, 12mM. Running conditions were 70V for 1-3 hours as was required for separate experiments detailed below. Unless otherwise stated, agarose running buffer contained 1x TAE, 12mM MgCl<sub>2</sub>. Running of the AGE was carried out in a fridge at 4<sup>0</sup>C or in an ice bath. 2-5uL of DNA was mixed with 5-10uL purple 6x SDS-free loading dye (New England Biolabs). A 1kb ladder was used as reference along with unfolded m13mp18 ssDNA. DNA bands were visualized with ethidium bromide and UV illumination. Fluorescence scanning of AlexaFlour-647 labelled DNA origami was carried out using a Typhoon FLA 7000 with 633nm laser line.

SUV binding assays were analyzed according to the above instructions using ethidium bromide. The method used for the SUV-binding assays are described in section 10.8.

### **11.6. AFM Analysis**

DNA origami nanostructures were imaged using tapping mode in liquid suspension, with multimode AFM nanoscope; Bruker AXS, Multimode 8, equipped with a type E scanner (Veeco Instruments, Santa Barbara, USA). The AFM was equipped with silicon tipped nitride cantilevers (Bruker AFM Probes, cat. no. MSNL-10). Agarose gel purified DNA origami was incubated on fresh mica at a final concentration of 1-2nM for 5 minutes prior to removal of excess solution and adding of resuspension buffer, 50-100uL MgCl<sub>2</sub>, 14mM, 0.5x TAE.

### **11.7. TEM Analysis**

Glow-discharge TEM grids (carbon film on 300 mesh copper grids; Agar Scientific, cat. No. AGS160-3H). were placed on a glass slide wrapped with a piece of freshly cleaved parafilm. The slide holding TEM grids were then loaded into a glow discharger and sealed before subjecting to vacuum (from -0.2pa to 0.6 or 0.8pa) by slowly opening the vacuum 'leak' knob. Glow discharging was then applied for 45s. Air pressure was restored after the glow discharge process.

For each sample, two droplets of fresh 2% uranyl formate staining solution (6uL each) were applied to a freshly unrolled parafilm. DNA origami was diluted to a concentration of 1 – 10nM in a 1X TAE solution containing  $MgCl_2^{2+}$ , 14mM and applied to glow-discharged TEM grids for approximately 10 seconds before carefully removing the solution by blotting with filter paper. TEM grids were then placed face-down on the first droplet of staining solution and immediately removed along with blotting of the solution onto filter paper. After removing excess liquid, the grid was submerged for 10 seconds in a second droplet of staining solution and followed by blotting again with filter paper to remove excess liquid. TEM grids were allowed to air-dry for at least 30 minutes before imaging. Images were produced using Gatan Microscopy suite V.3.0 and analysed using ImageJ, W. Rasband, NIH.

### **11.8. SUV Formation**

To analyse origami – GALA POC interaction and ability of GALA POC to mediate binding of origami to lipid membranes, POPC small unilamellar vesicles (SUVs) were generated using thin-film hydration method. POPC (Sigma Aldrich, UK) was dissolved in chloroform to 10mg/mL from which 300uL was taken and pipetted into an oven-dried 50mL round-bottom flask. The POPC solution was dried under vacuum using a rotary evaporator (Buchi R100) for 30 minutes to 1 hour. The dried POPC film was then re-suspended in 1X PBS and adjusted to either pH5 or 7, to a final concentration of 3mM. The solutions were sonicated for 30 minutes at room temperature, interceded by brief vortexing every 5-10 minutes. Solutions were then passed through an SUV extruder (Avanti Polar Lipids) with 0.2 um polycarbonate membrane filters (Avanti Polar Lipids) at least 25 times. SUVs were

used within 48 hour after preparation and were stored at 4°C between experiments.

Dynamic Light Scattering (DLS) was carried out to confirm vesicle sizes (Punk D 0037 Dynamic Light Scattering Analyser – Unchained Labs).

### **11.9. Vesicle Binding Assays**

POPC SUVs (approx. 200 nm diameter) were used for gel-shift binding assays to assess peptide-mediated binding of DNA origami. GALA POC (Alta Bioscience, Reddich, UK) was incubated with origami for 1 hour at RT, at a final concentration of 1uM. 2-5uL of DNA origami containing GALA POC was then incubated with 2-5uL of vesicle suspension solution and mixed with 5uL 6x SDS-free Loading dye (New England Biolabs), for loading into agarose gels. DNA origami with handles ('100H') or without handles ('0H') were normalized in concentration using UV-VIS absorption at 260nm, in DI H<sub>2</sub>O with or without MgCl<sub>2</sub>, 12mM, as is described in the results section 7.1. Agarose gels were supplemented with MgCl<sub>2</sub> or were MgCl<sub>2</sub> free (for the reduced non-specific binding assay). GALA POC concentration was confirmed with UV-VIS absorption at 260nm. Lyophilized aliquots of GALA POC were re-suspended in the required buffer and stored at -20°C for no more than 7-days between experiments.

### **11.10. Flow Cytometry Analysis on DNA Origami-GALA Interaction with HeLa Cells**

SEC pure AlexaFlour-647 tagged DNA origami was incubated with either GALA POC or GALA peptide for 1 hour at RT, using the designated molar ratio excess over DNA origami handle number (approximated by multiplication of the DNA concentration by the origami handle number. I.e., 10nM DNA origami \* 100 ssDNA handles = 10,000nM or 1uM equivalent handles). Origami-peptide samples were then diluted into FBS-free opti-MEM cell media (Gibco, UK) to achieve the desired concentrations and incubated with cells for 3 hours. Cells were grown to confluence at 37°C, 5% CO<sub>2</sub>, and seeded into 48-well plates at a density of 25,000 cells per well. Prior to sample loading, cells were washed thrice with 1x PBS and again washed thrice with PBS following aspiration of samples. Cells were then trypsinized with TrypLE Express Enzyme (Gibco) for 10-15 minutes at 37°C, followed by trypsin inactivation and resuspension with DMEM (Gibco). Cells were brought into solution by gentle pipetting at least 20 times, prior to transfer into a 96-well plate for flow cytometry analysis. Consistent gating based on cell size and granularity (forward and side scatter) was used to select viable single cells for analysis. Median fluorescence intensity was calculated for each sample by averaging after background subtraction.

### **11.11. Cell Microscopy Assays for Origami-GALA Binding and Uptake**

HeLa cells were prepared to confluence then seeded into 8-well ibidi chambers at a density of 25000 cells per well. Cells were grown overnight, at 37°C, 5% CO<sub>2</sub> prior to experiments. DNA origami samples were prepared in the same fashion as with flow cytometry assays with the exception that a higher final concentration of MgCl<sub>2</sub> (5mM) was used for the origami solution buffer. GALA POC or GALA peptide were incubated with origami at a final concentration of 8uM prior to sample dilution into cell media, which was subsequently supplemented with GALA POC or GALA to maintain the same concentration (8uM). Cells were washed thrice with 1x PBS prior to sample incubation for 3 hours at 37°C, 5% CO<sub>2</sub>. After 3 hours, samples were aspirated followed by incubation for 1 hour with LysoTracker Red DND-99 (Thermo Fischer). LysoTracker was prepared to a final concentration of

100nM in phenol containing DMEM + 10% FBS. LysoTracker containing solution was aspirated off prior to imaging. Cells were washed thrice with 1x PBS followed by re-incubation of cells into DMEM + 10% FBS. Images were then collected at 4 and 24-hours after sample incubation initiation, using an Olympus inverted confocal microscope with a 40x oil immersion objective lens. Laser lines 633 and 559 were used respectively for AlexaFluor-647 and LysoTracker excitation, with appropriate band-pass filters. The sequential image acquisition mode was used for image collection, to prevent cross talk between the fluorophore probes.

### **11.12. Electrophoresis analysis of GALA handle hybridization**

Gel electrophoresis analysis was used to assess duplex hybridization of the GALA POC DNA sequence to the DNA origami ssDNA handle. A titration was carried out as shown in figure 50, keeping the reaction volume fixed at 20uL and incubating the solutions for 1 hour at RT.  $MgCl_2$  was maintained at 2mM across the titration series. 10uL of each sample was taken and mixed with 5uL SDS-free 6x gel loading dye (New England Biolabs), then loaded into native PAGE (4-20% Mini-PROTEAN TGX Precast Gels, Bio Rad). The gel was pre-run at 240V for 30 minutes at 4°C, 1x TAE prior to sample loading. Gel running conditions were 140V for 45 minutes.

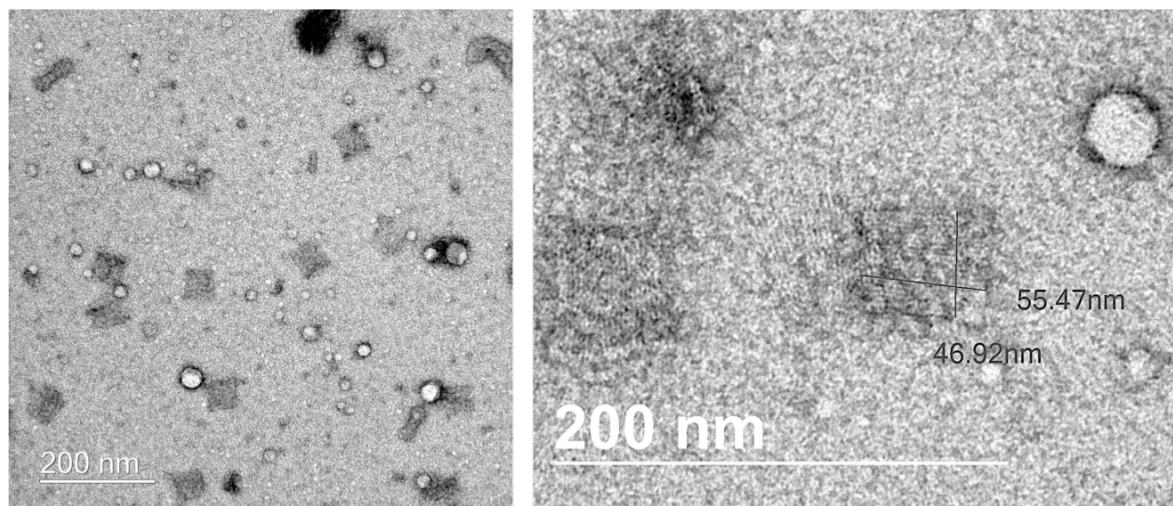
### **11.13. Biotin-Streptavidin binding Assay**

5' Biotin (IDT, Leuven, Belgium) was incubated with SEC pure DNA origami, 10nM, 10uL, at a 2:1 molar ratio over origami handles (final concentration, 2uM). Streptavidin (Invitrogen, UK) was then added to the origami – biotin mixture at a final concentration of 1uM, and left to incubate for 1 hour at RT. Samples were then mixed with 6X SDS-free loading dye (New England Biolabs) and analyzed by agarose gel (2%) electrophoresis, run at 70V for 3 hours. The agarose gel was removed from the electrophoresis tank and imaged three times, once per hour.

### 11.14. Cy3-oligonucleotide Binding Competition Assay

Cy3-tagged GALA competition strand (IDT, Leuven, Belgium) was incubated at a fixed equimolar ratio to DNA origami handles (final concentration 1 $\mu$ M), either before or after incubation of GALA POC (final concentration 1-20 $\mu$ M). Samples were left to incubate for 1 hour at RT, then mixed with 5 $\mu$ L SDS-free 6X gel loading dye (New England Biolabs) prior to loading into a 1.5% agarose gel, 0.5x TAE, 12mM MgCl<sub>2</sub>. Agarose gel analysis was carried out using fluorescence scanning with Cy3 excitation/emission settings (Typhoon FLA 7000).

## 12. Supporting information



**S1. TEM images of DNA origami scaffold.** Assembly of the rectangular DNA origami scaffold is confirmed using TEM Transmission electron microscope (Jeol, model no. JEM-2100 equipped with an Orius, model no. SC200 camera) - (see methods section 11.7, pg. 128).

## 13. Bibliography

- (1) Modi, S.; Bhatia, D.; Simmel, F. C.; Krishnan, Y. Structural DNA Nanotechnology: From Bases to Bricks, from Structure to Function. *J. Phys. Chem. Lett.* **2010**, *1* (13), 1994–2005. <https://doi.org/10.1021/jz1004957>.
- (2) Wang, W.; Arias, D. S.; Deserno, M.; Ren, X.; Taylor, R. E. Emerging Applications at the Interface of DNA Nanotechnology and Cellular Membranes: Perspectives from Biology, Engineering, and Physics. *APL Bioeng.* **2020**, *4* (4). <https://doi.org/10.1063/5.0027022>.
- (3) Deluca, M.; Shi, Z.; Castro, C. E.; Arya, G. Dynamic DNA Nanotechnology: Toward Functional Nanoscale Devices. *Nanoscale Horizons* **2020**, *5* (2), 182–201. <https://doi.org/10.1039/c9nh00529c>.
- (4) Tateishi-Karimata, H.; Sugimoto, N. Chemical Biology of Non-Canonical Structures of Nucleic Acids for Therapeutic Applications. *Chem. Commun.* **2020**, *56* (16), 2379–2390. <https://doi.org/10.1039/c9cc09771f>.
- (5) Seeman, N. C. DNA in a Material World. *Nature* **2003**, *421* (6921), 427–431. <https://doi.org/10.1038/nature01406>.
- (6) Aldaye, F. A.; Palmer, A. L.; Sleiman, H. F. Assembling Materials with DNA as the Guide. *Science (80- )*. **2008**, *321* (5897), 1795–1799. <https://doi.org/10.1126/science.1154533>.
- (7) Fu, T. J.; Seeman, N. C. DNA Double-Crossover Molecules. *Biochemistry* **1993**, *32* (13), 3211–3220. <https://doi.org/10.1021/bi00064a003>.
- (8) Li, X.; Wang, H.; Seeman, N. C. Direct Evidence for Holliday Junction Crossover Isomerization †. *Biochemistry* **1997**, *36* (14), 4240–4247. <https://doi.org/10.1021/bi9629586>.
- (9) Sa-Ardylen, P.; Vologodskii, A. V.; Seeman, N. C. The Flexibility of DNA Double Crossover Molecules. *Biophys. J.* **2003**, *84* (6), 3829–3837. [https://doi.org/10.1016/S0006-3495\(03\)75110-8](https://doi.org/10.1016/S0006-3495(03)75110-8).
- (10) Shih, W. M.; Quispe, J. D.; Joyce, G. F. A 1.7-Kilobase Single-Stranded DNA That Folds into a Nanoscale Octahedron. *Nature* **2004**, *427* (6975), 618–621. <https://doi.org/10.1038/nature02307>.
- (11) Dietz, H.; Douglas, S. M.; Shih, W. M. Folding DNA into Twisted and Curved Nanoscale Shapes. *Science (80- )*. **2009**, *325* (5941), 725–730. <https://doi.org/10.1126/science.1174251>.
- (12) Douglas, S. M.; Dietz, H.; Liedl, T.; Hogberg, B.; Shih, W. M. Self-Assembly of DNA into Nanoscale Three-Dimensional Shapes. *Nature* **2009**, *459* (7245), 414–418. <https://doi.org/10.1038/nature08016>. Self-assembly.
- (13) Casini, A.; Storch, M.; Baldwin, G. S.; Ellis, T. Bricks and Blueprints: Methods and Standards for DNA Assembly. *Nat. Rev. Mol. Cell Biol.* **2015**, *16* (9), 568–576. <https://doi.org/10.1038/nrm4014>.
- (14) Wang, W.; Chen, S.; An, B.; Huang, K.; Bai, T.; Xu, M.; Bellot, G.; Ke, Y.; Xiang, Y.; Wei, B. Complex Wireframe DNA Nanostructures from Simple Building Blocks. *Nat. Commun.* **2019**, *10* (1), 1–8. <https://doi.org/10.1038/s41467-019-08647-7>.
- (15) Fu, D.; Reif, J. 3d DNA Nanostructures: The Nanoscale Architect. *Appl. Sci.* **2021**, *11* (6). <https://doi.org/10.3390/app11062624>.
- (16) Green, L. N.; Amodio, A.; Subramanian, H. K. K.; Ricci, F.; Franco, E. PH-Driven Reversible Self-Assembly of Micron-Scale DNA Scaffolds. *Nano Lett.* **2017**, *17* (12), 7283–7288. <https://doi.org/10.1021/acs.nanolett.7b02787>.
- (17) Kekic, T.; Barisic, I. In Silico Modelling of DNA Nanostructures. *Comput. Struct. Biotechnol. J.* **2020**, *18*, 1191–1201. <https://doi.org/10.1016/j.csbj.2020.05.016>.
- (18) Chen, Z.; Liu, Y.; Xin, C.; Zhao, J.; Liu, S. A Cascade Autocatalytic Strand Displacement Amplification and Hybridization Chain Reaction Event for Label-Free and Ultrasensitive Electrochemical Nucleic Acid

- Biosensing. *Biosens. Bioelectron.* **2018**, *113* (April), 1–8. <https://doi.org/10.1016/j.bios.2018.04.046>.
- (19) Huang, Y.; Nguyen, M. K.; Natarajan, A. K.; Nguyen, V. H.; Kuzyk, A. A DNA Origami-Based Chiral Plasmonic Sensing Device. *ACS Appl. Mater. Interfaces* **2018**, *10* (51), 44221–44225. <https://doi.org/10.1021/acsami.8b19153>.
- (20) Woods, D.; Doty, D.; Myhrvold, C.; Hui, J.; Zhou, F.; Yin, P.; Winfree, E. Diverse and Robust Molecular Algorithms Using Reprogrammable DNA Self-Assembly. *Nature* **2019**, *567* (7748), 366–372. <https://doi.org/10.1038/s41586-019-1014-9>.
- (21) Zhou, C.; Duan, X.; Liu, N. A Plasmonic Nanorod That Walks on DNA Origami. *Nat. Commun.* **2015**, *6*. <https://doi.org/10.1038/ncomms9102>.
- (22) Wager, M. G. T. and J. F. S. Tug of War in Motor Protein Ensembles Revealed with a Programmable DNA Origami Scaffold. *Bone* **2011**, *23* (1), 1–7. <https://doi.org/10.1126/science.1226734>.Tug.
- (23) Funke, J. J.; Ketterer, P.; Lieleg, C.; Schunter, S.; Korber, P.; Dietz, H. Uncovering the Forces between Nucleosomes Using DNA Origami. *Sci. Adv.* **2016**, *2* (11). <https://doi.org/10.1126/sciadv.1600974>.
- (24) Sun, W. DNA Nanotechnology: DNA Robots That Sort Cargoes. *Nat. Nanotechnol.* **2017**, *12* (12), 1120. <https://doi.org/10.1038/nnano.2017.236>.
- (25) List, J.; Falgenhauer, E.; Kopperger, E.; Pardatscher, G.; Simmel, F. C. Long-Range Movement of Large Mechanically Interlocked DNA Nanostructures. *Nat. Commun.* **2016**, *7*, 1–7. <https://doi.org/10.1038/ncomms12414>.
- (26) Lauback, S.; Mattioli, K. R.; Marras, A. E.; Armstrong, M.; Rudibaugh, T. P.; Sooryakumar, R.; Castro, C. E. Real-Time Magnetic Actuation of DNA Nanodevices via Modular Integration with Stiff Micro-Levers. *Nat. Commun.* **2018**, *9* (1). <https://doi.org/10.1038/s41467-018-03601-5>.
- (27) Chi, Q.; Yang, Z.; Xu, K.; Wang, C.; Liang, H. DNA Nanostructure as an Efficient Drug Delivery Platform for Immunotherapy. *Front. Pharmacol.* **2020**, *10* (January), 1–17. <https://doi.org/10.3389/fphar.2019.01585>.
- (28) Huang, Y.; Huang, W.; Chan, L.; Zhou, B.; Chen, T. A Multifunctional DNA Origami as Carrier of Metal Complexes to Achieve Enhanced Tumoral Delivery and Nullified Systemic Toxicity. *Biomaterials* **2016**, *103*, 183–196. <https://doi.org/10.1016/j.biomaterials.2016.06.053>.
- (29) Gerngross, M. D.; Carstensen, J.; Adelung, R. Nanoscale Horizons. *Nanoscale Horizons* **2016**, No. 2.
- (30) Rothmund, P. W. K. Folding DNA to Create Nanoscale Shapes and Patterns. *Nature* **2006**, *440* (7082), 297–302. <https://doi.org/10.1038/nature04586>.
- (31) Svozil, D.; Kalina, J.; Omelka, M.; Schneider, B. DNA Conformations and Their Sequence Preferences. *Nucleic Acids Res.* **2008**, *36* (11), 3690–3706. <https://doi.org/10.1093/nar/gkn260>.
- (32) Tan, Z. J.; Chen, S. J. Nucleic Acid Helix Stability: Effects of Salt Concentration, Cation Valence and Size, and Chain Length. *Biophys. J.* **2006**, *90* (4), 1175–1190. <https://doi.org/10.1529/biophysj.105.070904>.
- (33) Castro, C. E.; Kilchherr, F.; Kim, D. N.; Shiao, E. L.; Wauer, T.; Wortmann, P.; Bathe, M.; Dietz, H. A Primer to Scaffolded DNA Origami. *Nat. Methods* **2011**, *8* (3), 221–229. <https://doi.org/10.1038/nmeth.1570>.
- (34) Marras, A. E.; Zhou, L.; Koliopoulos, V.; Su, H. J.; Castro, C. E. Directing Folding Pathways for Multi-Component DNA Origami Nanostructures with Complex Topology. *New J. Phys.* **2016**, *18* (5). <https://doi.org/10.1088/1367-2630/18/5/055005>.
- (35) Sobczak, J. P. J.; Martin, T. G.; Gerling, T.; Dietz, H. Rapid Folding of DNA into Nanoscale Shapes at Constant Temperature. *Science (80- )*. **2012**, *338* (6113), 1458–1461. <https://doi.org/10.1126/science.1229919>.
- (36) Kopielski, A.; Schneider, A.; Csáki, A.; Fritzsche, W. Isothermal DNA Origami Folding: Avoiding Denaturing Conditions for One-Pot, Hybrid-Component Annealing. *Nanoscale* **2015**, *7* (5), 2102–2106.

- <https://doi.org/10.1039/c4nr04176c>.
- (37) Song, J.; Arbona, J. M.; Zhang, Z.; Liu, L.; Xie, E.; Elezgaray, J.; Aime, J. P.; Gothelf, K. V.; Besenbacher, F.; Dong, M. Direct Visualization of Transient Thermal Response of a DNA Origami. *J. Am. Chem. Soc.* **2012**, *134* (24), 9844–9847. <https://doi.org/10.1021/ja3017939>.
- (38) Schneider, F.; Möritz, N.; Dietz, H. The Sequence of Events during Folding of a DNA Origami. *Sci. Adv.* **2019**, *5* (5), 1–11. <https://doi.org/10.1126/sciadv.aaw1412>.
- (39) Hayden, M. J.; Nguyen, T. M.; Waterman, A.; Chalmers, K. J. Multiplex-Ready PCR: A New Method for Multiplexed SSR and SNP Genotyping. *BMC Genomics* **2008**, *9*, 1–12. <https://doi.org/10.1186/1471-2164-9-80>.
- (40) Schnitzbauer, J.; Strauss, M. T.; Schlichthaerle, T.; Schueder, F.; Jungmann, R. Super-Resolution Microscopy with DNA-PAINT. *Nat. Protoc.* **2017**, *12* (6), 1198–1228. <https://doi.org/10.1038/nprot.2017.024>.
- (41) Zwirgmaier, K. Fluorescence in Situ Hybridisation (FISH) - The next Generation. *FEMS Microbiol. Lett.* **2005**, *246* (2), 151–158. <https://doi.org/10.1016/j.femsle.2005.04.015>.
- (42) Hao, M.; Qiao, J.; Qi, H. Current and Emerging Methods for the Synthesis of Single-stranded DNA. *Genes (Basel)*. **2020**, *11* (2). <https://doi.org/10.3390/genes11020116>.
- (43) Kosuri, S.; Church, G. M. Large-Scale de Novo DNA Synthesis: Technologies and Applications. *Nat. Methods* **2014**, *11* (5), 499–507. <https://doi.org/10.1038/nmeth.2918>.
- (44) Marchi, A. N.; Saaem, I.; Tian, J.; Labean, T. H. One-Pot Assembly of a Hetero-Dimeric DNA Origami from Chip-Derived Staples and Double-Stranded Scaffold. *ACS Nano* **2013**, *7* (2), 903–910. <https://doi.org/10.1021/nn302322j>.
- (45) Jonathan Posner and Bradley S. Peterson, J. A. R. Enzymatic Production of Monoclonal Stoichiometric SingleStranded DNA Oligonucleotides. *Nat. Methods* **2008**, *23* (1), 1–7. <https://doi.org/10.1038/nmeth.2503>.Enzymatic.
- (46) Svensen, N.; Díaz-Mochón, J. J.; Bradley, M. Microarray Generation of Thousand-Member Oligonucleotide Libraries. *PLoS ONE* **2011**, *6* (9). <https://doi.org/10.1371/journal.pone.0024906>.
- (47) Agbavwe, C.; Kim, C.; Hong, D. G.; Heinrich, K.; Wang, T.; Somoza, M. M. Efficiency, Error and Yield in Light-Directed Maskless Synthesis of DNA Microarrays. *J. Nanobiotechnology* **2011**, *9* (57), 1–17. <https://doi.org/10.1186/1477-3155-9-57>.
- (48) Egeland, R. D.; Southern, E. M. Electrochemically Directed Synthesis of Oligonucleotides for DNA Microarray Fabrication. *Nucleic Acids Research*. Nucleic Acids Research 2005, pp 1–7. <https://doi.org/10.1093/nar/gni117>.
- (49) Hadi, T.; Nozzi, N.; Melby, J. O.; Gao, W.; Fuerst, D. E.; Kvam, E. Rolling Circle Amplification of Synthetic DNA Accelerates Biocatalytic Determination of Enzyme Activity Relative to Conventional Methods. *Sci. Rep.* **2020**, *10* (1), 1–8. <https://doi.org/10.1038/s41598-020-67307-9>.
- (50) Ali, M. M.; Li, F.; Zhang, Z.; Zhang, K.; Kang, D. K.; Ankrum, J. A.; Le, X. C.; Zhao, W. Rolling Circle Amplification: A Versatile Tool for Chemical Biology, Materials Science and Medicine. *Chem. Soc. Rev.* **2014**, *43* (10), 3324–3341. <https://doi.org/10.1039/c3cs60439j>.
- (51) Hughes, R. A.; Ellington, A. D. Synthetic DNA Synthesis and Assembly: Putting the Synthetic in Synthetic Biology. *Cold Spring Harb. Perspect. Biol.* **2017**, *9* (1). <https://doi.org/10.1101/cshperspect.a023812>.
- (52) Rothmund, P. W. K. Design of DNA Origami. *IEEE/ACM Int. Conf. Comput. Des. Dig. Tech. Pap. ICCAD* **2005**, *2005*, 471–478. <https://doi.org/10.1109/ICCAD.2005.1560114>.
- (53) Tapio, K.; Bald, I. The Potential of DNA Origami to Build Multifunctional Materials. *Multifunct. Mater.* **2020**, *3* (3). <https://doi.org/10.1088/2399-7532/ab80d5>.

- (54) Zhao, W.; Ali, M. M.; Brook, M. A.; Li, Y. Rolling Circle Amplification: Applications in Nanotechnology and Biodetection with Functional Nucleic Acids. *Angew. Chemie - Int. Ed.* **2008**, *47* (34), 6330–6337. <https://doi.org/10.1002/anie.200705982>.
- (55) Hong, C. A.; Jang, B.; Jeong, E. H.; Jeong, H.; Lee, H. Self-Assembled DNA Nanostructures Prepared by Rolling Circle Amplification for the Delivery of siRNA Conjugates. *Chem. Commun.* **2014**, *50* (86), 13049–13051. <https://doi.org/10.1039/c4cc03834g>.
- (56) Liu, H.; Li, L.; Duan, L.; Wang, X.; Xie, Y.; Tong, L.; Wang, Q.; Tang, B. High Specific and Ultrasensitive Isothermal Detection of MicroRNA by Padlock Probe-Based Exponential Rolling Circle Amplification. *Anal. Chem.* **2013**, *85* (16), 7941–7947. <https://doi.org/10.1021/ac401715k>.
- (57) Ouyang, X.; Li, J.; Liu, H.; Zhao, B.; Yan, J.; Ma, Y.; Xiao, S.; Song, S.; Huang, Q.; Chao, J.; et al. Rolling Circle Amplification-Based DNA Origami Nanostructures for Intracellular Delivery of Immunostimulatory Drugs. *Small* **2013**, *9* (18), 3082–3087. <https://doi.org/10.1002/sml.201300458>.
- (58) Lin, C.; Rinker, S.; Wang, X.; Liu, Y.; Seeman, N. C.; Yan, H. In Vivo Cloning of Artificial DNA Nanostructures. *Proc. Natl. Acad. Sci. U. S. A.* **2008**, *105* (46), 17626–17631. <https://doi.org/10.1073/pnas.0805416105>.
- (59) Lin, C.; Wang, X.; Liu, Y.; Seeman, N. C.; Yan, H. Rolling Circle Enzymatic Replication of a Complex Multi-Crossover DNA Nanostructure. *J. Am. Chem. Soc.* **2007**, *129* (46), 14475–14481. <https://doi.org/10.1021/ja0760980>.
- (60) Sung, Y. K.; Kim, S. W. Recent Advances in the Development of Gene Delivery Systems. *Biomater. Res.* **2019**, *23* (1), 1–7. <https://doi.org/10.1186/s40824-019-0156-z>.
- (61) Li, S. D.; Huang, L. Gene Therapy Progress and Prospects: Non-Viral Gene Therapy by Systemic Delivery. *Gene Ther.* **2006**, *13* (18), 1313–1319. <https://doi.org/10.1038/sj.gt.3302838>.
- (62) Hu, Q.; Li, H.; Wang, L.; Gu, H.; Fan, C. DNA Nanotechnology-Enabled Drug Delivery System. *Chem. Rev.* **2019**, *119* (32), 6459–6506.
- (63) Kalia J.; Raines, R. Advances in Bioconjugation. *Curr Org Chem.* **2012**, *29* (2), 997–1003.
- (64) Cho. Bioconjugated Oligonucleotides: Recent Developments and Therapeutic Applications. *Bioconjug. Chem.* **2019**, *30* (2), 366–388. <https://doi.org/10.1021/acs.bioconjchem.8b00761>. Bioconjugated.
- (65) Xu, F.; Xia, Q.; Wang, P. Rationally Designed DNA Nanostructures for Drug Delivery. *Front. Chem.* **2020**, *8* (September), 1–13. <https://doi.org/10.3389/fchem.2020.00751>.
- (66) Chandrasekaran, A. R. Nuclease Resistance of DNA Nanostructures. *Nat. Rev. Chem.* **2021**, *5* (4), 225–239. <https://doi.org/10.1038/s41570-021-00251-y>.
- (67) Kim, H.; Surwade, S. P.; Powell, A.; O'Donnell, C.; Liu, H. Stability of DNA Origami Nanostructure under Diverse Chemical Environments. *Chem. Mater.* **2014**, *26* (18), 5265–5273. <https://doi.org/10.1021/cm5019663>.
- (68) Ochoa, S.; Milam, V. T. Modified Nucleic Acids: Expanding the Capabilities of Functional Oligonucleotides. *Molecules* **2020**, *25* (20), 1–23. <https://doi.org/10.3390/molecules25204659>.
- (69) Stephanopoulos, N. Strategies for Stabilizing DNA Nanostructures to Biological Conditions. *ChemBioChem* **2019**, *20* (17), 2191–2197. <https://doi.org/10.1002/cbic.201900075>.
- (70) Ramakrishnan, S.; Ijäs, H.; Linko, V.; Keller, A. Structural Stability of DNA Origami Nanostructures under Application-Specific Conditions. *Comput. Struct. Biotechnol. J.* **2018**, *16*, 342–349. <https://doi.org/10.1016/j.csbj.2018.09.002>.
- (71) Zagorovsky, K.; Chou, L. Y. T.; Chan, W. C. W. Controlling DNA-Nanoparticle Serum Interactions. *Proc. Natl. Acad. Sci. U. S. A.* **2016**, *113* (48), 13600–13605. <https://doi.org/10.1073/pnas.1610028113>.
- (72) Wahlestedt, C.; Salmi, P.; Good, L.; Kela, J.; Johnsson, T.; Ho, T.; Broberger, C.; Porreca, F.; Lai, J.; Ren, K.; et al. Potent and Nontoxic Antisense Oligonucleotides. *Proc. Natl. Acad. Sci. U. S. A.* **2000**, *97*

- (10), 5633–5638.
- (73) Keum, J.-W.; Bermudez, H. Enhanced Resistance of DNA Nanostructures to Enzymatic Digestion. *Chem. Commun.* **2009**, No. 45, 7036. <https://doi.org/10.1039/b917661f>.
- (74) Conway, J. W.; McLaughlin, C. K.; Castor, K. J.; Sleiman, H. DNA Nanostructure Serum Stability: Greater than the Sum of Its Parts. *Chem. Commun.* **2013**, *49* (12), 1172. <https://doi.org/10.1039/c2cc37556g>.
- (75) Conway, J. W.; Mc Laughlin, C. K.; Castor, K. J.; Sleiman, H. DNA Nanostructure Serum Stability: Greater than the Sum of Its Parts. *Chem. Commun.* **2013**, *49* (12), 1172–1174. <https://doi.org/10.1039/c2cc37556g>.
- (76) Goltry, S.; Hallstrom, N.; Clark, T.; Kuang, W.; Lee, J.; Jorczyk, C.; Knowlton, W. B.; Yurke, B.; Hughes, W. L.; Graunard, E. DNA Topology Influences Molecular Machine Lifetime in Human Serum. *Nanoscale* **2015**, *7* (23), 10382–10390. <https://doi.org/10.1039/c5nr02283e>.
- (77) Hahn, J.; Wickham, S. F. J.; Shih, W. M.; Perrault, S. D. Addressing the Instability of DNA Nanostructures in Tissue Culture. *ACS Nano* **2014**, *8* (9), 8765–8775. <https://doi.org/10.1021/nn503513p>.
- (78) Chandrasekaran, A. R.; Vilcapoma, J.; Dey, P.; Wong-Deyrup, S. W.; Dey, B. K.; Halvorsen, K. Exceptional Nuclease Resistance of Paranemic Crossover (PX) DNA and Crossover-Dependent Biostability of DNA Motifs. *J. Am. Chem. Soc.* **2020**, *142* (14), 6814–6821. <https://doi.org/10.1021/jacs.0c02211>.
- (79) Koohy, H.; Down, T. A.; Hubbard, T. J. Chromatin Accessibility Data Sets Show Bias Due to Sequence Specificity of the DNase I Enzyme. *PLoS One* **2013**, *8* (7), 1–9. <https://doi.org/10.1371/journal.pone.0069853>.
- (80) Burns, J.; Howorka, S.; Burns, J. R.; Howorka, S. Structural and Functional Stability of DNA Nanopores in Biological Media. *Nanomaterials* **2019**, *9* (4), 490. <https://doi.org/10.3390/nano9040490>.
- (81) El-Sagheer, A. H.; Brown, T. Combined Nucleobase and Backbone Modifications Enhance DNA Duplex Stability and Preserve Biocompatibility. *Chem. Sci.* **2014**, *5* (1), 253–259. <https://doi.org/10.1039/c3sc51753e>.
- (82) Rinaldi, C.; Wood, M. J. A. Antisense Oligonucleotides: The next Frontier for Treatment of Neurological Disorders. *Nat. Rev. Neurol.* **2018**, *14* (1), 9–22. <https://doi.org/10.1038/nrneuro.2017.148>.
- (83) Wilner, O.; Willner, I. Functionalized DNA Nanostructures. *Chem. Rev.* **2012**, *112* (4), 2528–2556.
- (84) Börjesson, K.; Tumpene, J.; Ljungdahl, T.; Marcus Wilhelmsson, L.; Nordén, B.; Brown, T.; Mårtensson, J.; Albinsson, B. Membrane-Anchored DNA Assembly for Energy and Electron Transfer. *J. Am. Chem. Soc.* **2009**, *131* (8), 2831–2839. <https://doi.org/10.1021/ja8038294>.
- (85) Johnson-Buck, A.; Jiang, S.; Yan, H.; Walter, N. G. DNA-Cholesterol Barges as Programmable Membrane-Exploring Agents. *ACS Nano* **2014**, *8* (6), 5641–5649. <https://doi.org/10.1021/nn500108k>.
- (86) Xiao, F.; Chen, Z.; Wei, Z.; Tian, L. Hydrophobic Interaction: A Promising Driving Force for the Biomedical Applications of Nucleic Acids. *Adv. Sci.* **2020**, *7* (16), 1–34. <https://doi.org/10.1002/advs.202001048>.
- (87) Ohmann, A.; Göpfrich, K.; Joshi, H.; Thompson, R. F.; Sobota, D.; Ranson, N. A.; Aksimentiev, A.; Keyser, U. F. Controlling Aggregation of Cholesterol-Modified DNA Nanostructures. *Nucleic Acids Res.* **2019**, *47* (21), 11441–11451. <https://doi.org/10.1093/nar/gkz914>.
- (88) Darley, A. E.; Singh, J. K. D.; Ridone, P.; Abbas, A.; Wickham, S. F. J. Binding of DNA Origami to Lipids: Maximising Yield and Switching via Strand-Displacement. *bioRxiv* **2021**, 1–29.
- (89) Darley, E.; Singh, J. K. D.; Surace, N. A.; Wickham, S. F. J.; Baker, M. A. B. The Fusion of Lipid and DNA Nanotechnology. *Genes (Basel)*. **2019**, *10* (12). <https://doi.org/10.3390/genes10121001>.
- (90) Loew, M.; Springer, R.; Scolari, S.; Altenbrunn, F.; Seitz, O.; Liebscher, J.; Huster, D.; Herrmann, A.; Arbuzova, A. Lipid Domain Specific Recruitment of Lipophilic Nucleic Acids: A Key for Switchable Functionalization of Membranes. *J. Am. Chem. Soc.* **2010**, *132* (45), 16066–16072.

- <https://doi.org/10.1021/ja105714r>.
- (91) Burns, J. R.; Göpfrich, K.; Wood, J. W.; Thacker, V. V.; Stulz, E.; Keyser, U. F.; Howorka, S. Lipid-Bilayer Spanning DNA Nanopores with a Bifunctional Porphyrin Anchor. *Angew. Chemie - Int. Ed.* **2013**, *52* (46), 12069–12072. <https://doi.org/10.1002/anie.201305765>.
  - (92) Arulkumaran, N.; Lanphere, C.; Gaupp, C.; Burns, J. R.; Singer, M.; Howorka, S. DNA Nanodevices with Selective Immune Cell Interaction and Function. *ACS Nano* **2021**, *15* (3), 4394–4404. <https://doi.org/10.1021/acsnano.0c07915>.
  - (93) Heck, C.; Torchinsky, D.; Nifker, G.; Gularek, F.; Michael, Y.; Weinhold, E.; Ebenstein, Y. Label as You Fold- Methyltransferase-Assistedfunctionalization of DNA Nanostructures. *Nanoscale* **2020**, *3* (39), 20049–20548.
  - (94) Franquelim, H. G.; Khmelinskaia, A.; Sobczak, J. P.; Dietz, H.; Schwille, P. Membrane Sculpting by Curved DNA Origami Scaffolds. *Nat. Commun.* **2018**, *9* (1), 1–10. <https://doi.org/10.1038/s41467-018-03198-9>.
  - (95) Yang, Y.; Wang, J.; Shigematsu, H.; Xu, W.; Shih, W. M.; Rothman, J. E.; Lin, C. Self-Assembly of Size-Controlled Liposomes on DNA Nanotemplates. *Nat. Chem.* **2016**, *8* (5), 476–483. <https://doi.org/10.1038/nchem.2472>.
  - (96) Grome, M.; Zhang, Z.; Pincet, F.; Lin, C. Vesicle Tubulation with Self-Assembling DNA Nanosprings. *Angew. Chem. Int. Ed. Engl.* **2019**, *57* (19), 5330–5334. <https://doi.org/10.1002/anie.201800141>.
  - (97) Howorka, S. Building Membrane Nanopores. *Nat. Nanotechnol.* **2017**, *12* (7), 619–630. <https://doi.org/10.1038/nnano.2017.99>.
  - (98) Villaverde, G.; Baeza, A. Targeting Strategies for Improving the Efficacy of Nanomedicine in Oncology. *Beilstein J. Nanotechnol.* **2019**, *10* (1), 168–181. <https://doi.org/10.3762/bjnano.10.16>.
  - (99) D'antonio, C.; Passaro, A.; Del Signore, E.; Marinis, F.; Gori, B.; Migliorino, M. R.; Ricciardi, S.; Fulvi, A. Bone and Brain Metastasis in Lung Cancer: Recent Advances in Therapeutic Strategies. *Ther. Adv. Med. Oncol.* **2014**, *6* (3), 101–114. <https://doi.org/10.1177/1758834014521110>.
  - (100) Patra, J. K.; Das, G.; Fraceto, L. F.; Campos, E. V. R.; Rodriguez-Torres, M. D. P.; Acosta-Torres, L. S.; Diaz-Torres, L. A.; Grillo, R.; Swamy, M. K.; Sharma, S.; et al. Nano Based Drug Delivery Systems: Recent Developments and Future Prospects. *J. Nanobiotechnology* **2018**, *16* (1), 1–33. <https://doi.org/10.1186/s12951-018-0392-8>.
  - (101) Mitchell, M. J.; Billingsley, M. M.; Haley, R. M.; Wechsler, M. E.; Peppas, N. A.; Langer, R. Engineering Precision Nanoparticles for Drug Delivery. *Nat. Rev. Drug Discov.* **2021**, *20* (2), 101–124. <https://doi.org/10.1038/s41573-020-0090-8>.
  - (102) Choi, H. S.; Liu, W.; Misra, P.; Tanaka, E.; Zimmer, J. P.; Iltis Ipe, B.; Bawendi, M. G.; Frangioni, J. V. Renal Clearance of Nanoparticles. *Nat. Biotechnol.* **2009**, *25* (10), 1165–1170. <https://doi.org/10.1038/nbt1340>.
  - (103) Jiang, D.; Ge, Z.; Im, H.; England, C. G.; Ni, D.; Hou, J.; Zhang, L.; Kutyreff, C. J.; Yan, Y.; Liu, Y.; et al. DNA Origami Nanostructures Can Exhibit Preferential Renal Uptake and Alleviate Acute Kidney Injury. *Nat. Biomed. Eng.* **2019**, *2* (11), 865–877. <https://doi.org/10.1038/s41551-018-0317-8>.
  - (104) Tikhomirov, G.; Petersen, P.; Qian, L. Fractal Assembly of Micrometre-Scale DNA Origami Arrays with Arbitrary Patterns. *Nature* **2017**, *552* (7683), 67–71. <https://doi.org/10.1038/nature24655>.
  - (105) Wagenbauer, K. F.; Sigl, C.; Dietz, H. Gigadalton-Scale Shape-Programmable DNA Assemblies. *Nature* **2017**, *552* (7683), 78–83. <https://doi.org/10.1038/nature24651>.
  - (106) Chenthamara, D.; Subramaniam, S.; Ramakrishnan, S. G.; Krishnaswamy, S.; Essa, M. M.; Lin, F. H.; Qoronfleh, M. W. Therapeutic Efficacy of Nanoparticles and Routes of Administration. *Biomater. Res.* **2019**, *23* (1), 1–29. <https://doi.org/10.1186/s40824-019-0166-x>.

- (107) Baimanov, D.; Cai, R.; Chen, C. Understanding the Chemical Nature of Nanoparticle-Protein Interactions. *Bioconjug. Chem.* **2019**, *30* (7), 1923–1937. <https://doi.org/10.1021/acs.bioconjchem.9b00348>.
- (108) Lundqvist, M.; Augustsson, C.; Lilja, M.; Lundkvist, K.; Dahlbäck, B.; Linse, S.; Cedervall, T. The Nanoparticle Protein Corona Formed in Human Blood or Human Blood Fractions. *PLoS One* **2017**, *12* (4), 1–15. <https://doi.org/10.1371/journal.pone.0175871>.
- (109) Arami, H.; Khandhar, A.; Liggitt, D.; Krishnan, K. In Vivo Delivery, Pharmacokinetics, Biodistribution and Toxicity of Iron Oxide Nanoparticles. *Chem. Soc. Rev.* **2015**, *44* (23), 8576–8607. <https://doi.org/10.1039/c5cs00541h>.
- (110) Park, S. J. Protein–Nanoparticle Interaction: Corona Formation and Conformational Changes in Proteins on Nanoparticles. *Int. J. Nanomedicine* **2020**, *15*, 5783–5802. <https://doi.org/10.2147/IJN.S254808>.
- (111) Michelle Longmire, Peter L. Choyke, M.D., and Hisataka Kobayashi, M.D., P. . Clearance Properties of Nano-Sized Particles and Molecules as Imagin Agents: Consideration and Caveats. *Nanomedicine (london)* **2008**, *3* (5), 703–717. <https://doi.org/10.2217/17435889.3.5.703>.Clearance.
- (112) Ehrenberg, M. S.; Friedman, A. E.; Finkelstein, J. N.; Oberdörster, G.; McGrath, J. L. The Influence of Protein Adsorption on Nanoparticle Association with Cultured Endothelial Cells. *Biomaterials* **2009**, *30* (4), 603–610. <https://doi.org/10.1016/j.biomaterials.2008.09.050>.
- (113) Whitehouse, W. L.; Noble, J. E.; Ryadnov, M. G.; Howorka, S. Cholesterol Anchors Enable Efficient Binding and Intracellular Uptake of DNA Nanostructures. *Bioconjug. Chem.* **2019**, *acs.bioconjchem.9b00036*. <https://doi.org/10.1021/acs.bioconjchem.9b00036>.
- (114) Upadhyay, R. K. Drug Delivery Systems, CNS Protection, and the Blood Brain Barrier. *Biomed Res. Int.* **2014**, *2014*. <https://doi.org/10.1155/2014/869269>.
- (115) Veiseh, O.; Sun, C.; Fang, C.; Bhattarai, N.; Gunn, J.; Du, K.; Pullar, B.; Lee, D.; Ellenbogen, R. G. Specific Targeting of Brain Tumors with an Optical/Magnetic Resonance Imaging Nanoprobe across the Blood-Brain Barrier. *Cancer Res.* **2009**, *69* (15), 6200–6207. <https://doi.org/10.1158/0008-5472.CAN-09-1157>.Specific.
- (116) Ceña, V.; Játiva, P. Nanoparticle Crossing of Blood-Brain Barrier: A Road to New Therapeutic Approaches to Central Nervous System Diseases. *Nanomedicine* **2018**, *13* (13), 1513–1516. <https://doi.org/10.2217/nnm-2018-0139>.
- (117) Xiao, F.; Lin, L.; Chao, Z.; Shao, C.; Chen, Z.; Wei, Z.; Lu, J.; Huang, Y.; Li, L.; Liu, Q.; et al. Organic Spherical Nucleic Acids for the Transport of a NIR-II-Emitting Dye Across the Blood–Brain Barrier. *Angew. Chemie* **2020**, *132* (24), 9789–9797. <https://doi.org/10.1002/ange.202002312>.
- (118) Chan, T. G.; Morse, S. V.; Copping, M. J.; Choi, J. J.; Vilar, R. Targeted Delivery of DNA-Au Nanoparticles across the Blood–Brain Barrier Using Focused Ultrasound. *ChemMedChem* **2018**, *13* (13), 1311–1314. <https://doi.org/10.1002/cmdc.201800262>.
- (119) Tian, T.; Li, J.; Xie, C.; Sun, Y.; Lei, H.; Liu, X.; Xia, J.; Shi, J.; Wang, L.; Lu, W.; et al. Targeted Imaging of Brain Tumors with a Framework Nucleic Acid Probe. *ACS Appl. Mater. Interfaces* **2018**, *10* (4), 3414–3420. <https://doi.org/10.1021/acsami.7b17927>.
- (120) Zhang, Y.; Ma, W.; Zhu, Y.; Shi, S.; Li, Q.; Mao, C.; Zhao, D.; Zhan, Y.; Shi, J.; Li, W.; et al. Inhibiting Methicillin-Resistant Staphylococcus Aureus by Tetrahedral DNA Nanostructure-Enabled Antisense Peptide Nucleic Acid Delivery. *Nano Lett.* **2018**, *18* (9), 5652–5659. <https://doi.org/10.1021/acs.nanolett.8b02166>.
- (121) Meng, L.; Ma, W.; Lin, S.; Shi, S.; Li, Y.; Lin, Y. Tetrahedral DNA Nanostructure-Delivered DNAzyme for Gene Silencing to Suppress Cell Growth. *ACS Appl. Mater. Interfaces* **2019**, *acsami.8b22444*. <https://doi.org/10.1021/acsami.8b22444>.
- (122) Xie, X.; Shao, X.; Ma, W.; Zhao, D.; Shi, S.; Li, Q.; Lin, Y. Overcoming Drug-Resistant Lung Cancer by

- Paclitaxel Loaded Tetrahedral DNA Nanostructures. *Nanoscale* **2018**, *10* (12), 5457–5465. <https://doi.org/10.1039/c7nr09692e>.
- (123) Cutler, J. I.; Auyeung, E.; Mirkin, C. A. Spherical Nucleic Acids. *J. Am. Chem. Soc.* **2012**, *134* (3), 1376–1391. <https://doi.org/10.1021/ja209351u>.
- (124) Masserini, M. Nanoparticles for Brain Drug Delivery. *ISRN Biochem.* **2013**, *2013*, 1–18. <https://doi.org/10.1155/2013/238428>.
- (125) Stapleton, M.; Sawamoto, K.; Alméciga-Díaz, C. J.; Mackenzie, W. G.; Mason, R. W.; Orii, T.; Tomatsu, S. Development of Bone Targeting Drugs. *Int. J. Mol. Sci.* **2017**, *18* (7), 1–15. <https://doi.org/10.3390/ijms18071345>.
- (126) Dong, X.; Chu, D.; Wang, Z. Leukocyte-Mediated Delivery of Nanotherapeutics in Inflammatory and Tumor Sites. *Theranostics* **2017**, *7* (3), 751–763. <https://doi.org/10.7150/thno.18069>.
- (127) Murugan, K.; Choonara, Y. E.; Kumar, P.; Bijukumar, D.; du Toit, L. C.; Pillay, V. Parameters and Characteristics Governing Cellular Internalization and Trans-Barrier Trafficking of Nanostructures. *Int. J. Nanomedicine* **2015**, *10*, 2191–2206. <https://doi.org/10.2147/IJN.S75615>.
- (128) Choi, H. S.; Ashitate, Y.; Lee, J. H.; Kim, S. H.; Matsui, A.; Insin, N.; Bawendi, M. G.; Semmler-behnke, M.; Frangioni, J. V. Rapid Translocation of Nanoparticles from the Lung Airspaces to the Body. *Nat. Biotechnol.* **2010**, *28* (12), 1300–1303. <https://doi.org/10.1038/nbt.1696.Rapid>.
- (129) Fröhlich, E. The Role of Surface Charge in Cellular Uptake and Cytotoxicity of Medical Nanoparticles. *Int. J. Nanomedicine* **2012**, *7*, 5577–5591. <https://doi.org/10.2147/IJN.S36111>.
- (130) Nakamura, H.; Watano, S. Direct Permeation of Nanoparticles across Cell Membrane: A Review. *KONA Powder Part. J.* **2018**, *2018* (35), 49–65. <https://doi.org/10.14356/kona.2018011>.
- (131) Sun, H.; Jiang, C.; Wu, L.; Bai, X.; Zhai, S. Cytotoxicity-Related Bioeffects Induced by Nanoparticles: The Role of Surface Chemistry. *Front. Bioeng. Biotechnol.* **2019**, *7* (December), 1–22. <https://doi.org/10.3389/fbioe.2019.00414>.
- (132) Lundqvist, M.; Stigler, J.; Elia, G.; Lynch, I.; Cedervall, T.; Dawson, K. A. Nanoparticle Size and Surface Properties Determine the Protein Corona with Possible Implications for Biological Impacts. *PNAS* **2008**, *105* (38), 14265–14270.
- (133) Green, C. M.; Mathur, D.; Medintz, I. L. Understanding the Fate of DNA Nanostructures inside the Cell. *J. Mater. Chem. B* **2020**, *8* (29), 6170–6178. <https://doi.org/10.1039/d0tb00395f>.
- (134) Bei, Y. Endocytic Pathways and Endosomal Trafficking: A Primer. *Vienna Med. Wkly.* **2016**, *166* (7), 196–204. <https://doi.org/10.1007/s10354-016-0432-7.Endocytic>.
- (135) Battaglia, G.; Canton, I. Endocytosis at the Nanoscale. *Chem. Soc. Rev.* **2012**, *41* (7). <https://doi.org/10.1039/c2cs15260f>.
- (136) Schmid, S. L.; Conner, S. D. Regulated Portals of Entry into the Cell. *Nature* **2003**, *422* (March), 37–44.
- (137) Hillaireau, H.; Couvreur, P. Nanocarriers' Entry into the Cell: Relevance to Drug Delivery. *Cell. Mol. Life Sci.* **2009**, *66* (17), 2873–2896. <https://doi.org/10.1007/s00018-009-0053-z>.
- (138) Kaksonen, M.; Roux, A. Mechanisms of Clathrin-Mediated Endocytosis. *Nat. Rev. Mol. Cell Biol.* **2018**, *19* (5), 313–326. <https://doi.org/10.1038/nrm.2017.132>.
- (139) Lee, D. S.; Qian, H.; Tay, C. Y.; Leong, D. T. Cellular Processing and Destinies of Artificial DNA Nanostructures. *Chem. Soc. Rev.* **2016**, *45* (15), 4199–4225. <https://doi.org/10.1039/c5cs00700c>.
- (140) Popova, N. V.; Deyev, I. E.; Petrenko, A. G. Clathrin-Mediated Endocytosis and Adaptor Proteins. *Acta Naturae* **2013**, *5* (18), 62–73. <https://doi.org/10.32607/20758251-2013-5-3-62-73>.
- (141) Balakrishnan, D.; Wilkens, G. D.; Heddle, J. G. Delivering DNA Origami to Cells. *Nanomedicine* **2019**, *14* (7), 911–925. <https://doi.org/10.2217/nnm-2018-0440>.
- (142) Halley, P. D.; Lucas, C. R.; McWilliams, E. M.; Webber, M. J.; Patton, R. A.; Kural, C.; Lucas, D. M.; Byrd,

- J. C.; Castro, C. E. Daunorubicin-Loaded DNA Origami Nanostructures Circumvent Drug-Resistance Mechanisms in a Leukemia Model. *Small* **2016**, *12* (3), 308–320. <https://doi.org/10.1002/sml.201502118>.
- (143) al., R. et. Kinetics of Cellular Uptake of Viruses and Nanoparticles via Clathrin-Mediated Endocytosis. *Phys. Biol.* **2018**, *176* (5), 139–148. <https://doi.org/10.1088/1478-3975/13/1/016005>. Kinetics.
- (144) Fu, X.; Peng, F.; Lee, J.; Yang, Q.; Zhang, F.; Xiong, M.; Kong, G.; Meng, H. M.; Ke, G.; Zhang, X. B. *Aptamer-Functionalized DNA Nanostructures for Biological Applications*; Springer International Publishing, 2020; Vol. 378. <https://doi.org/10.1007/s41061-020-0283-y>.
- (145) Ranallo, S.; Prévost-Tremblay, C.; Idili, A.; Vallée-Bélisle, A.; Ricci, F. Antibody-Powered Nucleic Acid Release Using a DNA-Based Nanomachine. *Nat. Commun.* **2017**, *8* (May). <https://doi.org/10.1038/ncomms15150>.
- (146) Kim, K. R.; Kim, D. R.; Lee, T.; Yhee, J. Y.; Kim, B. S.; Kwon, I. C.; Ahn, D. R. Drug Delivery by a Self-Assembled DNA Tetrahedron for Overcoming Drug Resistance in Breast Cancer Cells. *Chem. Commun.* **2013**, *49* (20), 2010–2012. <https://doi.org/10.1039/c3cc38693g>.
- (147) Li, X.; Xu, F.; Yang, D.; Wang, P. A DNA-Binding, Albumin-Targeting Fusion Protein Promotes the Cellular Uptake and Bioavailability of Framework DNA Nanostructures. *Nanoscale* **2021**, *13* (12), 6038–6042. <https://doi.org/10.1039/d0nr07967g>.
- (148) Choi, C. H. J.; Hao, L.; Narayan, S. P.; Auyeung, E.; Mirkin, C. A. Mechanism for the Endocytosis of Spherical Nucleic Acid Nanoparticle Conjugates. *Proc. Natl. Acad. Sci.* **2013**, *110* (19), 7625–7630. <https://doi.org/10.1073/pnas.1305804110>.
- (149) Lim, K. S.; Lee, D. Y.; Valencia, G. M.; Won, Y.-W.; Bull, D. A. Nano-Self-Assembly of Nucleic Acids Capable of Transfection without a Gene Carrier. *Adv. Funct. Mater.* **2015**, *25* (34), 5445–5451. <https://doi.org/10.1002/adfm.201502067>.
- (150) Nam, K.; Im, B. I.; Kim, T.; Kim, Y. M.; Roh, Y. H. Anisotropically Functionalized Aptamer-DNA Nanostructures for Enhanced Cell Proliferation and Target-Specific Adhesion in 3D Cell Cultures. *Biomacromolecules* **2021**, *22* (7), 3138–3147. <https://doi.org/10.1021/acs.biomac.1c00619>.
- (151) Zeng, Y.; Nixon, R. L.; Liu, W.; Wang, R. The Applications of Functionalized DNA Nanostructures in Bioimaging and Cancer Therapy. *Biomaterials* **2021**, *268* (November 2020), 120560. <https://doi.org/10.1016/j.biomaterials.2020.120560>.
- (152) Maezawa, T.; Ohtsuki, S.; Hidaka, K.; Sugiyama, H.; Endo, M.; Takahashi, Y.; Takakura, Y.; Nishikawa, M. DNA Density-Dependent Uptake of DNA Origami-Based Two-or Three-Dimensional Nanostructures by Immune Cells. *Nanoscale* **2020**, *12* (27), 14818–14824. <https://doi.org/10.1039/d0nr02361b>.
- (153) Bastings, M. M. C.; Anastassacos, F. M.; Ponnuswamy, N.; Leifer, F. G.; Cuneo, G.; Lin, C.; Ingber, D. E.; Ryu, J. H.; Shih, W. M. Modulation of the Cellular Uptake of DNA Origami through Control over Mass and Shape. *Nano Lett.* **2018**, *18* (6), 3557–3564. <https://doi.org/10.1021/acs.nanolett.8b00660>.
- (154) Czogalla, A.; Franquelim, H. G.; Schwill, P. DNA Nanostructures on Membranes as Tools for Synthetic Biology. *Biophys. J.* **2016**, *110* (8), 1698–1707. <https://doi.org/10.1016/j.bpj.2016.03.015>.
- (155) Kocabey, S.; Kempter, S.; List, J.; Xing, Y.; Bae, W.; Schiffels, D.; Shih, W. M.; Simmel, F. C.; Liedl, T. Membrane-Assisted Growth of DNA Origami Nanostructure Arrays. *ACS Nano* **2015**, *9* (4), 3530–3539. <https://doi.org/10.1021/acs.nano.5b00161>.
- (156) Winkler, J. Oligonucleotide Conjugates for Therapeutic Applications. *Ther. Deliv.* **2013**, *4* (7), 791–809. <https://doi.org/10.4155/tde.13.47>.
- (157) Karaki, S.; Benizri, S.; Mejías, R.; Baylot, V.; Branger, N.; Nguyen, T.; Vialet, B.; Oumzil, K.; Barthélémy, P.; Rocchi, P. Lipid-Oligonucleotide Conjugates Improve Cellular Uptake and Efficiency of TCTP-Antisense in Castration-Resistant Prostate Cancer. *J. Control. Release* **2017**, *258*, 1–9. <https://doi.org/10.1016/J.JCONREL.2017.04.042>.

- (158) Burns, J. R.; Seifert, A.; Fertig, N.; Howorka, S. A Biomimetic DNA-Based Channel for the Ligand-Controlled Transport of Charged Molecular Cargo across a Biological Membrane. *Nat. Nanotechnol.* **2016**, *11* (2), 152–156. <https://doi.org/10.1038/nnano.2015.279>.
- (159) Birkholz, O.; Burns, J. R.; Richter, C. P.; Psathaki, O. E.; Howorka, S.; Piehler, J. Multi-Functional DNA Nanostructures That Puncture and Remodel Lipid Membranes into Hybrid Materials. *Nat. Commun.* **2018**, *9* (1). <https://doi.org/10.1038/s41467-018-02905-w>.
- (160) Bai, X. C.; Martin, T. G.; Scheres, S. H. W.; Dietz, H. Cryo-EM Structure of a 3D DNA-Origami Object. *Proc. Natl. Acad. Sci. U. S. A.* **2012**, *109* (49), 20012–20017. <https://doi.org/10.1073/pnas.1215713109>.
- (161) Lanphere, C.; Offenbartl-Stiegert, D.; Dorey, A.; Pugh, G.; Georgiou, E.; Xing, Y.; Burns, J. R.; Howorka, S. Design, Assembly, and Characterization of Membrane-Spanning DNA Nanopores. *Nat. Protoc.* **2021**, *16* (1), 86–130. <https://doi.org/10.1038/s41596-020-0331-7>.
- (162) Burns, J. R.; Stulz, E.; Howorka, S. Self-Assembled DNA Nanopores That Span Lipid Bilayers. *Nano Lett.* **2013**, *13* (6), 2351–2356. <https://doi.org/10.1021/nl304147f>.
- (163) Abercrombie, M.; Ambrose, E. J. The Surface Properties of Cancer Cells: A Review. *Cancer Res.* **1962**, *22*, 525–548.
- (164) VANECKO, S.; LASKOWSKI, M. Studies of the Specificity of Deoxyribonuclease I. *J. Biol. Chem.* **1961**, *236* (4), 1135–1140. [https://doi.org/10.1016/S0021-9258\(18\)64255-3](https://doi.org/10.1016/S0021-9258(18)64255-3).
- (165) Burns, J. R.; Howorka, S. Defined Bilayer Interactions of DNA Nanopores Revealed with a Nuclease-Based Nanoprobe Strategy. *ACS Nano* **2018**, *12* (4), 3263–3271. <https://doi.org/10.1021/acsnano.7b07835>.
- (166) Francis, G. L. Albumin and Mammalian Cell Culture: Implications for Biotechnology Applications. *Cytotechnology* **2010**, *62* (1), 1–16. <https://doi.org/10.1007/s10616-010-9263-3>.
- (167) Walsh, A. S.; Yin, H.; Erben, C. M.; Wood, M. J. A.; Turberfield, A. J. DNA Cage Delivery to Mammalian Cells. *ACS Nano* **2011**, *5* (7), 5427–5432. <https://doi.org/10.1021/nn2005574>.
- (168) Ohmann, A.; Li, C. Y.; Maffeo, C.; Al Nahas, K.; Baumann, K. N.; Göpfrich, K.; Yoo, J.; Keyser, U. F.; Aksimentiev, A. A Synthetic Enzyme Built from DNA Flips 107 Lipids per Second in Biological Membranes. *Nat. Commun.* **2018**, *9* (1). <https://doi.org/10.1038/s41467-018-04821-5>.
- (169) Chen, L.; Li, X.; Zhang, Y.; Chen, T.; Xiao, S.; Liang, H. Morphological and Mechanical Determinants of Cellular Uptake of Deformable Nanoparticles. *Nanoscale* **2018**, *10* (25), 11969–11979. <https://doi.org/10.1039/c8nr01521j>.
- (170) Bagheri, Y.; Chedid, S.; Shafiei, F.; Zhao, B.; You, M. A Quantitative Assessment of the Dynamic Modification of Lipid-DNA Probes on Live Cell Membranes. *Chem. Sci.* **2019**, *10* (48), 11030–11040. <https://doi.org/10.1039/c9sc04251b>.
- (171) Paddock, S. W. Laser Scanning Confocal Microscopy. *Mol. Biotechnol.* **2000**, *16*, 127–149.
- (172) Han, Y.; Li, M.; Qiu, F.; Zhang, M.; Zhang, Y. H. Cell-Permeable Organic Fluorescent Probes for Live-Cell Long-Term Super-Resolution Imaging Reveal Lysosome-Mitochondrion Interactions. *Nat. Commun.* **2017**, *8* (1). <https://doi.org/10.1038/s41467-017-01503-6>.
- (173) Yapici, N. B.; Bi, Y.; Li, P.; Chen, X.; Yan, X.; Mandalapu, S. R.; Faucett, M.; Jockusch, S.; Ju, J.; Gibson, K. M.; et al. Highly Stable and Sensitive Fluorescent Probes (LysoProbes) for Lysosomal Labeling and Tracking. *Sci. Rep.* **2015**, *5*, 1–8. <https://doi.org/10.1038/srep08576>.
- (174) Smith, S. A.; Selby, L. I.; Johnston, A. P. R.; Such, G. K. The Endosomal Escape of Nanoparticles: Toward More Efficient Cellular Delivery. **2018**. <https://doi.org/10.1021/acs.bioconjchem.8b00732>.
- (175) Leopold, P. L. Endosomal Escape Pathways for Delivery of Biologics. *Lysosomes Biol. Dis. Ther.* **2016**, *151* (3), 383–407. <https://doi.org/10.1002/9781118978320.ch16>.
- (176) Muro, S. A DNA-Device That Mediates Selective Endosomal Escape and Intracellular Delivery of Drugs

- and Biologicals. <https://doi.org/10.1002/adfm.201303188>.
- (177) Liang, L.; Li, J.; Li, Q.; Huang, Q.; Shi, J.; Yan, H.; Fan, C. Single-Particle Tracking and Modulation of Cell Entry Pathways of a Tetrahedral DNA Nanostructure in Live Cells. *Angew. Chemie - Int. Ed.* **2014**, *53* (30), 7745–7750. <https://doi.org/10.1002/anie.201403236>.
- (178) Chan, M. S.; Lo, P. K. Nanoneedle-Assisted Delivery of Site-Selective Peptide-Functionalized DNA Nanocages for Targeting Mitochondria and Nuclei. *Small* **2014**, *10* (7), 1255–1260. <https://doi.org/10.1002/sml.201302993>.
- (179) de Smidt, P. C.; Le Doan, T.; de Falco, S.; van Berkel, T. J. Association of Antisense Oligonucleotides with Lipoproteins Prolongs the Plasma Half-Life and Modifies the Tissue Distribution. *Nucleic Acids Res.* **1991**, *19* (17), 4695–4700.
- (180) Gissot, A.; Oumzil, K.; Patwa, A.; Barthélémy, P.; Gissot, A.; Oumzil, K.; Patwa, A.; Barthélémy, P. A Hybrid Lipid Oligonucleotide : A Versatile Tool for Supramolecular Chemistry. *New J. Chem.* **2014**, *38* (11), 5129–5134.
- (181) Young, J. D. E.; Hengartner, H.; Podack, E. R.; Cohn, Z. A. Purification and Characterization of a Cytolytic Pore-Forming Protein from Granules of Cloned Lymphocytes with Natural Killer Activity. *Cell* **1986**, *44* (6), 849–859. [https://doi.org/10.1016/0092-8674\(86\)90007-3](https://doi.org/10.1016/0092-8674(86)90007-3).
- (182) Peraro, M. D.; Van Der Goot, F. G. Pore-Forming Toxins: Ancient, but Never Really out of Fashion. *Nat. Rev. Microbiol.* **2016**, *14* (2), 77–92. <https://doi.org/10.1038/nrmicro.2015.3>.
- (183) Burns, J. R.; Al-juffali, N.; Janes, S. M.; Howorka, S. Angewandte Membrane-Spanning DNA Nanopores with Cytotoxic Effect \*\*. **2014**, 12466–12470. <https://doi.org/10.1002/anie.201405719>.
- (184) Kondratskyi, A.; Kondratska, K.; Skryma, R.; Prevarskaya, N. Ion Channels in the Regulation of Apoptosis. *Biochim. Biophys. Acta - Biomembr.* **2015**, *1848* (10), 2532–2546. <https://doi.org/10.1016/j.bbamem.2014.10.030>.
- (185) Galluzzi, L.; Vitale, I.; Aaronson, S. A.; Abrams, J. M.; Adam, D.; Agostinis, P.; Alnemri, E. S.; Altucci, L.; Amelio, I.; Andrews, D. W.; et al. Molecular Mechanisms of Cell Death: Recommendations of the Nomenclature Committee on Cell Death 2018. *Cell Death Differ.* **2018**, *25* (3), 486–541. <https://doi.org/10.1038/s41418-017-0012-4>.
- (186) Bonnier, F.; Keating, M. E.; Wróbel, T. P.; Majzner, K.; Baranska, M.; Garcia-Munoz, A.; Blanco, A.; Byrne, H. J. Cell Viability Assessment Using the Alamar Blue Assay: A Comparison of 2D and 3D Cell Culture Models. *Toxicol. Vitro.* **2015**, *29* (1), 124–131. <https://doi.org/10.1016/j.tiv.2014.09.014>.
- (187) Czogalla, A.; Kauert, D. J.; Franquelim, H. G.; Uzunova, V.; Zhang, Y.; Seidel, R.; Schwille, P. Amphipathic DNA Origami Nanoparticles to Scaffold and Deform Lipid Membrane Vesicles. *Angew. Chemie - Int. Ed.* **2015**, *54* (22), 6501–6505. <https://doi.org/10.1002/anie.201501173>.
- (188) Kuhlmann, M.; Hamming, J. B. R.; Voldum, A.; Tsakiridou, G.; Larsen, M. T.; Schmøkel, J. S.; Sohn, E.; Bienk, K.; Schaffert, D.; Sørensen, E. S.; et al. An Albumin-Oligonucleotide Assembly for Potential Combinatorial Drug Delivery and Half-Life Extension Applications. *Mol. Ther. - Nucleic Acids* **2017**, *9* (December), 284–293. <https://doi.org/10.1016/j.omtn.2017.10.004>.
- (189) Karimi, M.; Bahrami, S.; Ravari, S. B.; Zangabad, P. S.; Mirshekari, H.; Bozorgomid, M.; Shahreza, S.; Sori, M.; Hamblin, R.; Education, U. S.; et al. Albumin Nanostructures as Advanced Drug Delivery Systems. *Expert Opin. Drug Deliv.* **2016**, *13* (11), 1609–1623. <https://doi.org/10.1080/17425247.2016.1193149>.Albumin.
- (190) Xu, X.; Fang, S.; Zhuang, Y.; Wu, S.; Pan, Q.; Li, L.; Wang, X.; Sun, X.; Liu, B.; Wu, Y. Cationic Albumin Encapsulated DNA Origami for Enhanced Cellular Transfection and Stability. *Materials (Basel)*. **2019**, *16* (6), 1–12. <https://doi.org/10.3390/ma12060949>.
- (191) Koren, E.; Torchilin, V. P. Cell-Penetrating Peptides: Breaking through to the Other Side. *Trends Mol.*

- Med.* **2012**, *18* (7), 385–393. <https://doi.org/10.1016/j.molmed.2012.04.012>.
- (192) Frankel, A. D.; Pabo, C. O. Cellular Uptake of the Tat Protein from Human Immunodeficiency Virus. *Cell* **1988**, *55* (6), 1189–1193. [https://doi.org/10.1016/0092-8674\(88\)90263-2](https://doi.org/10.1016/0092-8674(88)90263-2).
- (193) Green, M.; Loewenstein, P. M. Autonomous Functional Domains of Chemically Synthesized Human Immunodeficiency Virus Tat Trans-Activator Protein. *Cell* **1988**, *55* (6), 1179–1188. [https://doi.org/10.1016/0092-8674\(88\)90262-0](https://doi.org/10.1016/0092-8674(88)90262-0).
- (194) Derossi, D.; Joliot, A. H.; Chassaing, G.; Prochiantz, A. The Third Helix of the Antennapedia Homeodomain Translocates through Biological Membranes. *J. Biol. Chem.* **1994**, *269* (14), 10444–10450. [https://doi.org/10.1016/s0021-9258\(17\)34080-2](https://doi.org/10.1016/s0021-9258(17)34080-2).
- (195) Derakhshankhah, H.; Jafari, S. Cell Penetrating Peptides: A Concise Review with Emphasis on Biomedical Applications. *Biomed. Pharmacother.* **2018**, *108* (June), 1090–1096. <https://doi.org/10.1016/j.biopha.2018.09.097>.
- (196) Kardani, K.; Bolhassani, A. Cppsite 2.0: An Available Database of Experimentally Validated Cell-Penetrating Peptides Predicting Their Secondary and Tertiary Structures. *J. Mol. Biol.* **2021**, *433* (11), 166703. <https://doi.org/10.1016/j.jmb.2020.11.002>.
- (197) Ziegler, A.; Nervi, P.; Dürrenberger, M.; Seelig, J. The Cationic Cell-Penetrating Peptide CPPTAT Derived from the HIV-1 Protein TAT Is Rapidly Transported into Living Fibroblasts: Optical, Biophysical, and Metabolic Evidence. *Biochemistry* **2005**, *44* (1), 138–148. <https://doi.org/10.1021/bi0491604>.
- (198) Falanga, A.; Galdiero, M.; Morelli, G.; Galdiero, S. Membranotropic Peptides Mediating Viral Entry. *Pept. Sci.* **2018**, *110* (5). <https://doi.org/10.1002/pep2.24040>.
- (199) Lönn, P.; Kacsinta, A. D.; Cui, X.-S.; Hamil, A. S.; Kaulich, M.; Gogoi, K.; Dowdy, S. F. Enhancing Endosomal Escape for Intracellular Delivery of Macromolecular Biologic Therapeutics. *Sci. Rep.* **2016**, *6* (1), 32301. <https://doi.org/10.1038/srep32301>.
- (200) Maier, O.; Galan, D. L.; Wodrich, H.; Wiethoff, C. M. An N-Terminal Domain of Adenovirus Protein VI Fragments Membranes By Inducing Positive Membrane Curvature. *Virology* **2010**, *402* (1), 11–19. <https://doi.org/10.1016/j.virol.2010.03.043>.
- (201) Regberg, J.; Vasconcelos, L.; Madani, F.; Langel, Ü.; Hällbrink, M. PH-Responsive PepFect Cell-Penetrating Peptides. *Int. J. Pharm.* **2016**, *501* (1–2), 32–38. <https://doi.org/10.1016/j.ijpharm.2016.01.055>.
- (202) Lindberg, S.; Muñoz-Alarcón, A.; Helmfors, H.; Mosqueira, D.; Gyllborg, D.; Tudoran, O.; Langel, Ü. PepFect15, a Novel Endosomolytic Cell-Penetrating Peptide for Oligonucleotide Delivery via Scavenger Receptors. *Int. J. Pharm.* **2013**, *441* (1–2), 242–247. <https://doi.org/10.1016/j.ijpharm.2012.11.037>.
- (203) Zhang, Y.; Li, L.; Chang, L.; Liu, H.; Song, J.; Liu, Y.; Bao, H.; Liu, B.; Wang, R.; Ni, J. Design of a New PH-Activatable Cell-Penetrating Peptide for Drug Delivery into Tumor Cells. *Chem. Biol. Drug Des.* **2019**, *94* (5), 1884–1893. <https://doi.org/10.1111/cbdd.13537>.
- (204) Li, W.; Nicol, F.; Szoka, F. C. GALA: A Designed Synthetic PH-Responsive Amphipathic Peptide with Applications in Drug and Gene Delivery. *Adv. Drug Deliv. Rev.* **2004**, *56* (7), 967–985. <https://doi.org/10.1016/j.addr.2003.10.041>.
- (205) Nishimura, Y.; Takeda, K.; Ezawa, R.; Ishii, J.; Ogino, C.; Kondo, A. A Display of PH-Sensitive Fusogenic GALA Peptide Facilitates Endosomal Escape from a Bio-Nanocapsule via an Endocytic Uptake Pathway. *J. Nanobiotechnology* **2014**, *12* (1), 2–7. <https://doi.org/10.1186/1477-3155-12-11>.
- (206) Guidotti, G.; Brambilla, L.; Rossi, D. Cell-Penetrating Peptides: From Basic Research to Clinics. *Trends Pharmacol. Sci.* **2017**, *38* (4), 406–424. <https://doi.org/10.1016/j.tips.2017.01.003>.
- (207) Xie, J.; Bi, Y.; Zhang, H.; Dong, S.; Teng, L.; Lee, R. J.; Yang, Z. Cell-Penetrating Peptides in Diagnosis and Treatment of Human Diseases: From Preclinical Research to Clinical Application. *Front. Pharmacol.*

- 2020**, 11 (May), 1–23. <https://doi.org/10.3389/fphar.2020.00697>.
- (208) Kristensen, M.; Birch, D.; Nielsen, H. M. Applications and Challenges for Use of Cell-Penetrating Peptides as Delivery Vectors for Peptide and Protein Cargos. *Int. J. Mol. Sci.* **2016**, 17 (2). <https://doi.org/10.3390/ijms17020185>.
- (209) Goswami, D.; Machini, M. T.; Silvestre, D. M.; Nomura, C. S.; Esposito, B. P. Cell Penetrating Peptide (CPP)-Conjugated Desferrioxamine for Enhanced Neuroprotection: Synthesis and in Vitro Evaluation. *Bioconjug. Chem.* **2014**, 25 (11), 2067–2080. <https://doi.org/10.1021/bc5004197>.
- (210) Duan, Z.; Chen, C.; Qin, J.; Liu, Q.; Wang, Q.; Xu, X.; Wang, J. Cell-Penetrating Peptide Conjugates to Enhance the Antitumor Effect of Paclitaxel on Drug-Resistant Lung Cancer. *Drug Deliv.* **2017**, 24 (1), 752–764. <https://doi.org/10.1080/10717544.2017.1321060>.
- (211) Taylor, R. E.; Zahid, M. Cell Penetrating Peptides, Novel Vectors for Gene Therapy. *Pharmaceutics* **2020**, 12 (3), 1–21. <https://doi.org/10.3390/pharmaceutics12030225>.
- (212) Deshayes, S.; Konate, K.; Aldrian, G.; Crombez, L.; Heitz, F.; Divita, G. Structural Polymorphism of Non-Covalent Peptide-Based Delivery Systems: Highway to Cellular Uptake. *Biochim. Biophys. Acta - Biomembr.* **2010**, 1798 (12), 2304–2314. <https://doi.org/10.1016/j.bbamem.2010.06.005>.
- (213) Veldhoen, S.; Laufer, S. D.; Trampe, A.; Restle, T. Cellular Delivery of Small Interfering RNA by a Non-Covalently Attached Cell-Penetrating Peptide: Quantitative Analysis of Uptake and Biological Effect. *Nucleic Acids Res.* **2006**, 34 (22), 6561–6573. <https://doi.org/10.1093/nar/gkl941>.
- (214) Stewart, K. M.; Horton, K. L.; Kelley, S. O. Cell-Penetrating Peptides as Delivery Vehicles for Biology and Medicine. *Org. Biomol. Chem.* **2008**, 6 (13), 2242–2255. <https://doi.org/10.1039/b719950c>.
- (215) Walrant, A.; Alves, I. D.; Sagan, S. Molecular Partners for Interaction and Cell Internalization of Cell-Penetrating Peptides: How Identical Are They? *Nanomedicine* **2011**, 7 (1), 133–143.
- (216) Gräslund, A.; Madani, F.; Lindberg, S.; Langel, Ü.; Futaki, S. Mechanisms of Cellular Uptake of Cell-Penetrating Peptides. *J. Biophys.* **2011**, 2011. <https://doi.org/10.1155/2011/414729>.
- (217) Copolovici, D. M.; Langel, K.; Eriste, E. Cell-Penetrating Peptides: Design, Synthesis, and Applications. *Biochem. Soc. Trans.* **2014**, 8 (3), 1972–1994.
- (218) Baio, J. E.; Schach, D.; Fuchs, A. V.; Schmäser, L.; Billecke, N.; Bubeck, C.; Landfester, K.; Bonn, M.; Bruns, M.; Weiss, C. K.; et al. Reversible Activation of PH-Sensitive Cell Penetrating Peptides Attached to Gold Surfaces. *Chem. Commun.* **2015**, 51 (2), 273–275. <https://doi.org/10.1039/c4cc07278b>.
- (219) Haag, R. Multivalency as a Chemical Organization and Action Principle. *Beilstein J. Org. Chem.* **2015**, 11, 848–849. <https://doi.org/10.3762/bjoc.11.94>.
- (220) Kiessling, L. L.; Gestwicki, J. E.; Strong, L. E. Synthetic Multivalent Ligands in the Exploration of Cell-Surface Interactions. *Curr. Opin. Chem. Biol.* **2000**, 4 (6), 696–703. [https://doi.org/10.1016/S1367-5931\(00\)00153-8](https://doi.org/10.1016/S1367-5931(00)00153-8).
- (221) Mammen, M.; Choi, S. K.; Whitesides, G. M. Polyvalent Interactions in Biological Systems: Implications for Design and Use of Multivalent Ligands and Inhibitors. *Angew. Chemie - Int. Ed.* **1998**, 37 (20), 2754–2794. [https://doi.org/10.1002/\(sici\)1521-3773\(19981102\)37:20<2754::aid-anie2754>3.0.co;2-3](https://doi.org/10.1002/(sici)1521-3773(19981102)37:20<2754::aid-anie2754>3.0.co;2-3).
- (222) Yeldell, S. B.; Seitz, O. Nucleic Acid Constructs for the Interrogation of Multivalent Protein Interactions. *Chem. Soc. Rev.* **2020**, 49 (19), 6848–6865. <https://doi.org/10.1039/d0cs00518e>.
- (223) Dalal, C.; Jana, N. R. Multivalency Effect of TAT-Peptide-Functionalized Nanoparticle in Cellular Endocytosis and Subcellular Trafficking. *J. Phys. Chem. B* **2017**, 121 (14), 2942–2951. <https://doi.org/10.1021/acs.jpcc.6b12182>.
- (224) Oba, M.; Nagano, Y.; Kato, T.; Tanaka, M. Secondary Structures and Cell-Penetrating Abilities of Arginine-Rich Peptide Foldamers. *Sci. Rep.* **2019**, 9 (1), 1–9. <https://doi.org/10.1038/s41598-018-38063-8>.

- (225) Bode, S. A.; Wallbrecher, R.; Brock, R.; van Hest, J. C. M.; Löwik, D. W. P. M. Activation of Cell-Penetrating Peptides by Disulfide Bridge Formation of Truncated Precursors. *Chem. Commun.* **2014**, *50* (4), 415–417. <https://doi.org/10.1039/c3cc46826g>.
- (226) Monreal, I. A.; Liu, Q.; Tyson, K.; Bland, T.; Dalisay, D. S.; Adams, E. V.; Wayman, G. A.; Aguilar, H. C.; Saludes, J. P. Branched Dimerization of Tat Peptide Improves Permeability to HeLa and Hippocampal Neuronal Cells. *Chem. Commun.* **2015**, *51* (25), 5463–5466. <https://doi.org/10.1039/c5cc00882d>.
- (227) Kim, H.; Kitamatsu, M.; Ohtsuki, T. Enhanced Intracellular Peptide Delivery by Multivalent Cell-Penetrating Peptide with Bioreducible Linkage. *Bioorganic Med. Chem. Lett.* **2018**, *28* (3), 378–381. <https://doi.org/10.1016/j.bmcl.2017.12.035>.
- (228) Chakrabarti, A.; Witsenburg, J. J.; Sinzinger, M. D.; Richter, M.; Wallbrecher, R.; Cluitmans, J. C.; Verdurmen, W. P. R.; Tanis, S.; Adjobo-Hermans, M. J. W.; Rademann, J.; et al. Multivalent Presentation of the Cell-Penetrating Peptide Nona-Arginine on a Linear Scaffold Strongly Increases Its Membrane-Perturbing Capacity. *Biochim. Biophys. Acta - Biomembr.* **2014**, *1838* (12), 3097–3106. <https://doi.org/10.1016/j.bbamem.2014.08.001>.
- (229) Yessine, M. A.; Leroux, J. C. Membrane-Destabilizing Polyanions: Interaction with Lipid Bilayers and Endosomal Escape of Biomacromolecules. *Adv. Drug Deliv. Rev.* **2004**, *56* (7), 999–1021. <https://doi.org/10.1016/j.addr.2003.10.039>.
- (230) Hagino, Y.; Khalil, I. A.; Kimura, S.; Kusumoto, K.; Harashima, H. GALA-Modified Lipid Nanoparticles for the Targeted Delivery of Plasmid DNA to the Lungs. *Mol. Pharm.* **2021**, *18* (3), 878–888. <https://doi.org/10.1021/acs.molpharmaceut.0c00854>.
- (231) Locke, T.; Sofou, S. Clustered versus Uniform Display of GALA-Peptides on Carrier Nanoparticles: Enhancing the Permeation of Noncharged Fluid Lipid Membranes. **2017**. <https://doi.org/10.1021/acs.langmuir.7b03706>.
- (232) Haas, D. H.; Murphy, R. M. Design of a PH-Sensitive Pore-Forming Peptide with Improved Performance. *J. Pept. Res.* **2004**, *63* (1), 9–16. <https://doi.org/10.1046/j.1399-3011.2004.00098.x>.
- (233) Lou, B.; De Koker, S.; Lau, C. Y. J.; Hennink, W. E.; Mastrobattista, E. mRNA Polyplexes with Post-Conjugated GALA Peptides Efficiently Target, Transfect, and Activate Antigen Presenting Cells. *Bioconjug. Chem.* **2018**, *30*, 461–475. <https://doi.org/10.1021/acs.bioconjchem.8b00524>.
- (234) Kuehne, J.; Murphy, R. M. Synthesis and Characterization of Membrane-Active GALA-OKT9 Conjugates. *§Bioconjugate Chem.* **2001**, *12* (10), 742–749.
- (235) Nir, S.; Szoka, F. C. Orientation of the Pore-Forming Peptide GALA in POPC Vesicles Determined by a BODIPY-Avidin / Biotin Binding Assay. *Biophys. J.* **1999**, *76* (April), 2121–2141. [https://doi.org/10.1016/S0006-3495\(99\)77368-6](https://doi.org/10.1016/S0006-3495(99)77368-6).
- (236) Parente, R. A.; Nir, S.; Szoka, F. C. PH-Dependent Fusion of Phosphatidylcholine Small Vesicles. Induction by a Synthetic Amphipathic Peptide. *J. Biol. Chem.* **1988**, *263* (10), 4724–4730. [https://doi.org/10.1016/s0021-9258\(18\)68843-x](https://doi.org/10.1016/s0021-9258(18)68843-x).
- (237) Parente, R. A.; Nir, S.; Szoka, F. C. Mechanism of Leakage of Phospholipid Vesicle Contents Induced by the Peptide GALA. *Biochemistry* **1990**, *29* (37), 8720–8728. <https://doi.org/10.1021/bi00489a031>.
- (238) Lin, B. F.; Missirlis, D.; Krogstad, D. V.; Tirrell, M. Structural Effects and Lipid Membrane Interactions of the PH-Responsive GALA Peptide with Fatty Acid Acylation. *Biochemistry* **2012**, *51* (23), 4658–4668. <https://doi.org/10.1021/bi300314h>.
- (239) Parente, R. A.; Nadasdi, L.; Subbarao, N. K.; Szoka, F. C. Association of a PH-Sensitive Peptide with Membrane Vesicles: Role of Amino Acid Sequence. *Biochemistry*. 1990, pp 8713–8719. <https://doi.org/10.1021/bi00489a030>.
- (240) Williams, B. A. R.; Chaput, J. C. Synthesis of Peptide-Oligonucleotide Conjugates Using a

- Heterobifunctional Crosslinker. *Curr. Protoc. Nucleic Acid Chem.* **2010**, No. SUPPL. 42, 1–29.  
<https://doi.org/10.1002/0471142700.nc0441s42>.
- (241) Macculloch, T.; Buchberger, A.; Stephanopoulos, N. Emerging Applications of Peptide-Oligonucleotide Conjugates: Bioactive Scaffolds, Self-Assembling Systems, and Hybrid Nanomaterials. *Org. Biomol. Chem.* **2019**, *17* (7), 1668–1682. <https://doi.org/10.1039/c8ob02436g>.
- (242) Drygin, Y. F. Natural Covalent Complexes of Nucleic Acids and Proteins: Some Comments on Practice and Theory on the Path from Well-Known Complexes to New Ones. *Nucleic Acids Res.* **1998**, *26* (21), 4791–4796. <https://doi.org/10.1093/nar/26.21.4791>.
- (243) Stephanopoulos, N.; Ortony, J. H.; Stupp, S. I. Self-Assembly for the Synthesis of Functional Biomaterials. *Acta Mater.* **2013**, *61* (3), 912–930. <https://doi.org/10.1016/j.actamat.2012.10.046>.
- (244) Lou, C.; Martos-Maldonado, M. C.; Madsen, C. S.; Thomsen, R. P.; Midtgaard, S. R.; Christensen, N. J.; Kjems, J.; Thulstrup, P. W.; Wengel, J.; Jensen, K. J. Peptide-Oligonucleotide Conjugates as Nanoscale Building Blocks for Assembly of an Artificial Three-Helix Protein Mimic. *Nat. Commun.* **2016**, *7*, 1–9. <https://doi.org/10.1038/ncomms12294>.
- (245) Kern, N.; Dong, R.; Douglas, S.; Vale, R. D.; Morrissey, M. A. Tight Nanoscale Clustering of Fcγ Receptors Using DNA Origami Promotes Phagocytosis. *Elife* **2021**, *10*, 1–29. <https://doi.org/10.7554/eLife.68311>.
- (246) Stephanopoulos, N.; Freeman, R.; North, H. A.; Sur, S.; Jeong, S. J.; Tantakitti, F.; Kessler, J. A.; Stupp, S. I. Bioactive DNA-Peptide Nanotubes Enhance the Differentiation of Neural Stem Cells into Neurons. *Nano Lett.* **2015**, *15* (1), 603–609. <https://doi.org/10.1021/nl504079q>.
- (247) Freeman, R.; Stephanopoulos, N.; Álvarez, Z.; Lewis, J. A.; Sur, S.; Serrano, C. M.; Boekhoven, J.; Lee, S. S.; Stupp, S. I. Instructing Cells with Programmable Peptide DNA Hybrids. *Nat. Commun.* **2017**, *8* (May). <https://doi.org/10.1038/ncomms15982>.
- (248) Rosier, B. J. H. M.; Markvoort, A. J.; Gumí-Audenis, B.; Roodhuizen, J. A. L.; Hamer, A. den; Brunsveld, L.; Greef, T. F. A. de. A DNA-Based Synthetic Apoptosome. *bioRxiv* **2019**, 660183. <https://doi.org/10.1101/660183>.
- (249) Rooks, M. .; Garrett, W. . Programmable Multivalent Display of Receptor Ligands Using Peptide Nucleic Acid Nanoscaffolds. *Nat. Commun.* **2012**, *3* (614), 139–148. <https://doi.org/10.1038/ncomms1629.Programmable>.
- (250) Williams, B. A. R.; Diehnelt, C. W.; Belcher, P.; Greving, M.; Woodbury, N. W.; Johnston, S. A.; Chaput, J. C. Creating Protein Affinity Reagents by Combining Peptide Ligands on Synthetic DNA Scaffolds. *J. Am. Chem. Soc.* **2009**, *131* (47), 17233–17241. <https://doi.org/10.1021/ja9051735>.
- (251) Diezmann, F.; Von Kleist, L.; Haucke, V.; Seitz, O. Probing Heterobivalent Binding to the Endocytic AP-2 Adaptor Complex by DNA-Based Spatial Screening. *Org. Biomol. Chem.* **2015**, *13* (29), 8008–8015. <https://doi.org/10.1039/c5ob00943j>.
- (252) Janssen, B. M. G.; Lempens, E. H. M.; Olijve, L. L. C.; Voets, I. K.; van Dongen, J. L. J.; de Greef, T. F. A.; Merkx, M. Reversible Blocking of Antibodies Using Bivalent Peptide–DNA Conjugates Allows Protease-Activatable Targeting. *Chem. Sci.* **2013**, *4* (4), 1442–1450. <https://doi.org/10.1039/c3sc22033h>.
- (253) Hong, F.; Zhang, F.; Liu, Y.; Yan, H. DNA Origami: Scaffolds for Creating Higher Order Structures. *Chemical Reviews.* 2017, pp 12584–12640. <https://doi.org/10.1021/acs.chemrev.6b00825>.
- (254) Williams, B. A. R.; Lund, K.; Liu, Y.; Yan, H.; Chaput, J. C. Self-Assembled Peptide Nanoarrays: An Approach to Studying Protein-Protein Interactions. *Angew. Chemie - Int. Ed.* **2007**, *46* (17), 3051–3054. <https://doi.org/10.1002/anie.200603919>.
- (255) Lee, H.; Lytton-jean, A. K. R.; Chen, Y.; Love, K. T.; Park, A. I.; Karagiannis, E. D.; Sehgal, A.; Querbes, W.; Zurenko, C. S.; Jayaraman, M.; et al. Molecularly Self-Assembled Nucleic Acids... *Nat Nanotechnol*

- 2014**, 7 (6), 389–393. <https://doi.org/10.1038/nnano.2012.73>.Molecularly.
- (256) Ke, Y.; Douglas, S. M.; Liu, M.; Sharma, J.; Cheng, A.; Leung, A.; Liu, Y.; Shih, W. M.; Yan, H. Multilayer DNA Origami Packed on a Square Lattice. *J. Am. Chem. Soc.* **2009**, 131 (43), 15903–15908. <https://doi.org/10.1021/ja906381y>.
- (257) Couch, G. S.; Hendrix, D. K.; Ferrin, T. E. Nucleic Acid Visualization with UCSF Chimera. *Nucleic Acids Res.* **2006**, 34 (4), 1–5. <https://doi.org/10.1093/nar/gnj031>.
- (258) Roodhuizen, J. A. L.; Hendrikx, P. J. T. M.; Hilbers, P. A. J.; De Greef, T. F. A.; Markvoort, A. J. Counterion-Dependent Mechanisms of DNA Origami Nanostructure Stabilization Revealed by Atomistic Molecular Simulation. *ACS Nano* **2019**, 13 (9), 10798–10809. <https://doi.org/10.1021/acsnano.9b05650>.
- (259) Stahl, E.; Martin, T. G.; Praetorius, F.; Dietz, H. Facile and Scalable Preparation of Pure and Dense DNA Origami Solutions. *Angew. Chemie - Int. Ed.* **2014**, 53 (47), 12735–12740. <https://doi.org/10.1002/anie.201405991>.
- (260) Kobayashi, T.; Beuchat, M. H.; Chevallier, J.; Makino, A.; Mayran, N.; Escola, J. M.; Lebrand, C.; Cosson, P.; Kobayashi, T.; Gruenberg, J. Separation and Characterization of Late Endosomal Membrane Domains. *J. Biol. Chem.* **2002**, 277 (35), 32157–32164. <https://doi.org/10.1074/jbc.M202838200>.
- (261) Burns, J. R.; Lamarre, B.; Pyne, A. L. B.; Noble, J. E.; Ryadnov, M. G. DNA Origami Inside-Out Viruses. **2018**. <https://doi.org/10.1021/acssynbio.7b00278>.
- (262) Belouzard, S.; Millet, J. K.; Licitra, B. N.; Whittaker, G. R. Mechanisms of Coronavirus Cell Entry Mediated by the Viral Spike Protein. *Viruses* **2012**, 4 (6), 1011–1033. <https://doi.org/10.3390/v4061011>.
- (263) Huang, Hsiang-Ling, Hsiang-Wei Hsing, Tzu-Chia Lai, Yi-Wen Chen, Tian-Ren Lee, Hsin-Tsu Chan, Ping-Chiang Lyu, Chieh-Lin Wu, Ying-Chieh Lu, Szu-Ting Lin, Cheng-Wen Lin, Chih-Ho Lai, Hao-Teng Chang, H.-C. C. & H.-L. C. Research Trypsin-Induced Proteome Alteration during Cell Subculture in Mammalian Cells. *J. Biomed. Sci.* **2010**, 17 (36). <https://doi.org/10.1186/1423-0127-17-36>.
- (264) Lacroix, A.; Vengut-Climent, E.; De Rochambeau, D.; Sleiman, H. F. Uptake and Fate of Fluorescently Labeled DNA Nanostructures in Cellular Environments: A Cautionary Tale. *ACS Cent. Sci.* **2019**, 5 (5), 882–891. <https://doi.org/10.1021/acscentsci.9b00174>.